University of Maribor Press

ISSN 1854-0171

ACTA GEOTECHNICA SLOVENICA

2019/1

VOL. 16

ISSN: 1854-0171

ACTA GEOTECHNICA SLOVENICA

Ustanovitelji | Founders

Univerza v Mariboru, Fakulteta za gradbeništvo, prometno inženirstvo in arhitekturo
University of Maribor, Faculty of Civil Engineering, Transportation Engineering and Architecture

Univerza v Ljubljani, Fakulteta za gradbeništvo in geodezijo
University of Ljubljana, Faculty of Civil and Geodetic Engineering

Univerza v Ljubljani, Naravoslovnotehniška fakulteta
University of Ljubljana, Faculty of Natural Sciences and Engineering

Slovensko geotehniško društvo
Slovenian Geotechnical Society

Društvo za podzemne in geotehniške konstrukcije
Society for Underground and Geotechnical Constructions

Izdajatelj | Publisher

Univerza v Mariboru, Fakulteta za gradbeništvo, prometno inženirstvo in arhitekturo
Faculty of Civil Engineering, Transportation Engineering and Architecture

Naklada | Circulation

200 izvodov - issues

Cena | Price

25 EUR/letnik - 25 EUR/vol.; (50 EUR for institutions/za institucije)

Tisk | Print

Tiskarna Saje d.o.o.

Revija redno izhaja dvakrat letno. Članki v reviji so recenzirani s strani priznanih mednarodnih strokovnjakov. Baze podatkov v katerih je revija indeksirana: SCIE - Science Citation Index Expanded, JCR – Journal Citation Reports / Science Edition, ICONDA - The international Construction database, GeoRef. Izid publikacije je finančno podprla Javna agencija za raziskovalno dejavnost Republike Slovenije iz naslova razpisa za sofinanciranje domačih periodičnih publikacij.

Založnik | Published by

Univerzitetna založba Univerze v Mariboru
Slomškov trg 15, 2000 Maribor, Slovenija
e-pošta: zalozba@um.si, http://press.um.si/, http://journals.um.si/

University of Maribor Press
Slomškov trg 15, 2000 Maribor, Slovenia
e-mail: zalozba@um.si, http://press.um.si/, http://journals.um.si/

Naslov uredništva | Address

ACTA GEOTECHNICA SLOVENICA
Univerza v Mariboru, Fakulteta za gradbeništvo, prometno inženirstvo in arhitekturo
Smetanova ulica 17, 2000 Maribor, Slovenija
Telefon / Telephone: +386 (0)2 22 94 300
Faks / Fax: +386 (0)2 25 24 179
E-pošta / E-mail: ags@um.si

Spletni naslov | web Address

http://zalozba.um.si/index.php/ags/index

The journal is published twice a year. Papers are peer reviewed by renowned international experts. Indexation data bases of the journal: SCIE - Science Citation Index Expanded, JCR – Journal Citation Reports / Science Edition, ICONDA- The international Construction database, GeoRef. The publication was financially supported by Slovenian Research Agency according to the Tender for co-financing of domestic periodicals.

DETERMINING THE POSITION OF POINTS ON GEOLOGICALLY UNSTABLE LAND WITH GEODETIC MONITORING

DOLOČANJE POLOŽAJA TOČK NA GEOLOŠKO NESTABILNIH TLEH Z GEODETSKIM MONITORINGOM

Boštjan Kovačič
University of Maribor,
Faculty of civil engineering, transportation engineering and architecture
Smetanova 17, 2000 Maribor, Slovenia
E-mail: bostjan.kovacic@um.si

DOI https://doi.org/10.18690/actageotechslov.16.1.2-12.2019

Keywords

geodesy, geotechnics, engineering, monitoring, GNSS measurements

Ključne besede

geodezija, geotehnika, inženirstvo, monitoring, GNSS meritve

Abstract

An accurate determination of tectonic displacements is very important for the safety of people and animals as well as for natural and artificial objects. When establishing the short-term and long-term displacements of land or objects, the expected displacements should be anticipated in order to define the method of geodetic monitoring, which has become a regular feature in geotechnical monitoring.
In general, the land growling is determined by geodetic methods: the trigonometric method predominates in short--term monitoring, whereas the GNSS (Global Navigation Satellite System) method is mostly used for long-term monitoring, depending on the properties, complexity and duration of each project. Both methods provide reliable results with accuracy range of a few millimetres. This article focuses on the GNSS method, which has become irreplaceable for the monitoring of land growling. The article describes a procedure for determining the process in the case study of Razdrto-Vipava highway, where displacements have been monitored since 2007. Moreover, the process of contacting the European control point and procedure for levelling the measured values are explained.

Izvleček

Natančno ugotavljanje tektonskih pomikov je zelo pomembno za varnost ljudi, živali ter zgrajenih in naravnih objektov. Kadar ugotavljamo kratkoročne ali dolgoročne pomike moramo poznati pričakovane pomike, saj se na osnovi tega odločimo za metodo geodetskega monitoringa, ki je postala stalnica pri geotehničnih monitoringih. Z geodetskimi metodami največkrat ugotavljamo plazenje tal. Pri kratkoročnih monitoringih izstopa trigonometrična metoda medtem, ko se GNSS (Global Navigation Satellite System) metoda večinoma uporablja za dolgoročne monitoringe, ki so odvisni od lastnosti, kompleksnosti in trajanja projekta. Obe metodi nam dajeta zanesljive rezultate v območju natačnosti nekaj milimetrov. V prispevku se bomo osredotočili na metodo GNSS, ki je postala nenadomestljiva metoda pri spremljanju plazenja tal. Opisan je postopek določitve pomikov na primeru HC Razdrto-Vipava, kjer pomike spremljamo od leta 2007. Opisan je postopek navezave na evropske kontrolne točke in postopek izravnave izmerjenih vrednosti.

1 INTRODUCTION

The structures that are usually the main focus in deformation monitoring are often only an indirect indicator of the dynamic processes associated with land surface and undersurfaces. Today, artificial structures are built from materials and using methods to mitigate the effects of the deformation of natural objects in terms of their generation. Therefore, one of the primary tasks prior to construction is to determine the stability of the surface, which is related to the level of rock sliding or crawling under the surface as well as to the geotectonic movements deeper inside the earth. Thus, geological and geotectonic investigations, which often replace deformation monitoring and are focused exclusively on surface changes, are undertaken as urgent works before the construction of geotechnical facilities begins. These investigations usually start after the beginning, rather than before, or even after the completion of the structure's construction. As a rule, the reasons for this inconsistent sequence of events are economic. Crawling usually reveals itself through errors in the inclinations or the orientation of the investigated object that can be: new changes that do not show any signs of unexpected tilt in the past, changes in the currently active landslide, or the consequence of the proximity of the areas with the existing geodynamic events. The aim of deformation monitoring is to obtain the facts about the stability of the observed object or surface, expressed by the size of the movements of certain points. In addition to stability, the importance of determining movements lies in evaluating the potential hazard of built and natural objects for the environment and above all for human life and property. Therefore, the determination of movements and the deformations of natural and artificial structures are among the most engaging and most demanding tasks in geodesy. Deformation monitoring covers several temporal segments in terms of determining movements [1] at the time of the occurrence of natural forces leading to conditions for the emergence of the movement, at the time of the operation of natural forces or during the construction operation, triggering the realization of the movement of natural or man-made structures, at the time of the settling of natural forces or after the completion of the construction, establishing a long-term trend of movement of objects in a given area, at the time of the cessation of activity or natural forces or during the steady influence of natural forces on the buildings, resulting in the relative elimination of the movements or the occurrence of stagnation of the changes of these movements. So, deformation monitoring covers a number of spatial segments in terms of determining the movement:

at the site of the origin of the phenomena of the operation of natural forces, at the site of the effective functioning of the natural forces or in the immediate vicinity of the facility, at all detectable sites of the functioning of natural forces, in places, where according to the natural forces the influence is relatively stable, and indirectly also in places where according to the operation of natural forces, influences are absolutely stable. Given the fact that there are no absolutely stable points, especially on the earth's surface, the determination of displacements and deformations is presently practical in all scientific disciplines that are in one way or another related to the physical environment. The position for determining the land slide is defined by the geomechanics in cooperation with the surveyor who assesses the suitability of the position due to the purity of the signal for the purposes of satellite deformation monitoring. Global Navigation Satellite Systems (GNSSs) with Carrier Phase (CP) based on high-precision positioning techniques have been widely used in geodesy, altitude determination, engineering survey, agricultural applications, cataster mapping, etc. Considering the modernization of GNSS, multi-constellation and multi-frequency data processing is one of the focuses of current GNSS research. The GNSS development authorities have developed better designs for the new signals, which are aimed at fast acquisition for civil users, are less susceptible to interference and multipath and have a lower measurement noise. However, how good are the new signals in practice? The signal quality of the multi-GNSS (GPS, GLONASS, Galileo, BDS and QZSS) is assessed by looking at their zero-baseline Double Difference (DD) CP residuals. The impacts of multi-GNSS multi-frequency signals on single-epoch positioning are investigated in terms of accuracy, precision and fixed solution availability with known short baselines [2]. Today, GNSSs are used for a multitude of applications around the world, and there is a general quest for better positioning accuracy and reliability, as well as faster position acquisition from both user groups and the GNSS research community. Combining observations from multiple GNSSs in one positioning process and/or using multiple frequencies from one or more GNSSs is an important step towards reaching these goals. Accounting for all error sources in the positioning process, including hardware biases, is a prerequisite for accurate results [3].

2 MEASUREMENT METHODS

On the basis of previous research we decided to analyse our measurements in detail, which were performed with the GNSS method. The detailed measurements were performed using movements of the Slovenian GNSS

reference network named SIGNAL and the local reference points in the investigated area named BAZ1 and BAZ2. The network SIGNAL (Slovenia-Geodesy-Navigation-Location) is a Slovenian network of permanent GNSS-stations and is a basis for the country's geographic information infrastructure. It includes 16 stations that are evenly distributed across the country, as shown in Figure 1.

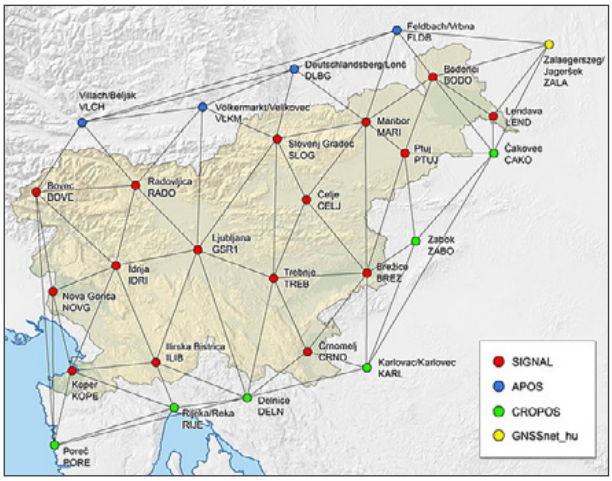

Figure 1. References point of network SIGNAL [4].

The GNSS station network is important for users when they want to determine the relative or differential position of their own receivers according to the chosen GNSS station in the network. Such a determination of the position is incomparably more accurate than the absolute position, established without connection to the network. In order to connect GNSS measurements with the physical realisation of the coordinate system, two GNSS receivers are needed. Obviously, the network allows for more rational measurements, because it replaces the users' reference receivers, so they only need a movable receiver, while the role of the reference receiver is taken by the SIGNAL network system. The Ljubljana permanent station is also included in the European Permanent Network, the data from this station are regularly sent to the data centre EUREF (European Reference Frame), which operates in the frame of the International Association of Geodesy – IAG. Two-frequency GNSS receivers with antennas are placed on all network stations and the continuous monitoring is performed 24 hours a day and 365 days a year.

The chosen station location allows for a fairly even distribution across the country, with maximum distances between the stations that are less than 70 km. This distance between permanent GNSS stations enables users to achieve high accuracy of the position determination in the whole area of the country if they use VRS observations. The calculation of VRS observations is possible only in the networks that are centrally controlled. In fact, GNNS service controls and manages the SIGNAL network from the network centre. This uses a programme package for the central network control (Trimble Pivot Platform) to collect and process the observations from all the GNSS stations in the network that flow into the centre in real time. The programme package enables the continuous calculation of corrections in the ionosphere, troposphere, satellite positions and an unknown number of ambiguities for each station in the network and the calculation of VRS observations for a random location in the network.

The user's receiver (BAZ1 and BAZ2) must enable two-way communication, i.e., data transmission and reception. After the determination of the absolute position, this is sent in the form of a NMEA message into the network centre. Based on observations of all the GNSS stations, the model of impacts on observation is generated in the centre, then the interpolated values of the impacts are calculated for the user's position. Furthermore, the values of the observations, performed by a physical receiver on the location near the user, are calculated regarding the modelled influence. These observations are called VRS observations; the position for which they are generated is named the Virtual Reference Station (VRS). The VRS data are then sent from the network centre in the form of an RTCM message; they are dealt with by the user in the same way as if they were RTCM messages observed by a GNSS station. The user's manner of position determination stays the same; despite the long distance from the nearest GNSS station, the accuracy of the position determination is very high [4].

2.1 Methods of Precision Geodetic Survey Techniques

Generally, specifications for the precision of geodetic survey techniques include the least angular count of instruments to be used, the number of observations, the rejection criteria of the observations, the spacing of major stations and the expected angular and positional tolerances. To obtain exact measurements, the surveyor must use precise equipment and precise techniques. Many of the techniques used in precise surveys are adapted from the conventional geodetic positioning methods and instrumentation, but with some differences, such as survey procedures. In addition, conventional horizontal and vertical survey

techniques use traditional ground survey instruments (electromagnetic distance measurement, robotic total stations, levelling) and the GNSS survey techniques [5]. The spatial geodetic monitoring of civil constructions is one of the most complicated tasks of engineering geodesy. Modern survey equipment allows for the simplification of many technological processes. At the same time, new equipment is leading to the invention of advanced spatial monitoring methods. Nowadays, accurate and precise total stations with automatic target recognition (ATR) and reflector less modes have become relatively common [6], [7]. Exceptionally popular are the motorized total stations [8]. In engineering practice, the deformation monitoring of large structures (bridges, viaducts, landscape, hydro power plants, etc.) uses various geodetic methods, such as levelling, trigonometric heights and GNSS Recently, the state geodynamics network is, more or less, observed by the application of these technologies. Although the GNSS allows positioning with accuracy comparable to conventional methods, the use in the past was limited due to the long duration of the observation. The development of instruments and in particular software, have significantly reduced the time of observation of the GNSS method so that they can, in some cases, ensure 1-mm accuracy in less than 1 hour of observation. However, due to the elimination of the global movement of ground water and land masses, it is recommended to increase the length of the measurement time, which should last at least 24 hours, continuously. Determining the position with GNSS depends on the types of observed quantities and the method of data processing: absolute, differential code and the relative phase-shift method. In addition to the classic kinematics and RTK methods, the modern approach also includes the VRS method (Virtual Reference Station) and the PPP (Precise Point Positioning) method. The latter is a more accurate method of determining the absolute position that can be carried out as static or kinematic. For the purposes of the geodetic monitoring, only the static mode with millimetres accuracy applies explicitly [9]. Research in recent years presents the use of GNSS for a precise determination of 3D positions in the control of hazardous natural phenomena. Detailed analysis of the landslide movements, especially for the needs of the security system installation, functioning in real time, requires a combination of accurate positioning in three dimensions (a few mm) and a high temporal resolution (less than 1 hour). Monitoring of landslides with GNSS technology is typically used in several epochs, measured as a complement to conventional methods. It is necessary to determine the time period of the observations to obtain a quality GNSS monitoring method, which is the only way to get the precision around 1 millimetre. Otherwise, all the described GNSS methods based on the same geometric principle, namely, that the position of a point in space is determined using the crossings of the spheres whose radius represents the distance measured from the new point to more distant points. These points in the GNSS system materialize themselves as satellites around the Earth. The principle is similar, almost the same as in terrestrial trilateration: according to the law of planar geometry, the position of a new point is determined by the intersection of the circular lines, where the values of the radii are determined by the measured distances, the centre of circles, however, determines the standing positions, from which distances are measured. In principle, three measured distances (receiver Satellite) would be enough, but it is required, for the movement of the satellites and the Earth and the difficulties in determining the exact status of clocks at the time of submission and acceptance of the signals, to obtain observations of at least four satellites. Namely, the determination of the exact signals receiving time demands an extremely accurate clock in the receiver. These requirements can be reduced by using the time signal of a fourth satellite, therefore, in such case only the time differences of the receptions of signals from various satellites can be measured. The method of GNSS in the deformation monitoring is a relatively new method, which brings enormous advantages versus the conventional method. Precision positioning and determination of the relative coordinates of the points by this method largely depends on the deployment of the satellites at the time of the quality and performance measurement of the observations (from the precision of the field measurements, the consistency of the data, from the observance of the rules for locating points for the duration measurements, etc.). The accuracy can be better described through the evaluation of the effects that cause measurement errors. The main sources of errors that contaminate the information obtained from GNSS technology can be divided into three groups [10]:

a) The spread of the signal error, tropospheric and ionospheric refraction, multipath.
b) Error in connection with the receiver: an error of determination of the antenna phase centre, the system noise of the receiver, irremovable effects of the multipath, incorrect coordinates of the standing points, which are in the process of processing proclaimed as given.
c) Error in connection with the satellites: the determination of the error of positions and tracks of satellites.

Of course, this applies for a 24-hour observation. Based on the code or phase of GNSS observations, the absolute and relative position of the GNSS receiver can

be obtained. Absolute position is determined solely on the basis of the positions of GNSS satellites in the chosen coordinate system at the time of the observations and the observed distances between the satellite and the receiver. The relative position is fixed relative to the known position of one or more points placed in the default coordinate system at the given positions of the satellites and the observed distance between the satellite and the receiver. In both cases, therefore, the basis for position determining is a measurement of the geometric distance between the satellite and the receiver.

3. GNSS MEASUREMENTS OF DISPLACEMENTS IN A SLOVENIAN MOTORWAY SECTION UNDER CONSTRUCTION

Prior to the observations, 50 points were permanently stabilized on the route. Half of them were positioned on the structures, while the rest were in the vicinity in the triangular network. Concrete pillars were used for the stabilization of plates installed on the objects. Since this is a very demanding configuration of the terrain, the measuring points were positioned in such a way that two points were outside the deformation area (BAZ1 and BAZ2), which also represents the base for the adjustment (Fig2a). Based on geomechanics research, two local reference points, BAZ1 and BAZ2, are placed in the area of the ground-displacement measurements and represent the beginning and the end of the observed area or base vector. These two points are reference points of our local GNSS network and are connected to four stations of the SIGNAL permanent network. According to the SIGNAL points, the displacement of the base vector BAZ1–BAZ2 is determined. In the process of calculating the other points on the motorway route, first these two points are levelled. All other observations at 50 points are then calculated according to these two base points. Principally, the base points should be connected to the four nearest GNSS points of the SIGNAL network that is included in the European GNSS network (IGS), which provides the reductions of displacement of the Eurasian Plate and transformation parameters so that the coordinates can be converted into the coordinate system (ETRS). It is important to choose those points from the SIGNAL network that are approximately equally far from the site and correctly distributed around it.

Other points were mostly placed on the landslide area. The changes in the position of the points in the deformation area are compared based on the base line. Furthermore, these points can serve to carry out classical geodetic surveying of each structure's movements. Eight Topcon HypePro, 1 Leica and 2 base CR3 Topon GNSS antennas were used (Fig 2b). In order to obtain better results according to the satellite positions, all the points were continuously measured for 24 hours. In that case, data capturing took place for 6 days for all the points. It is important to place exactly the same antenna at the same point in each epoch, because of the different phase centres of the different antennas. Consequently, some possible antenna errors can be avoided in this way, such as the error of the antenna centre, the different antenna centre heights, different frequencies, the antenna sensitivity to multipath, the sensitivity to deviation of a vertical line, etc.

Figure 2a. Base point BAZ1 and BAZ2.

Figure 2b. GNSS equipment.

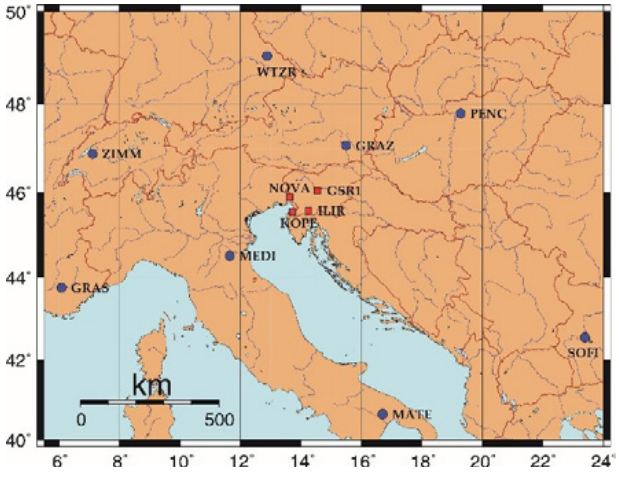

Figure 3. Reference points in Slovenia and orientation points [11].

First, it was necessary to define a geodetic datum that was provided by a set of given IGS points (International GNSS Service) with given coordinates and velocity vectors in the International Terrestrial Reference Frame 2005 with high accuracy. In addition, four GNSS points (KOPE, ILIR, NOVA, GSR1) of the Slovenian network of permanent GNSS stations SIGNAL were also considered in the processing, but as new points. The SIGNAL network points have lower accuracy, so that they cannot be treated as given. In Fig 3, the reference points in Slovenia are in red, the points in the surrounding area that were used for orientation and adjustment are in blue.

The digital orthophoto (Fig 4) shows the disposition of some points for observations.

The data in the antenna are stored according to the Julian calendar. The processing of observations is made separately for each for each Julian date (for example, 16 September 2018 is according to Julian calendar 2458391). For this reason, two sets of coordinates have to be obtained for each point. Based on the differences or the similarities of these two positions, the quality of the observations and the processing of these can be considered. The result of the processing is the evaluation of the coordinates of the points for each day with the respective accuracy. After the processing of observations, one set of coordinates in the ITRF2005 coordinate system is obtained for different time epoch for each point. The goal is to present the coordinates of points

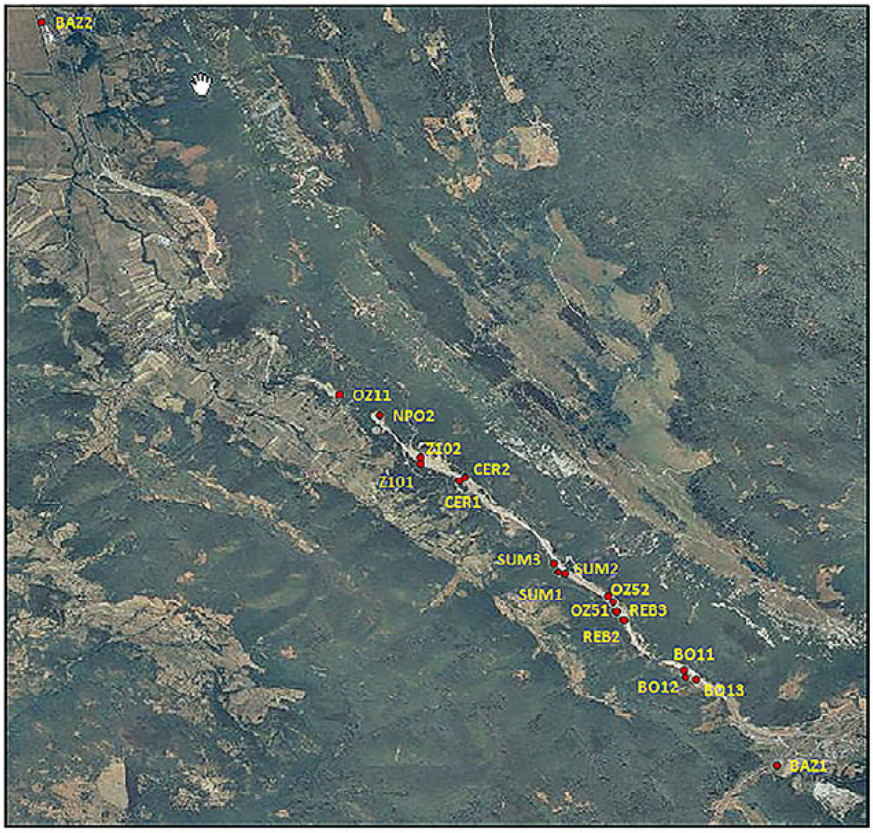

Figure 4. Digital orthophoto and location of observation points [11].

in the national projection, i.e., the transverse Mercator projection with its associated accuracy. The transition from the ITRF2005 to the state projection is carried out through the transition to the ETRF89 coordinate frame in which the positions (according to ITRF2005) are reduced for the movement of the Eurasian tectonic plate. The point's positions in ETRF89 are the basis for conversion into a national cartographic projection. The accuracy of the point coordinates in the cartographic projection assumes the same accuracy as the geodetic coordinates in the ITRF2005. In addition, it is assumed that the transition to the state cartographic projection (through ETRF89) does not change the precision of the coordinates significantly [11].

Table 1 presents the coordinates of the points in the transverse Mercator projection with the corresponding accuracy. The altitudes are obtained by decreasing the ellipsoid height, estimated through the observations of the GNSS for the geoid altitudes obtained from the current geoid model of Slovenia, as shown in Fig 5.

The coordinates of the points and their accuracy in the individual measurements are determined as superposition of two systems of normal equations. From Table 1 and Table 2 it can be seen that the data with a positional accuracy of 1 to 2 mm were obtained. For the high components, the accuracy is slightly worse due to the poor reception of the signal and the multi path. This was compensated with classic terrestrial geodetic measurements.

Tables 3 and 4 show calculated values of the displacement for base points 1 and 2 in the period from November 2007 to October 2014 according to single periods. The red field displays the common displacement for this period. The results show that the common position displacement of the BAZ1 point is 2.8 mm and BAZ2 is 22 mm. The reason for the displacement to BAZ2 seems to be the irregular position of a column and its poor installation, since it is placed next to the parking lot of road maintenance vehicles, which is subject to deformation of the land because of the weight. Fig 6 and 7 show a vector display of the BAZ1 2and BAZ2 point displacements in each period. The red vector presents the common displacement from the beginning of the monitoring. The displacement of 0.0126m was detected at the BAZ1 point by measurements in 2008. The results from this year show very dynamic displacements of the BAZ1 and two points that can be attributed to the poorer arrangement of the satellites in the time of measurements and shorter time of data gathering;

Table 1. Measured values and accuracy of measurements at the reference points in October 2008.

Point	Y [m]	X [m]	H [m]	σ_Y [mm]	σ_X [mm]	σ_H [mm]
BAZ1	426090,0469	68720,5530	627,0367	1,85	0,87	1,93
BAZ2	418920,5057	77178,8702	112,9227	1,29	0,67	5,33

Table 2. Measured values and accuracy of measurements at the reference points in October 2016.

Point	Y [m]	X [m]	H [m]	σ_Y [mm]	σ_X [mm]	σ_H [mm]
BAZ1	426090,0541	68720,5410	627,0282	1,13	1,01	1,32
BAZ2	418920,5132	77178,8854	112,8537	1,41	0,51	3,97

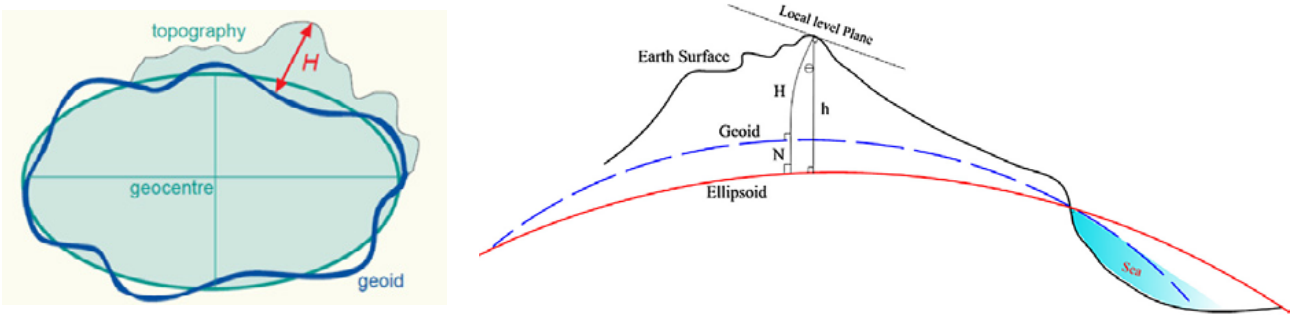

Figure 5. Altitudes on Geoid and reference ellipsoid (www.google.si/geoid).

Table 3. Calculated values for displacement of BAZ1 point [12].

	Y [m]	X [m]	Z [m]	d_y [m]	d_x [m]	σ_y [m]	σ_x [m]	Displacement 2D [m]	date
BAZ1	426462.018	68234.244	627.039	-	-	-	-	-	2007_11
	426462.0253	68234.2393	627.0248	0.0073	-0.0047	-	-	0.0087	2008_1
	426462.0197	68234.2423	627.0297	0.0017	-0.0017	-	-	0.0024	2008_2
	426462.0306	68234.2432	627.0350	0.0126	-0.0008	-	-	0.0126	2008_4
	426462.0231	68234.2410	627.0264	0.0051	-0.0030	-	-	0.0059	2008_10
	426462.0163	68234.2401	627.0299	-0.0017	-0.0039	-	-	0.0043	2009_3
	426462.0233	68234.2420	627.0254	0.0053	-0.0020	-	-	0.0057	2009_5
	426462.0240	68234.2403	627.0349	0.0060	-0.0037	-	-	0.0070	2010_2
	426462.0257	68234.2441	627.0102	0.0077	0.0001	-	-	0.0077	2010_10
	426462.0157	68234.2453	627.0407	-0.0023	0.0013	-	-	0.0026	2013_6
	426462.0210	68234.2415	627.0066	0.0030	-0.0025	-	-	0.0039	2013_10
	426462.0195	68234.2464	627.0222	0.0015	0.0024	0.0014	0.0016	0.0028	2014_10

Table 4. Calculated values for the displacement of the BAZ2 point [12].

	Y [m]	X [m]	Z [m]	d_y [m]	d_x [m]	σ_y [m]	σ_x [m]	Displacement 2D [m]	date
BAZ1	419292.449	76692.184	112.924	-	-	-	-	-	2007_11
	419292.4539	76692.1837	112.9186	0.0049	-0.0003	-	-	0.0049	2008_1
	419292.4610	76692.1860	112.9060	0.0120	0.0020	-	-	0.0122	2008_2
	419292.4496	76692.1816	112.9101	0.0006	-0.0024	-	-	0.0025	2008_10
	419292.4511	76692.1817	112.9185	0.0021	-0.0023	-	-	0.0031	2009_3
	419292.4505	76692.1845	112.9035	0.0015	0.0005	-	-	0.0016	2009_5
	419292.4465	76692.1848	112.9172	-0.0025	0.0008	-	-	0.0026	2010_2
	419292.4495	76692.1847	112.9234	0.0005	0.0007	-	-	0.0009	2010_10
	419292.4325	76692.1866	112.9143	-0.0165	0.0026	-	-	0.0167	2013_6
	419292.4312	76692.1844	112.8840	-0.0178	0.0004	-	-	0.0178	2013_10
	419292.4270	76692.1858	112.8912	-0.0220	0.0018	0.0015	0.0017	0.0221	2014_10

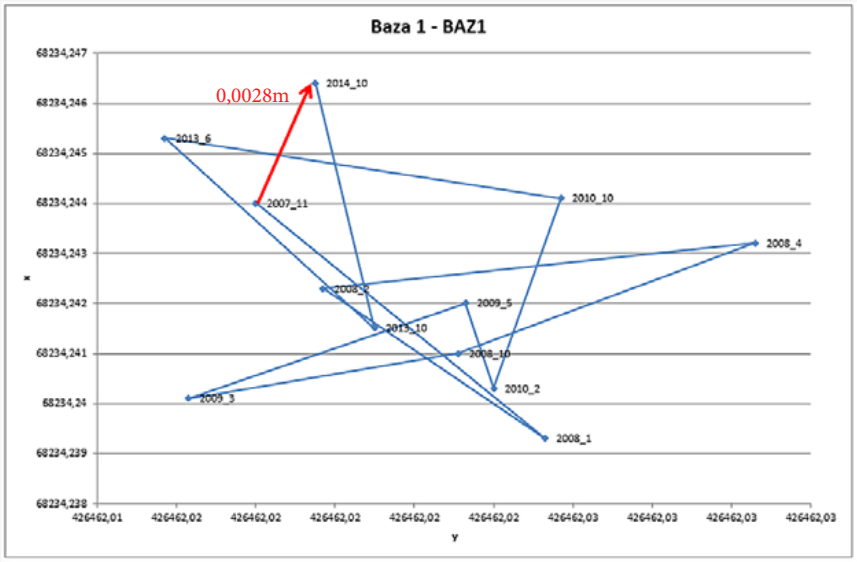

Figure 6. Vector display for the displacement of the BAZ1 point [12].

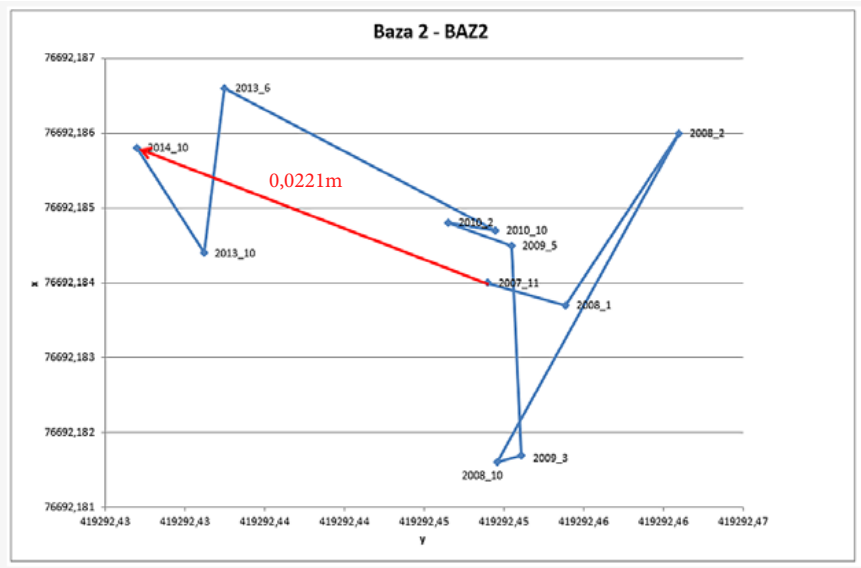

Figure 7. Vector display for the displacement of the BAZ2 point [12].

therefore four revisions were carried out this year. In fact, the displacement of the base points does not influence the results of the other observed points, because the displacement of the base points is levelled. The base points represent the base vector, from which the relative displacements of the observed points are calculated and they serve as control points. Two points of the motorway section, BAZ1 and BAZ2, were established in order to eventually define the coordinate base of the motorway section. The results of the data processing show that the coordinates of both points changed significantly. Furthermore, the transformation from the January and February 2008 measurements to the November 2007 results in coordinates of all measured points, where the coordinate base is determined by the reference points BAZ1 and BAZ2.

In principal, any assessment of possible movements of geodetic points obtained from GNSS measurements requires a determination of the coordinates for points in several time epochs. It is necessary to estimate the trend of possible coordinate changes based on a series of obtained coordinates. The trend of changes in the coordinate points can be well defined only in the case of high-quality coordinate points or by quality time series of coordinate points. Furthermore, the displacement results are only shown for one of the reference points of the SIGNAL network, named KOPE, which is obviously also included into European GNSS network (IGS). Displacements of the reference points should be taken into account when measuring base points, from which the displacements of the points are calculated within the base vector. As a rule, relative displacements in the relation base – vector – object are established. The points of the SIGNAL network are very important in this particular case because the displacement of the fundamental base vector is determined from them.

Fig 8 shows the changes in the coordinate points in time for a 1-year period (2007/08) for the KOPE reference point in the form of deviations from the mean for each coordinate of each point in the network. The coordinate in each epoch represents a deviation from this mean with the given standard deviation.

Furthermore, changes in the point coordinates can be displayed in the plane of the cartographic projection. Fig 7 shows the estimated point coordinates for each time epoch. However, on the basis of the calculated standard deviations of the estimated point coordinates and the method used for measurements, it would be difficult to reliably determine the size of the movements of the points. The movements at the other reference points of the SIGNAL network are shown in Fig 9.

4 DISCUSSION

Today, space overcrowding results in man-made structures erected on areas where we could not imagine buildings years ago. We need to be aware that new technologies enable us to build on the terrain that is very unpredictable, therefore monitoring is absolutely needed. In Slovenia, one highway section

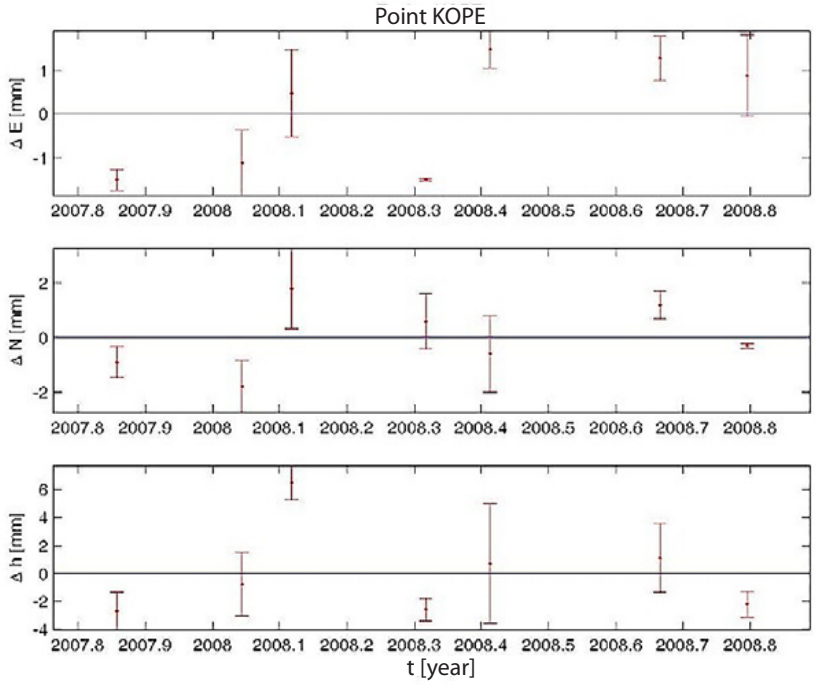

Figure 8. Changes in the coordinate points for a 1-year period [11].

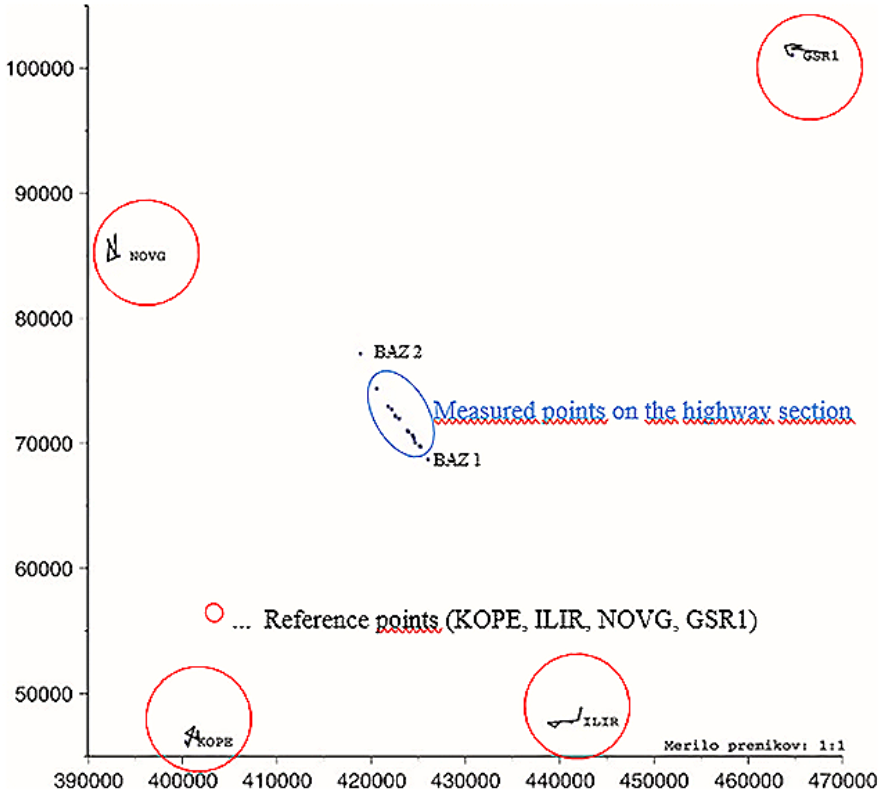

Figure 9. Movements of the reference points of the SIGNAL network [11].

was constructed on the ground, where the terrain was expected to slide under the weight of the objects, but only to the predicted values. Unfortunately, these values quickly reached their maximum and exceeded the permitted limits. In order to determine whether the terrain and objects are sliding according to the predictions, monitoring must be carried out. This is most often done using geodetic instruments such as GNSS. First, it is necessary to check the stability of the reference points from which we perform a variety of geodetic measurements. The position of the reference points is obtained by means of a deformation analysis. The main goal of the deformation analysis is to confirm the stability of the reference points, resulting in the determination of movements of the control points in the geodetic network, which is developed in the vicinity of the observed objects. We have described the process of data acquisition and the linearization of the distance between the satellite and the receiver. It should be recognized that geodetic monitoring is a very demanding and complex task, which must be carried out precisely and reliably.

5 CONCLUSION

A deformation analysis can be described as a set of methods for the detection and evaluation of movements or the deformations of natural or artificial objects. Given that attention is mainly focused on the processing of data, a deformation analysis often denotes only the process of determining the movements using the relevant analytical approaches or indicates the method of processing the measurement results. Geodetic deformation monitoring is therefore a wider concept, covering all the phases from planning and system set-up up to continuous operation, data processing, analysis and presentation of results, while the focus under deformation analysis is the processing of the measured data and their analysis. The deformation analysis of GNSS data for the monitoring of soil movements should also be used in the field of statistics, geomechanics, civil engineering and geology and as additional knowledge in the field of geophysics, geodynamics and surveying.

REFERENCES

[1] Savšek Safić, S. 2002. Optimalna metoda določanja stabilnih točk v deformacijski analizi. Dissertation, University of Ljubljana, FGG, Slovenija.

[2] Quan,Y., Lau, L., Gethin, R., Meng, X. 2016. Measurement signal Quality assessment on All Available and Signals of Multi – GNAA (GPS, GLONASS, Galileo, BDS and QZSS) with real Data. The journal of Navigation. 69(2), 313-334. DOI: 10.1017/S0373463315000624

[3] Håkansson, M., Jensen, A., Horemuz, M., Hedling, G. 2017. Review of code and phase biases in multi-GNSS positioning. GPS Solutions. 21(21), 849-860. DOI: 10.1007/s10291-016-0572-7

[4] http://www.gu-signal.si

[5] Ogundare, J.O. 2016. Precision Surveying. The Principles and Geomatics Practice. Wiley, Canada.

[6] Reda, A., Bedada, B. 2012. Accuracy analysis and Calibration of Total Station based on the Reflectorless Distance Measurement. Master of Science Thesis in Geodesy. School of Architecture and the Built Environment, Royal Institute of Technology (KTH). Stockholm. Sweden.

[7] Lutes, J.A. 2002. Automated Dam Displacement Monitoring Using a Robotic Total Station. Master of Science Thesis in Engineering. Department of Geodesy and Geomatics Engineering. University of New Brunswick.

[8] Paar, R., Kapović, Z., Ahmetović, S. 2005. Precision providing of motorized total station Topcon GMT-100 according to ISO 17123-3 and 17123-4. Geodetski list 4, 267–278.

[9] Kozmus Trajkovski, K. 2010. Study positioning with High sensitivity GPS sensors Under Adverse Conditions. Sensors 10(9), 8332-8347. DOI: 10.3390/s100908332

[10] Chrzanowski, A. 2007. Integrated Approach to the Design, Analysis and modelling of Deformation Surveys. Acta Scientiarum Polonorum seria Geodesia ET Description Terrarum. Wroclaw, Poland.

[11] Kovačič, B., Stopar, B., Sterle, O., Kamnik, R. 2008. 3D GPS meritve premikov na trasi AC Razdrto-Vipava za odbobje 2007-2008, Univerza v Mariboru, Fakulteta za gradbeništvo.

[12] Kovačič, B., Kamnik, R. 2013. Geotehnični monitoring po končani gradnji HC Razdrto - Vipava: 1. poročilo o GNSS meritvah, št. projekta 184/13 DARS d.d., trasa HC Razdrto - Vipava. Univerza v Mariboru, Fakulteta za gradbeništvo.

EXPERIMENTAL ANALYSIS OF A HIGH-SPEED-RAILWAY EMBANKMENT INTERSECTING STEEP GROUND FISSURES AT DIFFERENT ANGLES

EKSPERIMENTALNA ANALIZA ŽELEZNIŠKEGA NASIPA HITRE ŽELEZNICE, KI SEKA POD RAZLIČNIMI KOTI STRME RAZPOKE V TLEH

Jianbing Peng *(corresponding author)*
Chang'an University,
Key Laboratory of Western China's Mineral Resources and Geological Engineering of Ministry of Education
Xi'an 710054, China
E-mail: dicexy_01@126.com

Zhongjie Fan *(corresponding author)*
Changjiang River Scientific Research Institute of Changjiang Water Resources Commission, Wuhan 430010, China; and Chengdu University of Technology, State Key Laboratory of Geohazard Prevention and Geoenvironment Protection, Chengdu 610059, China
E-mail: stephenf88@163.com

Cong Liu
Chang'an University,
College of the Geology Eng. and Geomatics, Department of Geology Engineering
Xi'an 710054, China
E-mail: liucong@chd.edu.cn

Qiangbing Huang
Chang'an University,
College of the Geology Eng. and Geomatics, Department of Geology Engineering
Xi'an 710054, China
E-mail: dcdgx24@chd.edu.cn

Jigen Liu
Changjiang River Scientific Research Institute of Changjiang Water Resources Commission; and Research Center on Mountain Torrent and Geologic Disaster Prevention of Ministry of Water Resources
Wuhan 430010, China
E-mail: jigenliu@163.com

Hongyu Ren
Changjiang River Scientific Research Institute of Changjiang Water Resources Commission; and Research Center on Mountain Torrent and Geologic Disaster Prevention of Ministry of Water Resources
Wuhan 430010, China
E-mail: hongyuren@126.com

Ming Wu
Chang'an University,
College of the Geology Eng. and Geomatics, Department of Geology Engineering
Xi'an 710054, China
E-mail: eagleming@chd.edu.cn

Zhenjiang Meng
Chang'an University,
College of the Geology Eng. and Geomatics, Department of Geology Engineering
Xi'an 710054, China
E-mail: mengzj@chd.edu.cn

DOI https://doi.org/10.18690/actageotechslov.16.1.13-29.2019

Keywords

ground fissure; high-speed-railway embankment; orthogonal intersection; physical simulation experiments

Ključne besede

razpoka v tleh; nasip hitrih železnic; pravokotno sekanje; fizikalni simulacijski eksperiment

Abstract

A high-speed-railway (HSR) embankment intersection with ground fissures is a commonly encountered engineering problem. This paper reports a series of experiments conducted on a reduced scale to investigate the influence of different ground-fissure intersection angles on a HSR embankment. The tests revealed the presence of an integrated bend-tension failure mode in the embankment's reinforced concrete (RC) slab as a result of activities asso-

Izvleček

Križanja nasipov hitrih železnic (nasip HŽ) z zemeljskimi razpokami prestavljajo pogost inženirski problem. V prispevku je predstavljen niz eksperimentov, izvedenih v zmanjšanem merilu, s katerimi je raziskan vpliv različnih kotov križanja razpok v tleh z nasipom HŽ. Preizkusi so pokazali prisotnost integriranega načina upogibne natezne porušitve v armiranem betonu (AB) nasipa, kot posledico aktivnosti, povezanih z razpokami v tleh. Rezultati so

ciated with ground fissures. The results showed that the length and the area of the RC slab failure zone decreased nonlinearly with an increasing intersection angle, while the pile load and pile end-bearing varied to different extents in the foundations as they were affected by the slab deformation and rotation. Although the smallest effect on the embankment was observed when the ground fissure intersected the HSR orthogonally, traditional designs that incorporated this do not meet the minimum safety standards. The results of this study show that train-load-induced embankment settlement is insignificant compared with that induced by ground fissures. Therefore, this effect should be given priority in the design of alternative HSR embankments, especially for those in fissure-prone areas.

pokazali, da se dolžina in površina porušne cone AB plošče nelinearno zmanjšujeta z naraščajočim kotom križanja, medtem ko se obremenitev pilotov in nosilnost pilota na konici v temeljih različno razprostirajo, saj na njih vplivata deformacija in rotacija plošče. Čeprav je bil najmanjši učinek na nasip opazen, ko je razpoka v tleh sekala nasip HŽ ortogonalno, tradicionalni modeli, ki to vključujejo, ne izpolnjujejo minimalnih varnostnih standardov. Rezultati te študije kažejo, da je posedek nasipa zaradi obremenitve z vlakom neznaten v primerjavi s posedkom zaradi razpok v tleh. Zato je potrebno ta učinek prednostno upoštevati pri načrtovanju alternativnih nasipov HŽ, zlasti v območjih tal, kjer lahko nastanejo razpoke.

1 INTRODUCTION

Ground fissures are widespread geohazards that manifest as discontinuous, broken planes in the surface of the Earth [20, 28]. These fissures are generally divided into two categories, depending on their formation under the control of tectonics (i.e., tectonically or non-tectonically controlled) [26]. Of these, the latter is most often the result of human activity, dilative soil, soil collapse, and drought [9, 15, 18, 22]. Ground fissures caused by groundwater pumping are very common in areas where there is a shortage of water, including the southwestern American basin, the north China plain, and in northeastern Africa [29]. Tectonically controlled fissures usually develop in areas of intense structural activity and are dictated by the regional stress field, thereby exhibiting a stable strike orientation that is generally parallel to the substratum structural lines [6, 12, 14, 23]. Some tectonic ground fissures can also be strongly affected by groundwater pumping, thereby posing serious dangers to nearby buildings and residents [2, 8, 13]. To address these severe hazards, a number of studies have been conducted relating to the influence of ground fissures on buildings and underground constructions. The failure mechanisms associated with ground fissures have also been investigated in detail [20, 21, 27].

As construction has developed, additional engineering challenges have come to light, including the significant threat posed to HSRs by ground fissures [10]. Train-load and ground fissures are both vital factors that lead to the post-construction settlement of HSRs in areas of intense tectonic activity [5]. Of these, the former has been studied thoroughly, using a range of different approaches [1, 24, 25]. Various engineering methods, including geogrid-reinforced pile-raft-supported (GRPS) embankments and bridges, have been used to control the total and differential foundation settlement in regions where geological conditions are complicated, such as in areas where ground fissures are developed [3, 11, 19, 26]. At present, however, the design of GRPS embankments predominantly follows the engineering foundation design code [7, 17]. Studies that address their ability to cope with ground fissures and associated effects have rarely been reported in the literature.

In some mountainous areas, HSR routes inevitably intersect with ground fissures because of the terrain (Fig. 1). For example, 271 ground fissures have been mapped in the depressed Taiyuan Basin in Shanxi, China (Fig. 1). These tectonically controlled fissures are generally oriented parallel to the underlying fractures and are controlled by the regional stress field. Because these fractures are affected by the northwest-southeast tensile stress and the resultant sinistral shear couplet, they generally manifest as a series of northeast and north-northeast conjugate normal thrust faults (Fig. 1). The activities of these tectonically controlled fissures are known to be facilitated by the extraction of excess groundwater from the Taiyuan Basin [16]. As a result of our field investigation, 21 ground fissures developed in the Taiyuan Basin have been shown to pass through the Da-Xi HSR, which is currently under construction, at angles ranging from 15° to 90°; their interactions, combined with the extraction of excess groundwater, present significant risks to this ongoing project. Considering this problem, the Da-Xi HSR, built from Datong City of Shanxi Province to Xi'an City of Shaanxi Province with a total length of 859 km, has to reduce its maximum running speed to 250 km/h in the region of the Taiyuan Basin. In the basin, the railway line is designed generally along the strike direction of the flat area (Fig. 1). The lithology is relatively simple in the area. The main exposed layers of the Taiyuan Basin are Quaternary loess and silty clay

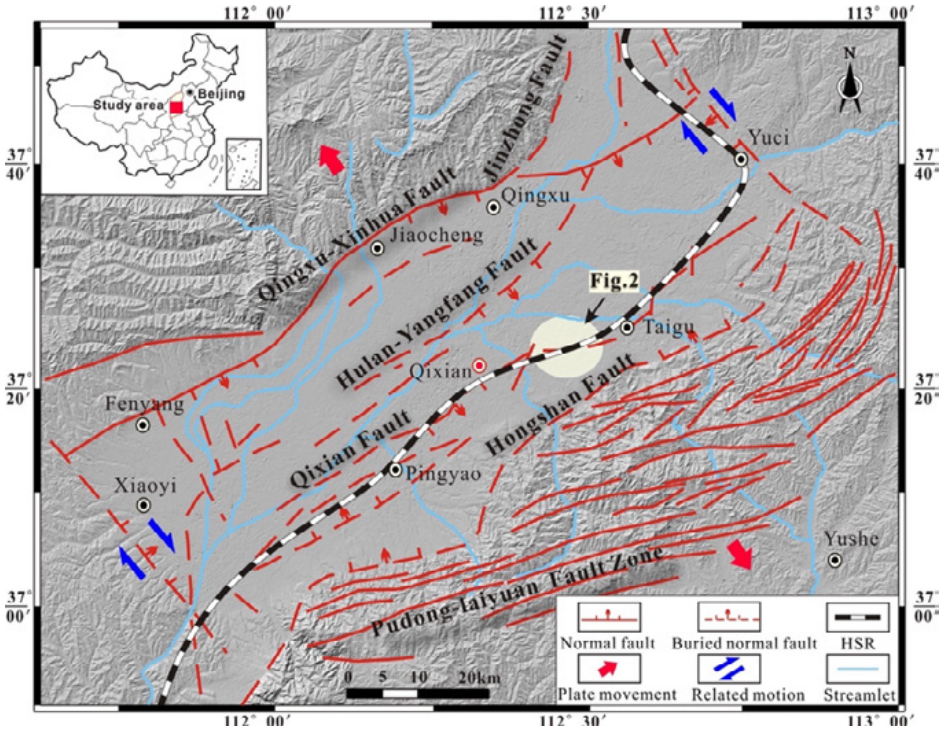

Figure 1. Regional tectonic map of the study area.

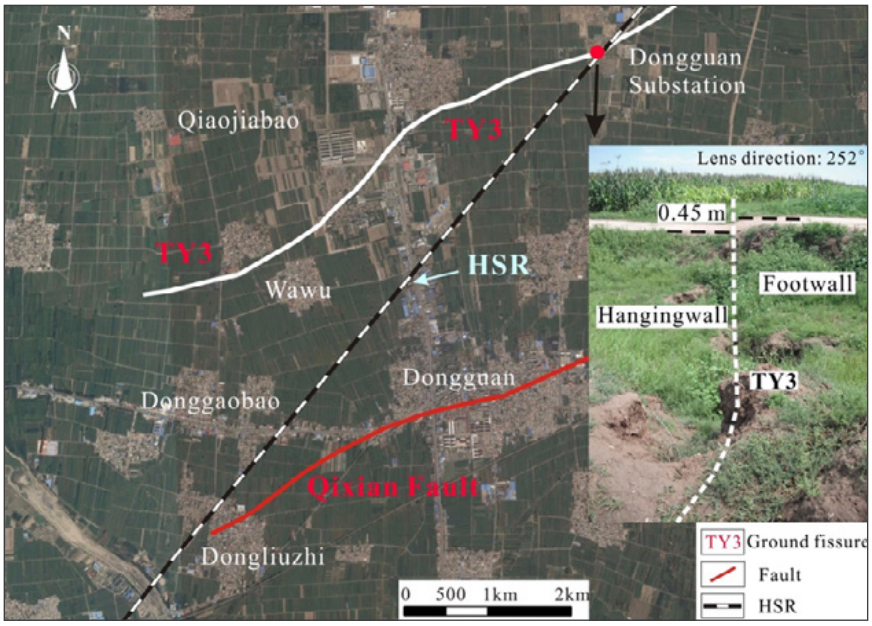

Figure 2. Map of the intersection angle between the TY3 fissure and the Da-Xi HSR.

with a thickness of approximately 50–80 m and 60–100 m, respectively, and the depth and thickness of the underground aquifer was investigated to be 50–80 m and 2–5 m, respectively.

Other than the relatively simple lithology under the HSR, the varied intersection angles between the fissures and the HSR will likely result in a range of different kinds of damage. Ground fissures that intersect with the HSR at low angles create more significant engineering issues, as they will have a larger area of overlap. For example, because the TY3 ground fissure passes through the Da-Xi HSR at an angle of 15°, the overlap area is close to 80 m in length (Fig. 2). The offset of the TY3

fissure can be up to 0.45 m in areas close to the railway, and the average settling rate has recently been measured to be 4 mm per year [16]. Thus, the TY3 fissure should be prioritized in any studies on the influence of ground fissures on the Da-Xi HSR.

This study reports a series of reduced-scale experiments that were conducted to investigate the influence of ground fissures occurring at different intersection angles on the GRPS embankments of the Da-Xi HSR.

First, a reduced-scale test at an intersection angle of 15° (referred to as test #1) was conducted to stimulate the embankment's response given at different TY3 ground--fissure offsets. Next, the effects of different intersection angles were investigated via additional reduced-scale tests at angles of 60° and 90°, respectively (referred to as tests #2 and #3, respectively). Finally, the ultimate cumulative settlement of the Da-Xi HSR subgrade induced by train loading was calculated and compared with the track settlement caused by ground fissures.

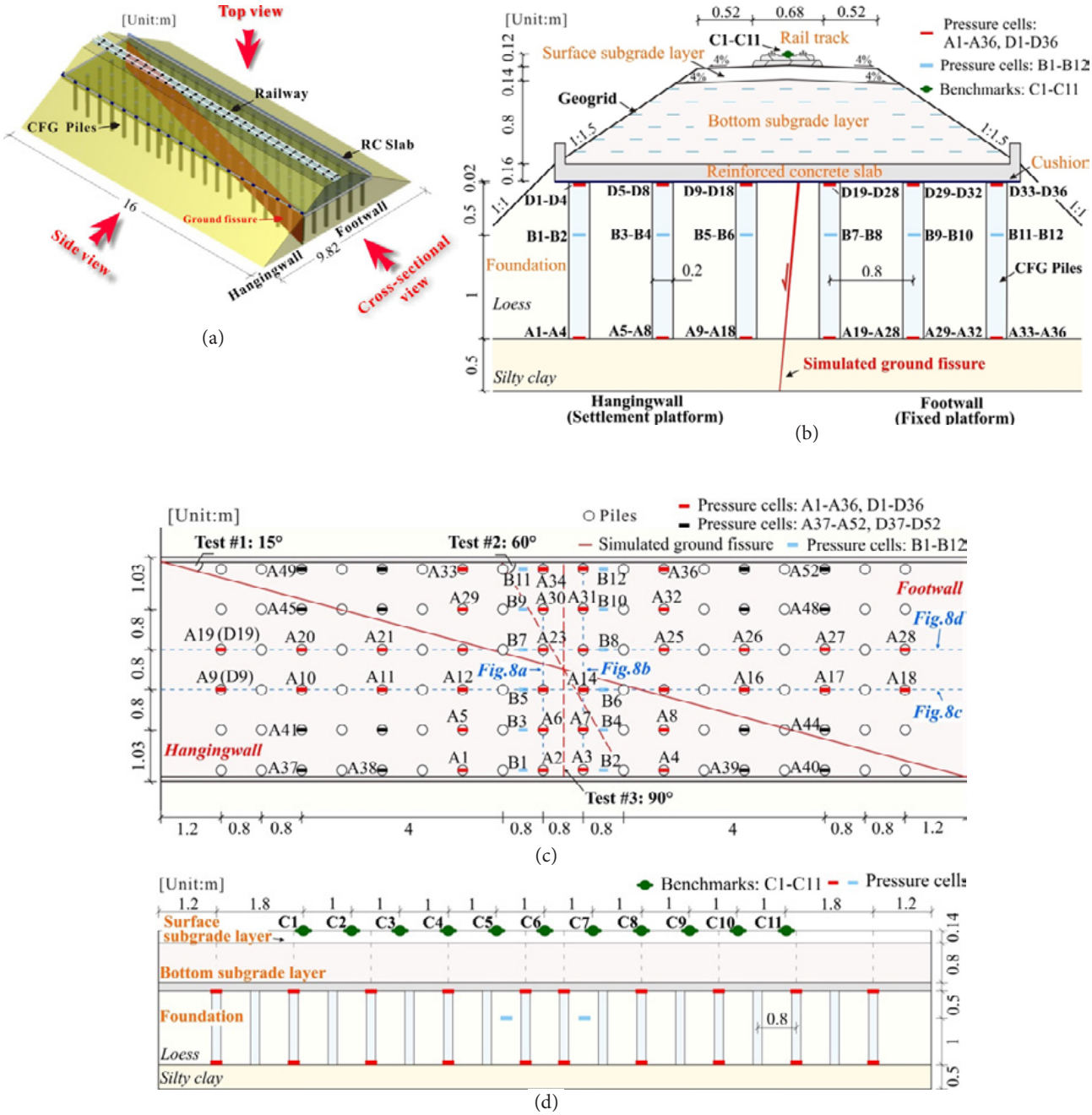

Figure 3. Setup of the reduced-scale physical model: (a) three-dimensional (3D) view; (b) cross-sectional view; (c) top view; (d) side view.

2 MATERIALS AND METHODS

2.1 Model construction

The TY3 ground fissure, which intersects with the Da-Xi HSR, was chosen as the case study, and a series of 1:5 scale embankment models were investigated (i.e., tests #1, #2, and #3). As part of the model-design process, geometric similarity $c_1 = 5$ with a primary variable was selected as the similarity criterion, while other physical quantities were derived using dimensional analyses. Thus, a model of the maximum dimensions was constructed, specifically a length of 16 m, a width of 9.82 m, and a height of 3.24 m (Fig. 3). The embankment models were designed strictly according to MRPRC guidelines [17], comprising a ballast-less rail track, subgrade, RC slab, and foundation (Fig. 3b).

In the models, the rail track is mainly comprised of a rail, an elastic fastener, double-block sleepers, a roadbed slab, and a support layer. The support layer is thus comprised a 0.03-m-thick layer of plain concrete with a strength class of C20, while a 0.05-m-thick RC layer with a concrete strength class of C40 was used to build the roadbed slab. The reinforced bars used in the roadbed slab were designed using the equal-strength principle, while the double-block sleepers were comprised of plain concrete blocks with a strength class of C40.

The subgrade layer was divided into two: graded gravel used to build the surface layer, while the lower layer was comprised of a mixture of coarse sand and graded gravel in the ratio 1:5.6. Several layers of polyester geogrid with a spacing of 0.12 m were also placed in the bottom subgrade layer (Fig. 3b). The particle size distribution in the graded gravel and coarse sand is shown in Fig. 4.

Loess and silty clay were used to remold the foundation, and the properties of the soil are summarized in Table 1. Note that the shear-strength parameters of the soil were determined using drained axial tests. A fine sand infill was used to simulate the ground fissures at a dip of 85°, as in the case study. Thus, the embankment passed obliquely through the ground fissure (Fig. 3b), while cement fly-ash grave piles with a strength class of C15 were imbedded into the foundation (Fig. 3b and 3c). The pile length, diameter, and spacing were 1.5 m, 0.2 m, and 0.8 m, respectively, and a 0.02-m-thick plain concrete cushion formed the top layer. A 0.16-m-thick RC slab was cast on top of the plain concrete cushion to create a raft structure. The concrete used for both the cushion and the RC slab had a strength class of C30 and was manufactured from a mixture of cement, water, coarse sand, and gravel in the ratio 1:0.4:1.4:2.6. Two layers of rebar were also emplaced into the RC slab, again designed using the equal-strength principle.

2.2 Measurements

A number of cells were installed in the embankment model to measure the pressure on the two ends of the

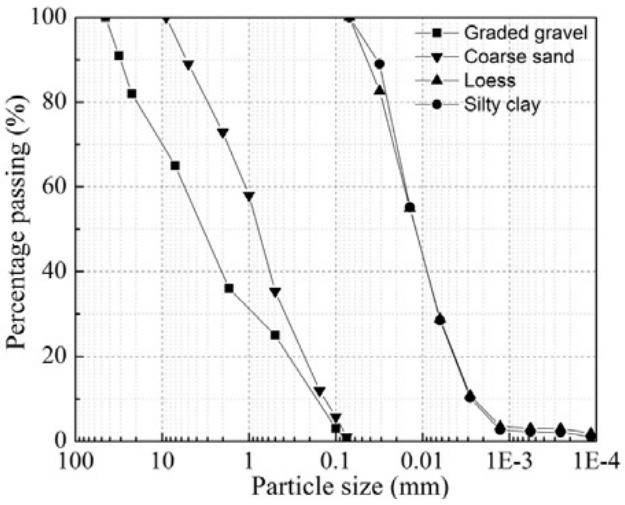

Figure 4. Particle size distribution of the materials used in the test.

Table 2. Reduced-scale model tests.

No.	Intersection angle (°)	Pile load (kPa)	Pile end-bearing (kPa)	Earth pressure (kPa)
#1	15°	D1-D36	A1-A36	B1-B12
#2	60°	D1-D52	A1-A52	B1-B12
#3	90°	D1-D52	A1-A52	B1-B12

Table 1. Properties of the soil used in the test.

Soil type	Specific gravity	Plastic limit (%)	Liquid limit (%)	Water content (%)	Unit weight (kN/m^3)	Cohesion (kPa)	Internal friction angle (°)
Loess	2.72	17.8	29.1	12	18	27	21
Silty clay	2.71	15.3	28.2	13.5	19.8	49	23

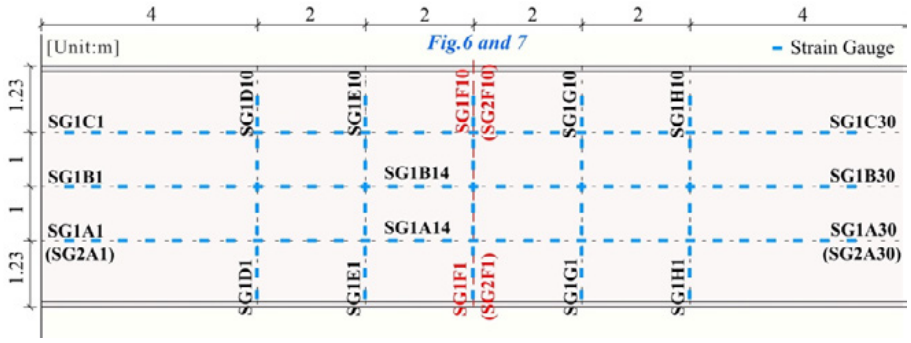

Figure 5. Layout of strain gauges used in the test.

piles (Fig. 3b-3d, Table 2). In tests #2 and #3, because the pressure cells D1-D52 installed on top of the piles were used to measure the pile load, 52 additional cells (A1-A52) were installed on the bottom of the piles to measure the end-bearing. In test #1, the lowest intersection angle, 36 pressure cells were installed on each end of the piles and were marked in red in Fig. 3c. In addition, 12 cells were installed in the loess layer to measure the foundation pressure, numbered B1-B12 (Fig. 3), while strain gauges were installed on both rebar layers to measure the deformation of the RC slab. The upper layer was numbered as the SG1 series, the lower layer was numbered as the SG2 series (Fig. 5), and the rail-track settlement was monitored in real time using precise levels from 11 benchmarks along the track (Fig. 3d).

2.3 Test implementation

The test procedure described here was implemented in the Foundation Settlement Simulation Laboratory at Chang'an University, China [20, 21]. To simulate the settlement of ground fissures in the hangingwall relative to the footwall, the side of the model with the settlement platform was set as the hangingwall, while the other side with a fixed platform was set as the footwall (Fig. 3b). Thus, the downward movement of the platform, which simulated the dislocation of the ground fissure, could be artificially controlled. In general, the measured average activity rate of the TY3 ground fissure has been about 4 mm per year. To predict the settling volumes of the ground fissures over the 50-year design service period of the HSR system, the offset in the test was set to 0.2 m, which is equivalent to the cumulative ground-

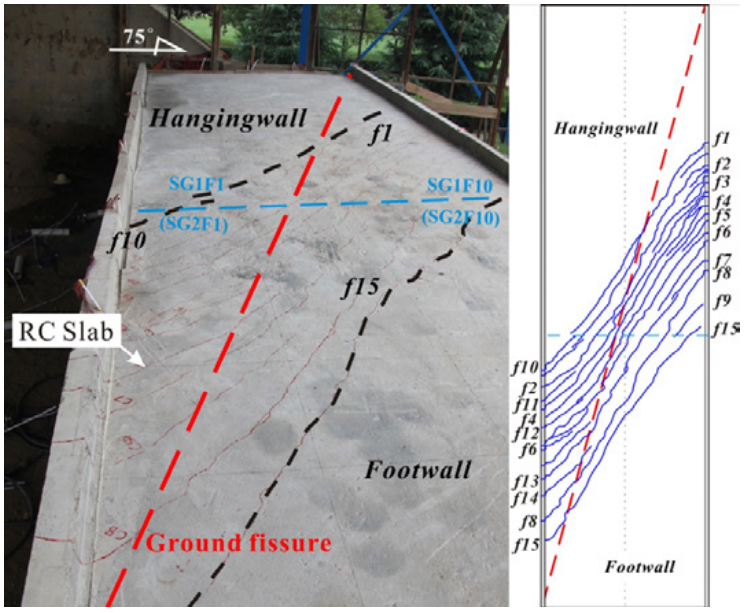

Figure 6. Photograph and diagram of cracks formed on the RC slab by the end of the experiment.

-fissure dislocation of 1.0 m in the case study. The test process was divided into 10 stages, each with a 0.02-m increment. At each stage, the model was stabilized for 24 h before the pressure, deformation, and settlement data were recorded.

3 TEST #1 OBSERVATIONS

3.1 Deformation of the RC slab

During test #1, as the settlement platform descended and the extent of the ground-fissure dislocation increased, such that the RC slab deformed a great deal, 15 cracks formed in the central area of the slab by the end of the test (Fig. 6). The area where these cracks formed is subsequently referred to in this paper as the failure zone. As this zone is concentrated around the central area of the intersection of the RC slab and the ground fissure, this region was chosen for further deformational analysis. Variation in the rebar strain in the RC slab with respect to an increasing ground-fissure offset is presented in Fig. 7, wherein the two rebar layers showed significant differences in the strain variation with respect to the increasing ground-fissure dislocation. At a ground-fissure dislocation of 0.02 m, tensile strain was observed on the footwall side of the upper rebar layer and compressive strain was detected on the hangingwall side of this layer (Fig. 7a). At the same time, compressive strain was observed on each side of the lower rebar layer (Fig. 7b). In contrast, when the ground-fissure dislocation was larger than 0.02 m and was continuously increasing, areas on the hangingwall side of the upper layer of rebar (e.g., SG1F4, SG1F5 and SG1F6) and the lower rebar layer (e.g., SG2F4 and SG2F5) transitioned to experience tensile rather than compressive strain (Fig. 7).

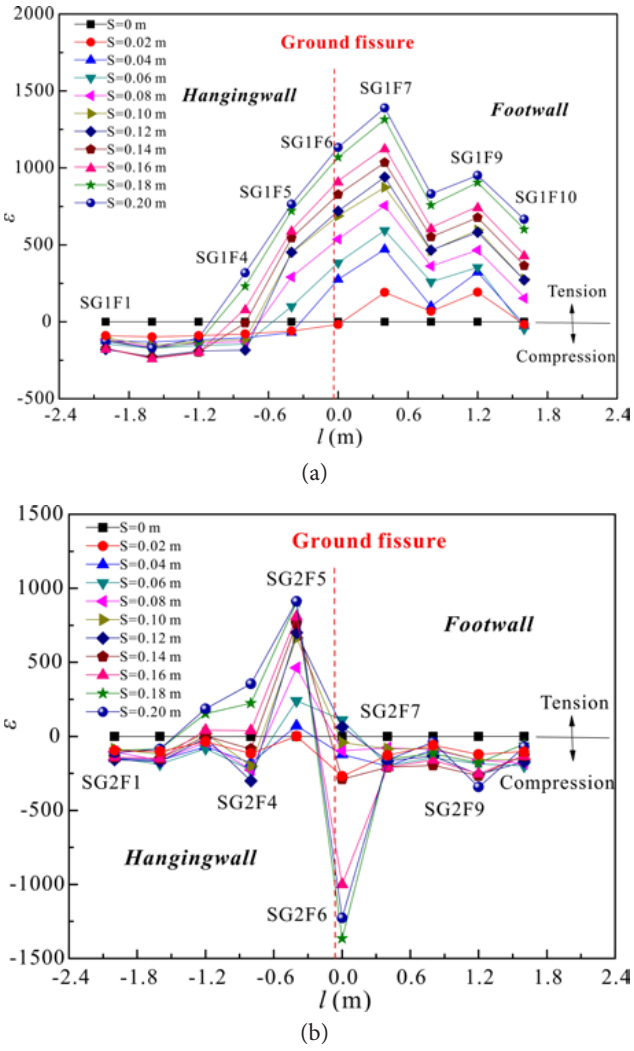

Figure 7. Variation in rebar strain in the RC slab with respect to the increasing dislocation of the ground fissure: (a) strain in the upper layer; (b) strain in the lower layer (Note *s*: dislocation of ground fissure; *ε*: rebar strain; *l*: position of the strain gauges in normal direction of the rail track)

As described above, the dislocation at 0.02 m acted as a boundary for the variation of the rebar strain status on the hangingwall side. To further analyze the deformation of the RC slab, variations in the ground-fissure dislocation were divided into two phases by the dislocation at 0.02 m. In the first phase, as the dislocation increased to 0.02 m, compression was observed on the hangingwall side of the RC slab (see Fig. 7). At the same time, on the footwall side of the RC slab, tension was observed in the upper part of the slab, while compression occurred in the lower part, indicating that the footwall side was bending upwards to form a convex shape. In the second phase, when the dislocation was larger than 0.02 m, the hangingwall side of the RC slab experienced tension in both the upper and lower regions, which simultaneously increased with the dislocation of the ground fissure. The results also indicated that the footwall side of the RC slab continued to bend upwards as the dislocation of the ground fissure increased (Fig. 7). Indeed, the variation of the rebar strain presented in Fig. 7 can be explained by the relative movement between the hangingwall side and the footwall side of the RC slab. When the hangingwall side of the ground fissure descended slightly (e.g., a dislocation of 0.02 m in the model), the RC slab rotated to the hangingwall side accordingly, thus inducing a pressure to the hangingwall side by the self-weight of the footwall side and leading to an upward convex bend in the footwall side. Note that the rotation mechanism of the RC slab will be illustrated in detail later in Fig. 11. As the dislocation increased, the hangingwall side of the RC slab continued to descend with the ground fissure, pulling down its other side and leading to a tensile deformation in itself, and at the same time, aggravating the

upward convex bend in the footwall side. Thus, under the effect of the pull force created by the hangingwall side, both the tensile deformation on the hangingwall side and upward convex bending deformation on the footwall side increased dramatically in the RC slab near the ground fissure as the dislocation increased (Fig. 7). Finally, as a result of the ground-fissure dislocation, an integrated bend-tension failure of the RC slab was observed in the region near the ground fissure (Fig. 6 and 7).

3.2 Bearing piles in the foundation

As the settlement platform descended and the dislocation of the ground fissure increased, the end-bearing of the piles in the foundation also varied significantly. As observed in Fig. 8, the rate of change in each end-bearing was not constant with the increase in the dislocation of the ground fissure. The results indicated that variations in the end-bearing with increasing ground-fissure dislocations can be divided into two stages based on the rate of change: (i) the saltation stage, which refers to the dislocation of the ground fissure up to 0.02 m; and (ii) the development stage, which refers to the period of ground-fissure dislocation between 0.02 m and 0.2 m. During the saltation state, the end-bearings in the piles on the hangingwall side decreased rapidly, wherein some decreased to zero, whereas those in the footwall all increased (Fig. 8). In contrast, during the development state, very small changes were observed in the pile end-bearings on the hangingwall side, whereas a good degree of variation was observed in those on the footwall side (Fig. 8). The results indicated that the pile

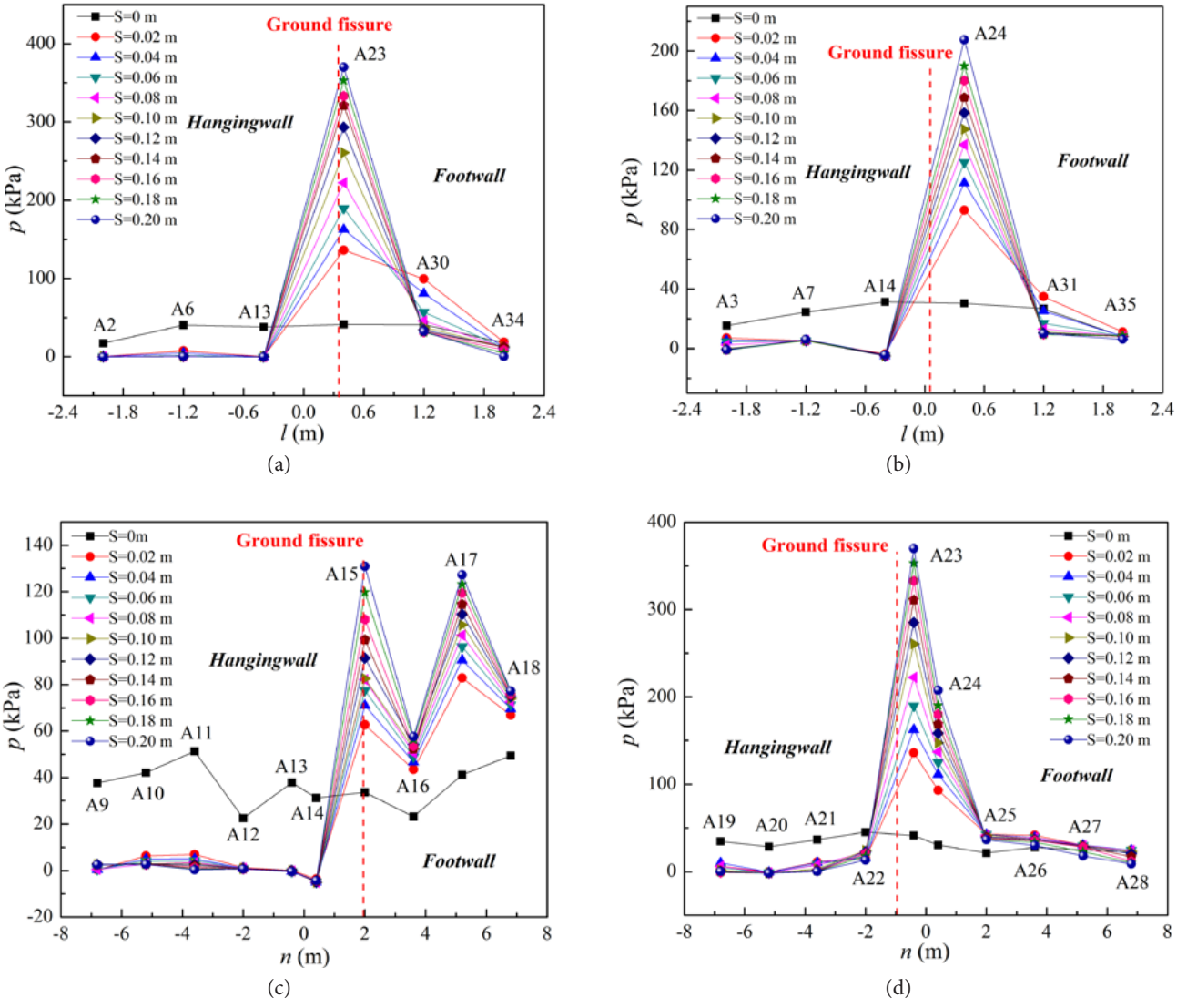

Figure 8. Variation in the end-bearing of piles with respect to the increasing ground-fissure dislocation (Note: *s*: ground-fissure dislocation; *p*: end-bearing of piles; *l*, *n*: position of the pressure cells in normal and tangential direction of rail track).

end-bearings closest to the ground fissure increased in concert with the dislocation (e.g., A23–A24 and A15–A16), whereas other end-bearings located further away from the fissure decreased with increasing dislocation (e.g., A30–A31 and A26–A28). These data indicate that variations in the end-bearings on the footwall side are correlated with the distance from the ground fissure.

Further analysis of all the end-bearings on the footwall side revealed a clear partition (Fig. 9); the end-bearings varied greatly during the development stage as the ground-fissure dislocation increased. Data from the end-bearings on the footwall side of the foundation can be divided into two zones according to the variations in the end-bearings. The test area that exhibited increased pile end-bearings following enhanced ground-fissure dislocation is referred to as zone *i* (Fig. 9a), and zone *ii* denotes the area where the pile end-bearings first increased and then decreased with enhanced ground-fissure dislocation (Fig. 9(b)). In addition, the term 'A-boundary' is introduced to refer to the boundary regions between the two zones, *i* and *ii*. It should be noted that the A-boundary is used here to divide the footwall side of the foundation based on variations in the end-bearing given that the precise location of this boundary cannot be accurately determined. This is illustrated, for example, by the fact that variations in the end-bearings of A24 and A25 were different; the position of the A-boundary can only be determined in this case in these two piles, and the accurate location between the piles varied.

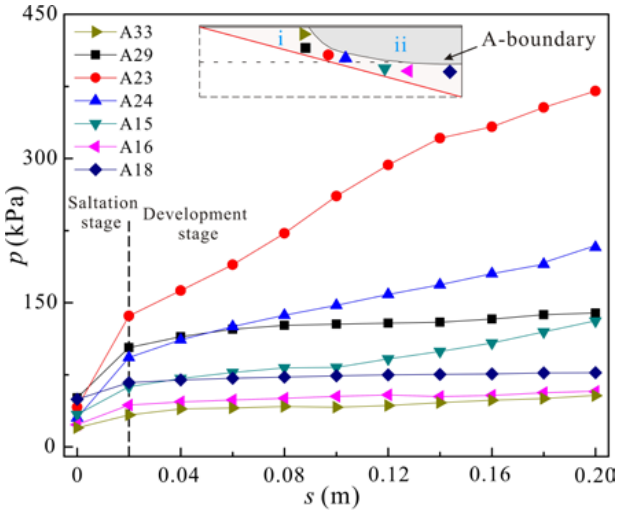

Figure 9. Variation in the end-bearing of the piles in footwall side with respect to the increasing ground-fissure dislocation: (a) zone i; (b) zone ii (Note: *s*: ground fissure dislocation; *p*: pile end-bearing).

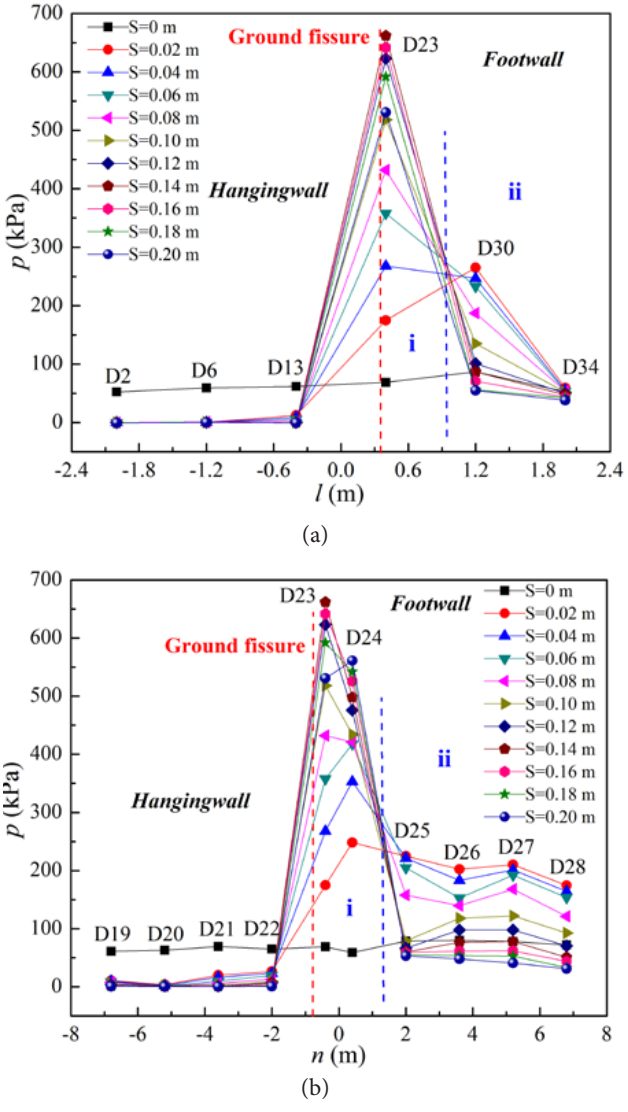

Figure 10. Variation in pile loads with respect to the increasing dislocation of the ground fissure (Note: *s*: ground fissure dislocation; *p*: pile loads; *l, n*: position of the pressure cells in normal and tangential direction of rail track)

The results show that loads on the hangingwall side decreased by a large amount when the ground-fissure dislocation increased up to 0.02 m, similarly to the variation seen in the end-bearings (Fig. 10). As discussed above, a 0.02-m-thick plain concrete cushion was emplaced between the RC slab and the piles, which entirely encapsulated the tops of the piles and the bottom of the RC slab. Thus, the decrease in the pile loads and the end--bearings on the hangingwall side was inferred to have been induced by the relative movement between the soil and the piles in the foundations (Fig. 11). The results indicated that as the settlement platform descended and the amount of ground-fissure dislocation increased, the soil in the foundation also descended and the pile settlement was controlled by the deformation of the RC slab. In places where the soil settlement in the foundation exceeded the pile settlement, the end-bearings decreased. In contrast, both the and end-bearings in the areas where the bottoms of the piles were out of contact with the surrounding soil (Fig. 11) decreased to zero (e.g., D2 and D6).

The data also indicated that the pile loads on the footwall side did not simply follow the division of the end-bearings. For example, the pile load D23 initially increased and then decreased as the ground-fissure dislocation increased; this pile was also divided into zone *i* due to variations in the end-bearing A23 (Figs. 8 and 10). Further analysis of all the pile loads classified into zone *i* increased as following enhancements in the dislocation, with the exception of D15 and D23, which increased initially before decreasing (Fig. 12a). The loads for the piles in zone *ii* exhibited the same trend for the end-bearing variation, wherein an initial increase was followed by a reduction as the ground-fissure dislocation was enhanced (Fig. 12b; noted that just some typical values are p\shown in Fig. 12 due to space limitations).

A comparison of the pile load and the end-bearing from the same pile (Fig. 12) indicated that the former was much larger than the latter, indicating that the pile side friction bore the majority of the load. It can thus be concluded that the piles in the foundation are end--bearing friction piles (Fig. 11). Thus, a decrease in the load in zones *i* and *ii* can be induced by mobilizing the piles to the maximum bearing capacity or unloading the upper structure. The results indicated that in zone *i* the pile loads on D15 and D23 increased to a significantly high value before subsequently decreasing, while all the other pile loads continued to increase in concert with the ground-fissure dislocation. Therefore, it can be concluded that these piles reached their ultimate bearing capacity during the course of the experiment. In contrast, none of the pile loads in zone *ii* increased to a value as high as those for D15 and D23 before decreasing; it can be inferred that this decrease in the pile loads in zone *ii* was induced by the unloading of the upper structure.

As observed in the deformation of the RC slab, the footwall side bent upwards to form a convex shape as a result of the ground-fissure dislocation. The deformation of the RC slab may have induced a decrease in the pile load in the area where the slab bent upwards. However,

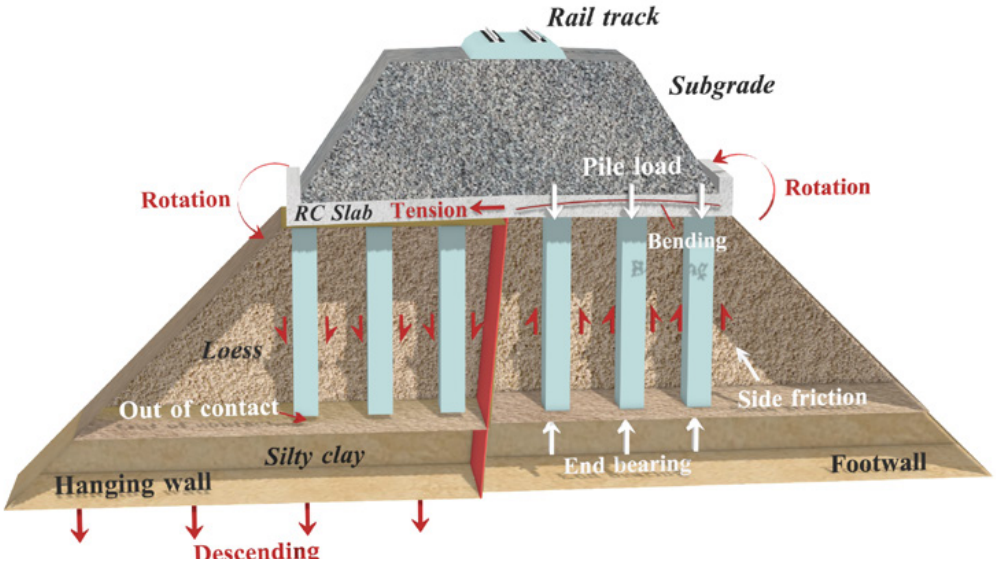

Figure 11. 3D illustration of bearing piles and mechanism of RC slab deformation.

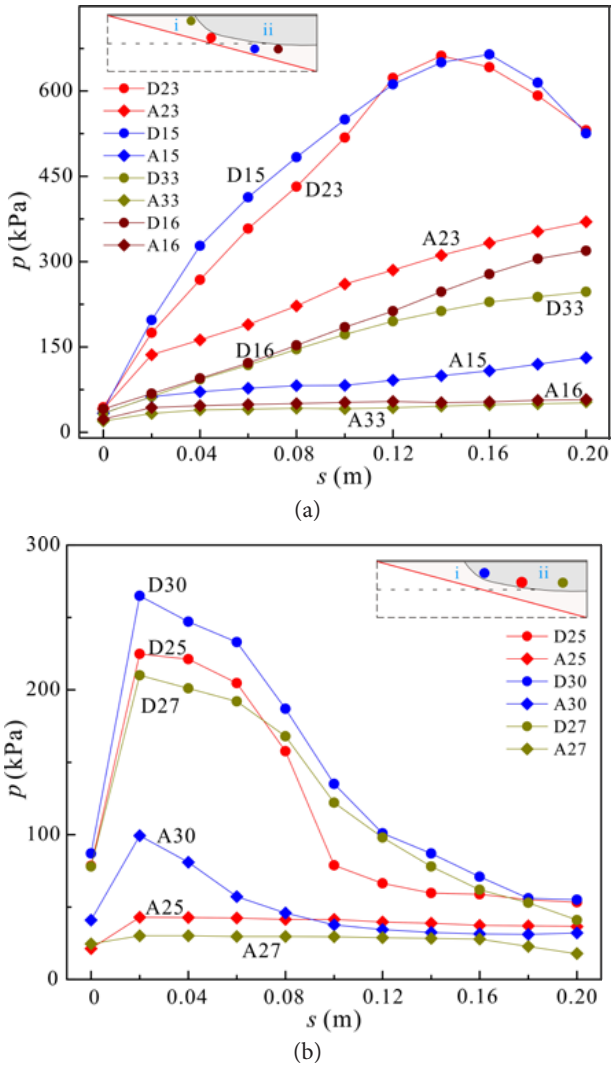

Figure 12. Comparison of pile load and pile end-bearing on the footwall side of the foundation: (a) zone i; (b) zone ii (Note: *s* is dislocation of ground fissure).

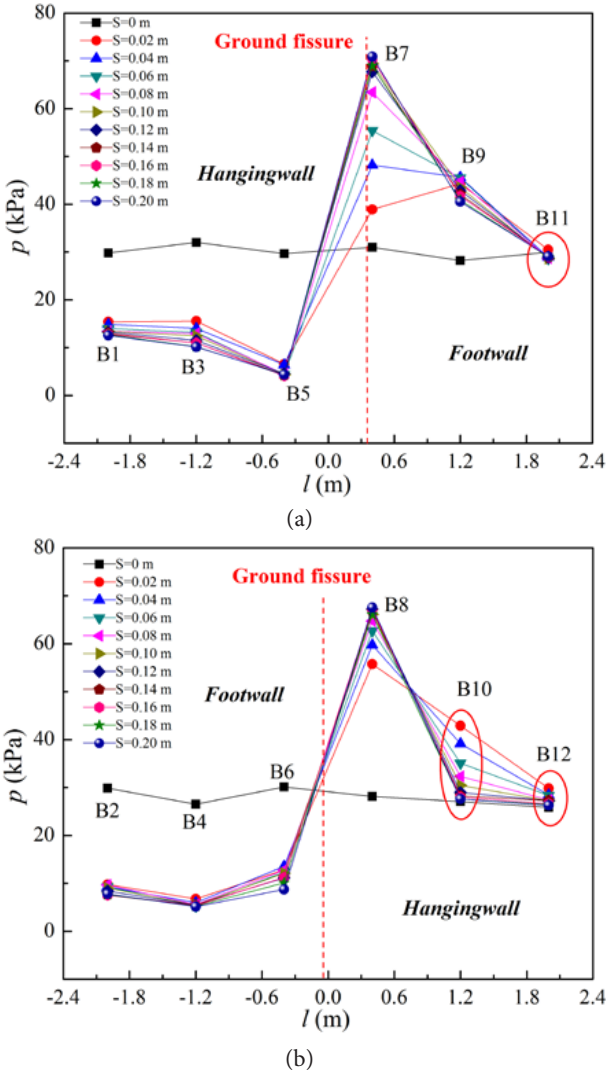

Figure 13. Variation in the earth pressure in the foundation with respect to the increasing dislocation of the ground fissure (Note: *s*: dislocation of ground fissure; *p*: earth pressure, *l*: position of the pressure cells in normal direction of rail track).

this shape change could not decrease the zone *ii* pile load while increasing the pile load in zone i. Thus, the variation in the pile loads indicates the RC slab was not just deformed because of the dislocation of the ground fissure, but was also rotated around this ground fissure (Fig. 11). The rotation of the RC slab induced load localization from the upper structure in zone *i* relatively closer to the ground fissure, while simultaneously unloading the upper structure in zone ii. Based on these results, the pile loads in zone *i* can continue to increase if it does not reach its ultimate bearing capacity. It should be noted that the rotation of the RC slab also induced the compression in the hanging side at a ground-fissure dislocation of 0.02 m.

The deformation and rotation of the RC slab was also reflected in the variations in the earth pressure in the foundation (Fig. 13). The results show that the foundation pressure decreased on the hangingwall side as the dislocation of the ground fissure increased, whereas the foundation pressure on the footwall side area close to the ground fissure increased with the enhanced dislocation. The pressures measured in the areas relatively far from the ground fissure initially increased before decreasing as the dislocation enhanced (Fig. 13).

3.3 Rail-track settlement

The rail-track settlement in the model is illustrated in Fig. 14, wherein a positive value refers to settling and a negative value indicates lifting. The results indicate that the rail track on the hangingwall side underwent significant settling, whereas that on the footwall side was

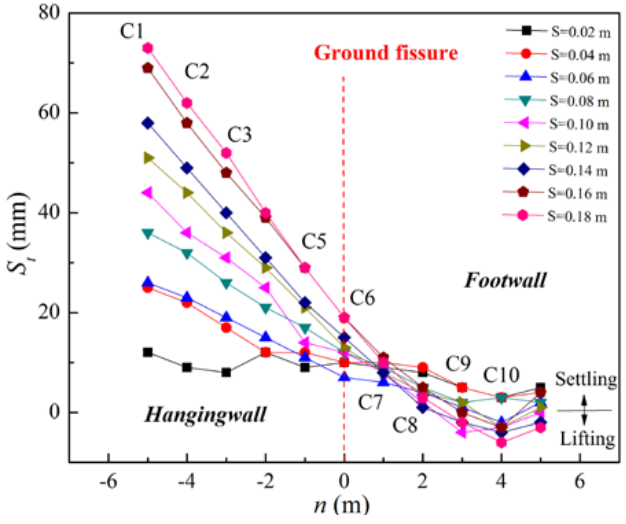

Figure 14. Variation in rail-track settlement as ground-fissure dislocation increased (Note: S_t: settlement of rail track; s: dislocation of ground fissure; n: position of the benchmarks in tangential direction of rail).

slightly raised (Fig. 14). Indeed, when the settlement platform descended by 0.02 m, the maximum rail-track settlement in the model reached 0.012 m. This indicates that a 0.1-m dislocation of the ground fissure in the case study can induce a maximum rail-track settlement of 0.06 m in the prototype scale. Based on the MRPRC guidelines [17], the post-settlement of the HSR should be less than 0.015 m. In other words, the 0.1-m dislocation of the ground fissure in the case study was already above the specified post-settlement limits. Given that the average measured activity rate of the TY3 ground fissure has recently been measured to be 4 mm per year [16], the presented data also indicates that the design of this embankment did not meet the 50-year service-period requirement at the point where it intersects the TY3 ground fissure.

4 EFFECT OF THE INTERSECTION ANGLES

4.1 Effect of the intersection angle on the RC slab deformation

Tests #2 and #3 were conducted to investigate the effects of the variable intersection angles that were run at 60° and 90°, respectively. The results indicated that the deformation and failure features of the RC slab on either side of the ground fissure in these tests were the same as in test #1. However, the failure zones, where the cracks formed on the RC slab when the settlement was 0.2 m, varied with the intersection angles (Fig. 15). The length of the failure zone was tangential to the rail track (i.e., the direction denoted by the axis x in Fig. 15) and decreased as the intersection angle increased. For example, the failure zone had lengths of $0.9W$, $0.49W$, and $0.31W$ for the intersection angles of 15°, 60°, and 90°, respectively, where W is the width of the RC slab. As presented in Fig. 15, the area of the failure zone on the footwall side, S_f, and the area on the hangingwall side, S_h, also varied as the intersection angle increased. S_f is slightly larger than S_h, thereby indicating that the footwall side of the RC slab was more affected by the dislocation of the ground fissure. The results indicated that both the length and the area of the failure zone decreased in a non-linear fashion as the intersection angle increased (Fig. 15). The accuracy of this non-linear correlation could be further enhanced if more model tests incorporating different intersection angles were to be conducted. Indeed, varying trends in the length and area of the failure zone indicate that orthogonal intersections between the embankment and the ground fissure exhibited the least effect on the RC slab.

4.2 Effect of the intersection angle on the A-boundary

Rapid decreases in both the pile loads and the end-bearing of the piles on the hangingwall side were also

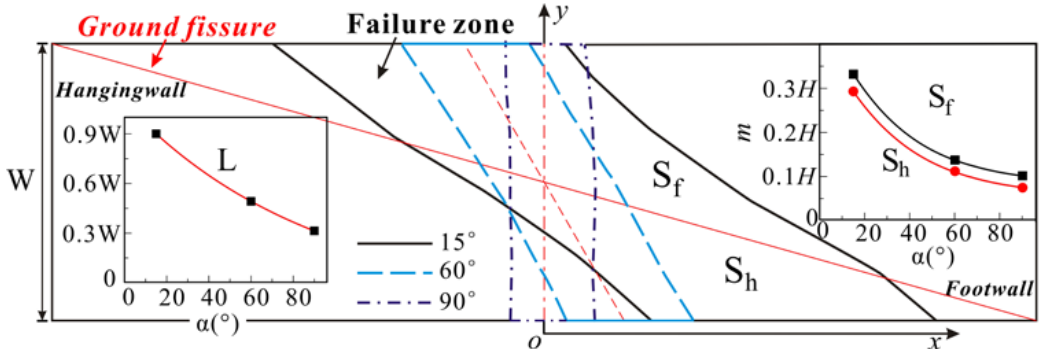

Figure 15. Analysis of the influence of the failure zone on the RC slab at different intersection angles (Note: S_f, S_h: area of the failure zone on the footwall and hanging wall side, respectively; m denotes the area of the failure zone at each side of the ground fissure; H: half area of the RC slab; α: intersection angle, L: length of failure zone in tangential direction of rail track).

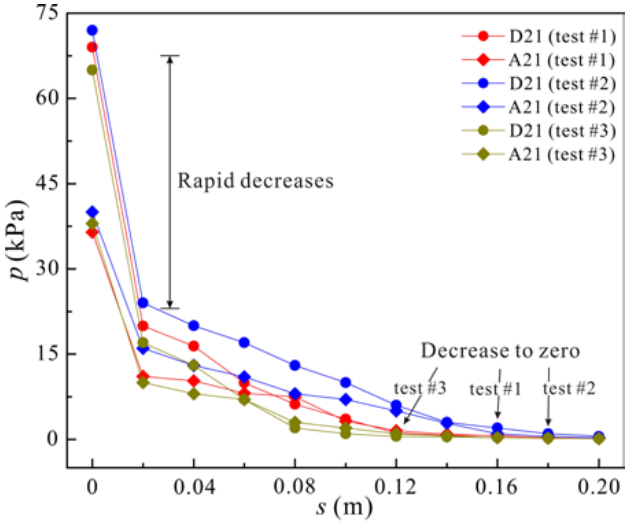

Figure 16. Rapid decreases in pile loads and end-bearing of piles on the hangingwall side.

detected in tests #2 and #3, as observed in D21 and A21 (Fig. 16). On the footwall side of the foundation, the results indicated that the A-boundary remained stable as the dislocation of the ground fissure increased, though this varied with the intersection angle (Fig. 17). The A-boundary remained approximately parallel to the ground fissure at different intersection angles, whereas the area of zone *i*, where the load of the upper structure was localized, decreased when the intersection angle increased. Indeed, at an intersection angle of 90°, zone *i* encompassed the smallest foundation area and exhibited the smallest number of piles mobilized to their ultimate bearing capacity (Fig. 17).

The results indicated that since the pile loads and the end-bearings exhibited differences in both characteristics and degrees of variation between zones *i* and *ii*, the A-boundary can be used to direct the foundation design of the embankment to intersect the ground fissures. For example, the number of piles in zone *ii* may be decreased, while simultaneously increasing the number in the zone to generate a more effective and economic design.

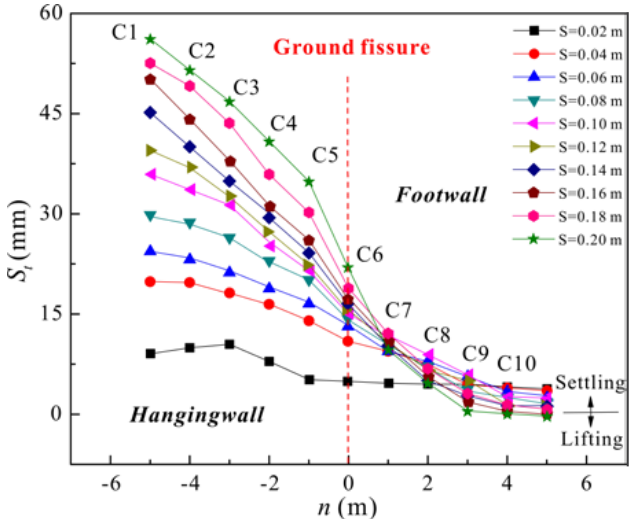

(a)

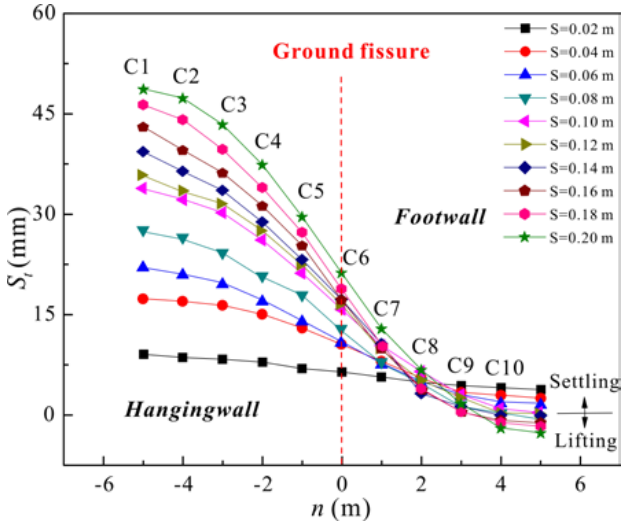

(b)

Figure 18. Analysis of the influence of different intersection angles on track settlement: (a) Test #2, (b) Test #3 (Note: S_t: settlement of rail track; *s*: dislocation of ground fissure; *n*: position of the benchmarks in tangential direction of rail).

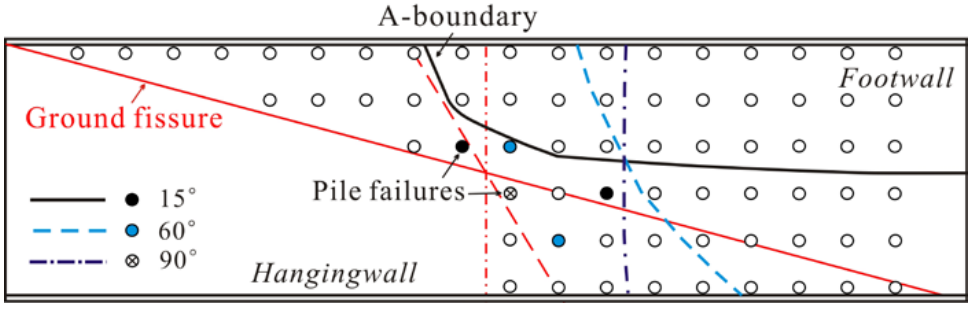

Figure 17. Analysis of the influence of different intersection angles on the position of the A-boundary.

4.3 Effect of the intersection angle on the rail-track settlement

The variations in the rail-track settlement as the ground--fissure dislocation increased (tests #2 and #3) are shown in Fig. 18. A comparison of the data presented in Figs. 18 and 14 indicates that, at the same ground-fissure dislocation, the maximum rail-track settlement decreased following an increase in the intersection angle. Indeed, in the case of the 0.02-m ground-fissure dislocation, the maximum rail-track settlements in tests #2 and #3 were 10.5 mm and 9 mm, respectively, which are 85% and 75% of that observed in test #1, respectively. Therefore, the results indicated that given one ground fissure with the same average activity rate, an HSR system with an orthogonally intersecting embankment will exhibit the longest service period. Taken in combination with the analysis of the effects of the intersection angle on the RC slab and foundations, embankments that intersect ground fissures orthogonally should be seriously considered when designing HSRs. Nevertheless, these results still do not prove that a GRPS embankment is suitable for the section of the Da-Xi HSR that intersects the TY3 ground fissure. As shown in test #3, a 0.02-m ground--fissure dislocation can induce a maximum settlement of 9 mm in the model track, which is equivalent to a 45-mm track settlement in the actual embankment and is above the limit specified by MRPRC [17]. Thus, to meet the required 50-year design service period for a HSR system, further research is necessary to develop a suitable embankment design that can cope with the bend-tension deformation of the RC slab and further decrease the rail-track settlement. In addition, it is suggested that the A-boundary was used as the reference to arrange the piles in the foundation.

5 RAIL-TRACK SETTLEMENT INDUCED BY TRAIN LOADING

During the operation of the Da-Xi HSR, the post--settlement of the rail track included a combination of ground-fissure dislocation-induced and train-loading post-settlement. Thus, the present study analyzed the train-loading-induced settlement to generate comparisons with the settlement induced by the ground fissures. Because the effects of the geogrid were ignored to simplify the presented calculation, the estimates for the train-loading-induced settlement were amplified and will be larger than the values observed in reality. The train-loading-induced settlement was estimated using a layer-wise summation method and was assumed to be equivalent to the strip load on the subgrade surface, as specified by German Railway Standards [7], due to the high stiffness of the ballast-less rail-track structure. Thus, the dynamic stress induced by train loading in the subgrade with respect to the depth can be calculated as follows:

$$\sigma_z = \frac{2p_0}{\pi}\left(\frac{n}{1+n^2} + \tan^{-1}\frac{1}{n}\right) \qquad (1)$$

where p_0 is the dynamic stress on the subgrade surface; z is the depth from the subgrade surface; and $n = z/b$, where b is the half width of the stress distribution on the subgrade surface.

However, since no field data for p_0 can be measured from the Da-Xi HSR, data from German Railway Standards [7] was used to estimate the dynamic stress in the subgrade. Applying p_0 to equation (1), the dynamic stress distribution along the depth of the subgrade in the Da-Xi HSR was obtained (Fig. 18). The results indicated a dynamic stress at the subgrade base of less than 2 kPa at a subgrade thickness in the actual embankment of 4.7 m (Fig. 18). In other words, the train loading insignificantly influenced the foundation settlement. The results of this study show that the cumulative settlement caused by the train loading was mainly limited to the subgrade zone. Thus, if this 4.7-m-thick subgrade layer was divided into 14 layers with thicknesses of 0.35 m, according to Chen et al. [4], the ultimate accumulative settlement of the Da-Xi HSR subgrade can be calculated by the layer-wise summation method as follows:

$$S_\infty = \sum_{i=1}^{n} \varepsilon_0^p \left(\frac{Li}{100}\right)^k \frac{p_{ref} + p_m}{s + m\left(p_{ref} + p_m\right) - \left(q_{ref} + q_m\right)} \qquad (2)$$

where n is the number of layers and i ranges from 1 to 14; $L = \sqrt{{p_{ref}}^2 + {q_{ref}}^2}$, where p_{ref} and q_{ref} refer to the peak

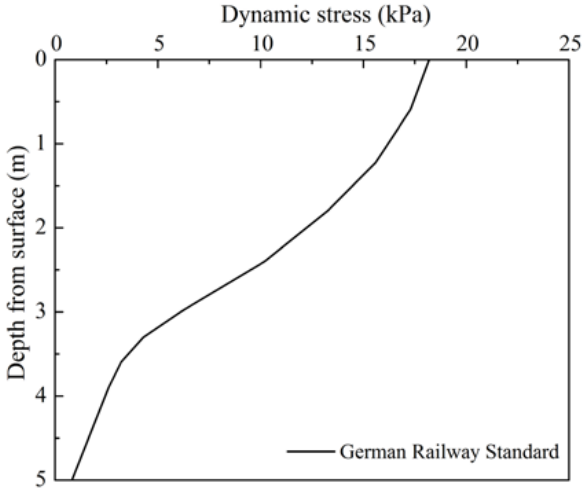

Figure 19. Graph showing the dynamic stress distribution as a function of depth.

mean stress and the peak deviatory stress caused by the cyclic train loading, respectively; p_m and q_m are the initial mean stress and the initial deviatory stress caused by the self-weight of the HSR subgrade, respectively; the material parameters ε_0^p and k can be determined using dynamic load tri-axial tests; and s and m are related to the strength parameters c and φ, respectively, which can be calculated as follows:

$$m = \frac{6\sin\varphi}{3-\sin\varphi},\ S = \frac{6\cdot\cos\varphi}{3-\cos\varphi} \qquad (3)$$

In the reduced-scale model, the water content of the surface and bottom layers of the subgrade were 4.5% and 5.8%, respectively. Thus, the tri-axial and dynamic load tri-axial tests were performed on the materials in these two subgrade layers with corresponding water contents. In the tri-axial tests, the apparent cohesion, c, and the internal friction angle, φ, were measured at 0 kPa and 42°, respectively, for the graded gravel in the surface subgrade layer, and 0 kPa and 46°, respectively, for the coarse sand and graded gravel mixture in the bottom layer of the subgrade. The material parameters ε_0^p and k were measured using dynamic load tests at 0.0019 and 0.318, respectively, for the surface subgrade layer, and 0.0015 and 0.357, respectively, for the bottom subgrade layer. Thus, incorporating these parameters into equations (2) and (3), the ultimate accumulative settlement of the Da-Xi HSR subgrade was calculated to be 3.7 mm. However, as noted above, even if this train-loading--induced settlement was magnified, it was still relatively small compared to that induced by the ground-fissure dislocation in the case study. Priority must, therefore, be given to the study of the embankment design to cope with the ground fissures.

6 CONCLUSIONS

The present study conducted and reported a series of reduced-scale experiments to investigate the influence of ground fissures on HSR embankments at different intersection angles. A sensitivity analysis was used to investigate the effects of the intersection angles on the RC slab deformation, the stress state of the bearing piles, and the track settlement. The train-load-induced settlement of the embankment was then estimated using the analytical model put forward by Chen et al. [4] and then compared with the settlement induced by the ground--fissure dislocation. Five conclusions can be drawn based on this research.

1. The deformation of the RC slab can be divided into two phases due to the differences in the strain features on the hangingwall side with respect to increases in the dislocation of the ground fissure. The strain data indicates that the RC slab underwent integrated bend-tension failure as a result of the action of the ground fissures, whereas the deformation phase and failure mode of the slab were independent of the intersection angle.
2. The pile load and the end-bearing of the piles on the hangingwall side of the foundations decreased rapidly when the dislocation of the ground fissure increased from zero to 0.02 m. Thus, the footwall side of the foundation can be divided into zones *i* and *ii* based on the variations in the pile loads and the end-bearings. A reduction in the pile loads of zone *i* was induced by the failure of the mobilized piles due to their ultimate bearing capacity, whereas the decrease in the pile loads and the end-bearings observed in zone *ii* was induced by the unloading of the upper structure associated with the deformation and rotation of the RC slab.
3. The analysis of the effect of the intersection angle quantitatively explained the minimal effect exerted by a ground fissure orthogonally intersecting on the embankment. The results indicated that the length and area of the failure zone of the RC slab decreased non-linearly following an increase in the intersection angle. In addition, the boundary between zones *i* and *ii*, termed the A-boundary, was dependent on the intersection angle and was independent of the ground-fissure dislocation.
4. As a result of the effect of the intersection angle on the track settlement, the GRPS embankment was deemed unsuitable for use in this specific Da-Xi HSR section. However, further research is required to propose an appropriate embankment design solution to cope with the bend-tension deformation in the RC slab. The A-boundary was suggested as a reference to arrange the foundation piles, thereby generating a more effective and economic overall design.
5. The ultimate cumulative settlement of the subgrade in the Da-Xi HSR was estimated to be 3.7 mm. The settlement induced by the train load was extremely small as compared to that induced by the ground fissure, and is a variable that should considered when designing the HSR.

Acknowledgments

This research was funded by the grants from the Major Program of National Natural Science Foundation of China (Grant No. 41790441), the National Key Research and Development Program of China (Grant Nos. 2017YFC1502506, 2017YFC0505304, 2017YFC050530302, 2018YFC1505201), the Opening Fund of State Key Laboratory of Geohazard Prevention

and Geoenvironment Protection, Chengdu University of Technology (Grant No. SKLGP2019K001), the Special Fund for Basic Scientific Research of Central Colleges, Chang'an University (Grant No. 300102269506), the National Natural Science Foundation of China (Grant No. 41807234, 41302252).

REFERENCES

[1] Augustin, S., Gudehus, G., Huber, G., Schünemann, A. 2003. Numerical model and laboratory tests on settlement of ballast track, in: Popp, K., Schiehlen, W. (Eds.), System dynamics and long-term behavior of railway vehicles, track and subgrade. Springer Verlag, Berlin, pp. 317-336.

[2] Bell, J.W., Price, J.G., Mifflin, M.D. 1992. Subsidence-induced fissuring along preexisting faults in Las Vegas Valley, Nevada. Pro. 35th Annual Meeting of the Association of Engineering Geologists, Los Angeles, pp. 66-75.

[3] Calcada, R., Delgado, R., Matos, A.C.E. 2009. Bridges for High-Speed railways. Taylor & Francis Group, London.

[4] Chen, R., Jiang, P., Ye, X., Bian, X. 2016. Probabilistic analytical model for settlement risk assessment of High-Speed Railway subgrade. J. Perform. Constr. Facil. 30, 3. doi: 10.1061/(ASCE)CF.1943-5509.0000789

[5] Dethy, B., Bouhenni, S. 2004. High Speed Lines in Belgium: Various engineering geological and geotechnical aspects. Engineering Geology for Infrastructure Planning in Europe 104, 485-503. doi: 10.1007/978-3-540-39918-6_55

[6] Filippis, L.D., Anzalone, E., Billi, A., Faccenna, C., Poncia, P.P., Sella, P. 2013. The origin and growth of a recently-active fissure ridge travertine over a seismic fault, Tivoli, Italy. Geomorphology 195, 2, 13-26. https://doi.org/10.1016/j.geomorph.2013.04.019

[7] German Railway Standard, 2008. Erdbauwerke planen, bauen und in-stand halten [Earthworks plan, build and maintain]. Ril 836, Berlin (in German).

[8] Holzer, T.L., Davis, S.N., Lofgren, B.E. 1979. Faulting caused by groundwater extraction in southcentral Arizona. Journal of Geological Research 84, 82, 603-612. doi: 10.1029/JB084iB02p00603

[9] Holzer, T.L. 1984. Ground failure induced by groundwater withdrawal from unconsolidated sediment. Reviews in Engineering Geology 6, 67-106. doi: 10.1130/REG6-p67

[10] Huang, R.Q., Li, Y.R., Qu, K., Wang, K. 2013. Engineering geological assessment for route selection of railway line in geologically active area: a case study in China. J. Mt. Sci. 10, 4, 495-508. doi: 10.1007/s11629-013-2660-2

[11] Jiang, Y., Han, J., Zheng, G. 2014. Numerical analysis of a pile-slab-supported railway embankment. Acta Geotechnica 9, 499-511. doi: 10.1007/s11440-013-0285-9

[12] Kreitler, C.W. 1977. Fault Control of Subsidence, Houston, Texas. Ground Water 15, 3, 203-214. doi: 10.1111/ j.1745-6584.1977.tb03165.x

[13] Lee, C., Zhang, J., Zhang, Y. 1996. Evolution and origin of the ground fissures in Xian, China. Engineering Geology 43, 1, 45-55. doi: 10.1016/0013-7952(95)00088-7

[14] Leonard, R.J. 1929. An earth fissure in southern Arizona. Journal of Geology 37, 8, 765-774.

[15] Lofgren, B.E. 1978. Hydraulic stresses cause ground movement and fissures, Picacho, Arizona. Geological Society of America Abstracts with Programs 10, 3, 113.

[16] Meng, L.C. 2011. Study on the Formation Mechanism of Ground Fissures in Shanxi Fault Basin. Dissertation, Chang'an University (in Chinese).

[17] Ministry of Railways of the People's Republic of China (MRPRC), 2009. Design code for High Speed Railway. TB10621-2009, China Railway Press, Beijing.

[18] Narasimhan, T.N. 1979. The significance of the storage parameter in saturated-unsaturated groundwater flow. Water Resources Research 15, 3, 569-576. doi: 10.1029/ WR015i003p00569

[19] Nordic Geotechnical Society, 2002. Nordic handbook. Reinforced soils and fills. Nordic Geotechnical Society, Stockholm.

[20] Peng, J.B., Chen, L.W., Huang, Q.B., Men, Y.M., Fan, W., Yan, J.K. 2013. Physical simulation of ground fissures triggered by underground fault activity. Engineering Geology 155, 14, 19-30. doi: 10.1016/j.enggeo.2013.01.001

[21] Peng, J.B., He, K., Tong, X., Huang, Q.B., Liu, C. 2016. Failure mechanism of an underground metro tunnel intersecting steep ground fissure at low angle. Int. J. Geomech. 17, 5, doi: 10.1061/(ASCE)GM.1943-5622.0000677

[22] Pratt, W.E., Johnson, D.W. 1926. Local subsidence of the Goose Creek oil field. Journal of Geology 34, 7, 557-590.

[23] Sarkar, I. 2004. The role of the 1999 Chamoli earthquake in the formation of ground cracks. J. Asian Earth Sci. 22, 5, 529-538. doi: 10.1016/S1367-9120(03)00093-2

[24] Shaer, A.A.l., Duhamei, D., Sab, K., Foret, G., Schmitt, L. 2008. Experimental settlement and dynamic behavior of a portion of ballasted railway

track under high speed trains. Journal of Sound and Vibration 316, 1, 211-233. doi: 10.1016 /j.jsv.2008.02.055

[25] Sun, Q., Indraratna, B., Nimbalkar, S. 2016. Deformation and degradation mechanisms of railway ballast under high frequency cyclic loading. J. Geotech. Geoenviron. Eng. 142, 1. doi: 10.1061/ (ASCE)GT.1943-5606.0001375

[26] Wang, J., Wang, J., Liu, J., Li, C., Yang, R. 2000. Theory of ground fissures hazards and its application. Shanxi Science and Technique Publishing House, Xi'an (in Chinese with English abstract).

[27] Wang, Z.F., Shen, S.L., Cheng, W.C., Xu, Y.S. 2016. Ground fissures in Xi'an and measures to prevent damage to the Metro tunnel system due to geohazards. Environ. Earth Sci. 75, 6, 511-522. doi: 10.1007/s12665-015-5169-x

[28] Xu, L.Q., Li, S.Z., Cao, X.Z., Somerville, I.D., Suo, Y.H., Liu, X., Dai, L.M., Zhao, S.J., Guo, L.L., Wang, P.C., Cao, H.H. 2016. Holocene intracontinental deformation of the northern North China Plain: Evidence of tectonic ground fissures. Journal of Asian Earth Sciences 119, 1, 49-64. doi: 10.1016/j. jseaes.2016.01.003

[29] Zhang, Y., Wang, Z.C., Xue, Y.Q., Wu, J.C., Yu, J. 2016. Mechanisms for earth fissure formation due to groundwater extraction in the Su-Xi-Chang area, China. Bull. Eng. Geol. Environ. 75, 2, 745-760. doi: 10.1007/s10064-015-0775-0

STRESS-STRAIN BEHAVIOR OF BLUE MARLS FROM THE GUADALQUIVIR RIVER BASIN IN SPAIN

NAPETOSTNO DEFORMACIJSKI ODZIV MODRIH LAPORJEV IZ POVODJA GUADALQUIVIRJA (ŠPANIJA)

Félix Escolano Sánchez
Polytechnical University of Madrid,
Civil Engineering Department
Alfonso XII, 3 y 5 - 28014 Madrid, Spain
E-mail: felix.escolano@upm.es

Manuel Bueno Aguado
PROES Consultores.
General Yagüe, 39, 28020 Madrid, Spain
E-mail: mbueno@proes.engineering

Svetlana Melentijevic
Complutense University of Madrid,
Faculty of Geology
Madrid, Spain
E-mail: svmelent@ucm.es

DOI https://doi.org/10.18690/actageotechslov.16.1.30-42.2019

Keywords

Guadalquivir blue marls, sedimentary clay, triaxial test, undisturbed and remolded samples, lime stabilization, stress-strain behavior

Ključne besede

Guadalquivirski modri lapor; sedimentirana glina; triosni preizkus; neporušeni in pregneteni vzorci; stabilizacija z apnom; odziv napetost-deformacija

Abstract

This paper describes the geotechnical behavior of the Blue Marls from the Guadalquivir River Basin in Southern Spain, defined as high-plasticity clays that behave as a stiff, over-consolidated clayey soil. These Blue Marls are, in general, classified as an inadequate material for reuse in various earthworks. In this study the comparison between the geotechnical properties of its natural and compacted remolded state, with and without additives, is studied based on different laboratory tests. A great variety of laboratory tests were performed, including triaxial tests under consolidated undrained conditions. Three types of samples were tested in triaxial tests to define different stress-strain behaviors: undisturbed and remolded samples of the in-situ clay material, as well as remolded clay samples mixed with lime. Lime stabilization is frequently used to improve the geotechnical properties of clayey soils for application in different earthworks. The back-analysis of the slope stability is performed for a comprehensive assessment of the condition of the slopes consisting of these remolded materials mixed with lime as well as without lime. The results of the retrospective analysis of man-made slopes permit an analysis of the operational geotechnical strength parameters necessary in the design of slopes as well as its comparison with the results of the triaxial consolidated undrained tests. The improvement of the strength parameters for the slope-stability analysis is confirmed under remolded conditions with and without the addition of the small amount of lime.

Izvleček

V članku je opisano geotehnično obnašanje modrih laporjev iz porečja reke Guadalquivir (južna Španija), ki so opredeljeni kot gline z visoko plastičnostjo in se obnašajo kot trdna prekonsolidirana glinasta zemljina. Obravnavani modri laporji so na splošno opredeljeni kot neustrezni material za njihovo ponovno uporabo v različnih zemeljskih delih. V tej študiji smo na podlagi različnih laboratorijskih preiskav preučili primerjavo med geotehničnimi lastnostmi njenega naravnega in zgoščenega pregnetenega stanja z dodatki in brez njih. Izvedle so se številne laboratorijske preiskave, vključno s triosnimi preizkusi v konsolidiranih nedreniranih pogojih. Da bi določili različno obremenitveno-deformacijsko obnašanje, smo v triosnih aparatih preizkusili tri vrste preizkušancev: neporušene in pregnetene preizkušance »in situ« glinastega materiala, kot tudi pregnetene preizkušance gline, pomešane z apnom. Stabilizacija z apnom se pogosto uporablja za izboljšanje geotehničnih lastnosti glinastih tal za uporabo v različnih zemeljskih delih. Za celovito oceno varnosti pobočij, sestavljenih iz teh predelanih materialov, zmešanih z apnom in brez apna, so bile izvedene povratne stabilnostne analize. Rezultati retrospektivne analize takšnih umetnih pobočij omogočajo analizo dejanskih geotehničnih parametrov strižne trdnosti, ki so potrebni pri načrtovanju pobočij ter primerjavo z rezultati triosnih konsolidiranih nedreniranih preizkusov. Izboljšanje parametrov strižne trdnosti v stabilnostni analizi pobočij je bila potrjena za pregnetene pogoje, tako z kot brez dodatka majhne količine apna.

1 INTRODUCTION

The Guadalquivir Blue Marls were studied at different points along the Guadalquivir River Basin in Southern Spain by different authors for the construction of various geotechnical structures and after a lot of damage that occurred in these materials after having this material as a foundation for specific structures. It was studied in relation to underground works associated with the construction of the subway for the city of Seville and for many slope-stability problems that happened during the construction of infrastructures (e.g., the slope-stability problem at Almodóvar del Rio at the high-speed railway Madrid–Seville) [1,2,3]. The study of these marls was a crucial part of the analysis of the 1998 failure of the Aznalcollar tailing dam, which was founded on this formation and caused one of the major environmental disasters in Spain [4,5,6,7]. These marls were also studied for the slope-stability analysis at the Cobre Las Cruces open pit mine [8,9]. This material is characterized by fragile shear strength and degradation after drying and wetting processes [4,8,10] that could provoke a sudden geotechnical failure in these materials. For that reason these Blue Marls are usually not suitable for reuse in the construction of different earthworks such as embankments, earth dams, pavement bases, etc. according to the Spanish standard PG-3 [11].

These marls represent a fine-grained soil with an average percentage of the clay fraction ranging from 50 to 60%, classified as high-plasticity clay (CH) with a high carbonate content. Its behavior is like a stiff soil, defined as over-consolidated clays [4,8,9,14].

This study is a comparison of the behavior of the undisturbed blue marls and compacted remolded samples with and without additives that are analyzed in order to quantify the improvement of the geotechnical properties. The improvement of the geotechnical properties by lime is studied. Lime is one of the most commonly used binders for an improvement of the geotechnical properties of clayey soils, due to its effect on the modification of soil particle packaging, soil plasticity, workability, dispersity, permeability, swelling and shrinkage properties, compressibility, etc. [12]. It is widely used for the soil stabilization of different types of structures, such as a foundation base, slope protection, embankments, highway and railway sub-grade, etc. due to its low cost and ease of application in construction [13].

For this paper, the observational method is conducted over man-made slopes constructed in these Blue Marls over a period of 10 years, to deduce the resistance parameters based on a slope-stability back analysis. These values are compared to laboratory strength parameters deduced from the triaxial consolidated undrained (CU) tests performed over undisturbed and remolded samples (with and without the addition of lime) to compare the stress-strain behavior of the undisturbed and remolded samples of Blue Marls.

This paper emphasizes the importance of the compacted remolded state of the material to be introduced in the earthworks in order to improve an inadequate clay material, such as blue marls (highly plastic and expansive) with and without lime for its application in different earthworks. In general, this kind of expansive clay can be encountered worldwide, and this subject could be of a great importance for the construction of different earthworks.

According to [15], slopes and cut-offs in blue marls have undergone instabilities despite its behavior as a soft rock/stiff soil. A wide range of factors affect its instability, making it very challenging to select the most suitable stabilization measures once the instability has occurred, as well as processes for its mitigation. Some of the factors that affect its instability is its great weathering, which is increased due to decompression during excavation, attributed to the existence of micro-discontinuities with low resistance and strain-softening behavior that is increased during the process of humidity draught (i.e., a rainfall period), in this way exhibiting a great variability in behavior with time. The effect of the drying and wetting cycles process on the changes of macro- and microstructure of undisturbed Guadalquivir blue marls were studied by [10].

2 RESEARCH METHODOLOGY

The investigation was divided into three stages, as described in Fig. 1.

During the first stage (5-year duration), a field research campaign was carried out based on a study of 41 slopes with different heights and inclination angles, on the unit of Guadalquivir Blue Marls. The geotechnical campaign was then supplemented by the rotary drilling of mechanical boreholes with the continuous taking of undisturbed samples. The samples were taken in the winter period after a long period of drought. These samples were taken during a wet season in which the area had received significant precipitation.

During the second stage, a laboratory-test campaign was carried out on 89 samples for the identification of properties (i.e., sieve analysis (wet-sieve analysis and sedimentation analysis), natural moisture content, Atterberg

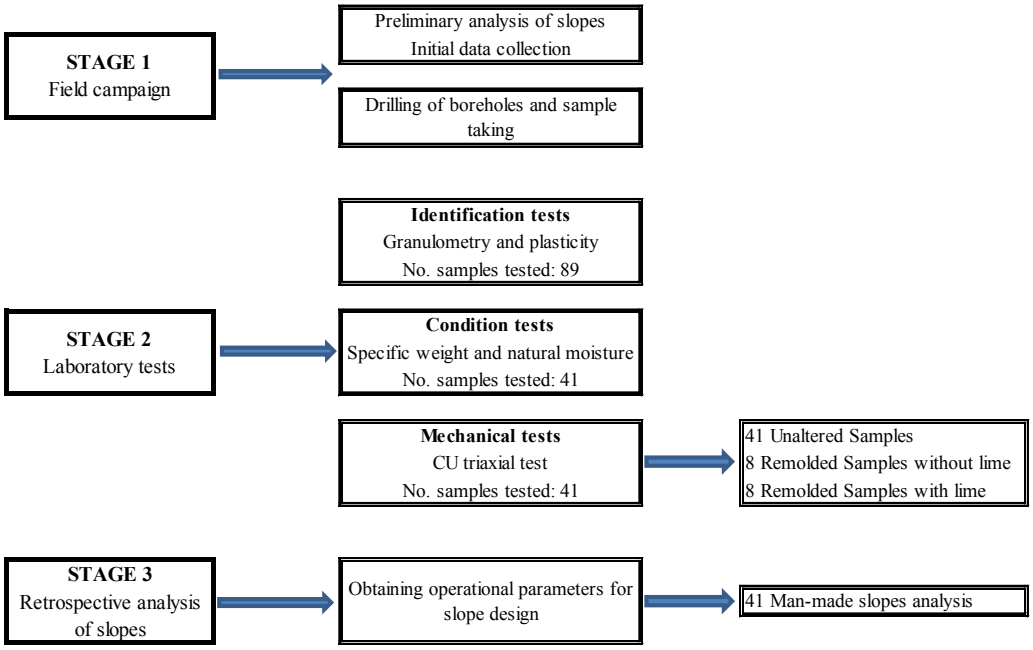

Figure 1. Research methodology.

limits, dry unit weight, unit weight of solid particles, etc.). Mostly, the samples were taken at shallow depths (down to 4 meters from the surface) due to its application for the possible reuse in the construction of man-made slopes. In order to study the stress-strain behavior, 57 triaxial tests were performed on: undisturbed samples (41), remolded samples (8) and remolded samples mixed with lime (8). The purpose of the tests carried out on remolded samples with and without lime was to study the improvement of their geotechnical behavior regarding strength properties (friction angle and cohesion) for its possible use as a material for the construction of different geotechnical structures (man-made slopes, pavement base, earth dams, embankments, etc.). The small amount of lime (2% of the weight) was added to the mixture of remolded samples in order to study its influence on the geotechnical parameters.

Finally, stage 3 is the retrospective analysis of the slopes studied during the first stage that makes it possible to reach conclusions regarding operational geotechnical strength parameters used for slope design, comparing them with the results obtained by laboratory tests (i.e., triaxial consolidated undrained tests).

3 GEOGRAPHIC AND GEOLOGICAL CLASSIFICATION OF THE GUADALQUIVIR BASIN

The Guadalquivir Basin occupies a large area in southern peninsular Spain. It takes the form of an elongated wedge running ENE–WSW, with the Guadalquivir River flowing through it. Geographically, to the north it is bordered by the terrain of the Sierra Morena, to the south by the terrain of the Baetic Range, and to the west by the Gulf of Cádiz. Although its topography is very gentle, there is a gradual decline in altitude from the eastern sector (800 m) to the west (sea level) [16].

In geological terms, it is a Tertiary exoreic basin which was formed during the Neogene. The northwestern edge of the basin is represented by the Iberian Massif, with very clear contact in a SW–NE direction as well, made up of materials from the Paleozoic Era (600–250 My) [17]. The southern edge of the depression, whose boundaries are not as well defined, is represented by materials from the Mesozoic Era (approximately 250–90 My), part of the Bética Range (Fig. 2) [18].

This basin began filling more than 10 My, the result of the erosion of the mountainous terrain bordering it. The northwestern edge always remained stable (without significant tectonic movements), providing a continuous supply of sediment to the basin from the stripping of the terrain. In contrast, the southeastern edge was constantly rising, with frequent movements and slides, supplying a smaller amount of sediment.

The largest amount of sediment was supplied by the erosion of the northwestern edge, with the deposits being more significant due to their representativeness: clayey or carbonated marls, in some cases slightly silty, bluish-gray in color (when they are intact) with zero stratification, and massive in appearance with concho-

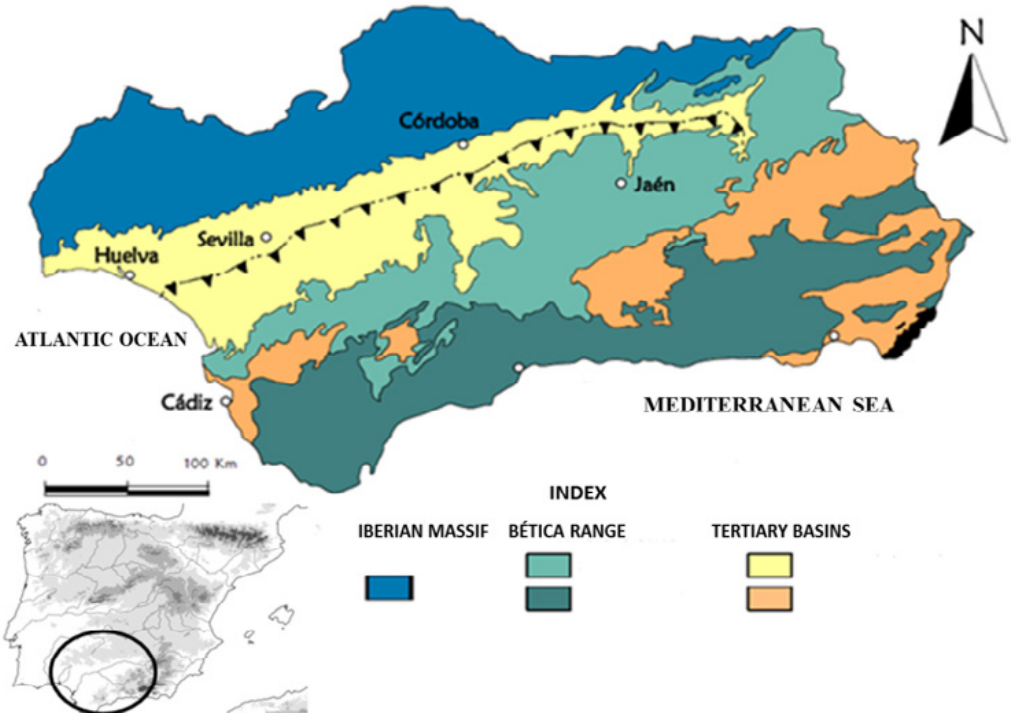

Figure 2. Geographic and geological locations of the Guadalquivir Basin (modified from [18]).

idal fracture. In an altered state (weathered), they take on a brown and yellowish gray-brown color due to the presence of iron oxides. Material is predominantly phyllosilicates (more than 65%). The rest of its components are carbonates and quartz. The clay minerals are formed mainly by illite and smectite. The presence of gypsum may also occasionally be observed.

There is extremely abundant microfauna, which has made it possible to date them to the Upper Miocene, specifically, the Messinian (6.3–5.2 My). This subject has already been a study of [18]. Due to their color (bluish--gray, when fresh), they are described in the geological and geotechnical literature as Guadalquivir Blue Marls. These deposits outcrop along some 800 km, from the province of Huelva, at the mouth of the Guadalquivir River, to the province of Jaén. The unit is present in the subsoil of major metropolitan areas such as the city of Seville.

4 GEOTECHNICAL CHARACTERIZATION OF THE GUADALQUIVIR BLUE MARLS

The geotechnical properties of Guadalquivir blue marls were extensively defined by different authors [2,4,8]. According to identification tests performed over 89 samples for this study, the material is primarily of a clayey nature, with over 80% of material passing through the No. 200 ASTM sieve mesh. The liquid limit values vary from 40 to 70%, while the plasticity index ranges from 15 to 40%. Therefore, these materials fall within the CH to CL category, according to the ASTM classification [19]. The Casagrande plasticity chart is given in Fig. 3, also indicating the suitability of the application of this material for the construction of highway subgrades according to the Spanish Code PG-3 [11]. Due to the nature of this material, classified as marginal to tolerable, the compaction is performed in order to study the behavior of remolded samples with and without the addition of lime.

The specific dry weight ranges from 14 to 16 kN/m^3, and the specific weight of the particles ranges from 25 to 27 kN/m^3. Regarding the carbonate content, most tested samples contain 20–55% $CaCO_3$, thus defining them as clayey marls and marls (Fig. 4).

Regarding the state conditions, Fig. 5 shows the initial moisture content and unit dry specific weight of both undisturbed and remolded samples. It is observed how the dry specific density is hardly modified with the remolding process. The unit dry weight is generally within a relatively narrow range from 14 to 16 kN/m^3, while the range of values for the initial natural moisture content is somewhat broader and mostly from 20 to 30%. It can be observed that these materials can be defi-

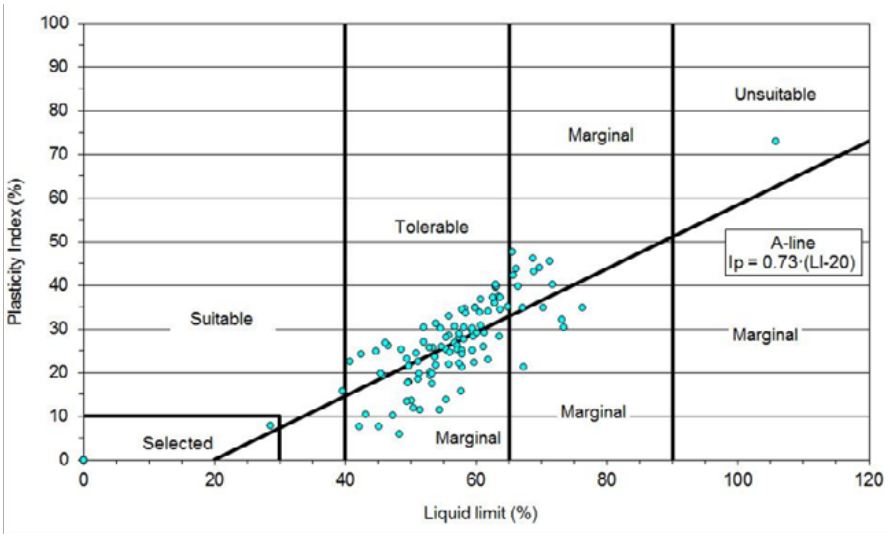

Figure 3. Plasticity chart of the studied undisturbed samples of blue marls.

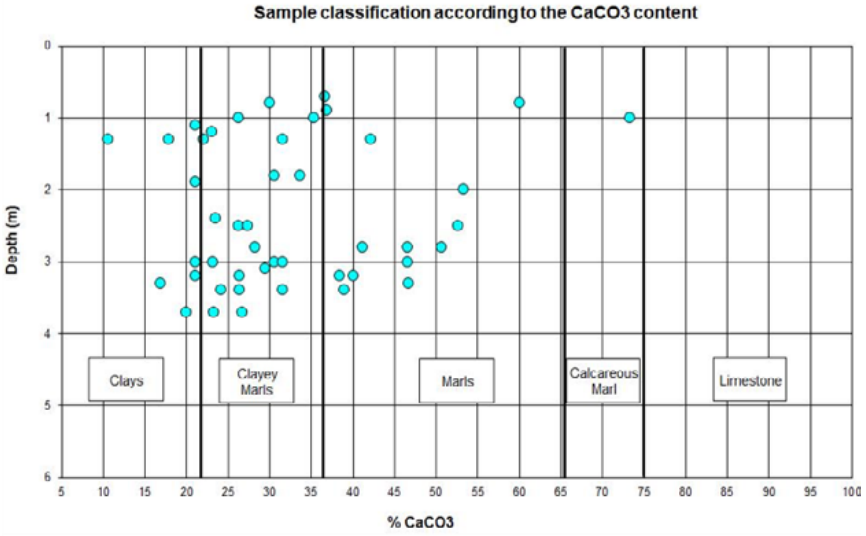

Figure 4. Relationship between % $CaCO_3$ and the depth of the undisturbed samples.

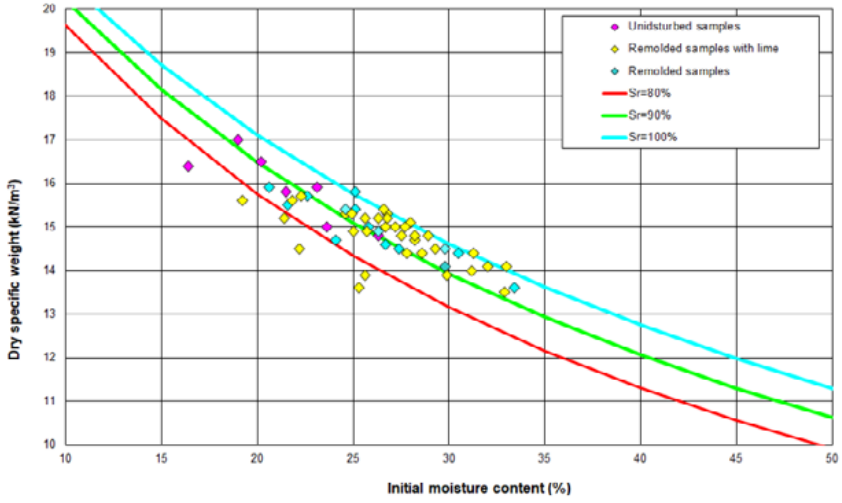

Figure 5. Initial state of the samples tested in the triaxial test (initial moisture content vs. specific dry weight).

ned between 80 and 100 % saturated, being closer to the full saturation the remolded samples with and without the addition of lime.

Of the 89 samples taken during the field research campaign, and tested for defining the identification properties, 57 were selected for testing in the triaxial apparatus under consolidated undrained conditions (CU) with a measurement of pore-water pressure according to the ASTM standard [20]. The following sets of samples were measured: 41 undisturbed samples, 8 remolded samples and 8 remolded samples mixed with lime. All the samples were consolidated under pressure ranging from 50 to 300 kPa. The minimum consolidation period for each tested sample was 24 hours, providing that the strains are stabilized during this period under the load application speed of 0.04 mm/min during the failure stage. The failure stage was conducted for the strains reaching a maximum of 20%. The outputs of these triaxial tests are discussed in the following sections.

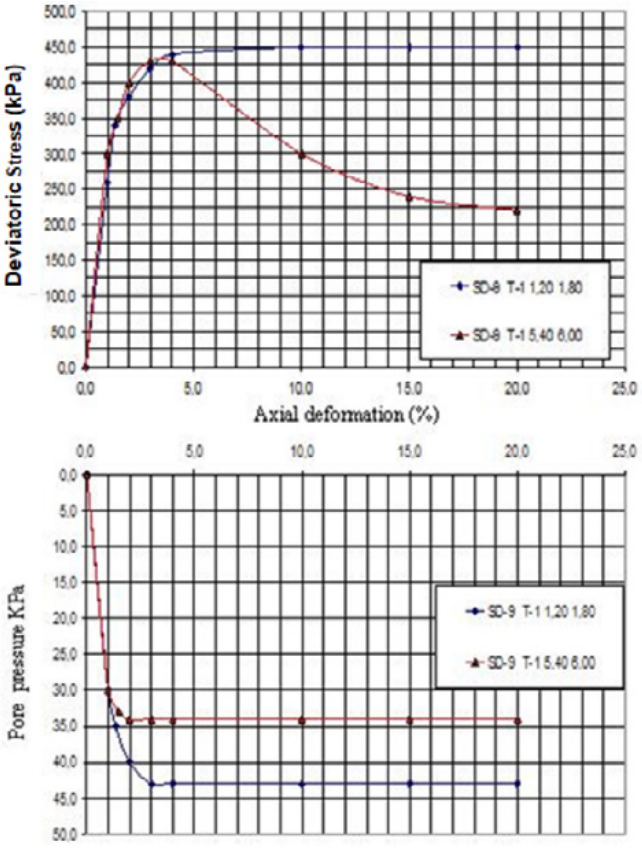

Figure 6. Triaxial test results on the undisturbed samples: deviatoric stress and pore pressure vs. axial deformation.

5 SHEAR-STRENGTH CHARACTERISTICS OF THE UNDISTURBED MARL SAMPLES

The tests performed on undisturbed samples show two different stress-strain behavior patterns under the same consolidation pressure, as can be observed in Fig.6. These two figures show a general trend of the stress--strain behavior for all the tested undisturbed samples.

Both behavior patterns presented in Fig. 6 reach almost the same maximum deviatory stress at approximately same strain level (1–3%), presenting after that different behavior. For the first case, the behavior is defined as an elasto-plastic one, where after reaching the maximum stress, with a relatively small increase in the deviatoric stress the strain continues its increase up to 20%, when the test is stopped. In this mode of ductile fracture, the tested sample takes on a barrel shape, so that the diameter of the central area increases without the appearance of failure surfaces. The second stress--strain type of behavior represents the strain softening behavior after achieving a peak deviatory stress for a strain level between 1 and 3 %. After reaching its peak value, the deviatoric stress decreases with the continuing increase of the strains until reaching its residual value (considered in this case at the end of the test). This mode of brittle failure is associated with the appearance of failure planes in the test sample. The elastic modulus ranges from 25 to 30 MPa for different failure patterns presented in Fig. 6, ductile and brittle respectively, under the same consolidation pressure [21]. The pore-water pressure increases during the failure stage for both types of behavior (brittle and ductile) till reaching its maximum value at the maximum level of deviatoric stress corresponding to the axial strain level of 2–3%, and after that remaining constant until failure.

Plotting the results of the triaxial tests in terms of Lambes variables on a *p*-*q* diagram the stress path is analyzed [22]. These Lambe parameters represent the following: $p=(\sigma_1'+\sigma_3')/2$ and $q=(\sigma_1'-\sigma_3')/2$. Fig. 7 shows the stress path reaching the $q = p/3$, being typical of materials with dilatant behavior or for over-consolidated clays. Plotting the failure points on *p*-*q* axes makes it possible to define a geometric location where the failure occurs (see Fig. 8).

Failure is considered to be the point where the deviatoric stress stops increasing with small strains ranging between 1 and 3% in this case. This geometric location is approximately a straight line, corresponding to the Mohr-Coulomb parameters:

- Cohesion 10 kN/m^2
- Angle of internal friction 25°

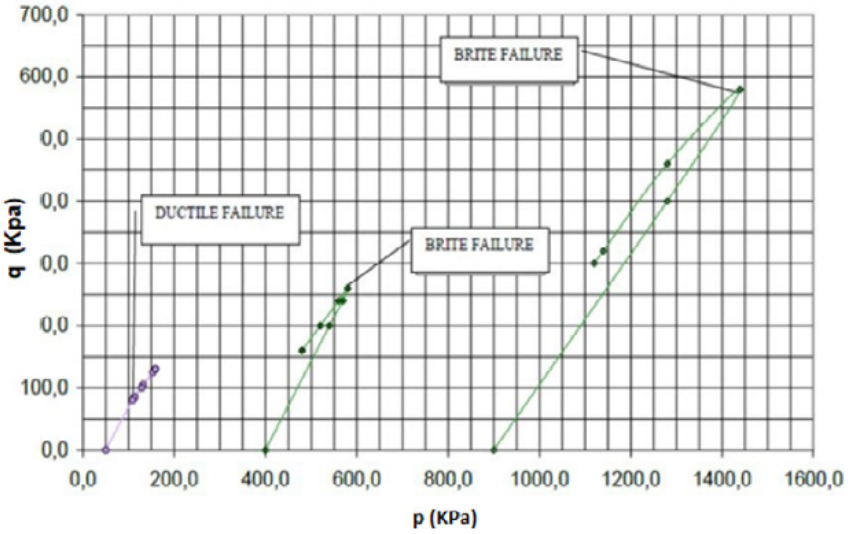

Figure 7. Stress paths of the undisturbed samples in the *p*-*q* diagram.

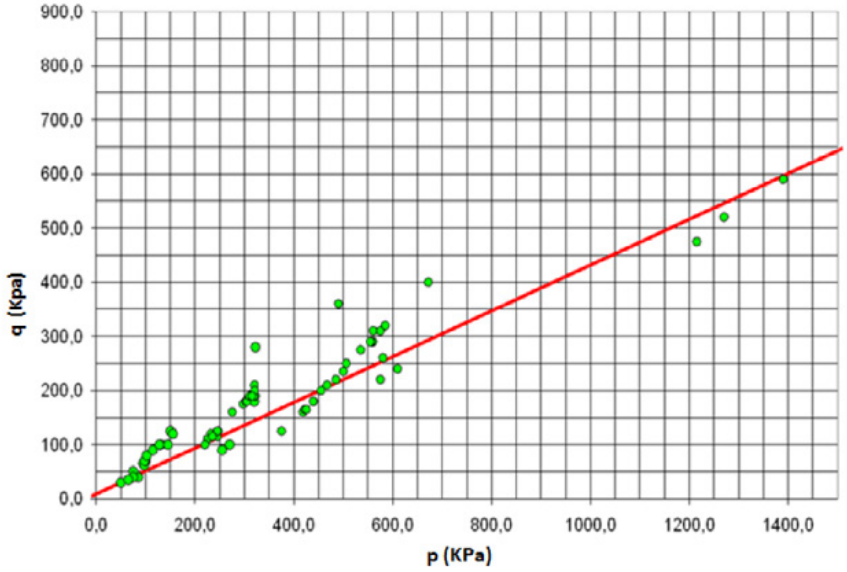

Figure 8. Failure criteria of the undisturbed samples.

6 SHEAR-STRENGTH CHARACTERISTICS OF THE REMOLDED MARL SAMPLES

Similar analyses to those described in Section 5 for undisturbed samples were performed on two types of remolded samples:

a) Eight remolded samples compacted to 100% of their normal Proctor density according to the ASTM standard [23] with moisture levels close to their initial moisture content. In this case, there is only one stress-strain behavior mode corresponding to the elasto-plastic one (ductile behavior). All the tested samples reach a given deviatoric stress at 1 to 5% of the axial strain, corresponding to a consolidation pressure of 50 and 300 kPa. After reaching these values of the axial strain level, a small increase can be observed until reaching the maximum strain of 20% when the test is stopped. Both curves for different consolidation pressures (50 and 300 kPa) present a similar elastic modulus (10 MPa) [21]. The pore--water pressure relationship represents an increase in the same range of axial strain (1 and 5% respectively), after which it shows the general tendency of remaining constant till the end of the test, as was already observed for the undisturbed samples, Fig. 9.

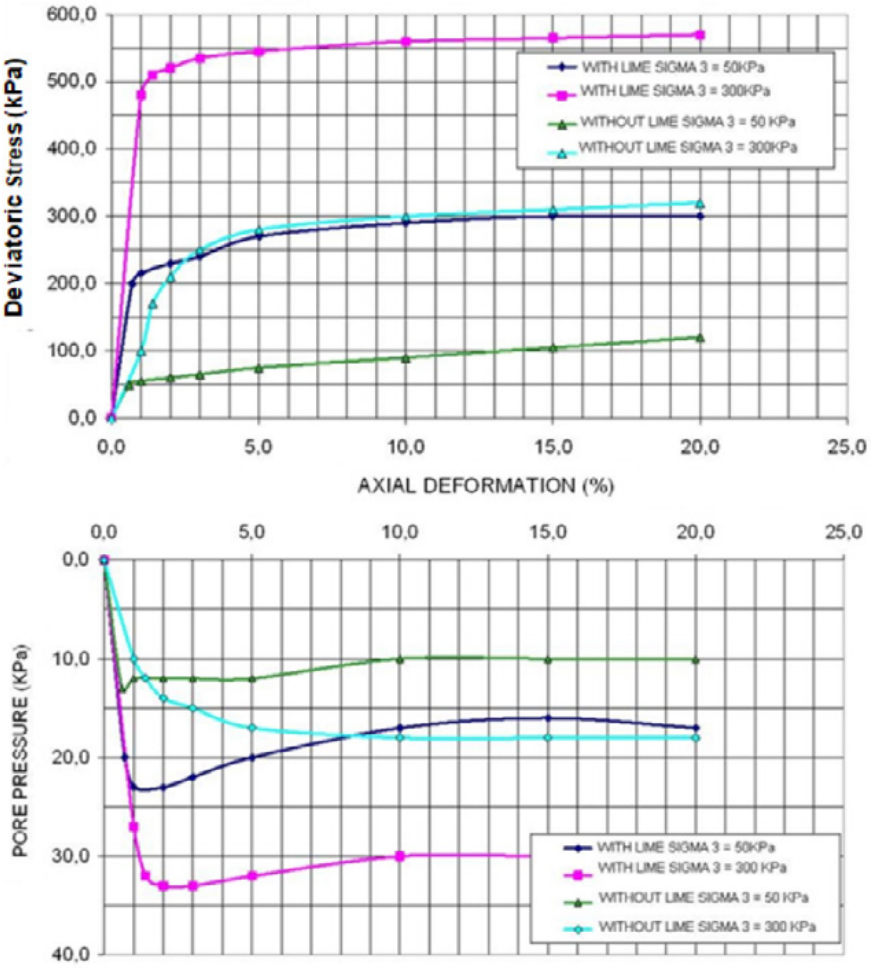

Figure 9. Stress-strain relationship for the remolded samples with and without lime.

b) Eight samples mixed with slake lime ($Ca(OH)_2$), 2% lime by weight of the dry soil, and then remolded and compacted to 100% of their normal Proctor density (15.2 kN/m^3) with moisture levels close to optimum (27%) (see Fig. 5). Samples had a maturation period of about 24 hours before testing. The tendency of the relationship curves is the same as for the remolded samples of the natural material, representing a greater deviatoric stress under the same confinement stress level necessary for the failure, as expected. The lime-treated samples again display the behavior pattern observed on undisturbed samples. The elastic stress-strain behavior is observed reaching axial strains at approximately 1%, and after that showing the small increase in deviatoric stress until the failure is reached (the test was stopped at 20% of the strain level). The elastic modulus [21] obtained is 25 and 48 MPa for different consolidation pressures of 50 and 300 kPa, respectively. These values of the initial elastic modulus are greater than the ones obtained for the natural material tested as a remolded sample under the same consolidation pressure. The pore-water pressure represents the contractive behavior until reaching the maximum strain level, after that representing slightly dilatant behavior until reaching the constant value until the end of the test (see Fig. 9).

The stress paths of both types of remolded samples in turn follow paths similar to those of the undisturbed samples (see Fig. 10). These stress paths are typical of over-consolidated clays [24].

Lastly, plotting the failure points, the geometric location of the failure is established in order to obtain the Mohr-Coulomb model parameters on the *p-q* diagram (see Fig. 11). These are:

- Remolded samples without lime:
  - Cohesion 15 kN/m^2
  - Angle of internal friction 28º

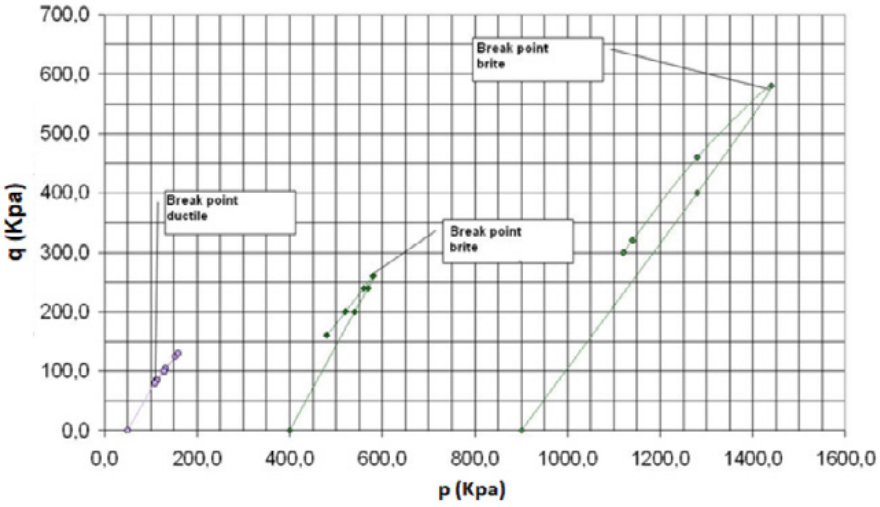

Figure 10. Stress paths of the remolded samples with and without lime.

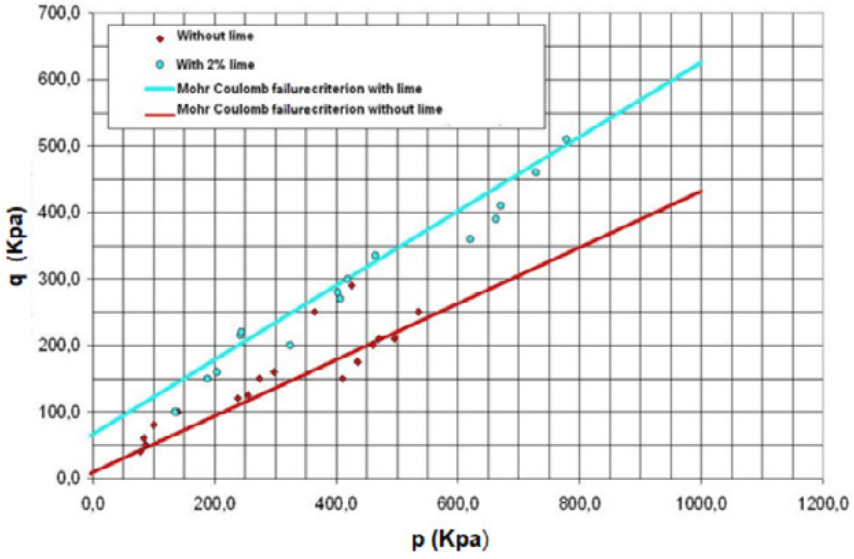

Figure 11. Failure line of the remolded samples with and without lime.

- Remolded samples with 2% lime:
  - Cohesion 80 kN/m^2
  - Angle of internal friction 34º

7 COMPARISON OF RESULTS FOR SAMPLES TESTED BY TCU

A comparison of the results for the three sets of tests described above allows us to reach several conclusions. First of all, undisturbed samples show greater unit dry density and lower initial moisture content than the remolded samples. The remolded samples with lime show a greater initial moisture content and a lower unit dry weight than the undisturbed and remolded samples. The undisturbed samples are stiffer, and they can show brittle and ductile behavior. Both types of remolded samples (with and without lime) display relatively similar stress-strain paths. The failure points are at the approximately same geometric location, representing the lowest strength parameters for undisturbed samples, as was expected.

The upper layers of the Blue Marls' formation are slightly over-consolidated deposits. Therefore, it is possible to conclude that the remolding and compaction process in a Proctor mold, and by extension, the compaction process in embankments on a real scale is equivalent

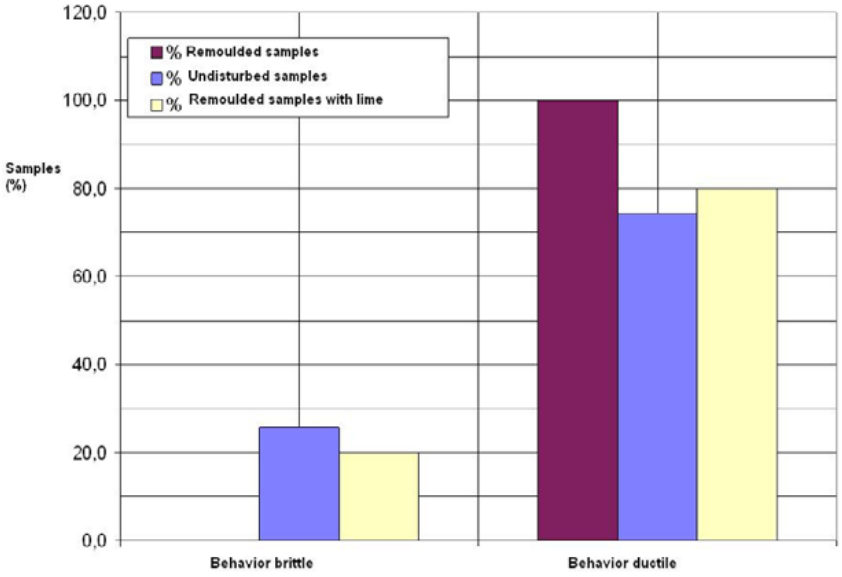

Figure 12. Relationship between the ductile and brittle behaviors for different samples.

to putting a light consolidation pressure on the spread material.

Fig. 12 summarizes the type of failure (brittle or ductile) according to the type of samples. A portion of undisturbed and remolded samples with lime displays brittle behavior, while the remolded samples of a natural material without any additive always display ductile behavior. This brittle behavior may be related to defects in the microstructure, which cannot be seen by the simple naked eye and should be the subject of further detailed analysis regarding the influence of the microstructure on the strength-strain behavior.

The remolded samples with a lime mixture constitute a material with different physicochemical conditions. The transformation of the clay when it is mixed with lime affects its mineralogical composition by replacing its exchangeable ions, as well as the presence of chemical compounds in proportions different to those in the original sediment. Therefore, the lime-treated clay is a new material. The most significant aspect of the comparison between the behavior of three types of samples, undisturbed, remolded and remolded with lime mixture, is that the remolded samples with lime mixture show a considerable improvement in the strength (cohesion and friction angle) and the deformation properties.

The lime mixture in the remolded samples also adds a certain brittleness to the material. Specifically, 20% of the samples remolded with lime tested by TCU display brittle behavior. The origin of this brittle behavior might be related to an unequal distribution of the lime within the test piece, which allows the properties of both types of materials to coexist.

8 RETROSPECTIVE ANALYSIS OF SLOPES IN GUADALQUIVIR BLUE MARLS

These Blue Marls have high plasticity, medium-high expansion and low strength parameters (angle of internal friction and cohesion). The typical residual values can be of the order from 10º to 15º for the angle of internal friction and from 0 to 5 kN/m^2 for the cohesion [16]. Under natural conditions, they evolve gravitationally, even with stable angle orders of magnitude on very low gradients (1V:2.5H and even 1V:3H) (see Fig. 13).

Figure 13. Long-term slopes in one of the studied area of the Guadalquivir basin.

Of the factors that trigger instability, the most important is usually the occurrence of a period of heavy precipitation, which significantly increases the pore-water pressure [2,25]. Nonetheless, these materials are subject to sudden instability, generally attributable to excavation processes, including elements re-excavated due to repairs.

The retrospective analysis of permanent slopes makes it possible to define certain operational geotechnical parameters with a safety coefficient that represents an acceptable risk. When the analysis is based on the limit equilibrium method with circular failures, this safety coefficient is of the order of 1.5 under permanent conditions.

Measurements were made of the height and inclination angle of 41 man-made slopes at the location where the samples for the identification and triaxial tests were taken. The results of these measurements, along with the results of the retrospective analyses, are shown in Fig. 14, which highlights the following:

- Points representing the observed man-made slopes in terms of height and slope angle.
- Line resulting from the retrospective analysis with a safety coefficient equal to 1.5 (red line). The design parameters used in the analysis are the values obtained for undisturbed samples:
  - Bulk density 20 kN/m^3
  - Angle of friction 25º
  - Cohesion 10 kN/m^2
- Line resulting from the retrospective analysis with a safety coefficient equal to 1.0 (green line).

This study indicates that the operational strength parameters used in the retrospective analysis are the same or greater than those deduced from the laboratory triaxial CU tests on undisturbed samples.

9 DISCUSSION AND CONCLUSIONS

The behavior of compacted soil is of special interest for its application in geotechnical structures such as embankments, pavement bases, earth dams, etc. A comparison of the results for undisturbed and remolded samples indicates that that they are similar materials with similar mechanical parameters, even though the undisturbed material is stiffer and sometimes shows brittle behavior.

The retrospective back-analysis study of the stable man-made slopes makes it possible to obtain mechanical operational strength parameters for the upper layer of the Blue Marls' formation. These operational parameters, when dry conditions are considered, are similar to the ones obtained by the triaxial tests performed on undisturbed samples. Therefore, engineering fills build with this material can be designed with a similar batter slope that the steepest ones observed in the surrounding landscape, as long as a dry condition for the embankment can be guaranteed. It was observed that landslides usually occur through existing failure surfaces or when water pressures build up within the slope, which is a reasonable consequence when considering the previous result. Therefore, again, slope cuts in this material can be designed with the steepest observed slopes as long

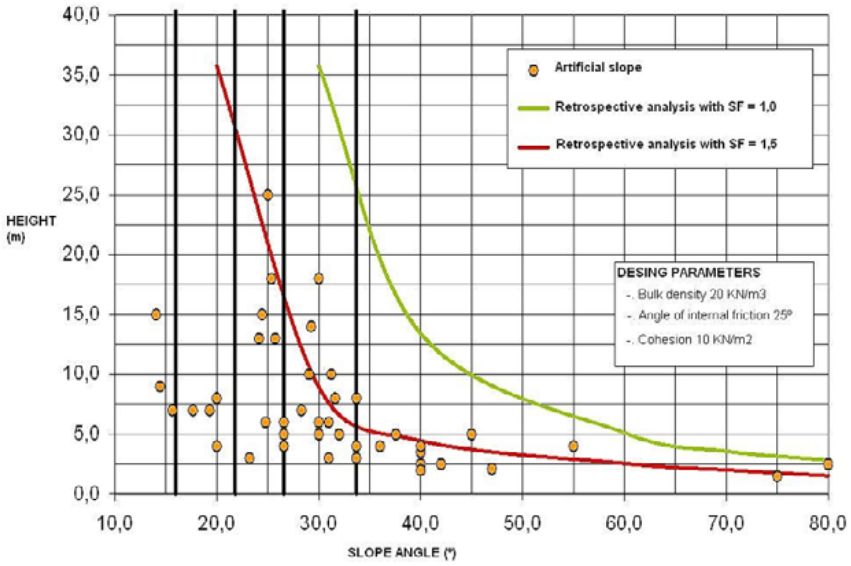

Figure 14. Retrospective analysis results.

as the drainage conditions are under control. Existing landslides require a separated approach. Some of the factors that affect its instability are the presence of a fault in its internal structure that is not easily detected during the site investigation. The observation of the stress-strain behavior in a triaxial test may be a clue to detect these internal faults.

The remolded samples mixed with lime drastically alter the form and chemical composition of the sediment and therefore result in different mechanical parameters. The improvement of the geotechnical strength parameters by the compaction of the sample with and without lime is emphasized, thus making this material adequate for its application in geotechnical structures. A small percentage of the lime content is enough for the improvement of the strength characteristics.

A comparison of the triaxial test results performed on undisturbed and remolded samples makes it possible to define the following conclusions: a) the behavior of undisturbed samples presents both ductile and fragile behavior, while the b) remolded samples undergo only a ductile stress-strain relationship and c) the remolded samples mixed with lime represent both fragile and ductile behavior.

The retrospective analysis of the stability of man-made slopes shows the failure line for the strength resistance characteristics being of same order as obtained with the triaxial tests.

REFERENCES

[1] Oteo, C., Sola, P. 1993 Stability problems in slopes constructed on Spanish Blue Marls. Proc. of Symposium on Indurated soils and soft rocks. Athens, pp. 341-362.

[2] Oteo, C. 2000. Las margas azules del Guadalquivir y la inestabilidad de taludes. Rutas: Revista de la Asociación Técnica de Carreteras 77, 17-27.

[3] Romero, E., Domenech, J.F. 1994. Back-analysisi of a landslide in overconsolidated tertiary clays of the Guadalquivir River Valley (Spain), XIII ICSMFE, New Delhi, India.

[4] Alonso, E., Gens, A. 2006. Aznalcóllar dam failure. Part 1: Field observations and material properties. Geotechnique 56, 165-183. https://doi.org/10.1680/geot.2006.56.3.185

[5] Alonso, E., Gens, A. 2006. Aznalcóllar dam failure. Part 2: Stability conditions and failure mechanism. Geotechnique 56, 185-202. https://doi.org/10.1680/geot.2006.56.3.185

[6] Olalla, C., Cuellar, V. 2001. Failure mechanism of the Aznalcóllar Dam, Seville, Spain. Geotechnique 51, 399-406. https://doi.org/10.1680/geot.2001.51.5.399

[7] Heras, J.G., Gumiel, P., Grima, J., Custodio, E. 2001. Contribuciones al estudio de la rotura de la balsa de lodos de Aznalcóllar. Boletín geológico y minero 112, 283-294.

[8] Galera, J.M., Checa, M., Pérez, C., Williams, B. 2009. Caracterización de detalle de las margas azules del Guadalquivir mediante ensayos in situ y de laboratorio. Ingeopres 186, 16-22.

[9] Cooper, S., Rodriguez, M.D., Pozo, V., Galera, J.M. 2015. Stability considerations for slopes excavated in fine hard soils/soft rocks at Cobre Las Cruces, Sevilla, Spain. Proceedings of the International Symposium on Rock Slope Stability in Open Pit Mining and Civil Engineering: 731-749.

[10] Vazquez-Boza, M., Justo, J.L., Durand, P., Morales-Esteban, A. 2014. Macro and microstructure of Guadalquivir blue marls in cyclic suction-controlled drying and wetting test. Unsaturated Soils: Research and Applications: 727-732.

[11] PG3 2002. Pliego de prescripciones técnicas generales para obras de carreteras y puentes. Ministerio de Fomento, Madrid.

[12] Elert, K., Nieto, F., Azañon, J.M. 2016. Effects of lime treatments on marls. Applied Clay Science 135, 611-619. http://dx.doi.org/10.1016/j.clay.2016.10.047

[13] Kumar Dash, S., Hussain, M. 2012. Lime stabilization of soils: Reappraisal. Journal of Materials in Civil Engineering ASCE 24(6), 707-714.

[14] Tsige, M. 1999. Microfábrica y mineralogía de las arcillas azules del Guadalquivir: influencia en su comportamiento geotécnico. Ministerio de Fomento. Centro de Publicaciones, Madrid.

[15] Tsige, M., Corral, M. 2013. Arcillas azules del Guadalquivir: influencia en su comportamiento geotécnico. VIII Simposio Nacional sobre Taludes y Laderas Inestables, España 3, 997-1008.

[16] Toscano, A., Abad, M., Ruiz, F., Muñiz, F., Álvarez, G., García, E., Caro, J.A. 2013. Nuevos restos de Scaldicetus (Cetacea, Odontoceti, Physeteridae) del Mioceno superior, sector occidental de la Cuenca del Guadalquivir (sur de España). Revista mexicana de ciencias geológicas 30, 436-445.

[17] Mayoral, E., González, I. 1986. Contribución al estudio de las facies de tránsito Mioceno-Plioceno en el sector noroccidental de la Cuenca del Guadalquivir. Acta geológica hispánica 21, 177-184.

[18] Mayoral, E., Abad de los Santos, M. 2008. Geología de la cuenca del Guadalquivir, Universidad de

Huelva, España.
[19] ASTM D2487-17 Standard Practice for Classification of Soils for Engineering Purposes (Unified Soil Classification System).
[20] ASTM D4767-04 Standard Test Method for Consolidated Undrained Triaxial Compression Test for Cohesive Soils.
[21] Duncan, J.M., Chang, C.Y. 1970. Nonlinear analysis of stress and strain in soils. Journal of the Soil Mechanics and Foundation division (ASCE) 96, 1629-1653.
[22] Lambe, T.W., Whitman, R.V. 1979. Soil mechanics. Wiley, New York.
[23] ASTM D698 Standard Test Methods for Laboratory Compaction Characteristics of Soil Using Standard Effort (12400ft-lbf/ft^3 (600 kNm/m^3)).
[24] Aubeny, C., Whittle, A., Ladd, C. 2000. Effects of disturbance on undrained strengths interpreted from pressuremeter tests. Journal of Geotechnical and Geoenvironmental Engineering 126, 1133-1144. DOI: 10.1061/(ASCE)1090-0241(2000)126:12(1133)
[25] Escolano, F., Bueno, M. 2015. Stress–strain behaviour of the sediments in the tertiary basins associated with the Alentejo–Plasencia fault in the province of Caceres (Spain). Bulletin of Engineering Geology and the Environment 74 (3), 733-743.

TWO- AND THREE-DIMENSIONAL ANALYSES OF THE EFFECT OF PILE SPACING IN PILED-RAFT FOUNDATIONS

DVO IN TRODIMENZIONALNE ANALIZE UČINKA RAZMIKA MED PILOTI POVEZANIMI S TEMELJNO BLAZINO

Osman Sivrikaya *(corresponding author)*
Nigde Omer Halisdemir University,
Civil Engineering Department,
Niğde, 51240, Turkey
E-mail: osivrikaya@ohu.edu.tr

Gürkan A. Yazıcı
Nigde Omer Halisdemir University,
Civil Engineering Department,
Niğde, 51240, Turkey

DOI https://doi.org/10.18690/actageotechslov.16.1.43-52.2019

Keywords

piled-raft foundations, pile spacing, finite-element method, undrained analysis

Ključne besede

piloti povezani s temeljno blazino; razmik med piloti; metoda končnih elementov; nedrenirana analiza

Abstract

One of the important factors that have to be considered in the design of piled-raft foundations is the selection of the spacing between the piles. In this study, a piled-raft foundation having different pile-spacing configurations and resting on clayey soil was modeled using PLAXIS numerical packages based on the 2D and 3D finite-element methods. The dimension effect is examined by comparing the 2D modeling analysis with the 3D modeling analysis. The results of the models with different pile spacings were compared and interpreted. As a general trend in accordance with the results of the two- and three-dimensional analyses, the total displacements, shear strains and volumetric strains decreased as the pile spacings (s/D) increased. In the case of s ≥ 6D as a threshold value there was no significant change in the aforementioned quantities (they remain constant) or decreased slightly. The maximum settlement was found to be greater in the 3D analyses than in the 2D analyses. It is thought that the dimension effect caused the differences in the results obtained with the 2D and 3D analyses.

Izvleček

Izbira razmika med piloti je eden od pomembnih dejavnikov, ki jih je treba upoštevati pri načrtovanju pilotov povezanih s temeljno blazino. V prispevku so bili na podlagi numeričnih analiz s programskim orodjem PLAXIS, zasnovanim po metodi 2D in 3D končnih elementov, modelirani piloti povezani s temeljno blazino z različnimi konfiguracijami razmika pilotov ter temeljeni na glinenih tleh. Učinek dimenzije je bil preverjen s primerjavo rezultatov analiz 2D in 3D modeliranja. Primerjali in interpretirali smo rezultate modelov z različnimi razmiki med piloti. Skladno z rezultati dvodimenzionalnih in tridimenzionalnih analiz, so se na splošno skupni pomiki ter strižne in volumske specifične deformacije zmanjševale pri povečanju razmikov med piloti (s/D). V primeru s ≥ 6D, kot mejne vrednosti, ni prišlo do bistvene spremembe v zgoraj navedenih količinah (ostale so konstantne) ali pa so se le nekoliko zmanjšale. Ugotovljeno je bilo, da je bila vrednost največjega posedka v 3D analizah večja kot pri 2D analizah. Menimo, da je učinek dimenzije povzročil razlike v rezultatih, dobljenih v 2D in 3D analizah.

1 INTRODUCTION

In engineering computations, in addition to safety, economical designs are also of great concern. This particular case is realized especially when the loads coming from the superstructure are of the order of greater magnitudes where the foundation system design requires economy next to safety. In many cases, piles are used in groups to transmit the structural loads to the soil. A pile cap is constructed on the group of piles. The pile cap can be well above the ground or in contact with the surface. The design principle of pile groups also applies to piled rafts [1]. Piled-raft systems are of importance for such cases where the base pressure beneath the footing is shared by the raft and the pile. Based on this fact, piled-raft systems, where the interactions among the pile, the raft and the soil are taken into consideration, are becoming more frequently used.

Piles may be installed under a raft for the purpose of reducing settlements [2]. Piled-raft foundations also contribute to avoiding differential settlements [3]. In addition, they reduce the magnitude of the internal stress and the bending moments in the raft. However, the biggest drawback is to model the interactions among the pile, the raft and the soil. In these cases, it is better to model with numerical methods, such as the finite-element method (FEM) [4, 5, 6].

For the settlement calculation of pile groups, there are several approaches, including, empirical, analytical and numerical methods. These methods can be classified as follows:

- Methods based on empirical formulations [7, 8]
- Approaches that take into account soil-structure interaction stress superposition [9]
- Methods based on modifying the load-settlement curves for individual piles by group-interaction factors [10]
- The equivalent raft method based on the assumption that the piles are represented by an imaginary raft resting at a specific depth [11]
- The pile group and the soil inside the pile group are regarded as a block and solved as an individual pile, where the rigidity of the pile and the soil is calculated and an average value is obtained [12]
- Numerical methods such as the finite-elements method (FEM) and the finite-difference method (FDM), etc.[13, 14]

1.1 Settlement of piled rafts in cohesionless soils

The settlement of a pile group (S_g) is normally greater than the settlement of a single pile (S_t) at an equal load per pile due to the larger depth of influence of a group as compared to that of a single pile (Fig. 1). There is a superposition of stresses that are transferred and the pile group capacity becomes less than the number of piles times the individual pile-load capacity, resulting in an increase in the total settlements.

Several investigations relating to the settlement of group piles, with widely varying results, have been reported in the literature. No general theory to predict pile-group settlements in cohesionless soils is available. Many empirical and semi-empirical methods with gross approximations are available, but they cannot be recommended without reservations [9].

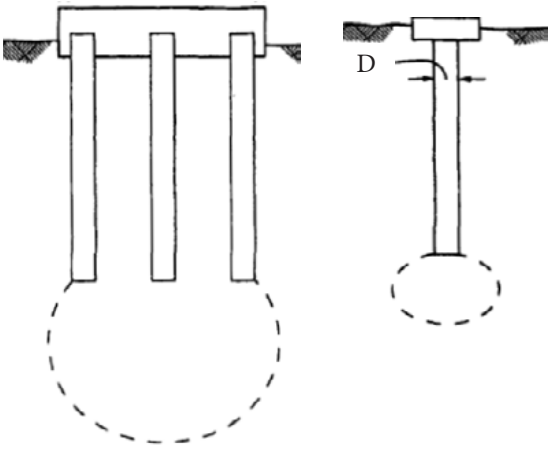

Figure 1. Zone of influences for a pile group and a single pile [9].

The simplest relation for the settlement of group piles was given by Vesic (1977) [15] as

$$S_g = S_t \cdot \sqrt{\frac{B_g}{D}} \qquad (1)$$

where S_g is the group settlement at a load per pile equal to that of the single pile, S_t is the settlement of a single pile estimated or determined from a pile-load test, B_g is the width of a pile group (smaller dimension) and D is the pile diameter.

In addition, empirical equations for elastic settlement related to in-situ test results such as the SPT-N value and the cone-penetration resistance are available in the literature [8, 16].

1.2. Settlement of piled rafts in cohesive soils

The settlement estimation of pile groups in cohesive soils is complex. The settlement of piles in cohesive

soils primarily consists of the sum of the short-term settlement occurring as the load is applied and the long-term consolidation settlement occurring gradually as the excess pore pressures generated by the loads are dissipated. Generally, the short-term settlement results from the elastic compression of cohesive soils. This component of the settlement constitutes a significant portion of the total settlement for partially saturated and over-consolidated saturated cohesive soils [9].

Fig.2 shows a simple method that can be used for the consolidation settlement estimation of pile groups in cohesive soils by assuming the 2:1 stress-distribution method.

This approximate method is based on the following assumptions:

- The pressure q_{all} is transferred to a 2/3L depth below the ground surface. The settlement of the soil above this depth is assumed to be small and therefore is neglected.
- Then estimate the settlement as if a footing of dimensions with the pressure q_{all} is placed at a 2/3L depth below the ground surface. The presence of a pile below this depth is disregarded.

According to these assumptions, the consolidation settlement can be calculated from the following relationship:

$$\Delta H = \left[C / \left(1 + e_0\right) \right] \cdot \left[H - 2/3L \right] \cdot \log \left[\left(\sigma_v' + \Delta\sigma_v' \right) / \sigma_v' \right] \quad (2)$$

where ΔH is the consolidation settlement, σ_v' is the present effective (vertical) overburden pressure at the middle of the layer (H-2/3L) (Fig.2), $\Delta\sigma_v'$ is the increased pressure from the pile load at the middle of the layer (H-2/3L), C is the compression index and e_0 is the initial void ratio of the soil.

There are several studies in the literature that focus on the effect of pile spacing on the total vertical bearing capacity of piled-raft foundation systems. In these studies, some physical model tests were performed or the problem was modeled using various software packages. With the aid of these models, the effect of pile spacing on the bearing capacity of the piled-raft system has been investigated and some recommendations for the design are given [9, 17, 18, 19]. However, there is only limited research in the literature on the effect of spacing on the settlement of piled-raft systems [6, 18, 20]. The main purpose of this study is to determine the effect of spacing on the settlement of a piled raft using 2D and 3D FEM-based software and to evaluate the findings from an engineering point of view.

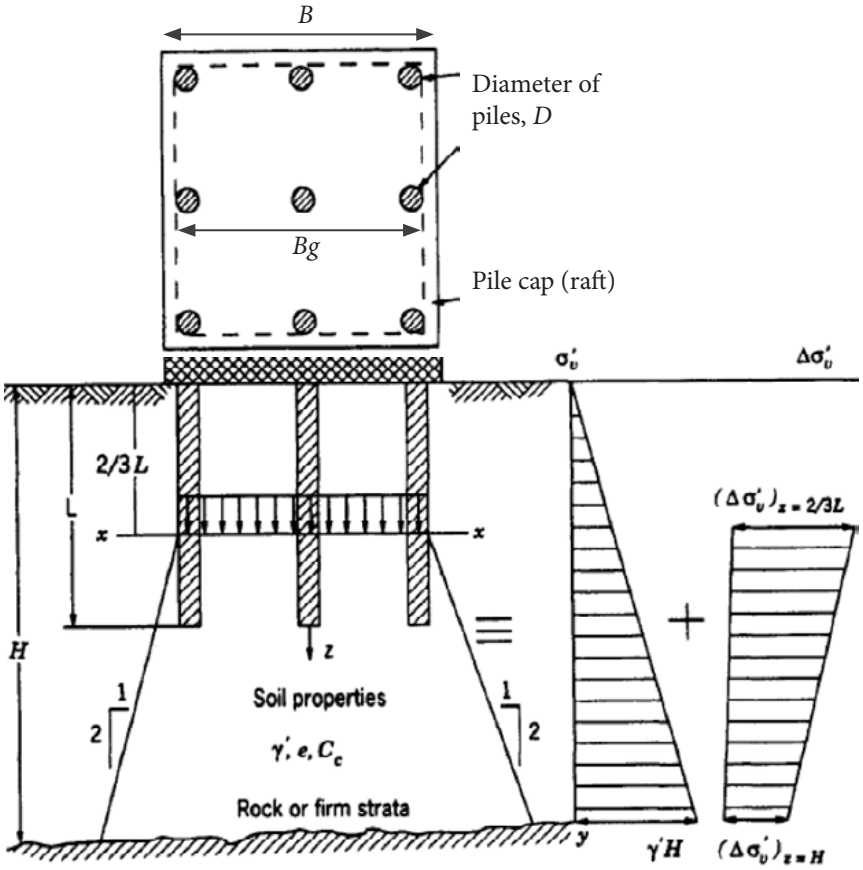

Figure 2. Stress distribution for a settlement estimation for friction piles in clay [9].

2 FINITE-ELEMENT MODELING

2.1 Finite-element mesh and boundary conditions

The behavior of the piled raft was examined in terms of the effect of the pile spacings by performing 2D and 3D numerical analyses. The finite-element package PLAXIS was used as a calculation tool. PLAXIS is a software program based on the finite-element method that is widely used in geotechnical engineering applications to analyze soil behavior with soil models [21, 22]. It is used in geotechnical application areas such as deep excavation and support systems, shallow and deep foundations, retaining structures, geotextile-reinforced and non-reinforced filler constructions, soil improvements, as well as dam and tunnel designs [23-28]. Figure 3 shows typical 2D and 3D FE meshes used in these parametric analyses. The piles were taken to be 0.6 m in diameter *D* and 18 m in length *Lp*. A square raft with a width *B* of 20 m (thickness, 1 m) was considered. The pile cap and the raft were considered as rigidly connected to each other. The raft–soil interface was considered to be rigid within a contact zone. Since the mobilization of the friction between the bored pile of the rough concrete shell and the clayey soil occurs in a short period of time after manufacture the interface properties are also assigned as rigid. The mesh was assumed to be on a rigid layer beyond the boundaries, and the vertical boundaries on the left- and right-hand sides were assumed to be on rollers to allow the downward movement of the soil layers. For the far-field boundaries, the distance of the boundary from the edge of the raft was set to 50 m, since the observed influence zone based on the finite-element analysis including interface was at most 8–10 m. After an initial equilibrium, the vertical loading was applied on the top of the raft surface. Since the modeling of the entire pile-installation process is rather complicated, the pile was assumed to be in a stress-free state at the start of the analysis. The stress change in the soil during the pile installation was therefore not included.

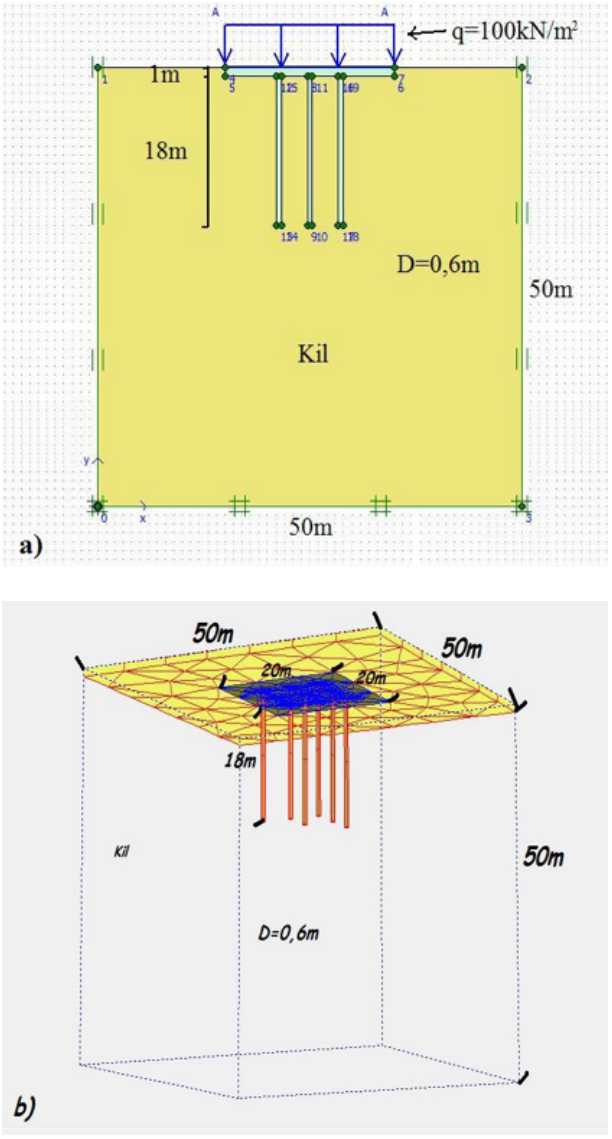

Figure 3. a) 2D model used in the analyse
b) 3D model used in the analyses.

In the 3D model of the soil and the piled raft, the geometry was divided into 15-node wedge elements. These elements were composed of the 6-node triangular faces in the workplanes, as generated by the 2D mesh generation [21, 22].

Choosing a larger number of elements where there is a high anticipated stress and/or the possibility of critical settlement behavior gives more precise results. Local mesh refinement in such zones is preferred, instead of choosing an equal mesh size, because it saves computational time. A relatively fine mesh was used near the pile–soil and raft–soil interfaces, while a coarser mesh was used further from the pile and the raft (Fig. 4 and Fig. 5).

The system of analysis should consist of a geometry that is sufficiently large in the *x*, *y* and *z* directions in order not to be influenced by the boundary conditions. In this context, it was found that by choosing a geometry of 50 m × 50 m for the 2D, and 50 m × 50 m × 50 m for the 3D models, the above-mentioned interactions from the boundary values were minimized (Fig. 3).

2.2 Constitutive modeling

The over-consolidated clay was considered as the soil material and the behavior of this layer was modeled with the hardening soil model, which gives more accurate

results and simplifies the analysis process. Constant (average) values of the material parameters were adopted for the soil layer, as stated in the literature [29]. The recommended method in the undrained analyses of clayey soils is to use the drained shear strength parameters [30, 31]. The properties of the soil profile used in the analyses are given in Table 1.

Table 1. Properties of the soil profile used in the analyses.

Parameter	Value	Unit
Soil unit weight above GWL, γ_{unsat}	18	kN/m^3
Soil unit weight below GWL, γ_{sat}	18.5	kN/m^3
Secant stiffness, E_{50}	2x10^4	kN/m^2
Tangent oedometer stiffness, E_{oed}	2x10^4	kN/m^2
Unloading/reloading stiffness, E_{ur}	6x10^4	kN/m^2
Friction angle, $ø'$	25	deg.
Cohesion, c'	2	kN/m^2
Interface reduction factor, R_{inter}	1.0	-

The foundation system was modeled as resting on a single soil layer. The raft and piles were modeled as isotropic linear-elastic materials. The material and behavior properties for the raft and piles are summarized in Table 2.

Table 2. Material properties of the pile and raft used in the analyses.

Parameter	Value	Unit
Unit weight, γ	24	kN/m^3
Young's modulus, E	3x10^7	kN/m^2
Poisson's ratio, v	0.2	-
Shear modulus, G	1.25x10^7	kN/m^2
Raft thickness, t	1	m
Pile diameter, D	0.6	m
Pile length, L	18	m

2.2.1 Modeling the piled raft with 2D and 3D FEM

The work flow for the analyses is as follows. During the initial stage the geometry and the boundary conditions were determined. The material properties and the constitutive model were determined and assigned to each soil and structural element. 2D and 3D meshes were generated with the inclusions of local refinements (Fig. 4 and Fig. 5). The initial stress state is updated. In the modeling, a piled-raft foundation was created in two stages: the first excavation of the soil and the second piled-raft construction. Then, the pre-determined load (100 kN/m^2) that acts on the raft was activated in the calculation stage.

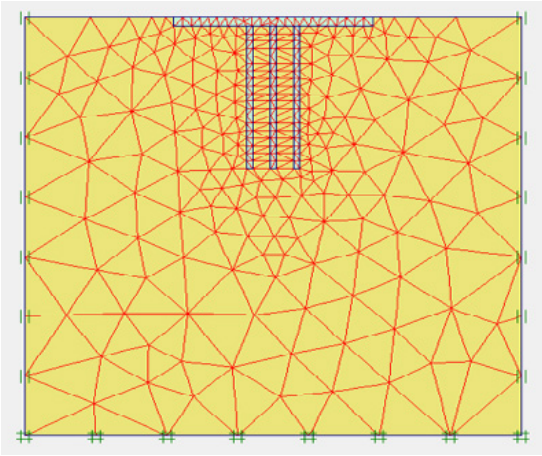

Figure 4. Generated mesh in 2D.

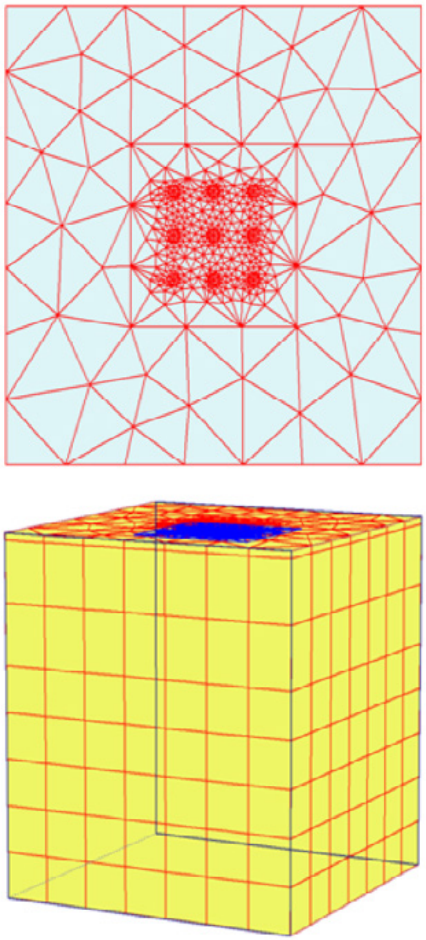

Figure 5. Generated mesh in 2D plan view and 3D utilization.

2.3. Numerical analyses

A series of 2D and 3D numerical analyses on piled rafts (PR) were performed for different pile spacings (s=2D, s=3D, s=4D, s=6D and s=8D) and configurations, as

shown in Fig.6. The piles were taken to be 0.6 m in diameter (D) and 18 m (floating) in length (Lp). A square raft with a width B of 20 m (thickness, 1 m) was considered.

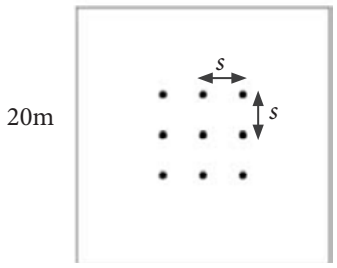

Figure 6. Analyzed cases for s=2D, s=3D, s=4D, s=6D and s=8D.

In this study, attention was focused on the undrained (short-term) response of a piled raft resting on an over-consolidated clay layer. As recommended by the literature, the clay was idealized using the drained shear strength parameters, c' and ϕ' (Table 1). Constant values of the drained Young's modulus and the drained shear strength parameters were adopted for the soil layer. For the structural components, the pile was based on a typical reinforced concrete pile and modeled with a solid section. The raft was assigned general concrete material parameters. Table 2 summarizes the material parameters used in the analyses. The loads transmitted from the superstructure were modeled as a uniformly distributed loading (i.e., uniform loading) and the load was assumed to be 1.5-times the load on the area of 20 m × 20 m (base pressure of 100 kPa) (Fig. 6). All the analyses were carried out under undrained conditions.

In this study, the 2D and 3D analyses of a piled-raft system under a vertical load were performed with respect to the short term. Their behaviors were examined and compared in accordance with 2D and 3D analyses. The raft in the piled-raft system was considered to be in contact with soil in the analyses. In this study five different piled-raft foundations were analyzed in plane strain (2D) and three dimensions (3D), which makes a total of 10 cases (Fig.6).

3 COMPUTED RESULTS AND DISCUSSION

3.1 Analyses of the 2D models

In the 2D modeling of the piled raft after the determination of the geometry, initial stress and superstructure loads consecutively, the outputs for the total deformations, shear strains, and volumetric strains were investigated. Each output representing the spacing between the piles s=2D, s=3D, s=4D, s=6D and s=8D was analyzed. The outputs for s=6D are reflected in Fig.7.

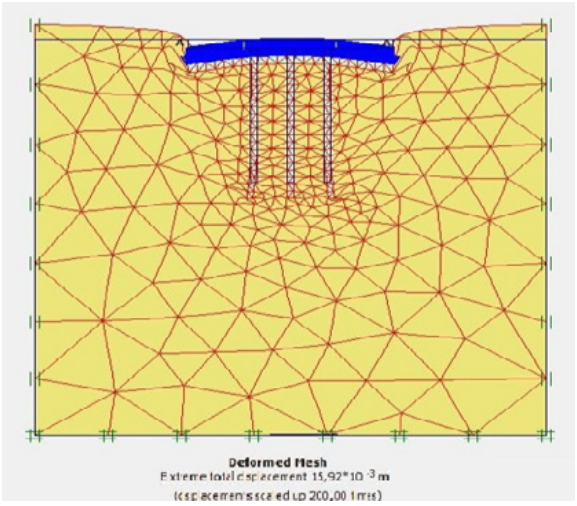

(a)

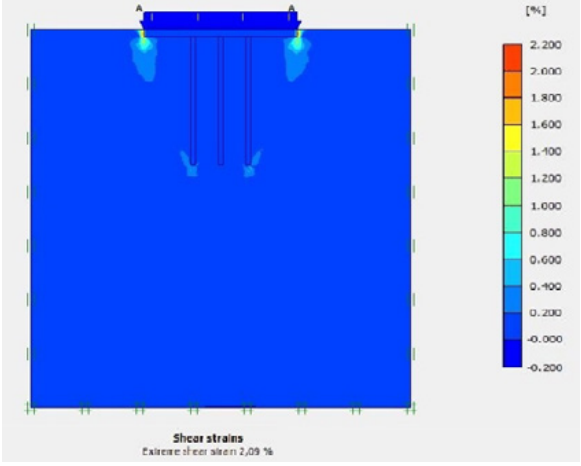

(b)

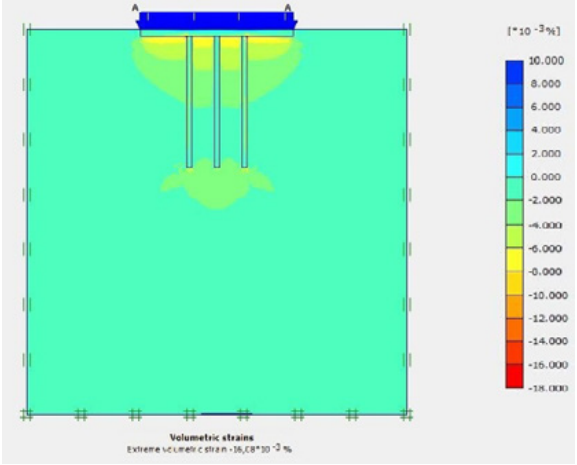

(c)

Figure 7. The output for s=6D a) total vertical displacement for piled-raft system, b) shear strains, c) volumetric strains.

The maximum vertical displacement for the 2D calculations was calculated as 18.31 mm, representing the axial spacing *s*=2D. The minimum vertical displacement was found to be 11.44 mm, representing the axial spacing *s*=8D. The shear strains were calculated to be in the range 1.71–3.20 % and they reach a maximum at the raft edges and fade near the pile shaft. The maximum value for the shear strains was calculated to be 3.20 %, representing *s*=3D. The highest volumetric strains were calculated to locate near the pile-raft connection locations. The maximum volumetric strain value was calculated to be 0.024 % for the axial spacing of *s*=8D. Values between 0.015 % and 0.024 % were obtained at the pile tip location level.

3.2 Analyses of the 3D models

In the 3D modeling of the piled raft after the determination of the geometry, initial stress and superstructure loads, consecutively, the outputs for the total deformations, shear strains, and volumetric strains are investigated. Each output representing the spacing between the piles *s*=2D, *s*=3D, *s*=4D, *s*=6D and *s*=8D was analyzed. The outputs for *s*=6D are reflected in Fig. 8 to Fig. 9.

For the 3D calculations, the maximum vertical displacement was observed in the *s*=2D model as 20.77 mm. The minimum vertical displacement was encountered for *s*=6D as 17.7 mm. Vertical displacements at the piled section varied between 8 mm and 17 mm. The settlements were at their minimum value in the piled region, while they were greater in the zones near the edge of the raft (Fig. 8).

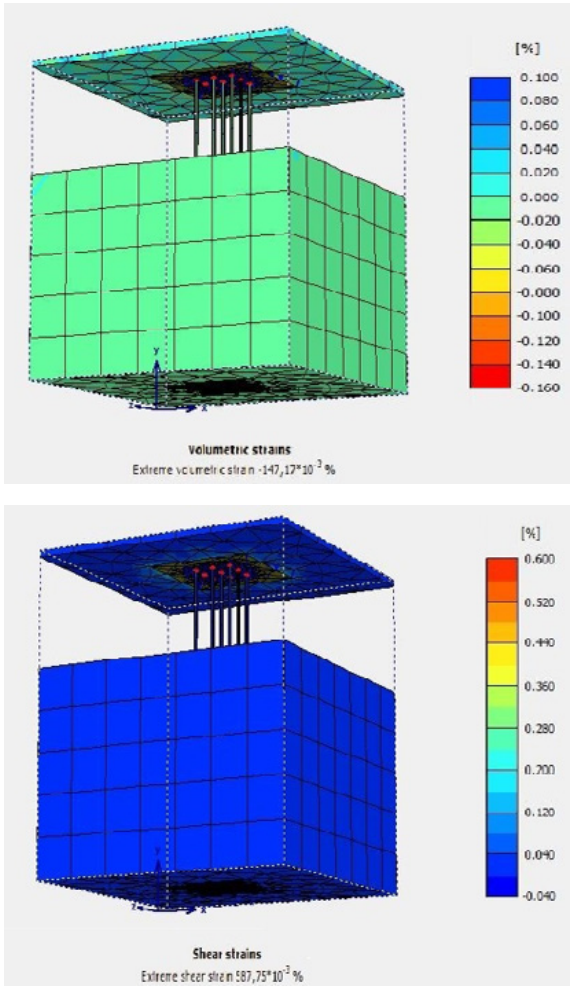

Figure 9. Volumetric strains and shear strains for *s*=6D in 3×3 piled-raft foundation.

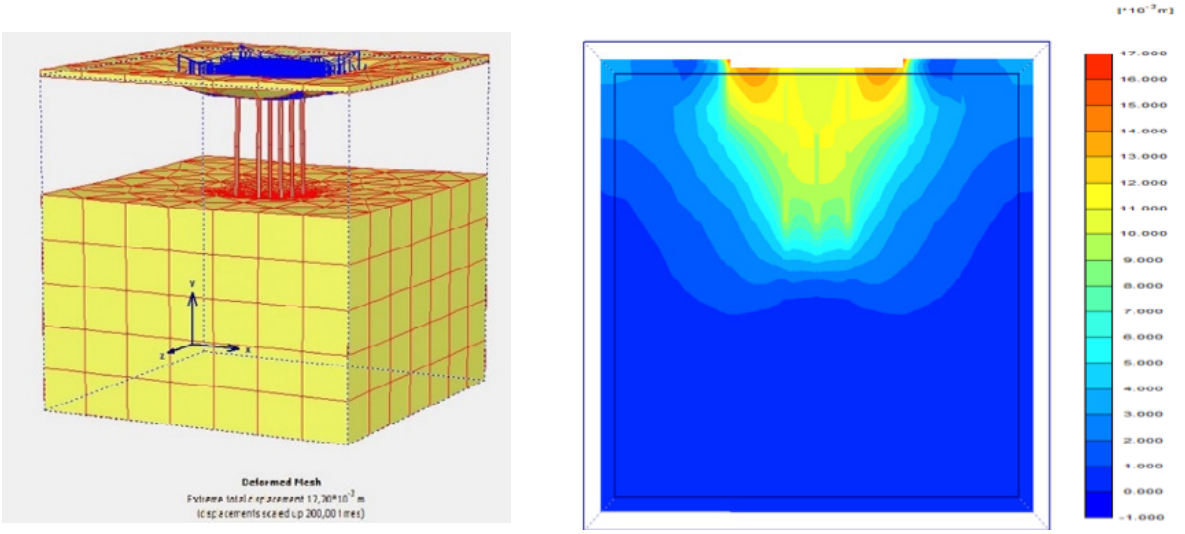

Figure 8. Total vertical displacements for *s*=6D in 3×3 piled-raft foundation and cross-section.

The magnitude of the shear strains in the system varied in the range 0.82–0.58 %. The maximum values were encountered around the pile-raft connection region. The maximum volumetric strain value reached 0.152 % for the *s*=2D axial spacing model. Values ranging between 0.152 % and 0.127 % were obtained at the zone around the pile tip (Fig. 9).

3.3. Comparison of results for the 2D and 3D modeling analyses

The effect of the pile spacing for the piled-raft foundation systems resting on clayey soil was investigated using 2D and 3D finite-element methods and a comparison was made based on the results. The variations of the settlement, shear strains and volumetric strains with respect to the pile spacing are presented in Fig. 10, Fig. 11 and Fig. 12, respectively.

The results taken from the 3D analyses reflect greater values for the average vertical displacements than the 2D analyses. It is clear from the 3D analyses (Fig. 10) that beyond the spacing value of *s*=6D the vertical displacements remained constant; however, in the 2D analyses this was not the case, where the spacing increased and the vertical displacements dramatically decreased.

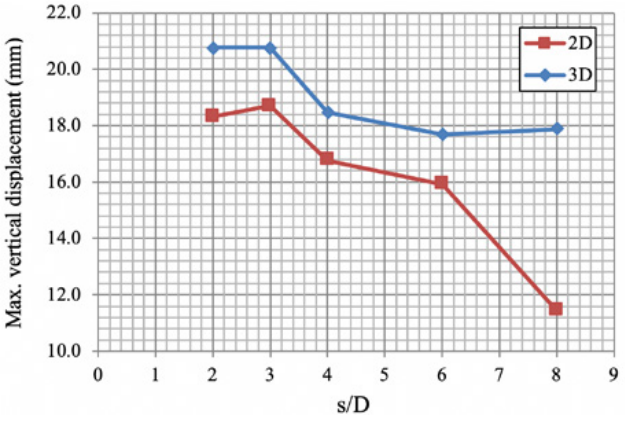

Figure 10. Variation of settlement (vertical displacement) with respect to the pile spacing.

As for the shear strain, the results show that in the 3D analyses the values remained almost constant for the spacing $s \geq 4D$. The shear strain values reached their maximum value in the 2D analysis at a spacing of *s*=3D, and beyond this value (s≥3D) they decreased linearly (Fig. 11).

In the 3D analyses, the volumetric strains were recorded as seven-times greater than in the 2D analyses (Fig. 12).

The volumetric strains decreased up to a specific value (*s*=4D), and beyond this value they remained steadier.

In the 2D analyses all the values for the raft, pile, soil, structural components and loads were defined for a unit depth. However, in the 3D analyses these parameters were defined in three dimensions, which give a more realistic identification and calculation. It is, therefore, believed that the 3D analyses give more realistic results than the 2D analyses. Moreover, the load-deformation behavior for the piled raft can be easily analyzed in detail in the 3D models; however, the effect of the third dimension cannot be analyzed with 2D models.

4 CONCLUSIONS AND RECOMMENDATIONS

A series of 2D and 3D elasto-plastic finite-element analyses were conducted to investigate the behavior of a square piled raft of 20 m × 20 m subjected to a vertical loading of 100 kPa. In this study, the pile positions on the raft were varied, and the effects of the pile spacings were examined. As expected, the development of the settlements and the pile loads for the piled raft was dependent

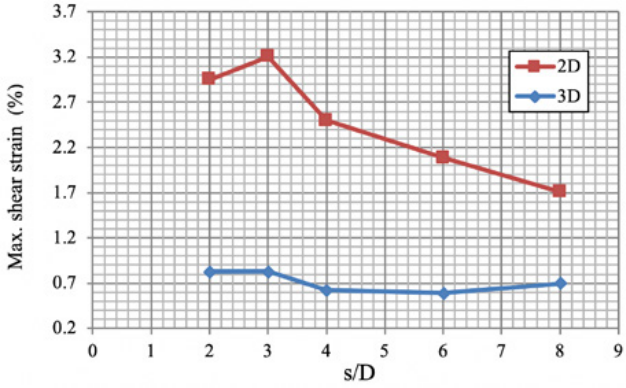

Figure 11. Distribution of shear strains with respect to spacing.

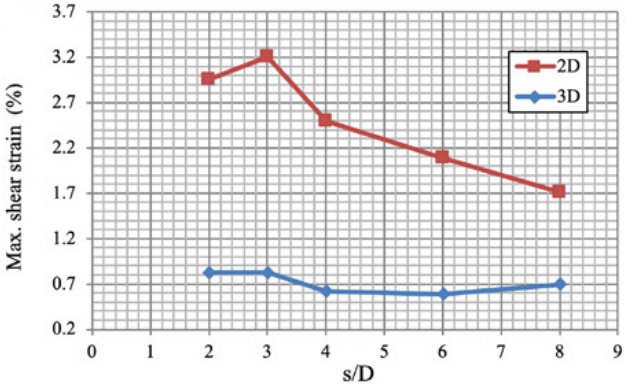

Figure 12. Volumetric strains vs. pile spacing.

on the pile–soil interface and the pile spacing.

In this study, the effect of the spacing of the piles in piled-raft systems resting on clayey soil was investigated by means of a literature survey, 2D and 3D FEM analyses and these results were obtained:

- The major parameters that define the load-settlement behavior are geometrical properties such as the area of the piled region/area of the raft, or the pile group dimension/raft dimension, the pile spacing, and the pile length. Various researchers recommend optimum values for these parameters.
- It is more realistic and convenient to utilize 3D FEM analysis to design the piled raft due to using the original dimensions of the soil and the structural elements in the calculation stage.
- The shear strains reached their maximum value at the edge of the raft and dissipated at the lower elevations of the other piles.
- The volumetric and shear strains remained steady beyond a specific value of the spacing (s=4D)
- The settlements reduced dramatically beyond a certain spacing value (s=6D) in the 2D analysis. However, they were reduced and remained constant in the 3D analyses to a specific spacing value (s=6D) and remained constant beyond that value.
- The vertical-displacement and the volumetric-strain results were greater in the (3D) analyses than in the 2D analyses.
- It is considered that the differences of the results obtained from 2D and 3D analysis come from the dimension effect and the analysis type.

REFERENCES

[1] Z[1] Randolph, M.F. 1994. Design Methods for Pile Groups and Piled Rafts. Proceedings of 13th International Conference of Soil Mechanics and Foundation Engineering, New Delhi, 61-82.

[2] Reul, O., Randolph, M.F. 2004. Design strategies for piled rafts subjected to non-uniform vertical loading. Journal of Geotechnical and Geoenvironmental Engineering 130, 1, 1-13. https://doi.org/10.1061/(ASCE)1090-0241(2004)130:1(1)

[3] Kim, K.N., Lee, S.H., Kim, K.S., Chung, C.K., Kim, M.M., Lee, H.S. 2001. Optimal pile arrangement for minimizing differential settlements in piled raft foundations. Computers and Geotechnics 28, 4, 235-253. https://doi.org/10.1016/S0266-352X(01)00002-7

[4] Pressley, J.S., Poulos, H.G. 1986. Finite element analysis of mechanics of pile group behavior. International Journal for Numerical and Analytical Methods in Geomechanics 10, 2, 213-221. https://doi.org/10.1002/nag.1610100208

[5] Gök, S. 2007. Design of piled raft foundations. Ph.D.Thesis. İstanbul Technical University, İstanbul, Turkey.

[6] Kalpakcı, V., Özkan, M.Y. 2012. A simplified approach to the settlement estimation of piled rafts. Acta Geotechnica Slovenica 9, 1, 77-85.

[7] Vesic, A.S. 1970. Load Transfer in Pile Soil Systems. Proceeding Conference and Design Installation of Piled Foundations, Lehigh University, Bethlehem, 47-73.

[8] Meyerhof, G.G. 1976. Bearing capacity and settlement of pile foundations. ASCE Journal of the Geotechnical Engineering Division 102, 3, 195-228.

[9] Poulos, H.G., Davis, E.H. 1980. Pile Foundation Analysis and Design. John Wiley: New York.

[10] Chow, Y.K. 1986. Analysis of vertically loaded pile groups. International Journal for Numerical and Analytical Methods in Geomechanics 10, 1, 59-72. https://doi.org/10.1002/nag.1610100105

[11] Castelli, F., Maugeri, M. 2002. Simplified Nonlinear Analysis for Settlement Prediction of Pile Groups. ASCE Journal of Geotechnical and Geoenvironmental Engineering 128, 1, 76-84. https://doi.org/10.1061/(ASCE)1090-0241(2002)128:1(76)

[12] Poulos, H.G. 2002. Prediction of Behavior of Building Foundations due to Tunneling Operations. Proc. 3rd Int. Symp. On Geot. Aspects of Tunneling in Soft Ground, Toulouse, 4, 55-61.

[13] Reul, O., Randolph, M.F. 2003. Piled rafts in overconsolidated clay: comparison of in situ measurements and numerical analyses. Geotechnique 53, 3, 301-315. https://doi.org/10.1680/geot.2003.53.3.301

[14] Prakoso, W.A., Kulhawy, F.H. 2001. Contribution to piled raft optimum design, ASCE Journal of Geotechnical and Geoenvironmental Engineering 127, 1, 17-24. https://doi.org/10.1061/(ASCE)1090-0241(2001)127:1(17)

[15] Vesic, A.S. 1977. Design of Pile Foundations. Transportation Research Board, National ResearchCouncil.

[16] Skempton, A.W. 1953. Discussion on Piles and Pile Foundation. Proceedings 3rd International Conference on Soil Mechanics and Foundation Engineering, Zurich, Switzerland, 3, 172.

[17] Kishida, H., Meyerhof, G.G. 1965. Bearing Capacity of Pile Groups under Eccentric Loads in Sand, Proc. Fifth Int. Conf. Soil Mech. 2, 270-274.

[18] Brand, E.W., Muktabhant, C., Taechathummarak, A.1972. Load tests on small foundation in soft clay.

Proc.ASCE Conf. on Performance of Earth and Earth Supported Structures, Purdue University, 1, 2, 903–928.
[19] Engin, H.K., Septanika, E.G., Brinkgreve, R.B.J. 2008. Estimation of pile group behavior using embedded piles, The 12th International Conference of International Association for Computer Methods and Advances in Geomechanics. Goa, India, 3231-3238.
[20] Comodromos, E.M., Papadopoulos, M.C., Rentzeperis, I.K. 2009. Pile foundation analysis and design using experimental data and 3-D numerical analysis. Computers and Geotechnics 36, 5, 819-836. https://doi.org/10.1016/j.compgeo.2009.01.011
[21] Brinkgreve, R.B.J., Broere, W. 2006. Plaxis 3D Foundation V1.6 Manual, Delft University, Netherlands.
[22] Brinkgreve, R.B.J, Engin, E., Swolfs, W.M. 2014. Plaxis 2014 Manuals, Delft University of Technology, The Netherlands, ISBN-13: 978-90-76016-15-3.
[23] Athania, S.S., Solankia, C.H., Dodagoudarb, G.R. 2015. Seepage and stability analyses of earth dam using finite element method. Aquatic Procedia 4, 876-883. https://doi.org/10.1016/j.aqpro.2015.02.110
[24] Houari, N., Allal, M.A., Bekr, N.A. 2011. Numerical Simulation of the Mechanical Response of the Tunnels in the Saturated Soils by Plaxis. Jordan Journal of Civil Engineering 5, 1, 9-31.
[25] Kasim, F., Martob, A., Othman B.A., Bakar, I., Othmane, M.F. 2013. Simulation of safe height embankment on soft ground using Plaxis, APCBEE Procedia 152-156, 2013. https://doi.org/10.1016/j.apcbee.2013.05.027
[26] Likitlersuang, S., Surarak, C., Wanatowski, D., Oh, E., Balasubramaniam, A. 2013. Finite element analysis of a deep excavation: A case study from the Bangkok MRT. Soils and Foundations 53, 5, 756-773. https://doi.org/10.1016/j.sandf.2013.08.013
[27] Salimath, R.S., Pender, M.J. 2015. Moment-rotation behavior of shallow foundations with fixed vertical load using PLAXIS 3D. 6th International Conference on Earthquake Geotechnical Engineering, Christchurch, New Zealand, 1-4 November.
[28] Sanjei, C., Silva, L.I.N. 2015. Numerical analysis of the backfilling sequence effect on gravity retaining wall behavior. 6th International Conference on Structural Engineering and Construction Management, Kandy, Sri Lanka, 11-13 December.
[29] Sert, S. 2003. Three-Dimensional (3D) analysis of piled raft foundations on alluvial environments. Ph.D. Thesis, Sakarya University, Sakarya, Turkey.
[30] Berilgen, M. 2010. Computational Geotechnical Course with Plaxis. Istanbul Culture University, 24 - 26 May, Istanbul, Turkey.
[31] Brinkgreve, R.B.J. 2014. PLAXIS Version 8, Materials Models Manual 2, Delft University of Technology, The Netherlands.

NUMERICAL ANALYSIS OF THE BEHAVIOUR OF A LARGE-DIAMETER MONOPILE FOR OFFSHORE WIND TURBINES

NUMERIČNA ANALIZA OBNAŠANJA POSAMIČNEGA PILOTA VELIKEGA PREREZA ZA VISOKE VETRNE TURBINE

Marx Ferdinand Ahlinhan *(corresponding author)*
National University of Sciences, Technologies, Eng. and Mathematics,
Department of civil engineering
Abomey, Republic of Benin
E-mail: ahlinhan@yahoo.fr

Edmond Codjo Adjovi
National University of Sciences, Technologies, Eng. and Mathematics,
Department of civil engineering
Abomey, Republic of Benin

Valery Doko
University of Abomey-Calavi,
Department of civil engineering
Abomey-Calavi, Republic of Benin

Herbert Nelson Tigri
National University of Sciences, Technologies, Eng. and Mathematics,
Department of civil engineering
Abomey, Republic of Benin

DOI https://doi.org/10.18690/actageotechslov.16.1.53-69.2019

Keywords

offshore wind turbines, monopile, sand, combined loading, numerical modelling, loading capacity, pile-soil interaction

Ključne besede

vetrne turbine na morju, posamični pilot, pesek, kombinirana obtežba, numerično modeliranje, nosilnost

Abstract

Very-large-diameter monopiles are widely used foundations for offshore wind turbines, despite the limited guidance in the codes of practice. In the present study, three-dimensional finite-element (FE) analyses were carried out to determine the static capacity of a monopile embedded in sand subjected to combined loading. A hardening soil model (HSM) accounting for the stress dependence of the soil stiffness was used for the numerical model, which was calibrated with the results of published centrifuge tests. Based on a parametric study for different length-to-diameter ratios of the monopile, lateral load-moment interaction diagrams for the ultimate limit state as well as for the serviceability limit state were developed for different relative densities of the foundation sand. Furthermore, the initial stiffness formulations for the monopile system by Carter and Kulhawy (1992), and Shadlou and Bhattacharya (2016) accounting for the effect of the pile diameter were compared to the FE results.

Izvleček

Kljub omejenim smernicam v praksi se posamični piloti zelo velikega premera pogosto uporabljajo za temeljenje vetrnih turbin na morju. V tej študiji so bile izvedene tridimenzionalne analize na osnovi končnih elementov (FE) za določitev statične nosilnosti posamičnega pilota, vgrajenega v pesek, obremenjenega s kombinirano obtežbo. Za numerični model, ki je bil kalibriran z rezultati centrifugalnih testov, se je uporabil model tal z utrjevanjem (HSM), ki upošteva napetostno odvisnost od togosti tal. Na podlagi parametrične študije za različna razmerja med dolžino in premerom posamičnega pilota so bili, za različne relativne gostote peska, izdelani interakcijski diagrami bočna obtežba-upogibni moment za mejni stanji nosilnosti in uporabnosti. Narejena je bila tudi primerjava rezultatov analiz s končnimi elementi z rezultati formulacije začetne togosti sistema posamičnega pilota, ki upošteva učinek premera pilotov, avtorjev Carter in Kulhawy (1992), ter Shadlou in Bhattacharya (2016).

1 INTRODUCTION

In recent decades there has been an increase in the significance of renewable energy with the aim of limiting the global temperature increase to 1.5°C with respect to the period before industrialization. This has stimulated the development of the competitive source of renewable energy, including offshore wind farms to reduce the reliance on fossil fuels and control greenhouse-gas emissions.

For offshore wind turbines there are several foundation concepts, which include monopiles, a jacket structure with four piles, a tripod with three piles, a suction caisson, a gravity base foundation, tension legs foundations, etc. The foundation design can be optimized while taking the economic and environmental optimisation issue factors into account. The cost of the foundations for offshore wind-farm developments is a significant fraction of the overall installed cost and can range from 15% to 40%, Houlsby et al. (2000) [1]. The cost-effectiveness of a particular foundation concept depends to a large extent on the site-specific conditions (water depth, soils conditions, etc.) and the power of the wind turbine. Reference can be made to Aissa et al. (2018) [2], and Kallehave et al. (2015) [3] for the applicability of each foundation structure in the function of the site-specific conditions.

Most currently used foundations are monopiles, 75% according Blanco (2009) [36] and Arshad and O´Kelly (2016) [37], and 80% according to EWEA (2015) [35] and Negro et al. (2017), [4]. Monopiles are stiff, open, steel pipe piles with a large diameter up to 8m and more, driven 30 to 45 m into the seabed with a length-to-diameter ratio ranging from 4 to 7. Fig. 1 illustrates a typical offshore wind turbine supported by a monopile foundation. The criteria for rigid or flexible behaviour have been suggested by some researchers, e.g., Dobry et al. (1982) [39] Budhu and Davies (1987) [40], and Carter and Kulhawy, 1988) [41]. According to Poulos and Hull (1989) [38] the range of transition from flexible to rigid pile behaviour can be evaluated by:

$$4.8 \leq \frac{E_{soil} L^4}{E_{pile} I_{pile}} \leq 388.6 \qquad (1)$$

Based on equation 1, LeBlanc et al. (2010) [32] demonstrated that the monopile tends towards the rigid case for most sands.

The methods of analysis for pile behaviour under lateral loads range from simple empirical methods with closed-form formulae to three-dimensional finite-element methods. Reference can be made to Gurbuz (2018) [5] for the different methods of analysis for a pile under lateral loads.

The design analysis of the monopile foundation is commonly carried out based on the theory of laterally loaded piles, which relies on empirical data originating from the oil and gas industry, Reese and Matlock (1956) [6], McClelland and Focht (1958) [7], API RP (2007) [8], and DNV J 101 (2014) [9]. The lateral capacity is determined by modelling the pile as a beam column with the appropriate stiffness and the soil reaction is idealised with a system of uncoupled non-linear springs acting at discrete points along the embedded length of the monopile. This approach is known as the Winkler model. The springs are described by *p-y* curves defining the load-displacement relationship for the interaction between the soil and the pile, API (2007) [8], DNV J 101 (2014) [9] and ISO 19901(2016) [10]. The formulation of these *p-y* curves was originally calibrated to long slender and flexible piles with a diameter ranging from 0.34 m to 0.64 m, O'Neill et al. (1983) [11], Reese et al. (1975) [12], Reese et al. (1974) [13], and Seed et al. (1975) [14]. Furthermore, the API p-y model was calibrated with the response to a small number of cycles, i.e., a maximum 200 cycles for offshore fixed-platform applications, Reese et al. (1975) [12], Reese et al. (1974) [13] and Matlock (1970) [15]. However, the monopile for offshore wind turbines behaves as a stiff pile and may undergo 10^7 and 10^8 cycles of loading over a lifetime of 20–30 years. Moreover, in the API recommendations, the initial stiffness of the *p-y* curve is independent of the diameter of the pile, which is also questionable. In the practice, the current *p-y* method of API can be safely applied for a pile diameter of about 2 m, without a consideration of the effect of a large pile size and the effect of a large cyclic number. These effects have to be considered for the design analysis of the typical large-diameter monopile foundation for offshore wind turbines.

To understand the behaviour of a large monopile in sand, investigations were performed in the past for both static and cyclic loading conditions, e.g., Cuellar, (2011) [16], Lesny and Wiemann (2006) [17] Sørensen (2012) [19] Abdel-Rahman et al. (2005) [20] Achmus et Thieken (2010) [21], and Achmus et al. (2013) [22]. However, the behaviour of the monopile foundation under cyclic loading is not discussed further because it is excluded from the scope of this present study. These investigations of the monopile foundation included physical modelling, numerical modelling, analytical modelling and modification of the *p-y* curves, taking the large monopile size and the large cyclic number effects into account. Rosquet et al. (2004) [23] reported the response of a small-scale model pile under static and cyclic loading installed in sand. Centrifuge tests were performed for analysing the behaviour of the monopile in sand under monotonic and cyclic loading. Numerical and physical models of large-diameter

monopiles showed that the stiffness of the load-displacement curves increases with the monopile diameter and the common API p-y approach overestimates the initial stiffness. Therefore, the original API p-y approach underestimates the monopile deflection and overestimates the structure stiffness under the operation load, Lesny and Wiemann (2006) [15], Abdel-Rahman et al. (2005) [20], Achmus and Thieken (2010) [21], Sørensen et al. (2010) [18] Sørensen (2012) [19], and Ashford et al. (2003) [24]. The safe design analysis of a large-diameter monopile shall take the effect of the large monopile diameter and the effect of the large cyclic number into account in the case that the original API approach is applied.

Most of the above FE analyses were carried out using the Mohr-Coulomb soil model. However, the soil stiffness depends on the actual stress, and that should be considered in numerical modelling for a better understanding of the response of a monopile embedded in sand.

The main objective of this paper is to provide information for understanding the interaction soil-monopile structure for offshore wind turbines and developing conceptual interaction diagrams capable of predicting the response of a large-diameter monopile embedded in sand and subjected to combined loading. A realistic soil model that accounts for the key features of the stress-strain behaviour of sand is adopted in the FE modelling. A simplified method is also proposed for a preliminary estimation of the load capacity of the monopile in the ultimate limit state as well as in the serviceability limit state. Furthermore, the initial stiffness required for the modal analysis has been evaluated and compared with the published results in the literature.

(a) (b)

Figure 1. Monopile foundation system a) monopile-foundation-supported offshore wind turbine, (b) monopile structure.

2 FINITE-ELEMENT MODEL AND MODEL CALIBRATION

A three-dimensional finite-element model of a system consisting of the monopile and the surrounding soil was developed and analysed. The finite-element program PLAXIS 3D Foundation [25] was used for the simulations. In order to reduce the computational effort, only one half of the monopile foundation and the surrounding soil were modelled due to the symmetry of the geometrical and loading conditions. A mesh based on 15-node wedge elements, which are available in the PLAXIS 3D Foundations program [25], was applied.

Preliminary analyses were carried out for the determination of the model geometries and the mesh size in order to reach sufficient accuracy of the results and to avoid the influence of the boundary conditions. These analyses led to a soil model with a length of ten times the monopile diameter D, a soil model with a width of five times the monopile diameter D, and a soil model with a depth of 1.6 times the embedded length L of the monopile. Fig.3 shows the finite-element model with the geometric sizes.

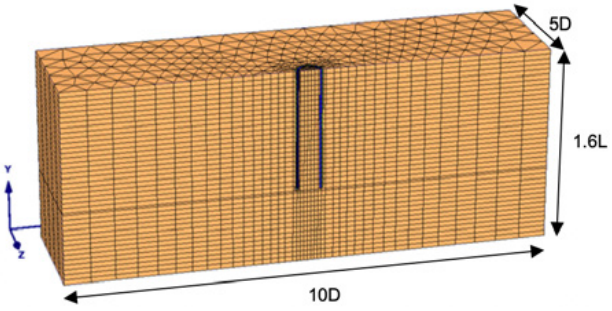

Figure 2. Finite-element mesh of a monopile foundation system.

Published results of field tests for a large-diameter monopile under monotonic lateral loading are scarce, since only pile tests under axial load are recommended by some design guidelines, and lateral loading tests for an offshore monopile at an offshore construction site would be very time-consuming. Therefore, back-calculations of the centrifuge tests reported in Klinkvort et al. (2011) [26], Klinkvort (2012) [27], and Rosquoet (2004) [23] were carried out for the calibration of the numerical model. Data on these centrifuge tests were also presented in Klinkvort et al. (2011) [26] Klinkvort (2012) [27], and Rosquoet (2004) [23].

Klinkvort et al. (2011) [26] and Klinkvort (2012) [27] reported the results of the centrifuge tests (Ng) for the monopile foundation under lateral loading. Their centrifuge tests were carried out on five solid steel piles

with a diameter of 16–40 mm and embedded lengths of 96–240 mm. These experimental monopiles were scaled to a prototype monopile with a diameter of D=1 m and embedded length L=6 m, leading to a length-to-diameter ratio of L/D = 6. The tests were performed in dry Fontainebleau sand with an average grain size d_{50} of 0.18 mm, a specific particle density of 2.65, a coefficient of uniformity C_u of 1.6, a minimum void ratio e_{min} of 0.548 and a maximum void ratio e_{max} of 0.859. The average value of the relative density is I_D=0.924, and the void ratio is e=0.57, leading to a triaxial angle of internal friction of φ=38°.

Rosquoet (2004) [23] reported the results of the centrifuge tests for a prototype steel pile with an outer diameter of 0.72 m, an embedded length of 12 m, and a pile wall thickness of 17.5 mm. The tests were carried out with Fontainebleau sand having similar properties as described above.

For the calibration of the current numerical model, back-calculations of the tests results of Klinkvort et al. (2011) [26], Klinkvort (2012) [27], and Rosquoet (2004) [23] were carried out. The model pile geometries, soil parameters and loading conditions investigated by Klinkvort et al. (2011) [26], Klinkvort (2012) [27], and Rosquoet (2004) [23] are presented in the introduction of this paper. The load-displacement curves for the test reported by Klinkvort et al. (2011) [26] Klinkvort (2012) [27], and Rosquoet (2004) [23] were evaluated and compared with the results of the nonlinear FEM analysis in Fig. 3. It is clear that the test results and the numerical results are very comparable. Both results show a stiff behaviour of the monopile for small loads, followed by more flexible behaviour as plastic deformation occurs. The results of the back-calculations show that the finite-element model with the nonlinear hardening soil model is able to realistically reproduce the load-displacement behaviour of a monopile foundation embedded in sand under combined monotonic loading.

3 PARAMETRIC STUDY AND RESULTS

Some design aspects of a monopile for wind-energy foundations include the ULS design, i.e., the proof of sufficient bearing capacity under extreme load, and the SLS design, i.e., the proof of sufficient foundation capacity under operational loads, so that the permanent rotation is lower than the value provided by the manufacturer of the wind turbines. The serviceability limit state (SLS) design for the monopile foundation for offshore wind turbines exists to show that the permanent foundation rotation does not exceed the rotation limit provided by the offshore wind turbine's manufacturer. For the offshore wind turbines installed in the North Sea, a total permanent rotation limit of 0.5° (including 0.25° for pure permanent rotation and 0.25° for maximum installation rotation) was often specified and applied. The performed parametric study therefore focused on the ultimate capacity and the permanent rotation of the monopile foundations. Monopile foundations with a diameter (D) between 4 m and 8 m and with a penetration length (L) between 16 m and 56 m were considered, leading to L/D ratios between 4 and 7 (Table 1). The wall thickness is kept constant at t_s=0.06 m. The vertical load is kept constant at V=10 MN, typical for a large wind turbine with a capacity of 5 MW. The simulations were carried out for dense, medium dense, loose and very loose sand, as presented in Table 2. The lateral load and the overturning moment were increased

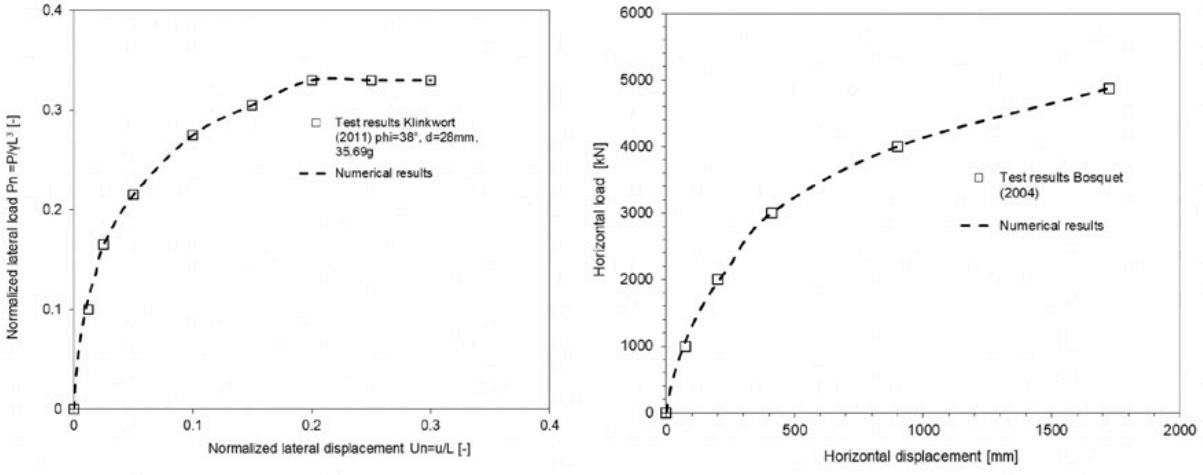

Figure 3. Comparison of the FEM and test results of Klinkvort et al. (2011) [26], Klinkvort (2012) [27], and Rosquoet (2004) [23].

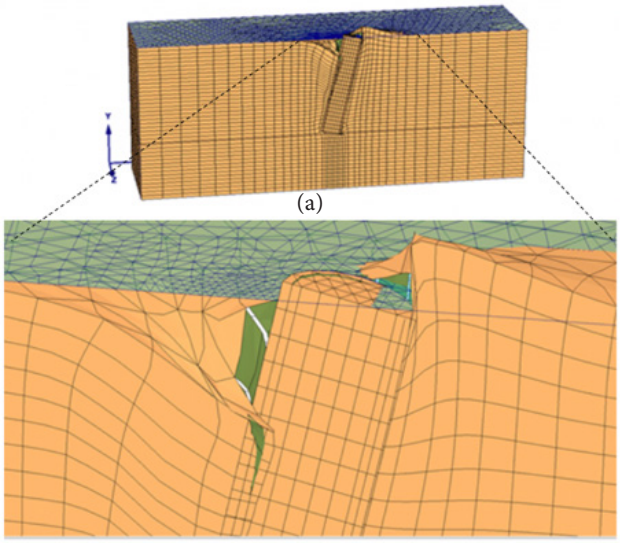

(a)

(b)

Figure 4. Deformed finite-element mesh for reference system in failure state, a) 3D view b) 3D view up scaled.

up to the failure of the numerical model at a large lateral displacement or rotation.

Table 1. Monopile size considered for parametric study.

L/*D*=4	*L*/*D*=5	*L*/*D*=6	*L*/*D*=7
D=4 m; *L*=16 m	*D*=4 m; *L*=20 m	*D*=4 m; *L*=24 m	*D*=4 m; *L*=28 m
D=5 m; *L*=20 m	*D*=5 m; *L*=25 m	*D*=5 m; *L*=30 m	*D*=5 m; *L*=35 m
D=6 m; *L*=24 m	*D*=6 m; *L*=30 m	*D*=6 m; *L*=36 m	*D*=6 m; *L*=42 m
D=7 m; *L*=28 m	*D*=7 m; *L*=35 m	*D*=7 m; *L*=42 m	*D*=7 m; *L*=49 m
D=8 m; *L*=32 m	*D*=8 m; *L*=40 m	*D*=8 m; *L*=48 m	*D*=8 m; *L*=56 m

Fig. 5 presents the total deformation for the monopile foundation system. The deformation is large at the top of the monopile level and decreases with the depth to reach zero at the monopile rotation point. Fig. 6 shows the contour plot of the mobilized horizontal soil pressure for the reference system of a monopile with a diameter of 6 m and an embedded length of 30 m in medium dense sand. The horizontal soil pressure is mobilized on the passive and active side. The pressure contours formed a pressure wedge with a bulb shape around the monopile. A large horizontal soil pressure is mobilized on the passive side above the rotation point, and a small horizontal soil pressure is mobilized below

Table 2. Considered soil parameters for dense, medium dense, loose and very loose sand applied for the parametric study.

Parameter	Name/Unit	Dense sand	Medium dense sand	Loose sand	Very loose sand
Material model	Model	Hardening soil model	Hardening soil model	Hardening soil model	Hardening soil model
Material behaviour	Type	Drained	Drained	Drained	Drained
Effective unit weight	γ' [kN/m^3]	9	9	8.5	8
Secant stiffness for consolidated drained triaxial test	E_{50}[MN/m^2]	39	29	15	7.5
Tangent oedometer stiffness	E_{oed} [MN/m^2]	39	29	15	7.5
Unloading and re-loading stiffness	E_{ur} [MN/m^2]	117	87	45	22.5
Power for stress-level dependency of stiffness	m [-]	0.5	0.5	0.5	0.5
Cohesion	c [kN/m^2]	0.1	0.1	0.1	0.1
Effective friction angle φ´	φ' [°]	40	36	30	25
Dilatancy angle	ψ [°]	10	6	0	0
Poisson´s ratio	ν [-]	0.25	0.25	0.25	0.25
Interface reduction factor	R_{inter} [-]	0.60	0.61	0.63	0.64
Over-consolidation ratio	OCR [-]	1	1	1	1

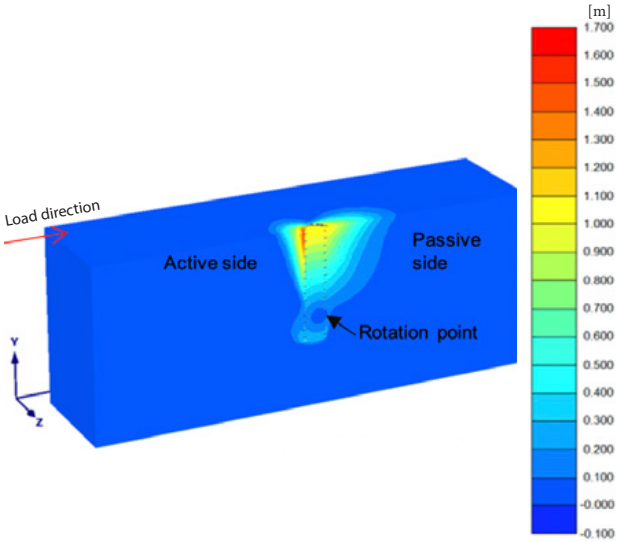

Figure 5. Contour plot of total displacement.

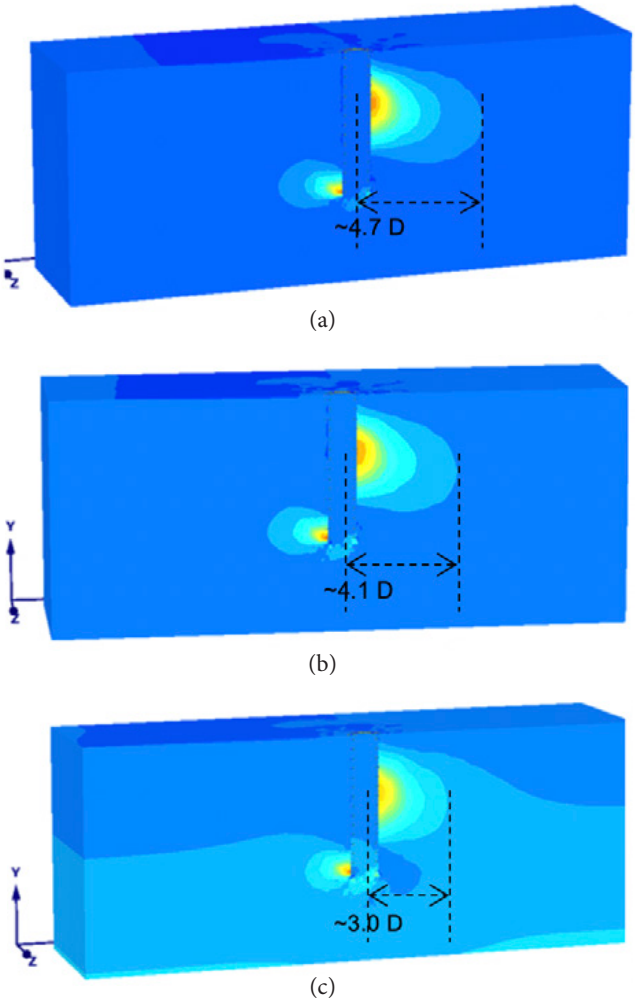

Figure 6. Contour plot of mobilized horizontal soil pressure a) dense sand b) medium dense sand c) loose sand.

the rotation point on the active side. From the horizontal soil pressure the mobilized three-dimensional passive earth pressure that resists the loading can be derived. The pressure contours generated around the monopile using the parameter study presented in Table 1 show that the horizontal earth-pressure change around the monopile extended as far as 5.4*D* from the pile surface for single, laterally loaded, rigid, stiff piles in the failure state. This result is comparable with the value of 6.1*D* reported by Lin et al. (2015) [28] based on the results of experimental tests with a pile diameter of 102 mm and a pile embedded length of 1.524 m using pressure sensors, and 5.5*D* reported by Hajialilue-Bonab et al. (2013) [29] based on the results of experimental tests with a pile diameter between 15 mm and 30 mm, and a pile embedded length between 250 mm and 550 mm using particle image velocimetry (PIV). Based on the above results a minimum lateral distance of 12*D* between two adjacent piles is recommended in order to avoid the pile group effect due to the superimposition of the stresses. However, API RP (2007) [8] recommended a lateral distance of 8*D* between two adjacent piles in order to avoid the pile group effect due to the superimposition of the stresses. Based on the above findings regarding the extension of the horizontal earth pressure, it can be assumed that this API recommendation might underestimate the lateral distance between large-diameter piles for the group effect analysis. Furthermore, the numerical results show the formation of a gap between the monopile and the surrounding soil located on the active side in the failure state (Fig. 4). Gapping is generally not considered as a design issue in a marine environment where sediment transport around the monopile is assumed to occur all the time and where free sand particles would migrate into any gaps formed. However, the sediment transport is influenced by many factors, including sediment type, wave- wind- and tide-induced current, the normal current, etc. Therefore, the migration of free sand particles into any gap can be considered to be a random process that should not be assumed for a robust monopile design of offshore wind turbines. Hence, the gap between the monopile and the surrounding soil should be taken into account in the design, or the possibility of the free sand migration should be analyzed based on the environmental data (sediment type, wave, wind, current, tide, etc.).

3.1 Ultimate capacity

The ultimate capacity of a monopile foundation in the ULS condition can be described using the force-moment interaction diagrams. Fig. 7 shows typical results of the numerical analysis in terms of the horizontal load–head

displacement (H–θ) and the moment–rotation (M–θ) relation. It can be seen that the ultimate horizontal load H_u=74.4 MN and the ultimate moment M_u=2250 MNm in the ULS condition.

The interaction diagrams of the ultimate capacity (H_u, M_u) derived from numerical simulations are presented in Fig. 8 and Fig. 9. The horizontal load-moment interaction is almost linear. A similar shape of the diagrams was reported by Achmus et al. (2013) [22] for a suction bucket foundation, and Sheikh et al. (2016) [30] for a monopile with a large diameter. As expected, the monopile size and the relative density of the foundation ground significantly affect the ultimate capacity of the foundation system. The larger the monopile size, the larger the ultimate capacity is. Likewise, the larger the relative density of the foundation sand, the larger the ultimate capacity is.

Fig. 10 presents the normalized ultimate capacity. The horizontal force and overturn moment were normalized as follows:

$$\bar{M}_u = \left[\frac{M_u}{\left(\gamma' \cdot L^3 \cdot D\right)} \right] \qquad (2)$$

$$\bar{H}_u = \left[\frac{H_u}{\left(\gamma' \cdot L^2 \cdot D\right)} \right] \qquad (3)$$

The trend lines for the dense, medium dense, loose and very loose sand can be described as follows:

Dense sand:

$$\bar{H}_u = -0.98 \cdot \bar{M}_u + 2.01 \qquad (4)$$

Medium dense sand:

$$\bar{H}_u = -0.93 \cdot \bar{M}_u + 1.39 \qquad (5)$$

Loose sand:

$$\bar{H}_u = -0.92 \cdot \bar{M}_u + 0.81 \qquad (6)$$

Very loose sand:

$$\bar{H}_u = -0.99 \cdot \bar{M}_u + 0.55 \qquad (7)$$

The normalized interaction diagrams for the ultimate capacity are almost linear and parallel to each other for the considered relative densities of the foundation soil. Evidently, an estimation of the ultimate load with a deviation of 12% is possible using the equations (4) to (7), which can be applied within a scope of the preliminary design of the monopile foundation in sand for determining the monopile size for a given extreme load combination or find the ultimate load for a given monopile size. Alternatively, the non-normalized interaction diagrams in Fig. 8 and Fig. 9 can be applied for the preliminary design.

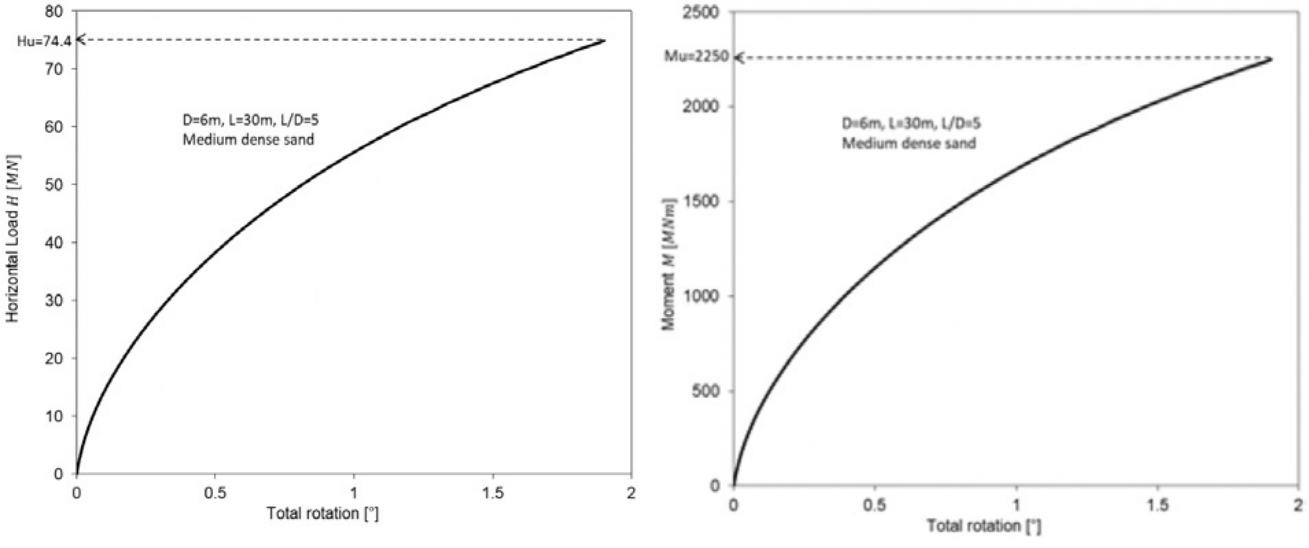

(a) (b)

Figure 7. Typical ultimate capacity for slenderness ratios L/D=4 and L/D=5, (a) H-θ relation, (b) M-θ relation.

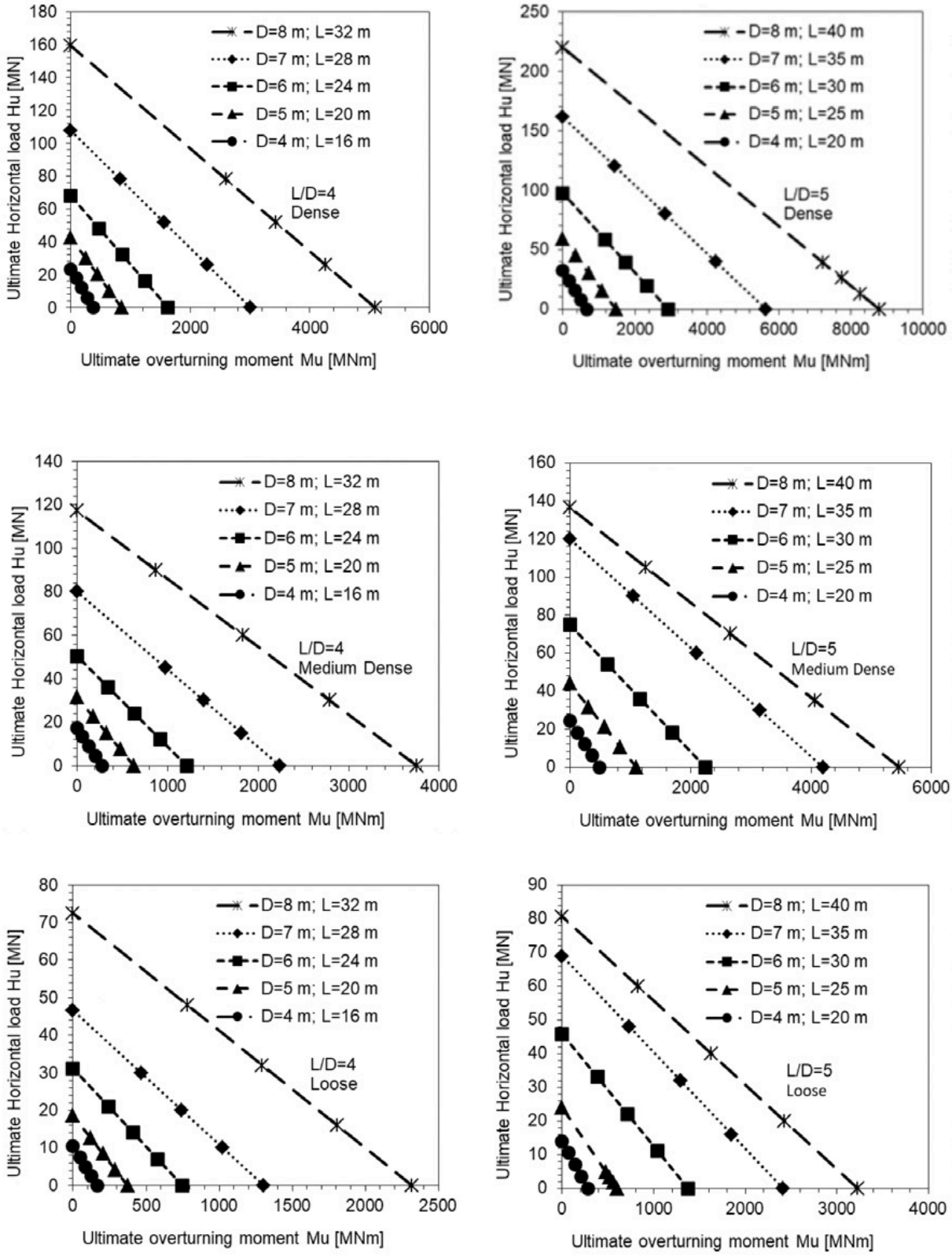

Figure 8. Ultimate capacity interaction diagrams for slenderness ratios L/D=4 and L/D=5.

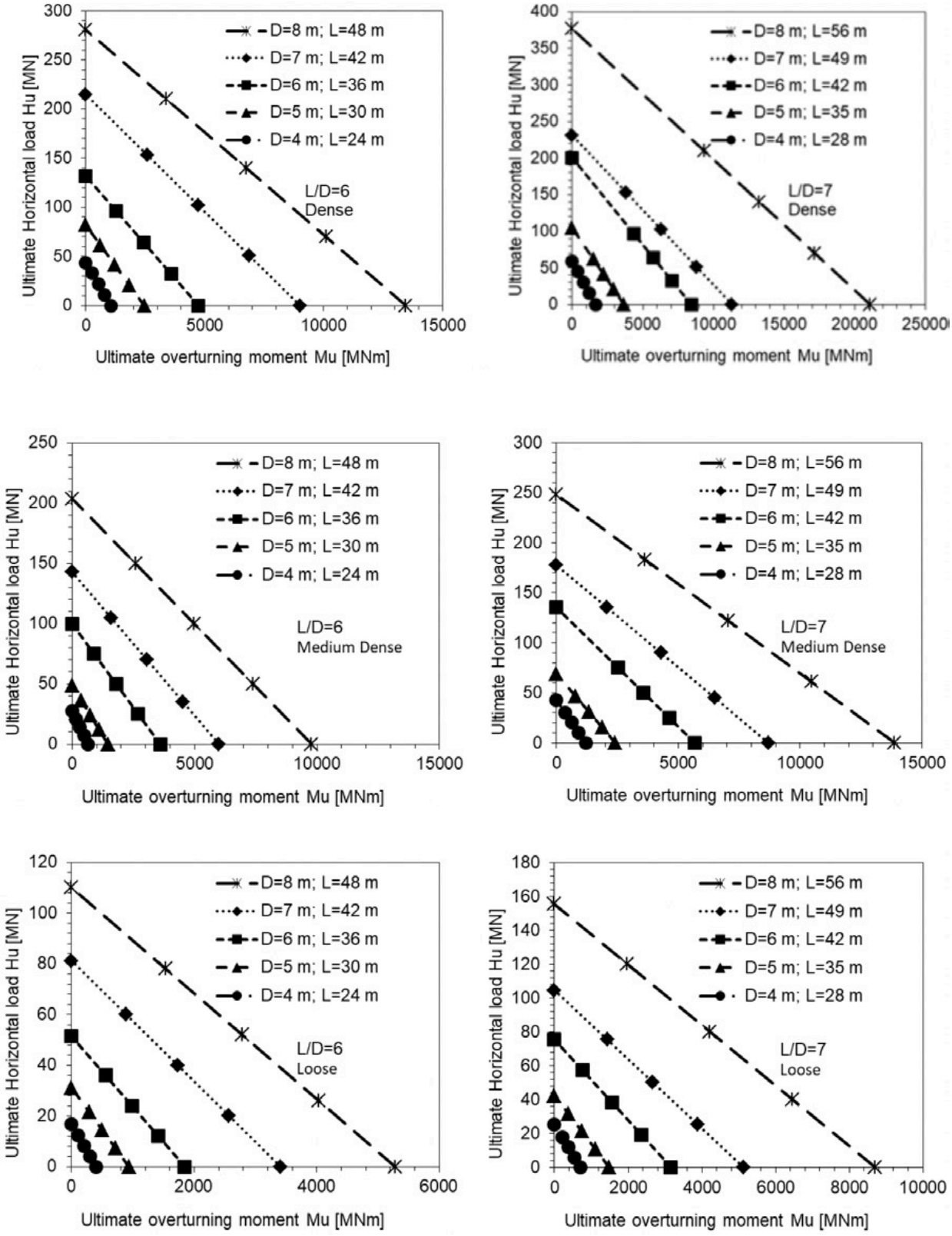

Figure 9. Ultimate capacity interaction diagrams for slenderness ratios L/D=6 and L/D=7.

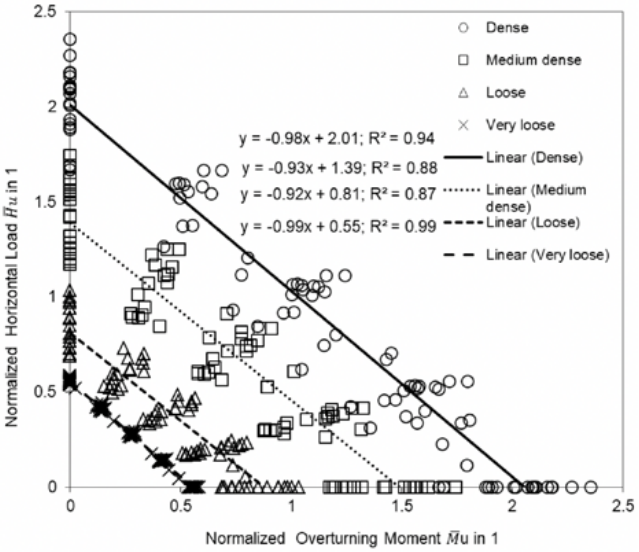

Figure 10. Normalized force moment interaction diagram for ultimate capacity.

3.2 Serviceability limit state

The serviceability limit state can be a governing load case for the design and the analysis of the monopile foundation for offshore wind turbines. In this case, the permanent or the plastic rotation of the monopile foundation subjected to an operating load is compared with the value provided by the wind-turbine manufacturer. A maximum permanent rotation of 0.5° including 0.25° from installation and 0.25° from the operation is often applied for the offshore wind turbines in the North Sea in the German sector. Fig. 11 illustrates the determination of the plastic rotation for the monopile foundation with diameter D=6m, and embedded length L=30m (L/D=5) in medium dense sand. A straight line passing through the origin point O and a tangent to the load-rotation curve is drawn, and then a straight line parallel to this tangent passing through the failure point F intersects the x-axis by J. A straight line parallel to the y-axis passing through the failure point F intersects the x-axis by K. Per definition, the value OJ represents the plastic rotation and JK represents the elastic rotation (Fig. 11). This preliminary simplified approach is first to estimate the plastic rotation under horizontal and moment loading (one-way loading). Of course, a detailed analysis is performed in the detailed design phase where the cyclic parameters of the soil are available from advanced laboratory tests. Hereby, the cyclic loading from the wave (two-way loading) and the pore-water pressure generation and dissipation will be considered.

Fig. 12 and Fig. 13 present typical interaction diagrams for a monopile foundation in sand for a permanent rotation of 0.25° and 0.50° based on the preliminary simplified approach. Likewise, the interaction diagrams for the normalized serviceability capacity for permanent rotations of 0.25°, 0.50° and 1° are presented in Fig. 14. In this case, the normalized horizontal load and the normalized overturn moment follow the Eqs. 2 and 3. As expected, the permanent rotation increases with increasing loading and decreases with the increasing monopile size and the relative density of the foundation sand.

The approach of Zhang et al. (2005) [31] for the calculation of the ultimate lateral load capacity of a rigid pile considering both soil pressure and pile-soil interface resistance is also presented in Fig. 14. Likewise, the approach of Scheikh and Bipul (2016) [30] is presented in Fig. 14 for sand with an angle of internal friction of φ'=38.8°, a coefficient of passive earth pressure k_p=4.36, and a permanent rotation of 1°. It can be seen that the results based on the approach of Scheikh and Bipul (2016) [30] lie mainly between the numerical results for loose sand φ'=30° and medium dense sand φ'=36°. The results based on the approach of Zhang et al. (2005) [31] lie mainly between the numerical results for medium dense sand φ'=36 and for dense sand φ'=40°. Therefore, the results of the numerical analysis are comparable with the results obtained from the approach of Zhang et al. (2005) and Scheikh and Bipul (2016).

The normalized interaction diagrams for the serviceability capacity are almost linear and parallel to each other for the considered monopile size and the relative density of the soil.

These normalized interaction diagrams can be applied within the scope of the preliminary design of the monopile embedded in sand in order to determine the monopile size for a given service-load combination or to find the ultimate service load for a given monopile size. Alternatively, the non-normalized interaction diagrams in Fig. 12 and Fig. 13 can be applied for the preliminary design.

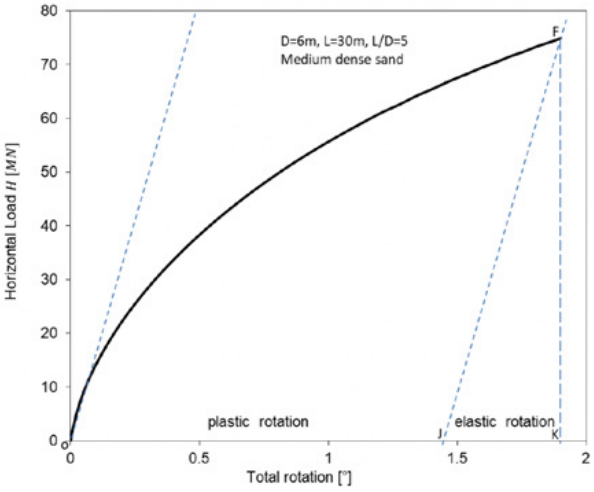

Figure 11. Determination of the plastic rotation for the reference monopile D=6m, L=30m (L/D=5).

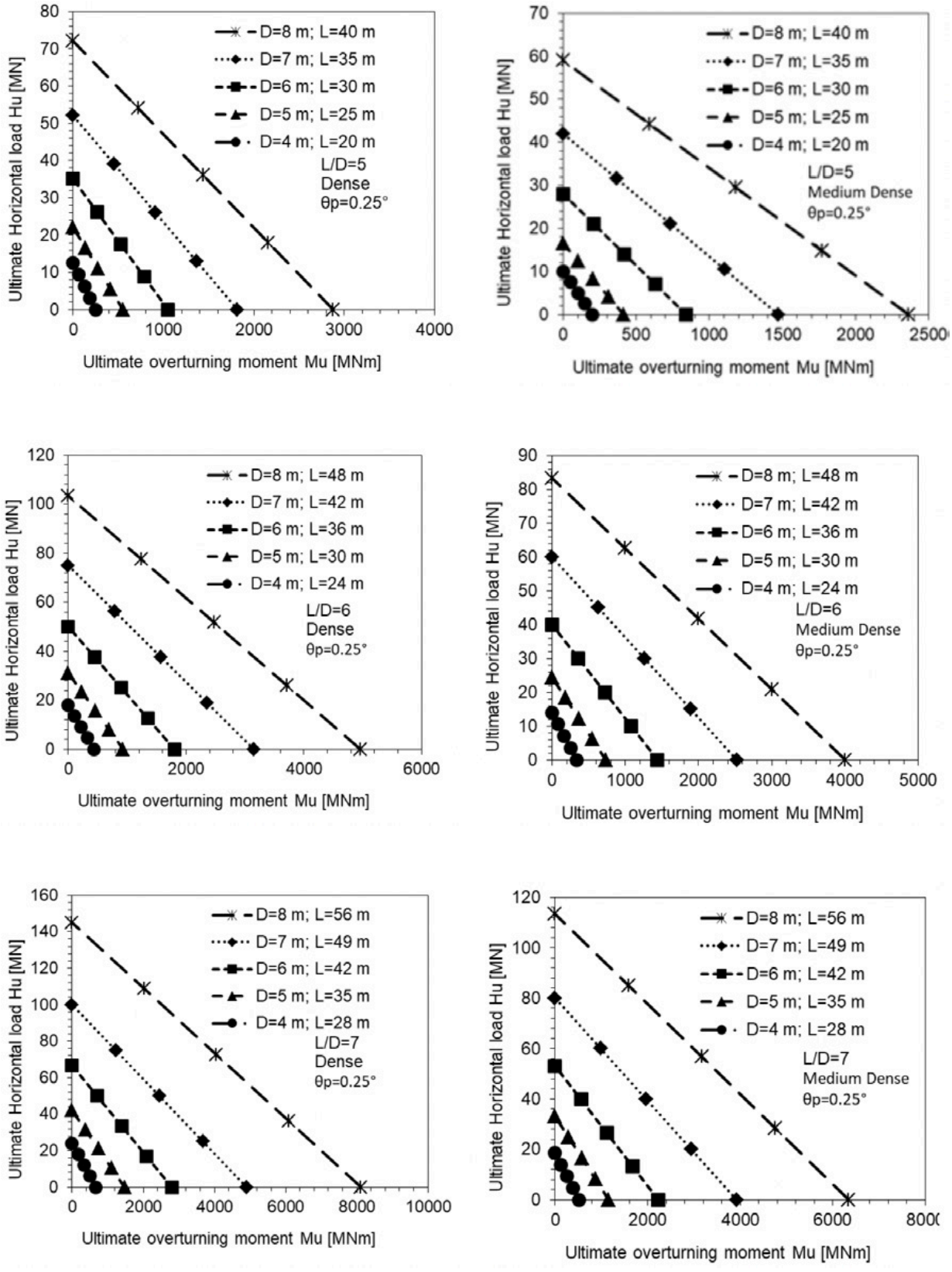

Figure 12. Force-moment interaction diagrams for permanent rotation θ_p=0.25°.

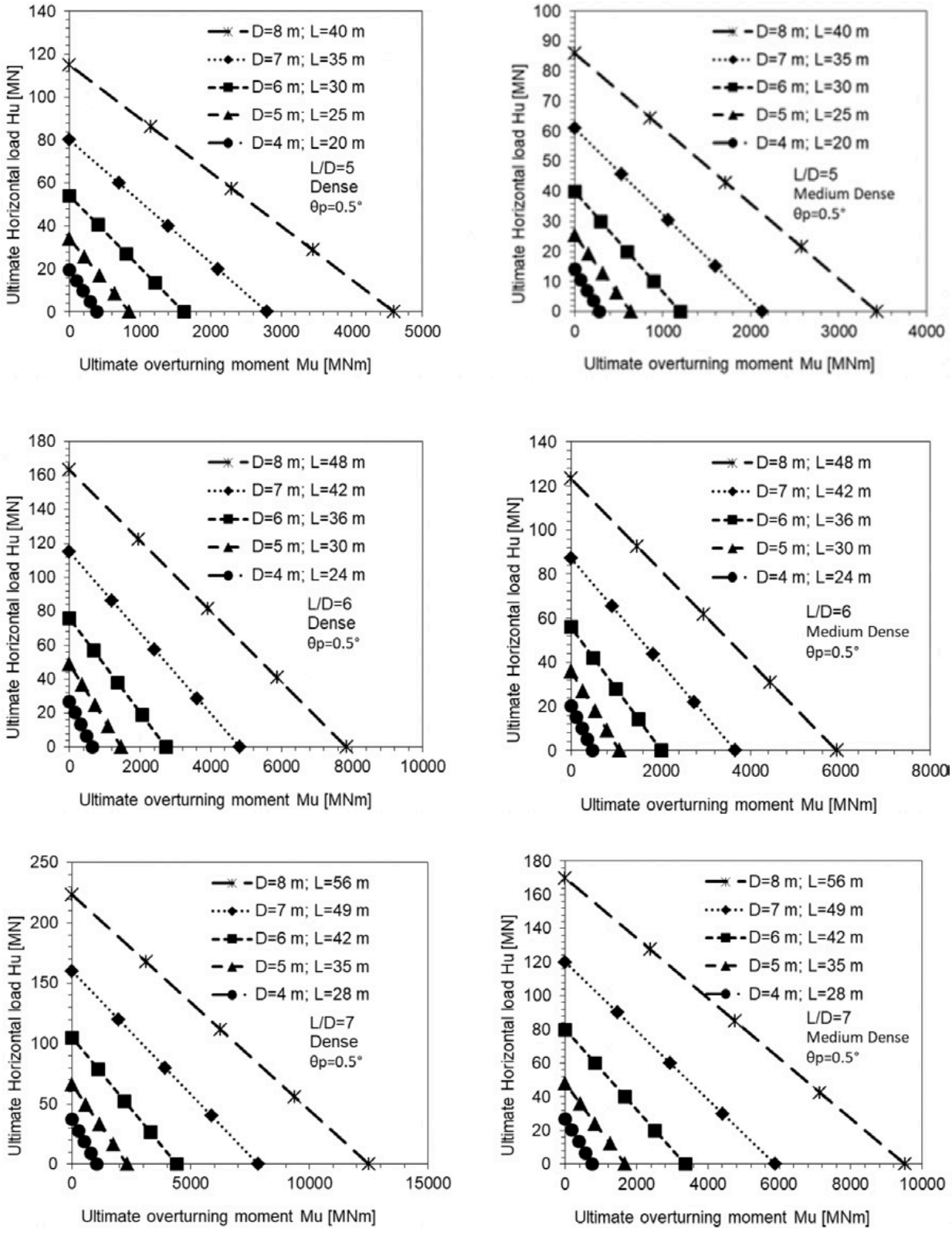

Figure 13. Force-moment interaction diagrams for permanent rotation θ_p=0.50°.

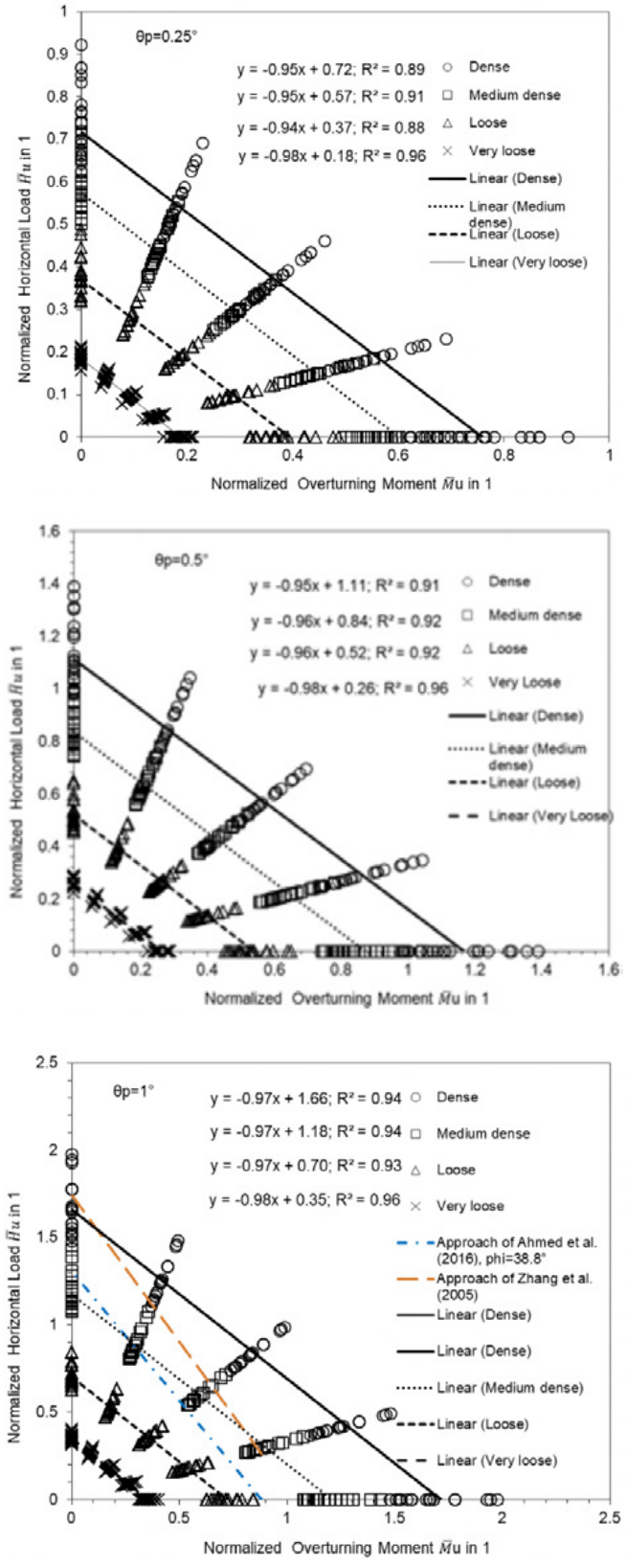

Figure 14. Normalized force-moment interaction diagrams for permanent rotation θ_p=0.25°, θ_p=0.50° and θ_p=1°.

3.3 Initial stiffness

The governing design issues for offshore wind-turbine foundations include the system stiffness. An offshore wind turbine is in a permanent interaction with three media, i.e., air, water and soil. Therefore, the main sources of excitation are wind and sea waves, whereas the main source of resistance is soil associated with the structure. The wave excitation generates relatively short waves with a significant wave height H_s around 1–1.5 m and a zero-crossing period T_z around 4–5 s, Aissa et al. (2018) [2]. The excitations generated by wind are the frequencies that are in the frequencies band of the rotor rotation 1*P* and the blade passing frequency (the blade/tower interaction), which depends on the number of blades. The blade passing frequency is often 3*P* as most turbines currently in the market have 3 blades. 1*P* and 3*P* are typically in the range of 0.3 Hz and 1 Hz, respectively, Leblanc et al. (2010) [32]. The first natural frequency of an offshore wind turbine along with its substructure has a significant effect on the behaviour of the whole system. Hence, the coincidence of the tower frequency with the above-mentioned frequencies (rotor and blade passing frequencies) will lead to dynamic amplification, resulting in large stress variations in the OWT structure. This situation could potentially lead to resonance, which has to be avoided due to the fact that resonance may induce an accelerated accumulation of fatigue.

The OWT design can be performed in such a way that the first natural frequency lies within three possible ranges: an interval before the 1*P* called the "soft–soft" region, a range after the 3*P* known as the "stiff–stiff" region and a region located between 1*P* and 3*P* called the "soft–stiff" region.

In order to avoid resonance, offshore wind turbines are designed as soft-stiff, such that the first natural frequency lies between the turbine (1*P*) and blade passing frequencies (3*P*). The design of the structure and the substructure of an offshore wind turbine should be carried out in such a way that it sustains the permanent dynamic forces induced by vibrations during its operational life. The natural frequency of typical offshore wind turbines is influenced by the foundation stiffness. The lateral initial stiffness k_{hi}, the rotation initial stiffness $k_{\theta i}$ and the cross-coupling initial stiffness $k_{h\theta i}$ can be distinguished. Carter and Kulhawy (1992) [33], and Shadlou and Bhattacharya (2016) [34] proposed the initial stiffness for a rigid monopile. Fig. 15 shows a comparison of the initial lateral stiffness between the results of the finite-element analysis and the approach of Carter and Kulhawy (1992) [33], and Shadlou and Bhattacharya (2016) [34]. It can be seen that the initial horizontal

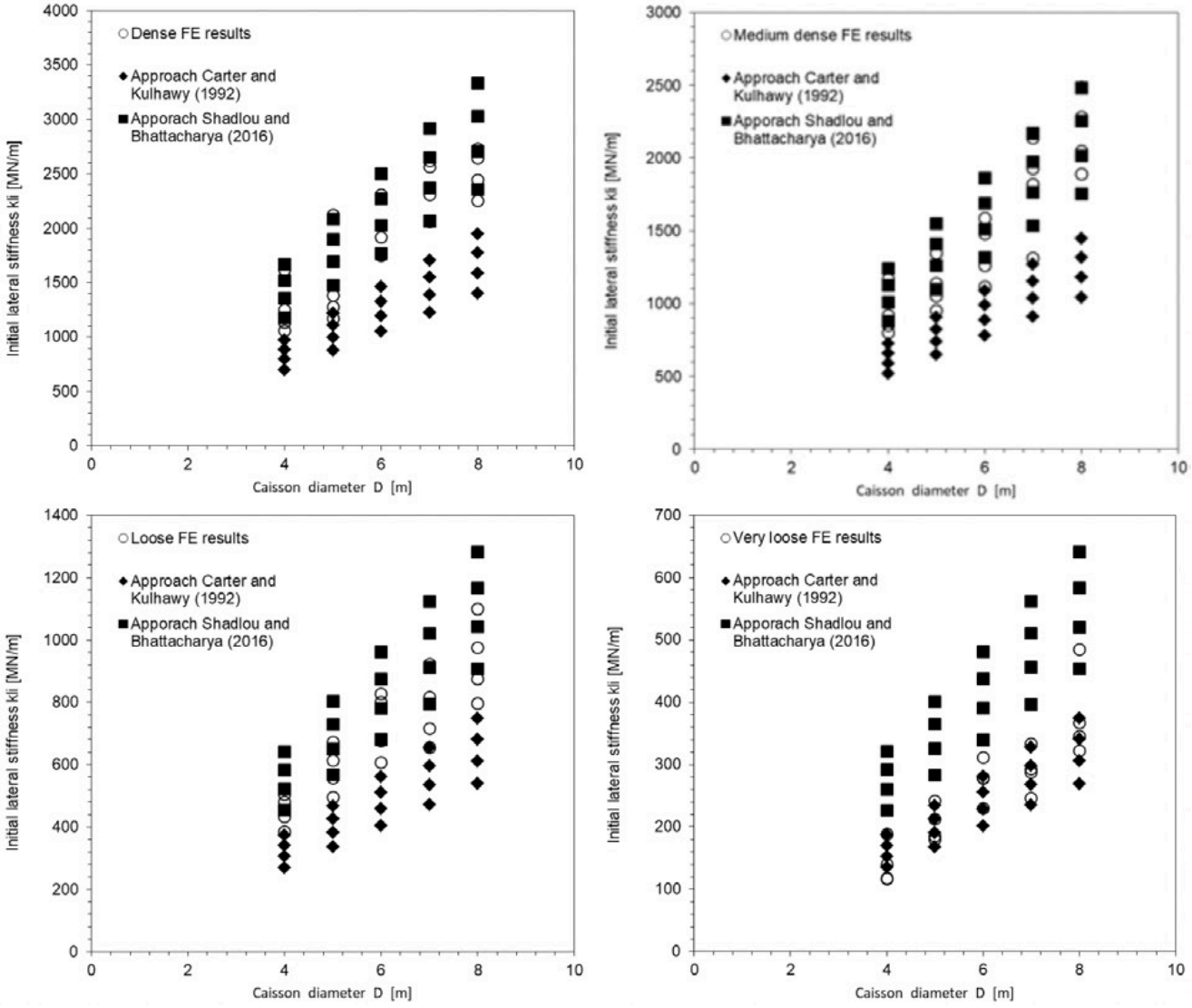

Figure 15. Comparison of initial lateral stiffness between results of a finite-element analysis and the approaches Carter and Kulhawy (1992) [33], and Shadlou and Bhattacharya (2016) [34].

stiffness is dependent on the monopile size as well as the soil stiffness. The results of the finite-element analysis are comparable with the results obtained from both the approaches. In general, the approach of Carter and Kulhawy (1992) [33] yields a slightly smaller horizontal initial stiffness than this numerical model analysis. The numerical horizontal initial stiffness and those obtained from the approach of Shadlou and Bhattacharya (2016) [34] are comparable.

4 CONCLUSIONS

The monopile foundation is presently the most used foundation system for offshore wind turbines. Three-dimensional FE analyses were carried out to investigate the behaviour of the monopile foundation in sand under combined loading (V=constant, H, M). Numerical analyses were carried out by applying the Hardening Soil Model, which describes the elasto-plastic and stress-dependent behaviour of sandy soil. The following main conclusions can be drawn from the results obtained:

- The numerical back-analysis of test results reported in the literature showed that the behaviour of a monopile foundation embedded in sand under combined monotonic loading can be well reproduced by means of a numerical model using the Hardening Soil Model (HSM).
- The results of the numerical simulations showed that

the mobilized earth pressure around the monopile extended as far as 5.4*D* from the pile surface for a single, laterally loaded, rigid, stiff pile in the failure state. This result is comparable with those reported by Li et al. (2014) [28] 6.1*D* and by Hajialilue-Bonab et al. (2013) [29] 5.5*D*. Therefore, it is recommended to have a lateral distance larger than 12*D* between two adjacent piles in order to avoid the pile-group effect due to the superimposition of the stresses.
- The results of the numerical simulations showed the formation of a gap between the monopile and the surrounding soil on the active side for the condition of ultimate loading. A robust design should quantify the effect of this gap on the monopile behaviour and take this into account.
- In the ultimate loading condition the depth of the monopile rotation point ranges from approximately 0.55*L* to 0.65*L* (*L* is the embedded length of the monopile) for a monopile foundation used for an offshore wind turbine.
- With respect to the load-bearing capacity, the SLS design of the monopile foundation for the offshore wind turbine more governs the monopile design than the ULS design, due to the total permanent rotation of the monopile, generally limited to 0.50°.
- Numerical results for the initial lateral stiffness are comparable with the analytical results derived from the approach of Carter and Kulhawy (1992) [33], and Shadlou and Bhattacharya (2016) [34].
- The results of the parametric study showed that the ultimate capacity of the monopile foundation at ULS and SLS strongly depends on the monopile size (diameter and embedded length), the relative density and accordingly the stiffness of the foundation sand.

Normalized equations for the load-moment interaction diagrams were developed, which described the bearing capacity of the monopile foundation dependent on the embedded length (*L*), the diameter (*D*) of the monopile and the relative density of the foundation sand. The derived normalized interaction diagrams and equations are appropriate tools for the preliminary design of the monopile foundation for offshore wind-energy turbines in drained sand under combined monotonic loading at ULS and SLS. The findings of this numerical study are interesting and useful, but some aspects of the monopile behaviour, which are not considered here, still need further investigation. These aspects include the installation effect on the surrounding soil, the effect of cyclic loading with pore-water accumulation and dissipation, the ageing effect, etc. Therefore, further research on monopile behaviour is still needed.

REFERENCES

[1] Houlsby, G.T., Byrne, B.W. 2000. Suction caisson foundations for offshore wind turbines and anemometer. Wind Engineering 24(4), 249-255. https://doi.org/10.1260/0309524001495611

[2] Aissa, M.H., Bouzid, D.A., Bhattacharya, S. 2018. Monopile head stiffness for serviceability limit state calculations in assessing the natural frequency of offshore wind turbines. International Journal of Geotechnical Engineering 12(3), 267-283. https://doi.org/10.1080/19386362.2016.1270794

[3] Kallehave, D., Byrne, B.W., LeBlanc Thilsted C., Mikkelsen, K.K. 2015. Optimization of monopiles for offshore wind turbines. Phil. Trans. R. Soc. A373: 20140100.

[4] Negro, V., López-Gutiérrez, J.S., Esteban, M.D., Alberdi, P., Imaz, M., Serraclara, J.M. 2017. Monopiles in offshore wind: Preliminary estimate of main dimensions. Ocean Engineering 133, 253–261. DOI: 10.1016/j.oceaneng.2017.02.011

[5] Gurhuz, A. 2018. Modified coefficient of subgrade reaction to laterally loaded piles. Acta Geotechnica Slovenica 15(1), 77-85. DOI https://doi.org/10.18690/1854-0171.15.1.77-85.2018

[6] Reese, L.C., Matlock, H. 1956. Non-dimensional solutions for laterally-loaded piles with soil modulus assumed proportional to depth. Proceedings of the 8th Texas Conference on Soil Mechanics and Foundation Engineering, Austin, Texas, 1-41.

[7] McClelland, B., Focht, J.A., Jr. 1958. Soil modulus for laterally loaded piles. Trans. ASCE, ASCE, Reston, VA, 1049–1063.

[8] API RP 2A-WSD 2007. Planning, Designing and Constructing Fixed Offshore Platforms - Working Stress Design, Twenty-Second Edition, American Petroleum Institute.

[9] DNV-OS-J101 2014. Design of Offshore Wind Turbine Structures, DET NORSKE VERITAS AS.

[10] ISO 19901-4 2016. Petroleum and natural gas industries -- Specific requirements for offshore structures -- Part 4: Geotechnical and foundation design considerations.

[11] O'Neill, M.W., Murchison, J.M. 1983. An evaluation of p-y relationships in sands. A report to the American Petroleum Institute (PRAC 82-41-1), University of Houston-University Park, Department of Civil Engineering, Research Report No. GTDF02-83.

[12] Reese, L.C., Cox, W.R., Koop, F.D. 1975. Field testing and analysis of laterally loaded piles in stiff clay. Proceedings, Offshore Technology Conference, Houston, Texas, Paper No. 2312.

[13] Reese, L.C., Cox, W.R., Koop, F.D. 1974. Field testing and analysis of laterally loaded piles in sand. Proceedings, Offshore Technology Conference, Houston, Texas, Vol. II, Paper No.2080.
[14] Seed, I., Makdise, B. 1975. Representation of irregular stress time histories by equivalent uniform stress series in liquefaction analyses. Report No. EERC 75-29, College of Engineering, University of California, Berkeley (USA).
[15] Matlock, H. 1970. Correlations for design of laterally loaded piles in soft clay. Proc., 2nd Offshore Technology Conf., American Institute of Mining, Metallurgical, and Petroleum Engineers Inc., Englewood, CO, 577–594.
[16] Cuellar, V.P. 2011. Pile Foundations for Offshore Wind Turbines: Numerical and Experimental Investigations on the Behaviour under Short-Term and Long-Term Cyclic Loading. PhD Thesis, Technical University of Berlin, 273 p.
[17] Lesny, K., Wiemann, J. 2006. Finite-element-modelling of large diameter monopiles for offshore wind energy converters. Proceedings of Geo Congress, Atlanta, GA. ASCE, Reston, VA, 1–6.
[18] Sørensen, S.P.H., Ibsen, L.B., Augustesen, A.H. 2010. Effects of diameter on initial stiffness of p-y curves for large-diameter piles in sand. Proceedings of the 7th European Conference on Numerical Methods in Geotechnical Engineering, 907-912.
[19] Sørensen, S.P.H. 2012. Soil-structure interaction for non-slender, large-diameter offshore monopiles. PhD Thesis, Aalborg University Denmark, Department of Civil Engineering.
[20] Abdel-Rahman, K., Achmus, M. 2005. Finite element modelling of horizontally loaded monopile foundations for offshore wind energy converters in Germany. Proceeding of International Symposium on Frontiers in offshore Geotechnics, Perth, Australia, 391-396.
[21] Achmus, M., Thieken, K. 2012. Investigations the interaction relationships for piles under combined loading in cohesive and non-cohesive soils. Geotechnik 35 (4), 217-228 (in German).
[22] Achmus, M., Akdag, C.T., Thieken, K. 2013. Load-bearing behaviour of suction bucket foundations in sand. Applied Ocean Research 43, 157-165. DOI: 10.1016/j.apor.2013.09.001
[23] Rosquoet, F. 2004. Pieux sous charge latérale cyclique. Thèse de Doctorat, Ecole Doctorale Mécanique Thermique et Génie Civil, Ecole Centrale de Nantes, Université de Nantes, 327 p.
[24] Ashford, S.A., Juirnarongrit, T. 2003. Evaluation of Pile Diameter Effect on Initial Modulus of Subgrade Reaction. Journal of Geotechnical and Geoenvironmental Engineering 129, (3), 234–242. DOI: 10.1061/(ASCE)1090-0241(2003)129:3(234)
[25] PLAXIS, 2006. Finite Element Code for Soil and Rock Analysis, 3D Foundation Version 2.
[26] Klinkvort, R.T., Hededal, O. 2011. Centrifuge modelling of offshore monopile foundation. Frontiers in Offshore Geotechnics II, ed. 1, Taylor & Francis, 581-586.
[27] Klinkvort, R.T. 2012. Centrifuge modelling of drained lateral pile – soil response: Application for offshore wind turbine support structures. PhD Thesis, Department of Civil Engineering, Technical University of Denmark, 232 p.
[28] Lin, H., Ni, L., Suleiman, M.T., Raich, A. 2014. Interaction between Laterally Loaded Pile and Surrounding Soil. Journal of Geotechnical and Geoenvironmental Engineering 141(4). https://doi.org/10.1061/(ASCE)GT.1943-5606.0001259
[29] Hajialilue-Bonab, M., Sojoudi, Y., Puppala, A.J. 2013. Study of strain wedge parameters for laterally loaded piles. Int. J. Geomech. 13(2), 143-152. DOI: 10.1061/(ASCE)GM.1943-5622.0000186
[30] Sheikh, S.A., Bipul, H. 2016. Numerical analysis of large-diameter monopiles in dense sand supporting offshore wind turbines. International Journal of Geomechanics 16 (5). DOI: 10.1061/(ASCE)GM.1943-5622.0000633
[31] Zhang, L., Silva, F., Grismala, R. 2005. Ultimate lateral resistance to piles in cohesionless soils. Journal of Geotechnical and Geoenvironmental Engineering, 131(1), 78-83.
[32] LeBlanc, C., Houlsby, G.T., Byrne, B.W. 2010. Response of stiff piles in sand to long-term cyclic lateral loading. Géotechnique 60(2), 79-90. DOI: 10.1680/geot.7.00196
[33] Carter, J.P., Kulhawy, F.H. 1992. Analysis of laterally loaded shafts in rock. ASCE Journal of Geotechnical Engineering 118(6), 839-855.
[34] Shadlou, M., Bhattacharya, S. 2016. Dynamic stiffness of monopiles supporting offshore wind turbine generators. Soil Dynamics and Earthquake 88, 15-32.
[35] EWEA 2015. The European offshore wind industry - key trends and statistics 2014. January 2015: Available at: http://www.ewea.org/fileadmin/files/library/publications/statistics/EWEA-European-Offshore-Statistics-2014.pdf (Accessed: 23th October 2018)
[36] Blanco, M.I. 2009. The economics of wind energy. Renewable and Sustainable Energy Reviews 13(6-7), 1372-1382. https://doi.org/10.1016/j.rser.2008.09.004
[37] Arshad, M., O´Kelly, B. 2016. Analysis and design of monopile foundations for offshore wind turbine structures. Marine Geosciences and Geotechnol-

ogy 34, 503-525. https://doi.org/10.1080/10641 19X.2015.1033070.
[38] Poulos, H., Hull, T. 1989. The role of analytical geomechanics in foundation engineering. In Foundation engineering: Current principles and practices 2, 1578–1606. Reston, VA:ASCE.
[39] Dobry, R., Vincente, E., O'Rourke, M., Roesset, J. 1982. Stiffness and damping of single piles. J. Geotech. Engng 108(3), 439–458.
[40] .Budhu, M., Davies, T. 1987. Nonlinear analysis of laterally loaded piles in cohesionless soils. Can. Geotech. J. 24 (2), 289–296.
[41] Carter, J., Kulhawy, F. 1988. Analysis and design of drilled shaft foundation socketed into rock. Project 1493-4, Final Report Cornell University, Ithaca, New York.

BEARING CAPACITY OF A SINGLE PILE IN SATURATED AND DRAINED CLAY

NOSILNOST POSAMIČNEGA PILOTA V ZASIČENI GLINI PRI DRENIRANIH POGOJIH

Yu Song
China University of Petroleum,
State Key Laboratory of Marine Oil and Gas Drilling and Completion
Beijing, China
E-mail: songyu_cup@163.com

Jin Yang *(corresponding author)*
China University of Petroleum,
State Key Laboratory of Marine Oil and Gas Drilling and Completion
Beijing, China
E-mail: cyjin1018@vip.sina.com

Hua Xiang
Gubkin Russian State University of Oil and Gas,
Department of development of offshore oil and gas fields
Moscow, Russia
E-mail: xiang.h@gubkin.ru

Bo Zhou
CNPC Engineering Technology R&D Company Limited,
Department of Oil and Gas Drilling and Completion
Beijing, China
E-mail: zhoubodr@cnpc.com.cn

DOI https://doi.org/10.18690/actageotechslov.16.1.70-78.2019

Keywords

laterally loaded pile; bend moment; force-displacement (p-y) curve; soil resistance

Ključne besede

bočno obtežen pilot; upogibni moment; krivulja sila--premik (p-y); odpornost tal

Abstract

In this study the pile-soil interaction behavior of single, long, laterally loaded, embedded piles was investigated in both saturated and drained clay. The piles were hollow steel pipes with a diameter of 114 mm, a thickness of 2.5 mm, and a length-to-diameter ratio of 35. The piles were installed in inhomogeneous, saturated clay and laterally loaded to test their mechanical behaviors in saturated and drained soil. The soil-pile interaction force-displacement relationships (p-y curves) were calculated from the soil reaction and combined with the directly measured lateral displacement. The results indicate that the lateral load--bearing capacity of the pile in drained clay is up to 27% greater than the initial value. Furthermore, the ultimate soil resistance in both types of clay increases linearly with depth. There is a large difference between drained clay and unsaturated loose clay. The soil resistance in drained clay is nearly two times larger than that in unsaturated clay. This study also compares and analyzes the difference between the measured p-y curves and the back-calculated values.

Izvleček

V predstavljeni študiji je bilo preučevano interakcijsko vedenje posamičnih, dolgih, bočno obteženih pilotov v zasičenih in dreniranih glinah. Piloti so bili izdelani iz votlih jeklenih cevi premera 114 mm, debeline 2,5 mm, razmerje med dolžino in premerom je bilo enako 35. Piloti so bili vgrajeni v nehomogenih zasičenih glinah in bočno obteženi, da bi preverili njihovo mehansko obnašanje v zasičeni in drenirani zemljini. Interakcijo zemljina-pilot v obliki relacije sila-pomik (p-y krivulje) smo izračunali iz reakcije zemljine in neposredno izmerjenim bočnim premikom. Rezultati kažejo, da je bočna nosilnost pilota v drenirani glini do 27% večja od njene začetne vrednosti. Poleg tega se mejna odpornost tal pri obeh vrstah gline linearno povečuje z globino. Obstaja velika razlika med drenirano glino in nezasičeno mehko glino. Odpornost tal v drenirani glini je skoraj dvakrat večja od njene vrednosti v nezasičeni glini. Študija vsebuje tudi primerjavo in analizo razlike med izmerjenimi krivuljami p-y in vrednostmi dobljenimi s povratnimi analizami.

1 INTRODUCTION

The stability of piles that are used to support oceanographic engineering, oil and gas wellheads, buildings, bridges, transmission lines, and highway structures is commonly governed by lateral loads [1]. In areas with high rainfall and numerous beaches and rivers, the soil around a pile will undergo a process of natural drainage from the saturated to the unsaturated state; this can lead to changes in the lateral bearing capacity of the pile.

The issue of soil modeling is also important in the perspective of ensuring sustainable production from the productive formations [2-3].

Many studies have investigated the pile-soil interface and lateral bearing capacity in saturated and unsaturated soil. However, a comparative study of soil resistance in saturated and drained clay has not been conducted. Studies have also analyzed the large horizontal deformation of piles in detail, in order to clarify the internal relations between the deformation and the internal forces and the lateral soil resistance [4-5]. These characteristics have important scientific and engineering significance for the development of a clay strata construction.

The response analysis of the lateral pile deflection and the lateral soil resistance is important for designing laterally loaded piles. Numerous studies have applied elastic and elastoplastic analytical methods to transverse piles [6-8]. Popular elastic analysis methods include the foundation-beam method, the finite-element method, and the boundary-element method. However, it is difficult to use these methods to accurately predict the actual behavior of a pile foundation when laterally loaded piles are deformed significantly [9-10].

The elastoplastic analysis model is more reasonable when the pile foundation has a large horizontal deformation. The engineering community considers the p-y curve method the most effective analytical method for a pile foundation with a large horizontal displacement [11]. The p-y curve is a comprehensive index that reflects the resistance of the surrounding soil to the pile body. It is influenced by many factors, such as the pile diameter, the pile foundation stiffness, the cross-sectional shape, the size effect, and the pile head restraint condition [12]. Matlock established the p-y curve of saturated soft clay and Reese established that of saturated sandy soil through experimental methods [5, 13]. The p-y curve method has subsequently been adopted and promoted by the American Petroleum Institute [14]. However, some experimental studies have noted a certain deviation when using the soil shear strength and pile bending moment to derive the soil resistance [5, 7, 15].

In recent years, studies have actively investigated pile-soil contact in unsaturated soils. Many studies have focused on finding differences between unsaturated and saturated soils and on establishing and modifying the mathematical functions of soil resistance [16-19]. However, the physical properties of saturated and unsaturated clays generally differ significantly. Experimental measurements normally use the direct shear test and the particle size of loose dry clay in saturated clay [20-21]. In addition, studies have measured the pile bending moment to estimate the soil resistance instead of using direct measurements. To the best of our knowledge, no study has investigated the soil-pile contact effect in the saturated clay drainage process.

In this study, advanced sensors were used to measure directly the pile bending moment, the pile body displacement, and the soil resistance. Subsequently, a reasonable p-y curve was derived for responses to changes in the soil properties.

2 METHOD

2.1 Experimental Materials

This experiment used clay soil samples obtained at China Bohai Beach. The saturated soil samples were prepared in the soil pool by using sorted soil that was collected on site. The laboratory measurement results of the saturated soil samples are based on the Unified Soil Classification System [22]. Figure 1 shows the particle size distribution and the composition of the slightly sandy silty clay soil samples (uniform coefficient, C_u 8.4). The maximum and minimum unit weights of the well-graded sand in an oven-dried condition were 2.05 and 1.61 kN/m^3, respectively.

The pile used in the test was a hollow circular steel tube with a measured elastic modulus of 206 GPa, an outside diameter of 114 mm, and a thickness of 2.5 mm. The yield bending moment of the pile body ([M]) obtained by the deflection measurement method was 7260 kN·m. Boominathan and Ayothiraman [23] divided the embedment length of the pile according to its mechanical behavior. Studies have already suggested that a pile with a length-to-diameter ratio (L/D) < 20 appears as a short stiff pile, a pile with L/D = 20 appears as an intermediate pile, and a pile with L/D > 25 appears as a long flexible pile. The experiment used a pile with a depth of 3990 mm and a L/D of 35. Table 1 shows the basic parameters of the pile and the relative stiffness of the soil. The load application point of the pile was 100 mm above the mud surface.

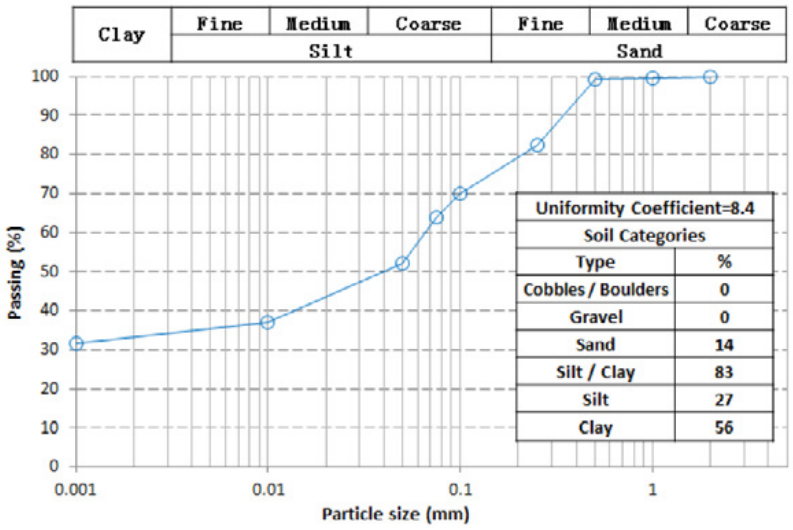

Figure 1. Properties of the slightly sandy silty clay soil used in the experiment.

Table 1. Parameters of the pile and the relative stiffness of the soil.

Outside diameter (mm)	Wall thickness (mm)	Stiffness (*EI*) ($\times 10^9$N/mm^2)	Embedment length (mm)	Pile length (mm)	Length-to-diameter ratio	Description
114	2.5	309	3990	4090	35	Long flexible

2.2 Pile-Soil Interaction Experimental Facility

The pile-soil interaction (PSI) facility comprised a testing soil pool, a lateral loading control system, and various sensor and data-acquisition components. The testing soil pool had dimensions of 6.0 × 3.0 × 5.0 m^3 and three drains installed in its bottom. The soil thickness was 4.8 m, and the length and width were more than 10 times the outside diameter of the pile. The measurement results were not affected by the boundary effect [24]. A lateral loading control system applied lateral loads to the pile head, and it controlled and recorded the output load value. The loads applied to the pile head were varied from 980 to 9800 N in increments of 980 N. For each load increment, the load was kept constant until the lateral displacement of the pile stabilized.

The PSI facility includes thin resistance strain gauges, a customized inclinometer sensor, and soil-pressure sensors. The resistance strain gauges, each having

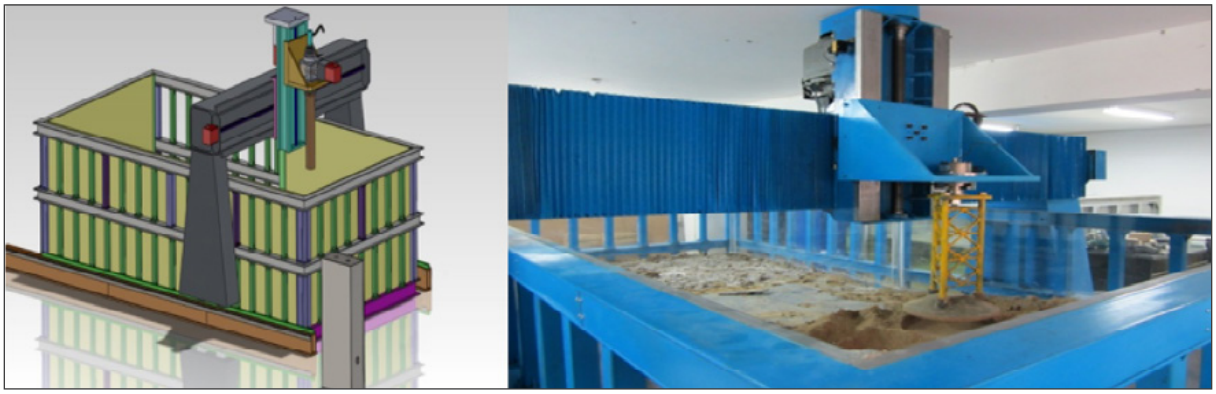

Figure 2. Pile-soil interaction experimental facility.

a length of 6 mm and a resistance of 120 Ω, were installed below the mud surface on the tension side of the pile at 228-mm intervals (0, 228, 456, 684, 912, 1140, 1368, 1596, 1824, 2052, 2280, 2508, 2736, 2964, 3192, 3420, 3648, and 3876 mm). All the attachments of the resistance strain gauges to the pile body were waxed to make them waterproof. Custom resistive soil-pressure sensors with an outside diameter of 20 mm and a thickness of 7 mm were attached to the pile surface along the pile length (114, 228, 342, 456, 570, 684, and 798 mm). The p-y curve and the ultimate soil resistance were studied through direct measurements of the soil resistance.

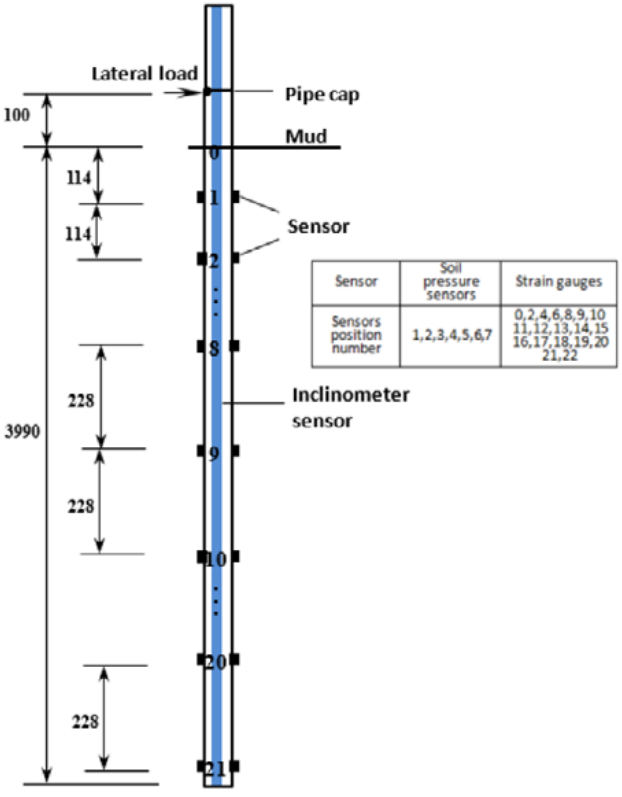

Figure 3. Pile instrumentation and the location of various sensors.

3 EXPERIMENTAL PROCESSES

3.1 Saturated clay preparation process

In the saturated-clay preparation process, uniform sand with a 0.5-mm particle size was first used to line the bottom of the soil pool to a depth of 500 mm. Next, drying clay was placed in the soil pool, and the soil was paved and compacted with each additional 20-mm-thick layer of clay. Saturated clay was prepared by saturating each layer of clay individually, with water slowly flowing in from the water inlet hole at the bottom of the soil pool. The water level was controlled to 200 mm above the soil surface in the soil pool, and a slow inflow rate was maintained. Each soil layer was kept standing for 4–5 h to ensure the uniform soil saturation. Following the completion of the clay saturation, the excess water on the clay surface was absorbed and the saturated clay was kept still for 5 days.

To characterize the soil, consolidated drained (CD) triaxial tests were performed. Then, 114-mm-diameter triaxial soil samples were tested at confining pressures of 25, 50, and 100 kPa from a depth of 75 mm. The strain rate was 0.01 mm/min. Figure 5 shows the measured deviator stress-axial strain and peak friction angle during the CD triaxial tests.

3.2 Soil drainage preparation process

Three drains at the bottom of the soil pool were opened following the completion of the first part of the test. The soil samples in the soil pool were weighed to calculate the water content at different depths every 2 h.

The permeability of the soil samples was high, as the water content over 7 days fell to 9.2%. We theorize that the clay moisture content is the optimal moisture content (Fig. 4). Figure 5 shows that the soil friction angle increased to 30.96° after the drainage of the soil samples (12.3%) and that the cohesion increased to 15.18 kPa (126.6%).

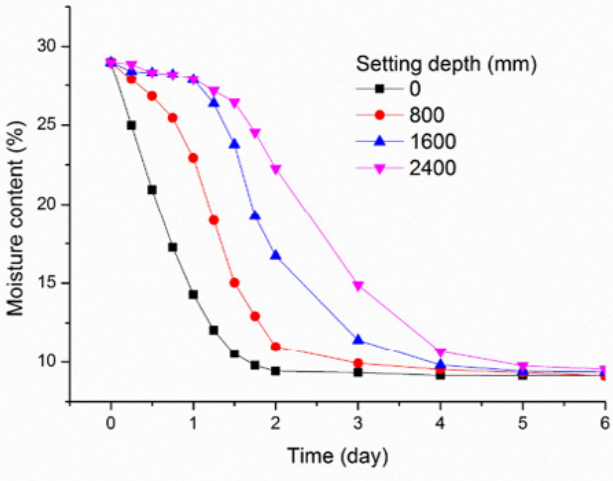

Figure 4. Drainage process at different soil moisture content depths.

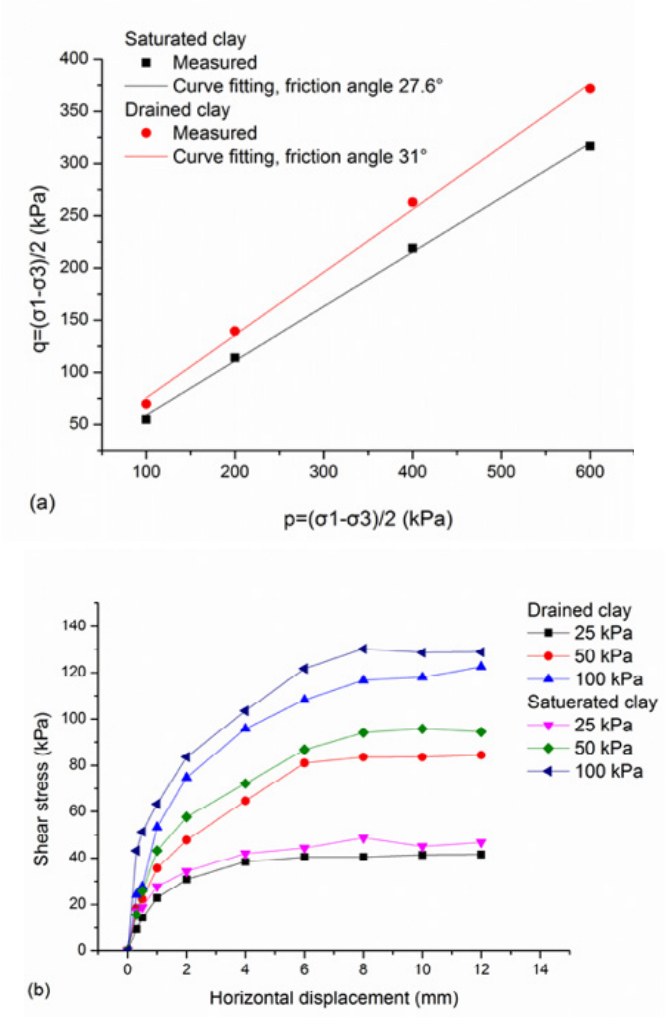

Figure 5. Properties of the soil used in the experiment: (a) results of CD triaxial tests performed on prepared soil samples and (b) p-q diagram of tested soil.

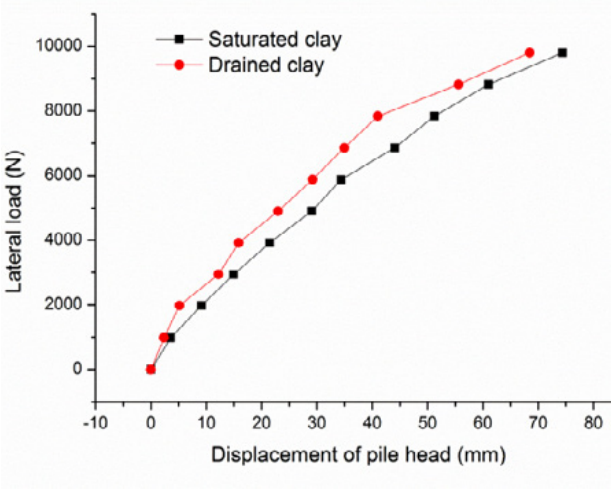

Figure 6. Lateral load-displacement curves at the pile head.

4 RESULTS

4.1 Load-displacement response at the pile head

Figure 6 shows the relationship between the measured lateral load and the pile-head displacement under saturated and unsaturated clay conditions. The figure shows that the lateral displacement of the pile head decreased with the increased *L/D*. Furthermore, as the load increased to 8330 N in the saturated clay, the displacement rate of the pile head increased; when the load increased to 9310 N after soil drainage, the pile-head displacement increased faster.

4.2 Strain along the pile length

The bending moments of the model pile can be calculated using Eq. (1) and the measurement results of the resistance strain gauges distributed along the pile length.

$$M_i = \frac{E \cdot \varepsilon \cdot I_i}{y} \qquad (1)$$

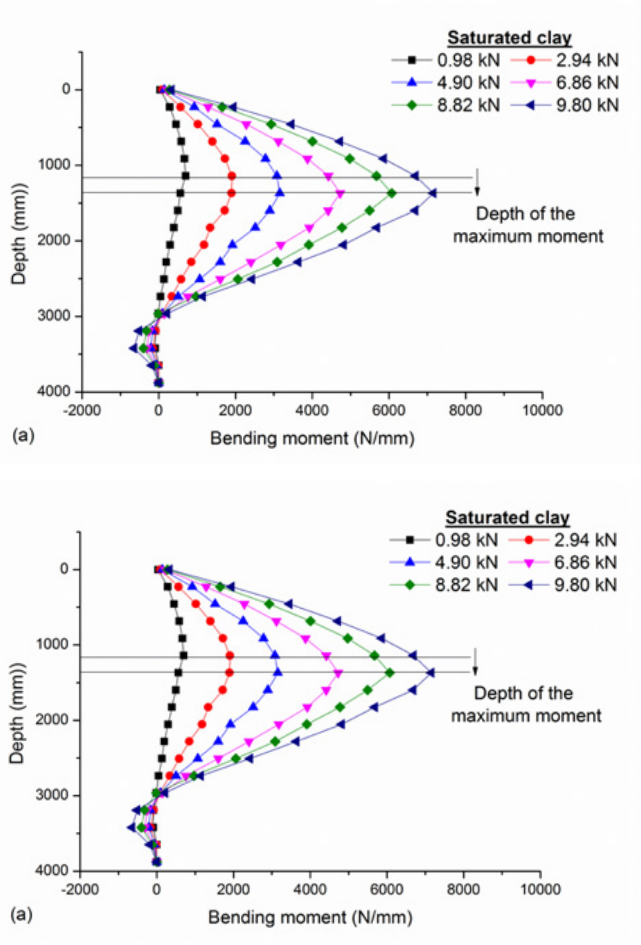

Figure 7. Bending-moment variation along the pile depth at different loading stages: (a) in saturated clay and (b) in drained clay.

where E is the elastic modulus of the model pile, Pa; ε is the strain value; I_i is the sectional moment of inertia, m4; and y is the resistance strain gauge distance from the neutral axis of the pile, m.

Figure 7 shows the lateral loading of the pile versus the bending moment in saturated and drained clays. The maximum peak moment of the pile was 7158 N·m (less than $[M]$) as the lateral load increased to 9.8 kN in the saturated soil. The depth of the maximum moment increased from 1140 to 1368 mm, and the zero point of the bending moment appeared 3 m below the surface of the mud.

In the drained soil samples, the maximum bending moment was 25% greater than that in the saturated soil. For the increased lateral load of 8.82 kN, the pile body appeared to undergo plastic deformation, and the depth of the maximum moment point was 1140 mm and did not increase further. As the lateral load was increased from 8.82 to 9.8 kN, the lateral displacement of the pile increased greatly. The same pile reached the plastic point earlier with a smaller load in the drained clay.

4.3 Pile-soil interaction along the pile length

In this study, the soil resistance of the piles was directly measured using soil-pressure sensors. The soil resistance can be calculated according to Eq. (2).

$$p = \mu\varepsilon \cdot K \qquad (2)$$

The p-y curve is a comprehensive index of the soil resistance around a pile. It is affected by the pile diameter, the stiffness, the cross-sectional shape, the size effect, and the pile end constraints. Soil resistance is normally calculated using an empirical formula; however, this result usually contains a large error. In fact, many studies have reported instances in which the p-y analysis results did not match the measured soil reaction profiles [13, 25].

Fig. 8 summarizes the measurements obtained using soil-pressure sensors installed along the pile length. Both figures show that the soil resistance increased as the applied lateral load increased.

Figure 9 shows the pile displacement during loading as measured using an inclinometer sensor and pile-head

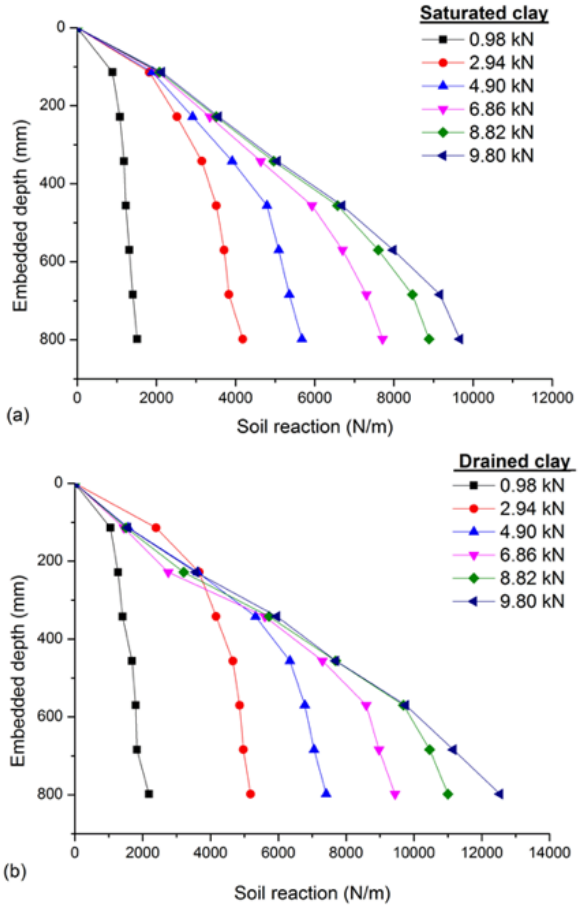

Figure 8. Measured soil reaction along the pile length at different loading stages: (a) in saturated clay and (b) in drained clay.

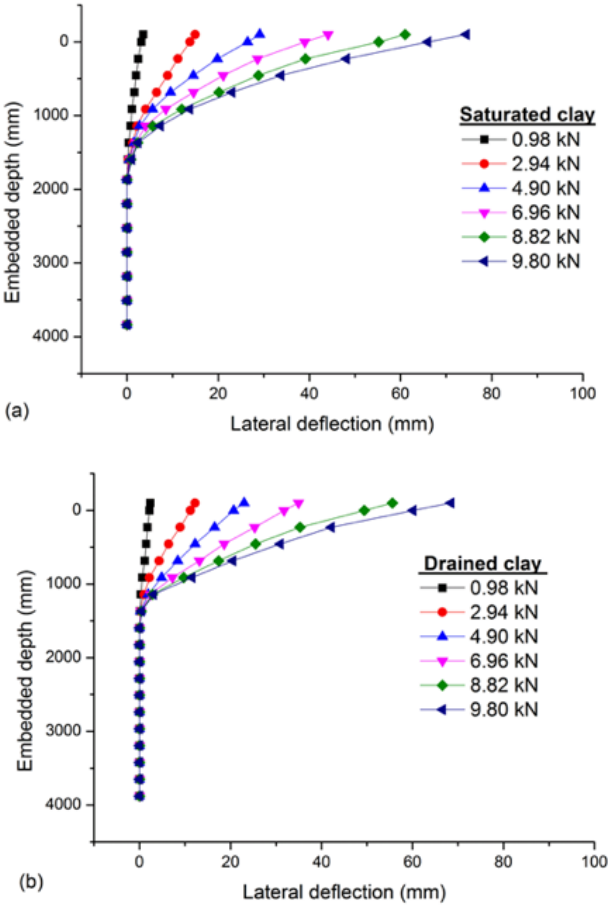

Figure 9. Lateral movement along the pile length at different loading stages: (a) saturated clay and (b) drained clay.

displacement sensor. In saturated soil, the loading point is located 100 mm above the mud line; the displacement at the top of the pile reaches 74.4 mm under a 9.8-kN lateral load, that at the mud surface is 66.0 mm, and a 10-mm bulge is seen on the mud surface with cracking. In drained clay, the lateral pile displacement is always lower than that in the saturated soil. The maximum displacement at the mud surface is 60.5 mm.

4.4 Soil-pile interaction force-displacement relationships (p-y curves)

The soil-pile interaction force per unit length (p) shown in Fig. 8 and the pile lateral displacement (y) shown in Fig. 9 were combined to produce directly measured p-y curves. Figure 10 shows directly measured p-y curves covering the pile length. The results show that the p-y curves increase with depth. There is no significant difference in the strength of shallow soils at depths of less than 228 mm. The soil resistance of the pile in drained clay is significantly reduced by a displacement of more than 15 mm with a 40% drop. This may be because of the shallow soil cracking caused by excessive pile displacement. However, in saturated clay, the soil resistance of the pile was not reduced. When the displacement reached 12 mm, the soil resistance became constant. In deeper soil layers, the soil resistance around the pile increased with the displacement, and the rate of increase was faster in drained clay, reflecting the increase in soil resistance after the clay drainage.

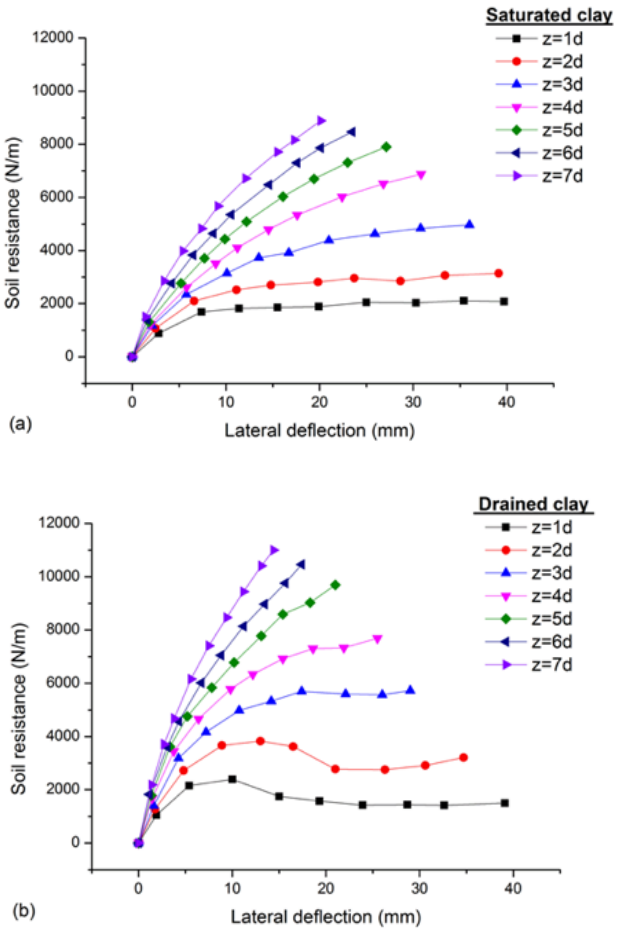

Figure 10. Relationship between the soil resistance and the displacement along the pile length at different depths: (a) pile in saturated clay; and (b) pile in drained clay.

5 DISCUSSION

Broms, Reese, Fleming, and Kim have established a model for the ultimate soil resistance around piles. In this study, the soil resistance was directly measured through a horizontal displacement experiment, and the soil resistance in drained clay was found to be increased compared with the initial value. The curve of the overlapping parts of the soil resistance at different loading stages is approximately a straight line. Figure 5 shows the measured soil friction angle (saturated soil friction angle φ_1=27.56°, drained clay friction angle φ_2=30.96°). According to Rankine's earth-pressure-calculation model, the ultimate resistance of the saturated and drained clay was expressed by Eqs. (3) and (4), respectively.

$$p_u = 4.76k_p \cdot \gamma \cdot z \qquad (3)$$

$$p'_u = 5.97k_p \cdot \gamma \cdot z \qquad (4)$$

Here, k_p is the passive earth-pressure coefficient (studies recommend a value of 3–9; [9, 14]); γ is the average effective weight of soil; and z is the embedded depth. The results reported in this study are ~24% lower than that

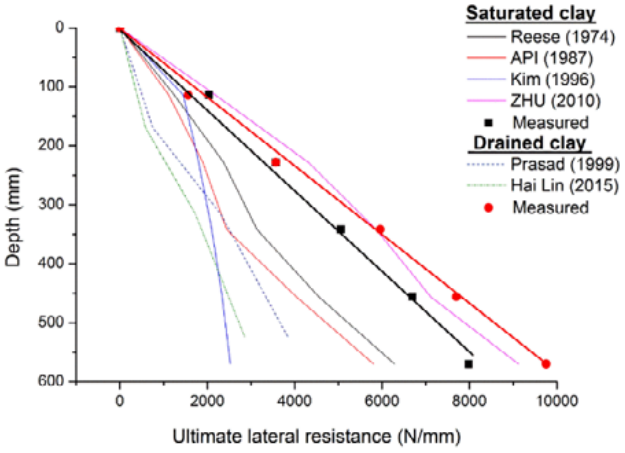

Figure 11. Comparison of the directly measured soil resistance at several depths and the p-y curves from other methods.

measured by Zhu [26] in saturated clays. The measured soil resistance in drained clay is up to 189% greater than that in unsaturated clay, as measured by Prasad and Chari [8]. The soil resistance in drained clay increased by 27% compared to that in saturated clay. At a depth of 114 mm the measured soil resistance deviated from the fitting curve; this is considered to be attributable to the bulging and cracks in the surface layer.

The directly measured p-y curves were compared with the p-y curves back-calculated from the measured strain profiles along the pile depth, which were obtained from the beam on elastic foundation theory. The measured bending moment of the pile was fitted by a sixth-order polynomial [26]. The soil resistance was calculated as $p(x) = d^2M / dx^2$. The soil resistance and pile lateral displacement at different loading stages were calculated as shown in Fig. 12. When compared with the back-calculated p-y curves at several depths along the pile length, the directly measured ultimate soil resistance per unit length showed smaller values than those back-calculated using the strain measurements. The difference was greater at depths closer to the maximum bending moment of the pile. The measured soil resistance at a depth of 798 mm was 37% smaller than the back-calculated one at a lateral load of 9.8 kN (Fig.12(a)). The difference in the soil resistance between the measured and back-calculated in drained clay was greater, up to 82%.

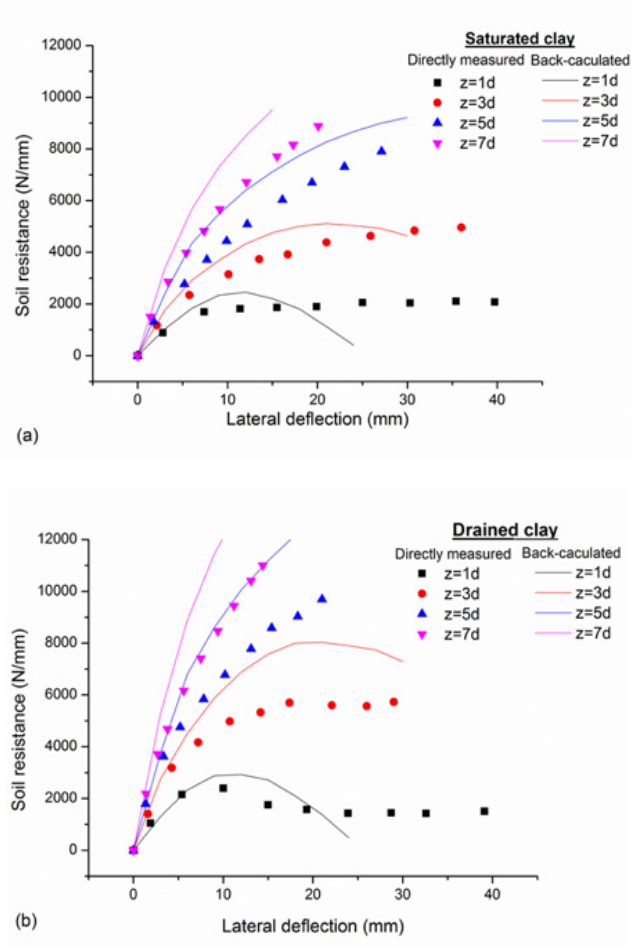

Figure 12. Comparison of the directly measured and the back-calculated p-y curves at several depths: (a) in saturated clay; and (b) in drained clay.

6 CONCLUSIONS

At present, the pile displacement, the bending moment, and the soil resistance around a pile are considered to be interrelated. Furthermore, several methods have been established for calculating the soil resistance around piles based on the displacement and bending moment. However, the measured results presented in this paper show that the results calculated by previous methods are not accurate, owing to the nonlinear characteristics of the soil.

The maximum bending moment depth of a pile first increases with the load and then remains constant, with the bottom of the pile fixed. When the pile body undergoes plastic deformation, the bending moment increases sharply; however, the soil resistance does not increase significantly, the pile still has a horizontal bearing capacity, and the level of deformation at this time increases significantly.

For bottom-fixed piles, the value of the maximum bending moment of the pile body in drained clay is greater for the same load, and the maximum bending moment depth is smaller. The lateral load-bearing capacity of the pile is greater than the initial value in saturated clay.

According to the test results, a model for the ultimate soil resistance of saturated and drained clays was established. The ultimate soil resistance of these two types of clay differed by 27%, and both increased linearly with depth. At a depth of 114 mm the measured soil resistance test deviated from the fitting curve. This is considered to be attributable to the bulging and cracks in the surface layer.

Although the bending moment of the pile is related to the soil resistance, there is a large error in building the polynomial anti-calculation soil resistance using the bending moment of the pile body. The back-calculated results of the soil resistance near the maximum bending moment depth deviate significantly from the measured values. This soil-resistance calculation method does not consider the fact that the distribution of the stiffness and the bending moment of the pile along the pile body is inconsistent with the distribution of the soil resistance along the depth.

REFERENCES

[1] Cheng, X., Jing, W., Yin, C., Li, C. 2018. Stability parameter analysis of a composite foundation of an oil storage tank in a loess area treated with compaction piles. Soils and Foundations, 58(2), 306-318. https://doi.org/10.1016/j.sandf.2018.02.004.

[2] Tananykhin, D., Tcvetkov, P., Kamoza, V. 2018. Wells. Journal of Physics: Conf. Series, 1072, 012022. https://doi.org/10.1088 / 1742-6596 / 1072/1/012022.

[3] Shagiakhmetov, A., Tananykhin, D., Terleev, A. 2018. Development of water-shutoff composition on the basis of carboxymethyl cellulose for fractured and fractured-porous oil and gas reservoirs. Acta Technica CSAV (Ceskoslovensk Akademie Ved), 63 (3), 475-480

[4] Brinch-Hansen, J. 1961. The ultimate resistance of rigid piles against transversal forces. Bulletin Representative No. 12, Danish Geotechnical Institute, Copenhagen, Denmark, 5-9.

[5] Reese, L.C., Cox, W.R., Koop, F.D. 1974. Analysis of laterally loaded piles in sand. Proceedings of the 6th Annual Offshore Technology Conference, Houston, Texas 2(OTC 2080), 473-485.

[6] Wesselink, B.D., Murff, J.D., Randolph, M.F., Nunez, I.L., Hyden, A.M. 1988. Analysis of centrifuge model test data from laterally loaded piles in calcareous sand. Engineering for calcareous sediments 1, 261-270.

[7] Yan, L., Byrne, P.M. 1992. Lateral pile response to monotonic pilehead loading. Canadian Geotechnical Journal 29, 955–970. https://doi.org/10.1139/t92-106.

[8] Prasad, Y.V., Chari, T.R. 1999. Lateral capacity of model rigid piles in cohesionless soils. Soils and Foundations 39(2), 21-29. https://doi.org/10.3208/sandf.39.2_21.

[9] Poulos, H.G., Davis, E.H. 1980. Pile foundation analysis and design. New York: John Wiley & Sons.

[10] Fleming, K., Weltman, A., Randolph, M., Elson, K. 2014. Piling engineering. CRC press.

[11] McClelland, B., Focht, J.A. 1958. Soil modulus for laterally loaded piles. Transactions, ASCE, 123, 1071-1074.

[12] Ashour, M., Norris, G. 2000. Modeling lateral soil-pile response based on soil-pile interaction. Geotechnique 126(5), 420–427. https://doi.org/10.1061/(ASCE)1090-0241.

[13] Matlock, H., Reese, L.C. 1960. Generalized solutions for laterally loaded piles. Soil Mech Found Division ASCE 86(5), 63-91.

[14] American Petroleum Institute. 1987. Recommended practice for planning, designing and constructing fixed offshore platforms. 17th ed. Washington D C: American Petroleum Institute, API-RP2A.

[15] O'Neill, M.W., Murchinson, J.M. 1983. An evaluation of p-y relationships in sand. Washington D C: American Petroleum Institute.

[16] Kondner, R.L. 1963. Hyperbolic stress-strain response: Cohesive soils. Journal of Soil Mechanics and Foundation Division 89(1), 115-144.

[17] King, G.J.W. 1994. The interpretation of data from tests on loaded piles. Centrifuge 94, 515-520.

[18] Duan, W.F., Liao, X.H., Jin, J.S., Wang, Y.Q. 2001. Numerical modeling of pile-soil interface and numerical analysis of single pile QS curve. Journal of Harbin University of Civil Engineering and Architecture 5, 007.

[19] Yinao, G.Z.S.K.S., Zhichuan, G., Kanhua, S. 2009. Analysis on lateral load-bearing capacity of conductor and surface casing for deepwater drilling. Acta Petrolei Sinica 2, 024.

[20] Kim, Y., Jeong, M.S., Lee, S. 2011. Wedge failure analysis of soil resistance on laterally loaded piles in clay. Geotech Geoenviron Eng 137(7), 678–694. https://doi.org/10.1061/(ASCE)GT.1943-5606.0000481.

[21] Yang, H.P., Zhang, R., Zheng, J.L. 2006. Variation of deformation and strength of expansive soil during cyclic wetting and drying under loading condition. Yantu Gongcheng Xuebao (Chinese Journal of Geotechnical Engineering) 28(11), 1936-1941.

[22] British Standards 1377. 1990. Parts 1 to 8 - Methods of Test for Soils Civil Engineering Purposes. British Standards Institution, London.

[23] Boominathan, A., Ayothiraman, R. 2007. Measurement and analysis of horizontal vibration response of pile foundations. Shock Vib 14(2), 89-106.

[24] Rao, S.N., Ramakrishna, V.G.S.T., Rao, M.B. 1998. Influence of rigidity on laterally loaded pile groups in marine clay. Journal of Geotechnical and Geoenvironmental Engineering 124(6), 542-549. https://doi.org/10.1061/(ASCE)1090-0241.

[25] Muthukkumaran, K. 2013. Effect of slope and loading direction on laterally loaded piles in cohesionless soil. International Journal of Geomechanics 14(1), 1-7. https://doi.org/10.1061/(ASCE)GM.1943-5622.0000293.

[26] Zhu, B., Zhu, R.Y., Luo, J., Chen, R., Kong, L. 2010. Model tests on characteristics of ocean and offshore elevated piles with large lateral deflection. Chinese Journal of Geotechnical Engineering 32(4), 521-530.

EFFECTS OF GRADATION ON THE MOBILIZED FRICTION ANGLE FOR THE INSTABILITY AND STEADY STATES OF SAND-SILT MIXTURES: EXPERIMENTAL EVIDENCE

VPLIVI ZRNAVOSTI NA MOBILIZIRANI KOT TRENJA V NESTABILNEM IN STABILNEM STANJU MEŠANIC PESKA IN MELJA: EKSPERIMENTALNI DOKAZ

Abdellah Cherif Taiba
University of Chlef,
Laboratory of Material Sciences & Environment
Algeria
E-mail: a.cheriftaiba@univ-chlef.dz

Youcef Mahmoudi
University of Chlef,
Laboratory of Material Sciences & Environment
Algeria

Leila Hazout
Saâd Dahlab University of Blida,
Algeria

Wiebke Baille
Bochum Ruhr University,
Laboratory of Foundation Engineering, Soil and Rock Mechanics
Bochum, Germany

Mostefa Belkhatir
University of Chlef,
Laboratory of Material Sciences & Environment
Algeria

DOI https://doi.org/10.18690/actageotechslov.16.1.79-95.2019

Keywords
mobilized instability friction angle, mobilized steady state friction angle, gradation, confining pressure, sand-silt mixtures

Ključne besede
mobilizirani kot trenja v nestabilnem stanju, mobilizirani kot trenja v stabilnem stanju, zrnavost, bočni tlak, mešanice peska in melja

Abstract

This paper deals with a laboratory study of the influence of low-plastic-fines content and grading characteristics on the instability and steady-state friction angle of sand-silt mixtures under monotonic loading conditions. For this purpose, a series of compression undrained triaxial tests were carried out on Chlef sand (Algeria) mixed with low plastic fines (I_p=5%) ranging from F_c=0% to F_c=30%. The samples were prepared in the laboratory with the dry--funnel-pluviation method and subjected to three different confining pressures (P_c'=100 kPa, 200 kPa and 300 kPa). The obtained results indicate that the fines content, void ratio and gradation have a significant influence on the mobilized friction angle for the instability and steady state of the sand-silt mixtures and confirm the existence of simple correlations between the mobilized instability

Izvleček

Prispevek obravnava laboratorijsko študijo vpliva finih delcev nizke plastičnosti in karakteristik zrnavosti na kot trenja v nestabilnem in stabilnem stanju za mešanice peska in melja pri monotonih obtežnih pogojih. V ta namen smo izvedli niz kompresijskih nedreniranih triaksialnih preizkusov na pesku Chlef (Alžirija), mešanih z drobnimi delci nizke plastičnosti (I_p=5%), z vsebnostjo finih delcev od F_c=0% do F_c=30%. Vzorci so bili pripravljeni v laboratoriju s postopkom suhega odlaganja pri treh različnih bočnih tlakih (P_c'=100 kPa, 200 kPa in 300 kPa). Dobljeni rezultati kažejo, da vsebnost finih delcev, količnik por in zrnavost pomembno vplivajo na mobilizirani kot trenja pri nestabilnem in stabilnem stanju mešanice peska in melja ter potrjujejo obstoj enostavnih korelacij med mobiliziranim kotom trenja v nestabilnem

and steady-state friction angles and granulometric characteristics (D_{10}, D_{30}, D_{50}, D_{60}, and C_u) of the soils under consideration. The introduced new granulometric characteristics ratios [effective diameter ratio (D_{10R}=D_{10sand}/$D_{10mixture}$), the mean grain size ratio (D_{50R}=D_{50sand}/$D_{50mixture}$), and the coefficient of uniformity ratio (C_{UR}=C_{usand}/$_{Cumixture}$)] appear as pertinent factors for the prediction of the mobilized friction angle of the sand-silt mixtures for the soil gradation under study.

Abbreviations:

a and c	constants of the Equation
B	Skempton pore-pressure coefficient
γ_s	Unit weight of grains
C_u	Coefficient of uniformity
C_{UR}	Coefficient of uniformity ratio ($C_{UR} = C_{usand}/C_{umixture}$)
C_c	Coefficient of gradation
D	Diameter of the sample
D_{10}	Effective diameter
D_{10R}	Effective diameter ratio ($D_{10R} = D_{10sand}/D_{10mixture}$)
D_{30}	Grain size corresponding to 30% finer
D_{50}	Mean grain size
D_{50R}	Mean grain size ratio ($D_{50R} = D_{50sand}/D_{50mixture}$)
D_{60}	Grain size corresponding to 60% finer
D_{max}	Maximum diameter of the grain
D_r	Initial relative density
e_{max}	Maximum global void ratio
e_{min}	Minimum global void ratio
e	Global void ratio
e_g	Intergranular void ratio
F_c	Fines content
G_s	Specific gravity
H	Height of the sample
H/D	Height-to-diameter ratio of the sample
I_p	Plasticity index
ML	Low plastic silt
P_c'	Initial confining pressure
q_{max}	Maximum shear strength
R^2	Coefficient of determination
SP	Poorly graded sand
SSL	Steady-state line
$USCS$	Unified Soil Classification System
V_T	Total volume
Φ_{ins}	Mobilized instability friction angle [$\sin\Phi_{ins} = (3\ \acute{\eta}_{ins}) / (6+\ \acute{\eta}_{ins})$]
Φ_{ss}	Mobilized steady-state friction angle [$\sin\Phi_{ins} = (3\ \acute{\eta}_{ins}) / (6+\ \acute{\eta}_{ins})$]
$\acute{\eta}_{ins}$	Instability stress ratio
M_{ss}	Steady-state ratio
Δu_{max}	Maximum positive excess pore-water pressure
ε_a	Axial strain

in stabilnem stanju ter granulometrijskimi karakteristikami. (D_{10}, D_{30}, D_{50}, D_{60}, in C_u) obravnavanih zemljin. Uvedena nova razmerja granulometrijskih lastnosti [razmerje efektivnega premera (D_{10R}=D_{10sand}/$D_{10mixture}$e), razmerje srednje velikosti zrn (D_{50R}=D_{50sand}/$D_{50mixture}$e) in razmerje koeficienta enakomernosti (C_{UR}=C_{usand}/$_{Cumixture}$)] predstavljajo ustrezne faktorje za predvidevanje mobiliziranega kota trenja mešanic peska in melja za obravnavano zrnavost zemljin.

1 INTRODUCTION

The northern part of Algeria is located on the boundary between the African and the Eurasian Plates. Therefore, there is a developing compressional area triggering several thrusts and faults. Several earthquakes occurred in this area due its location between the two tectonic plates. The recorded seismic activities over the last century in Algeria include the 1980 El-Asnam earthquake, where the liquefaction phenomenon appeared along the Chlef River banks (Figure 1). This earthquake was one of the most disastrous earthquakes, with a Richter Magnitude, M_L= 7.2, corresponding to a Surface Wave Magnitude, M_s = 7.3 to hit Chlef City and the surrounding areas on October 10, 1980 causing lateral spreading, flow failures, ground fissures and subsidence, sand boils, and slope failures. The earthquake epicenter of the main shock was located 12 km in the east region of Chlef City (210 km west of Algiers) at a latitude of 36.143°N and a longitude of 1.413°E with a focal depth of about 10 km. The approximate duration of the quake was between 35 and 40 s. The event, commonly referred to as the Chlef Earthquake, was among the most disastrous earthquakes to have affected the northern region of Algeria. The earthquake devastated the city of Chlef, population estimated at 125,000, and the nearby towns and villages. The large loss of life (reportedly 5,000–20,000 casualties) and property was attributed to the collapse of buildings. In several places in the affected area, especially along the Chlef river banks, great masses of sandy soils were ejected on to the ground surface level. This earthquake caused extensive damage to many civil engineering and hydraulics structures [7].

2 LITERATURE REVIEW

Liquefaction-induced ground failure due to the loss of the undrained shear strength is a major cause of damage to civil engineering and hydraulics structures such as buildings, tunnels, earth dams, bridges, nuclear reactors, etc. Liquefaction is a natural phenomenon that takes place in saturated sand and silty sand soil deposits subjected to static and dynamic loading conditions. The

experimental research regarding this phenomenon is usually linked to studying the variation of the excess pore-water pressure of silty sand soils. Liquefaction of sandy soils occurs due to an increase in the pore-water pressure and consequently to a significant decrease in the soil's effective stress, inducing the excessive settlement of buildings, landslides, failures of earth dams, etc. The understanding of the liquefaction phenomenon (loss of undrained shear strength) has significantly improved in recent years. Most liquefaction research was undertaken on clean sands, with the assumption that the behavior of silty sand is similar to that of clean sand. The published literature reports many liquefaction cases of sand and silty sand inducing different forms of soil-deposits subsidence failures observed during the 1964 Niigata (Japan) and Alaska (USA) earthquakes.

Several researches have considered different parameters affecting the soil-liquefaction phenomenon, such as the relative density, sample preparation, grain size and shape, grading characteristics, confining pressure, stress history, etc. [6, 8, 12, 14, 15, 16, 24, 25, 27, 30, 40]. The influence of the low-plastic-fines fraction is of major interest when assessing the undrained shear strength (liquefaction resistance) response of sand-silt mixture soils. However, the published literature reveals contradictory results about the effect of low-plastic-fines content on the liquefaction susceptibility of soil deposits [7, 8, 11, 12, 22, 23 and 26]. Table 1 summarizes most of the published work related to the influence of fines content and particle gradation on the liquefaction resistance of sand and silty sand soils.

One of the most important effects of silt on the behavior of sand and sand-silt mixtures is the effect on the stress path in terms of instability and steady states. The instability and steady states appear as pertinent parameters to identify the mechanical response of sand or sand-silt mixtures. The instability introduced by [34] is based on the collapse line, *CL*, as a straight line joining the peak points of the undrained effective stress path. The authors of [19] introduced the instability line, *IL*, as the one that joins the peak points of the undrained effective stress path, *ESP*, for the same void ratio, and it passes through the origin of stress space (Figure 2). Reference [3] defined the instability as a catastrophic failure phenomenon of loose saturated granular soils when the soil fails to sustain the current stress state and results in run off deformation.

Moreover, the steady state appears at medium-to-large deformations during the undrained shearing of silty sand. An assessment of the steady-state strength of soils based on static triaxial tests has been considered in previous studies [10, 16], where the soil's behavior can be expressed by the determination of the mobilized friction angle with the current proximity of the steady-state slope using the following equation:

$$\left[\sin\left(\Phi_{ss}\right)=\left(3M_{ss}\right)/\left(6+M_{ss}\right)\right] \qquad (1)$$

where M_{ss} is the steady-state slope or the steady-state ratio and Φ_{ss} is the mobilized friction angle at the steady state (*SS*). A better understanding of the instability and steady states of sand-silt mixtures is very important because of the wide distribution and common engineering problems of these materials. Moreover, [13, 26] indicated that the instability stress and steady-state ratios decrease linearly with a decrease in the maximum shear strength and an increase in the maximum excess pore-water pressure for Fontainebleau sand-silt mixtures. In addition, the fines content and void ratios, such as the initial void ratio and the intergranular void ratio, have a significant influence on these soil parameters, where the instability stress and steady-state ratios decrease with a decrease in the initial void ratio and an increase of the intergranular void ratio and fines content for the tested materials.

In the literature, few studies have reported the influence of low-plastic-fines content and grain size in terms of granulometric characteristics on the instability and steady-state friction angle of sand or silty sand soils from triaxial compression tests. For this purpose, the present experimental research work was performed to evaluate the effects of the gradation characteristics (D_{10}, D_{30}, D_{50}, D_{60} and C_u) and the granulometric characteristics ratios [($D_{10R} = D_{10sand}/D_{10mixture}$), ($D_{50R} = D_{50sand}/D_{50mixture}$), and ($C_{UR} = C_{usand}/C_{umixture}$)] and low plastic fines on the mobilized friction angle for the instability and steady states of Chlef silty sand samples reconstituted

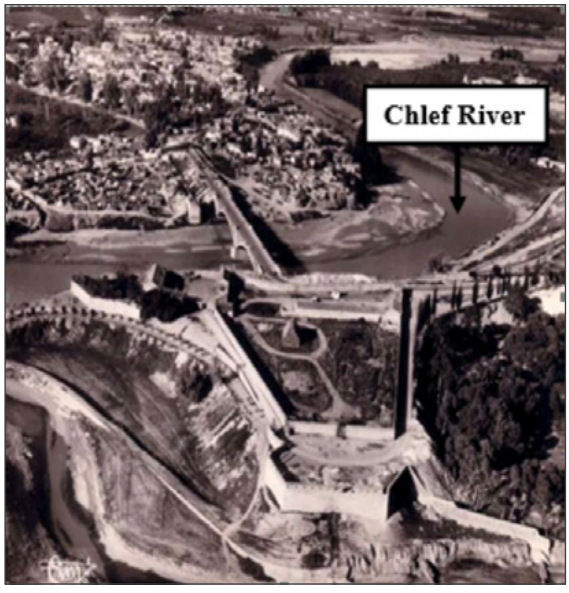

Figure 1. Location of the Chlef River.

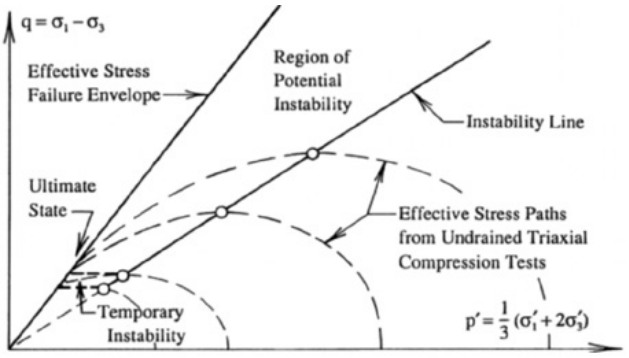

Figure 2. Schematic diagram of the location of the instability line in the (p', q) stress plane [19].

in the laboratory with the same silty fines fraction ranging from F_c=0% to 30 % at an initial relative density (D_r=52%) and subjected to three confining pressures (P_c'=100 kPa, 200 kPa and 300 kPa).

3 EXPERIMENTAL PROGRAM

3.1 Index properties of the tested materials

The laboratory tests were performed on Chlef sand (Algeria) "rounded shape" mixed with low-plastic Chlef silty fines "rounded shape" contents ranging from F_c=0% to F_c= 30%. A microscopic view of the tested materials is shown in Figure 3. The index properties of the materials

Table 1. Summary of the literature related to the effect of fines content and gradation on the liquefaction resistance of sand and silty sand soils.

Findings	References
The addition of low-plastic-fines particles up to 40% leads to more strain hardening of the sand-silt mixtures.	[31]
The strain softening seems to be more pronounced as the fines content increases up to 30%.	[17]
A continuous decrease in the peak shear strength up to a 50% fines content.	[5]
The peak shear strength decreases until the fines content reaches a threshold value and then it increases with a further increase in the low-plastic-fines fraction.	[39]
The grain size distribution of the soil affected considerably the cyclic liquefaction resistance response at lower relative densities in a manner that poorly graded samples have lower values compared to well-graded samples.	[36]
For clean sands, the obtained cyclic liquefaction resistance increases as the mean grain size (D_{50}) increases.	[32]
The liquefaction resistance is not considerably influenced by the mean grain size (D50) for the tested materials with D_{50} > 0.25 mm.	[32]
It was possible to establish a correlation between the cyclic resistance and the openings (D_{10}, D_{30}, and D_{50}) rather than with the coefficient of uniformity (C_u) or the coefficient of curvature (C_c).	[40]
If the mean grain size ratio ($D_{50\text{-}sand}/d_{50\text{-}silt}$) of the sand-to-silt particles is sufficiently small, the liquefaction potential of the sand increases steadily with increasing fines content for the selected range (0–20%). As $D_{50\text{-}sand}/d_{50\text{-}silt}$ increases, the liquefaction potential of the silty sand might actually be less than the liquefaction potential of the clean sand.	[28]
The undrained shear strength at the peak and the undrained residual shear strength can be correlated to the mean grain size (D_{50}) and the coefficient of uniformity (C_u).	[6]
For samples with the same relative density, the undrained shear strength and the phase transformation deviatoric stress gradually decrease with the increasing of the coefficient of uniformity C_u.	[21]
The granulometric characteristics have a significant effect on the generation of the excess pore-water pressure in the sand-silt mixture samples and the D_{10R} and D_{50R} appeared as pertinent parameters to predict the excess pore-water pressure response of the sand-silt mixtures for soil gradation.	[8]
The gradation and particle shape have a significant influence on the undrained shear strength (liquefaction resistance) of two silty sand soils under study. Moreover, their test results confirm the existence of simple correlations between the liquefaction resistance and the different grading characteristics (D_{10}, D_{30}, D_{50}, D_{60}, C_u, D_{10R}, D_{50R} and C_{UR}) of the soils under consideration.	[11, 12]
The liquefaction resistance of clean sand decreases with the decrease of D50 sand and Cusand with the same relative density for loose samples; however, the undrained shear strength of silty sand soils decreases with an increase of the coefficient of uniformity (C_u).	[29]
The instability stress and steady-state ratios can be correlated with the grading characteristics (D_{10}, D_{30}, D_{50}, D_{60}, C_u, D_{10R}, D_{50R} and C_{UR}). Indeed, they decrease in a logarithmic and linear manner with a decrease in the grain size (D_{10}, D_{30}, D_{50}, D_{60}) and an increase in the fines content, respectively. However, they decrease logarithmically with an increase in the coefficient of uniformity for the different graded sand-silt mixtures.	[13]

under study are presented in Table 2 and Table 3. The granulometric curves of the tested silty sand samples are shown in Figure 4. The maximum void ratio (e_{max}) corresponding to the loosest state of the soil sample and the minimum void ratio (emin) corresponding to the densest state of the soil sample were determined according to the [1] and [2] standards for 0–100% range of fines content (F_c). Vibratory-table [1] and standard and modified Proctor tests were used to determine the minimum index void ratio (e_{min}) for all the sand-silt mixtures in the study. The vibratory-table tests yielded minimum index void ratios similar to those produced by the modified Proctor test. The vibratory-table test minimum index void ratios were used in this laboratory investigation. The maximum index void ratios (e_{max}) for the different sand–silt mixtures were determined in general accordance with the specification [2], despite its limitation to a 15 % fines content. According to Figure 5, the extreme void ratios (e_{max} and e_{min}) decrease with an increase of the fines content up to F_c = 30%. This decrease could be explained by the fact that the silty grains act as voids and consequently the limit index void ratios of the sand–silt mixtures decrease. Beyond that, they increase with an increase of the fines content. The index void-ratios increase indicates clearly that the silty fines participate effectively in the structure of the sand-silt mixture.

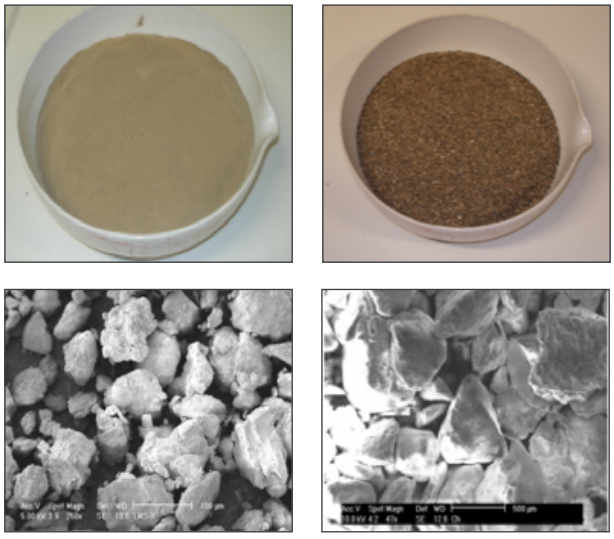

(a) (b)

Figure 3. Microscopic view of tested materials (a) Chlef silt (b) Chlef sand.

Table 2. Index properties of sands and silt.

Properties	Materials	
	Chlef sand	Chlef silt
G_s	2.652	2.667
D_{max} (mm)	2.000	0.080
D_{10} (mm)	0.266	0.003
D_{50} (mm)	0.596	0.032
D_{30} (mm)	0.431	0.013
D_{60} (mm)	0.700	0.04
C_u (-)	2.634	13.33
C_c (-)	0.999	1.40
e_{max} (-)	0.795	1.563
e_{min} (-)	0.632	0.991
e (-)	0.710	1.266
e_g (-)	0.710	-
W_L (%)	-	31.72
W_p (%)	-	26.71
I_p (%)	-	5.01
USCS	*SP*	*ML*
Grain Shape	Rounded	Rounded

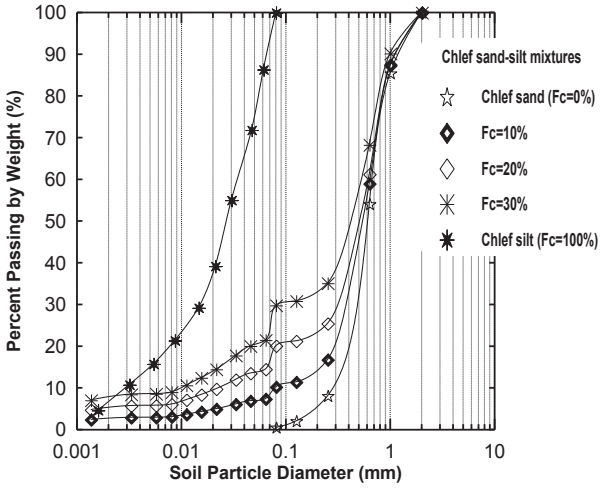

Figure 4. Grain size distribution of the tested materials.

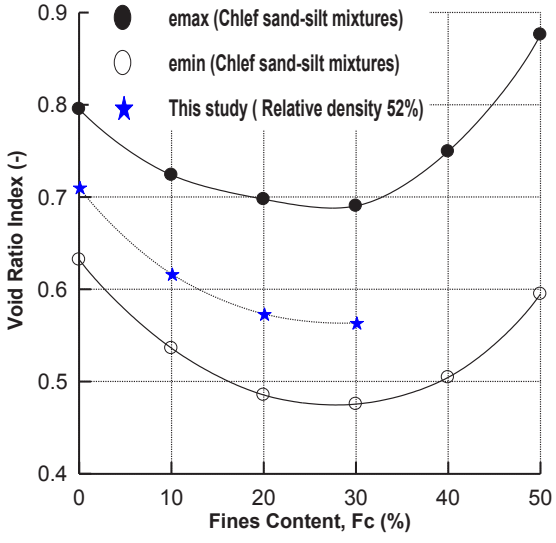

Figure 5. Voids-ratio index of the silty sands versus fines content.

3.2 Samples Preparation

Numerous studies have reported that the behaviour of granular soils can be greatly influenced by the samples' reconstitution. Dry funnel pluviation is one of the most important techniques used in this study to replicate the in-situ characteristics of the sand-silt mixtures [9, 37, 7, 12, 24 and 26]. All the samples were produced with a diameter of 100 mm and a height of 200 mm, so that the height-to-diameter ratio of 2 was kept constant. This height-to-diameter ratio of 2 is chosen in order to minimize the effects due to the end platens of the apparatus and to reduce the likelihood of buckling during testing [4]. The samples were prepared with the help of a mould consisting of two semi-cylindrical shells. The two shells can be easily joined or embossed, one with the other, with the help of a hose clamp. In order to maintain the cuff made of latex along the partitions of the mould, four aspiration ducts are pierced in the conducted shells. These ducts communicate with the inside of the mould through rows of small holes. They are joined to flexible hoses that are assembled in a single tube. This tube can be connected to a vacuum pump. The mass of sand-silt mixtures put inside the mould with the help of the funnel is computed according to the required relative density (initial volume is known), and the state of the density of the sample is defined as:

$$m_s = \left(V_T * \gamma_s\right) / \left(1 + e_{\max}\left(1 - D_r\right) + D_r * e_{\min}\right) \qquad (2)$$

where D_r is the relative density, e is the target void ratio, e_{max} is the maximum global void ratio, e_{min} is the minimum global void ratio, γ_s is the solid grains' unit weight, m_s is the mass of the sample and V_T is the total volume.

3.3 Samples saturation

Saturation is an important stage in the experimental procedure because the response of the sample under undrained loading depends on its quality. To obtain a good degree of saturation, the technique proposed in [18] using carbon dioxide is elaborated. This technique consists of making the carbon dioxide circulate through the circuits of the drainage and the sample to slow down the water flow during the saturation phase., in order to occupy all the voids and to expel the air contained in the sample. Then, we make the de-aerated and demineralized water circulate to expel the interstitial gas and occupy its place. In spite of the passage of water, some voids remain occupied by the carbon dioxide. As the solubility of the CO_2 compound in air is increased, water can dissolve what remains of the carbon dioxide after its passage. It generally permits us to ensure a good saturation of the sample. In this study, after making the necessary measurements, the samples were first subjected to CO_2 for at least 30 min and then saturated with de-aired water. The degree of saturation was controlled by means of the Skempton pore-pressure parameter *B*. The samples were considered to be fully saturated if B is at least equal to or greater than 0.98. In this study, a back pressure of 200 kPa was applied during the tests to achieve the saturation state.

3.4 Consolidation and loading

After the saturation process, the samples were subjected to a confining pressure for the consolidation. During consolidation, the difference between the confining pressure and the backpressure was arranged such that for each sample the effective consolidation pressure was fixed equal to 100, 200 and 300 kPa. The choice of 100, 200 and 300 kPa for the confining stress as a mean value in geotechnical practice purposes was based on various research works existing

Table 3. Index properties of the tested materials.

Properties	Chlef sand-silt mixtures		
F_c (%)	10	20	30
G_s	2.654	2.655	2.657
D_{10} (mm)	0.078	0.023	0.010
D_{30} (mm)	0.369	0.235	0.087
D_{50} (mm)	0.549	0.488	0.420
D_{60} (mm)	0.643	0.614	0.535
D_{10R} (-)	3.39	11.79	26.99
D_{50R} (-)	1.087	1.223	1.42
C_{UR} (-)	0.321	0.097	0.048
C_u (-)	8.202	27.24	54.32
C_c (-)	2.699	3.997	1.438
e_{max} (-)	0.704	0.697	0.687
e_{min} (-)	0.536	0.458	0.449
e (-)	0.616	0.573	0.564
e_g (-)	0.796	0.966	1.234

Table 4. Summary of monotonic triaxial tests of silty sand.

Properties	Chlef sand-silt mixtures			
F_c (%)	0	10	20	30
q_{max} (100kPa)	363.4	330.7	118.5	57.4
q_{max} (200kPa)	398.6	363.3	259.3	128.8
q_{max} (300kPa)	564.9	384.3	316	207.3
Δu_{max} (100kPa)	65.1	68.4	77.1	85.75
Δu_{max} (200kPa)	139.6	147.9	156.4	166.4
Δu_{max} (300kPa)	206.8	226.7	239.4	246.9
Φ_{ins} (°)	38.02	37.59	36.86	36.42
Φ_{ss} (°)	56.83	55.59	55.4	54.07

in literature [4, 13]. In this study, all the undrained triaxial tests were undertaken at a constant strain rate of 0.2 mm per minute, which was slow enough to allow the pore-pressure change to equalize throughout the sample with the pore pressure measured at the base of the samples. All the tests were continued up to 25% axial strain.

4 MONOTONIC TEST RESULTS

4.1 Undrained compression loading tests of the Chlef sand-silt mixtures

Figures 6, 7, 8 and 9 present the undrained monotonic behavior of the Chlef sand-silt mixture samples reconstituted in the laboratory with low plastic fines (F_c=0%, 10%, 20% and 30%) at an initial relative density (D_r=52%). The normally consolidated samples (OCR=1) are subjected to three different initial confining pressures (P_c'=100 kPa, 200 kPa and 300 kPa). It was observed that the undrained shear strength tends to increase with an increase of the confining pressure from P_c'=100 kPa to P_c'=300 kPa. This is parallel to the finding of [9, 16, 25 and 41]. Thus, the liquefaction resistance increases as indicated in Figures 6a, 7a, 8a and 9a. The effect of the confining pressure on increasing the undrained shear strength (P_c'=100 kPa, 200 kPa and 300 kPa) is clearly observed for F_c=0% (q_{max}= 363.49 kPa, q_{max}=398.69 kPa, q_{max}= 564.90 kPa) and becomes very pronounced for the other fines contents

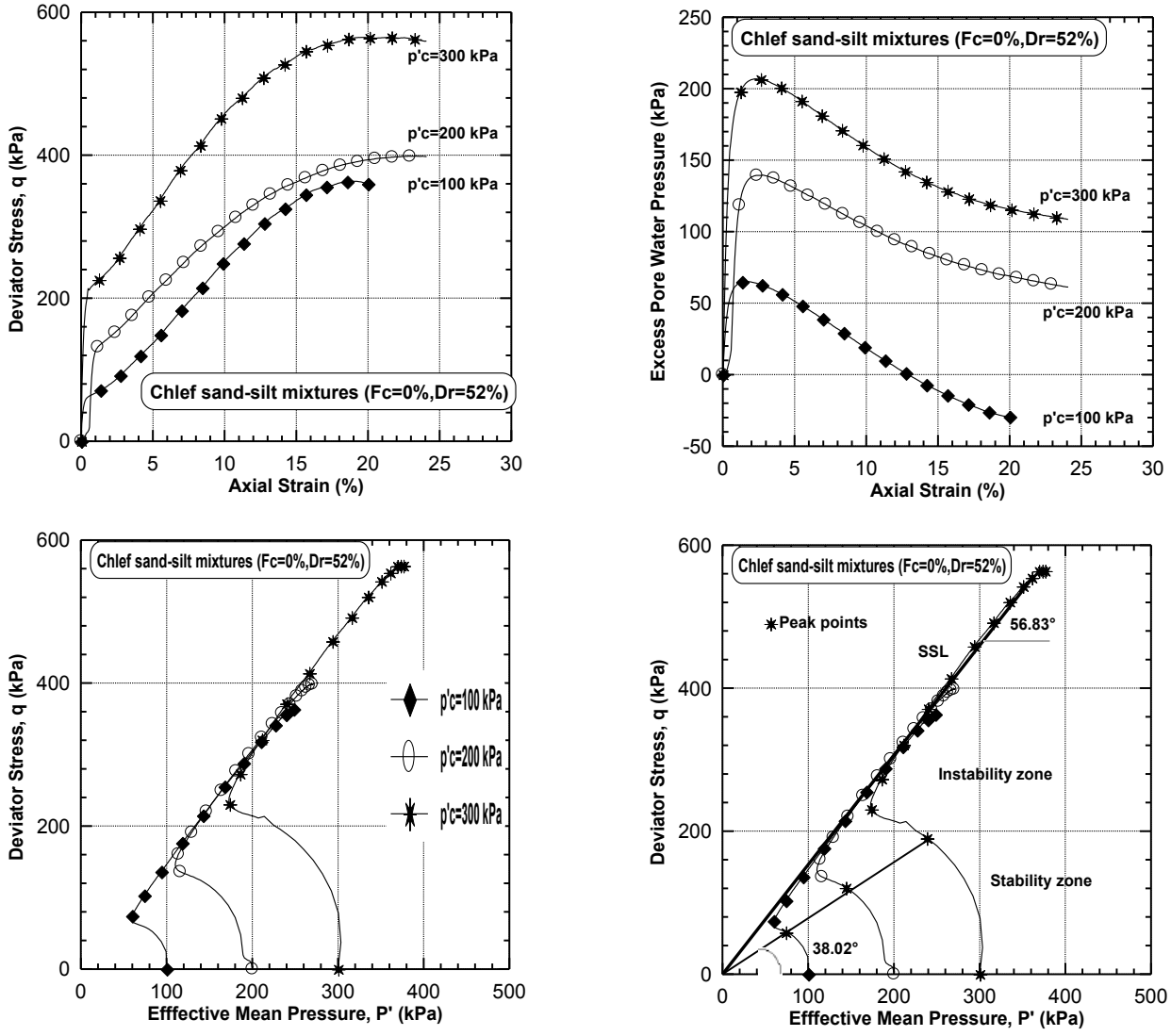

Figure 6. Undrained monotonic behavior of the Chlef sand-silt mixtures (F_c=0%, D_r=52%):
(a): Devitor stress versus axial strain, (b): Excess pore-water pressure versus axial strain,
(c): Deviator stress versus effective mean pressure, (d): Instability and steady-state lines on the effective stress path plane.

(F_c=10%, F_c=20% and F_c=30%). The 30% fines content induces the undrained shear strength values (q_{max}= 57.40 kPa, q_{max}=128.80 kPa, q_{max}= 207.30 kPa) for the initial relative density under consideration (D_r=52%). Moreover, it can be seen that the increase in the low plastic fines induces a decrease in the silty sand liquefaction resistance for all the confining pressures. This behavior results from the role of the fines in increasing the contractiveness of the sand-silt mixtures, leading to a decrease in the maximum shear strength of the mixtures, as illustrated in Figs 6a, 7a, 8a and 9a. The results of this laboratory investigation confirmed the similar tendencies observed by [6, 11, 12, 20, 33 and 40].

Figures 6b, 7b, 8b and 9b present the excess pore-water pressure versus the axial strain for the Chlef sand-silt mixtures, where we found that the influence of the confining pressure is clearly observed for F_c=0% (Δu_{max}=65.15kPa, Δu_{max}=139.6kPa, Δu_{max}=206.8kPa) and continues to increase for F_c=30% (Δu_{max}=85.75kPa,

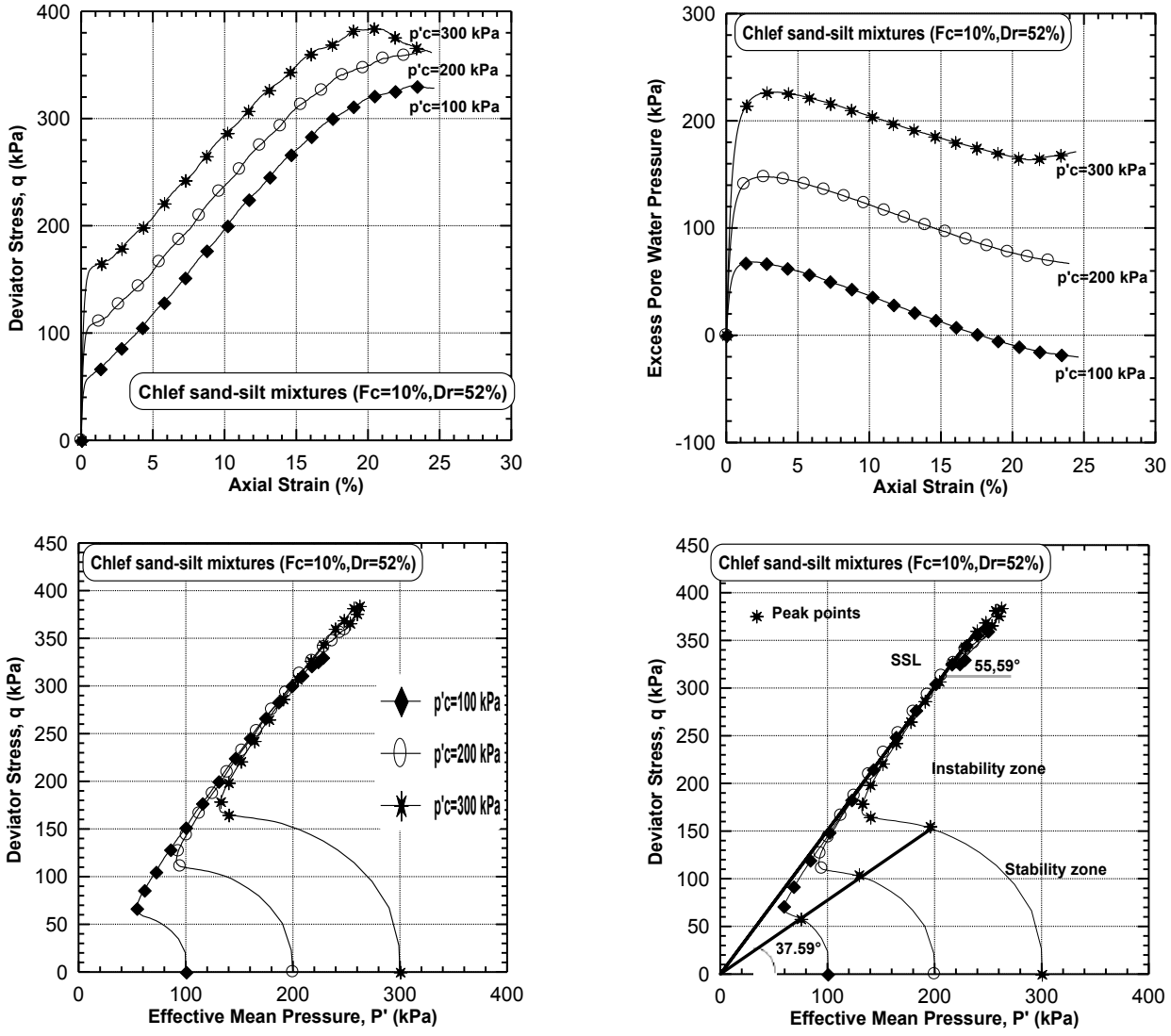

Figure 7. Undrained monotonic behavior of the Chlef sand-silt mixtures (F_c=10%, D_r=52%):
(a): Devitor stress versus axial strain,
(b): Excess pore-water pressure versus axial strain,
(c): Deviator stress versus effective mean pressure,
(d) :Instability and steady-state lines on the effective stress path plane.

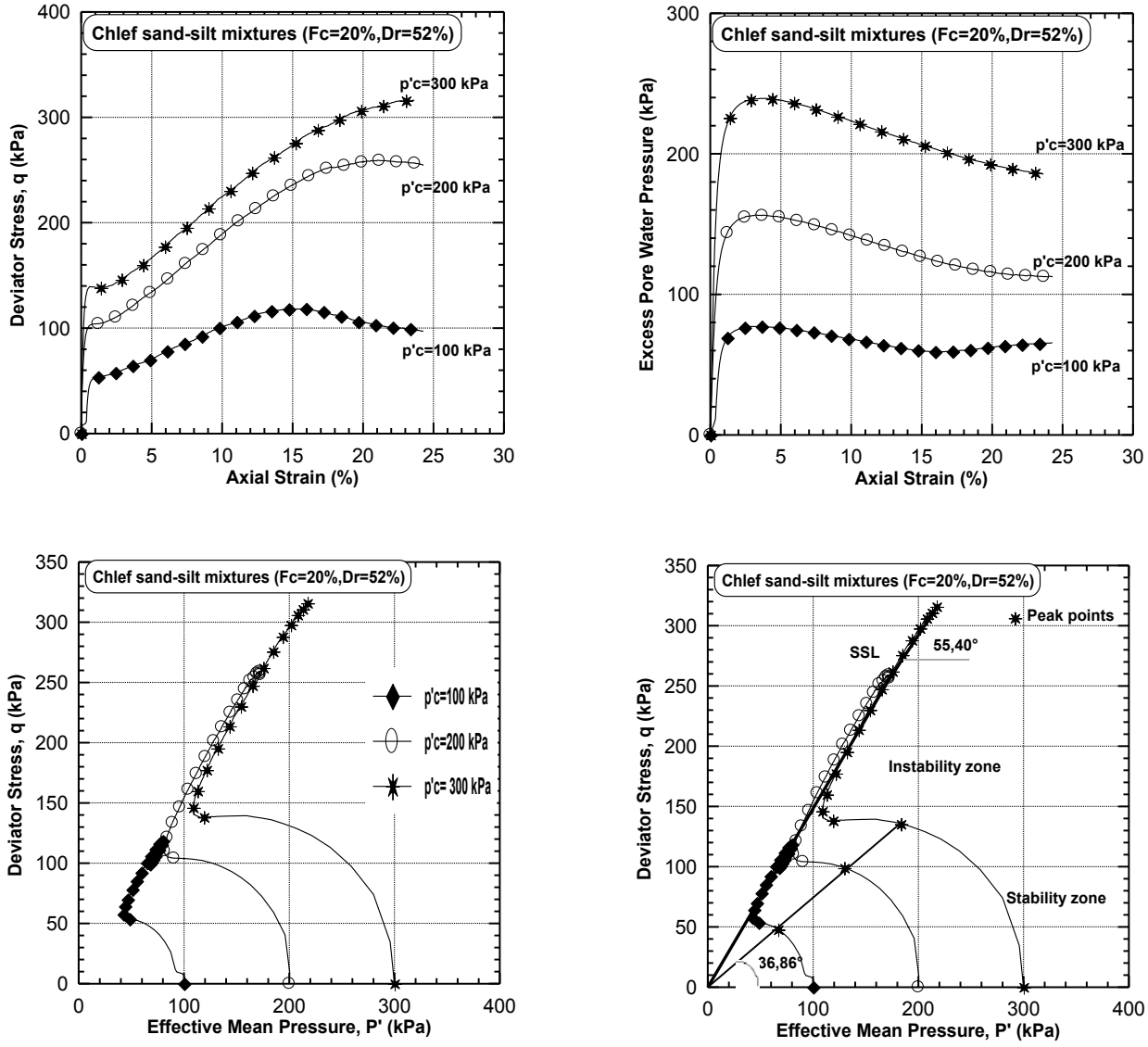

Figure 8. Undrained monotonic behavior of the Chlef sand-silt mixtures (F_c=20%, D_r=52%):
(a): Devitor stress versus axial strain,
(b): Excess pore-water pressure versus axial strain,
(c): Deviator stress versus effective mean pressure,
(d): Instability and steady-state lines on the effective stress path plane.

Δu_{max}=166.1kPa, Δu_{max}=246.9kPa). The stress path p', q shows the role of the confining pressure in increasing the average effective mean pressure and the maximum deviator stress and consequently an increase in the dilatant tendencies of the silty sand samples (Figs 6b, 7b, 8c and 9c). Moreover, Figures 6d, 7d, 8d and 9d show the mobilized instability friction angle (Φ_{ins}) and the mobilized steady-state friction angle (Φ_{ss}) determined from the peak points at the instability zones for the used confining pressures (P_c'=100 kPa, 200 kPa and 300 kPa) considering a single fines content and the steady-state slopes for the different tested Chlef sand-silt mixture samples. These mobilized friction angles decrease from fines fraction F_c=0% to F_c=30% due to the fines content that occupies the voids between the sand particles and consequently decreasing the mobilized friction angle and increasing the instability zones of the Chlef sand-silt mixture samples reconstituted at an initial relative density (D_r=52%) under consideration. Our results are in good agreement with the findings of [13, 27].

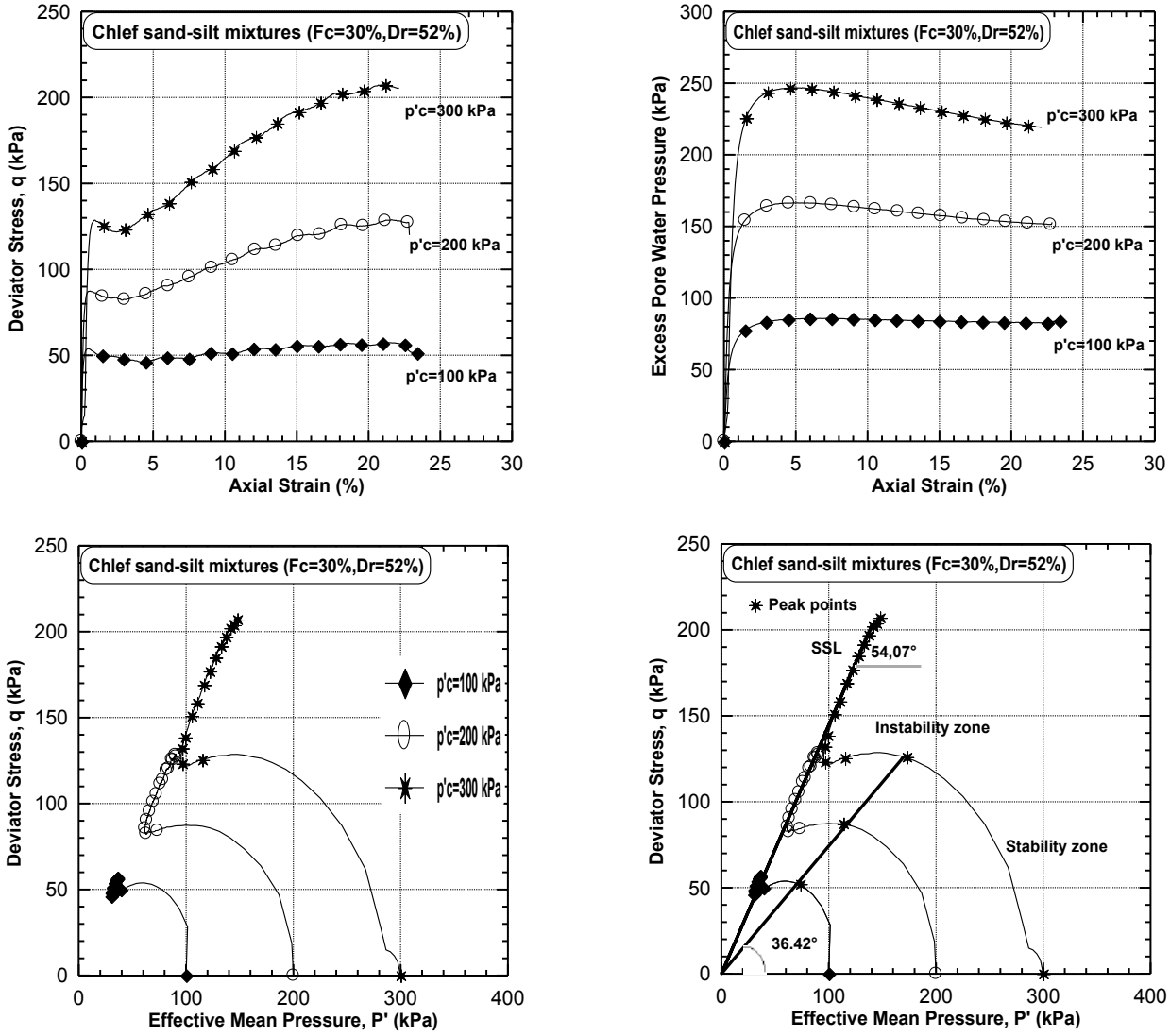

Figure 9. Undrained monotonic behavior of the Chlef sand-silt mixtures (F_c=30%, D_r=52%):
(a): Devitor stress versus axial strain,
(b): Excess pore-water pressure versus axial strain,
(c): Deviator stress versus effective mean pressure,
(d): Instability and steady-state lines on the effective stress path plane.

5 EFFECT OF FINES CONTENT ON THE MOBILIZED FRICTION ANGLES OF THE CHLEF SAND–SILT MIXTURES

For the purpose of analyzing the effect of the fines content (F_c) on the mobilized instability friction angle (Φ_{ins}) determined using the following equation

$$\left[\sin\Phi_{ins} = \left(3\eta'_{ins}\right)/\left(6+\eta'_{ins}\right)\right],$$

where $\acute{\eta}_{ins}$ is the instability stress ratio, which is defined as the slope between the peak stress and the mean effective stress at these peak points in the stress path diagram.

However, the mobilized steady-state friction angle (Φ_{ss}) was determined using the following equation

$$\left[\sin\Phi_{ss} = \left(3M_{ss}\right)/\left(6+M_{ss}\right)\right]],$$

where M_{ss} is the steady-state ratio, which is defined as the slope between the deviator stress and the mean effective stress at the steady state in the stress path diagram. Figure 10 summarizes the obtained results from the current study. It seems that the mobilized instability friction angle and the mobilized steady-state friction angle decrease with increases of the fines content from F_c=0% to F_c=30% and a good linear relationship may

express the correlation between the mobilized friction angle at instability and the steady states with the fines content for the Chlef sand-silt samples reconstituted at an initial relative density (D_r=52%) under consideration. The decrease is due to the role of the low plastic fines in increasing the contractiveness of the Chlef sand-silt mixtures and consequently leading to more unstable soil samples. This is parallel to the finding of [8]. Moreover, it can be shown from these figures that the mobilized steady-state friction angle is higher than the mobilized instability friction angle of the Chlef sand-silt mixtures for the initial relative density (D_r=52%) under study. This behavior is the result from the characterization of the dilitancy of the Chlef sand-silt mixture compared to the contractiveness of the silty sand for the instability state.

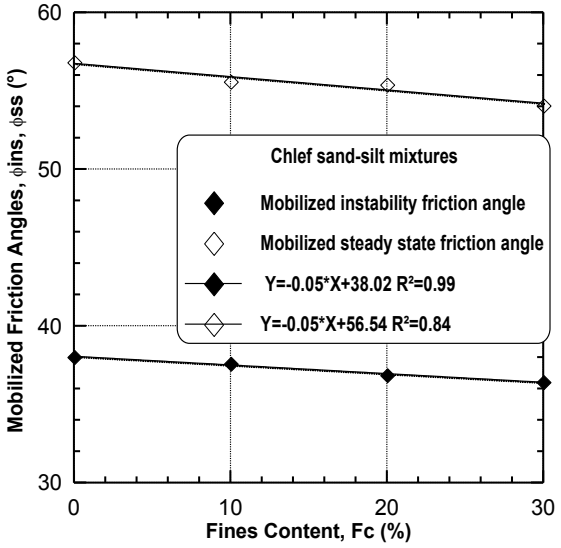

Figure 10. Mobilized friction angles versus fines content.

6 EFFECT OF THE VOID RATIOS ON THE MOBILIZED FRICTION ANGLES OF THE CHLEF SAND-SILT MIXTURES

Figure (11) illustrates the variation of the mobilized instability friction angle (Φ_{ins}) and the mobilized steady-state friction angle (Φ_{ss}) with the initial global void ratio (e) and the intergranular void ratio (e_g) of the Chlef sand-silt mixture samples reconstituted at an initial relative density (D_r=52%) and subjected to three initial confining pressures (P_c'=100 kPa, 200 kPa and 300 kPa) under consideration. The test results indicate that the mobilized friction angles at instability and steady state decrease in a linear manner with a decrease of the initial global void ratio and an increase of the fines content for the Chlef sand-silt mixture samples (Figure 11a). This is the result of the low plastic fines in decreasing the inter-silty sand particles and leading the decreasing of the friction angle between the sand-silt grains. Figure 11b indicates the reverse tendency regarding the relationship between the intergranular void ratio with the mobilized instability friction angle and the mobilized steady-state friction angle of the silty sand. It can be seen from this figure that the mobilized instability friction angle and the mobilized steady-state friction angle decrease with the increase of the intergranular void ratio and the fines content for the Chlef silty sand samples and a linear relationship can express the mobilized instability and the steady-state friction angles as a function of the intergranular void ratio. Moreover, the obtained data confirm the existence of a pertinent relationship

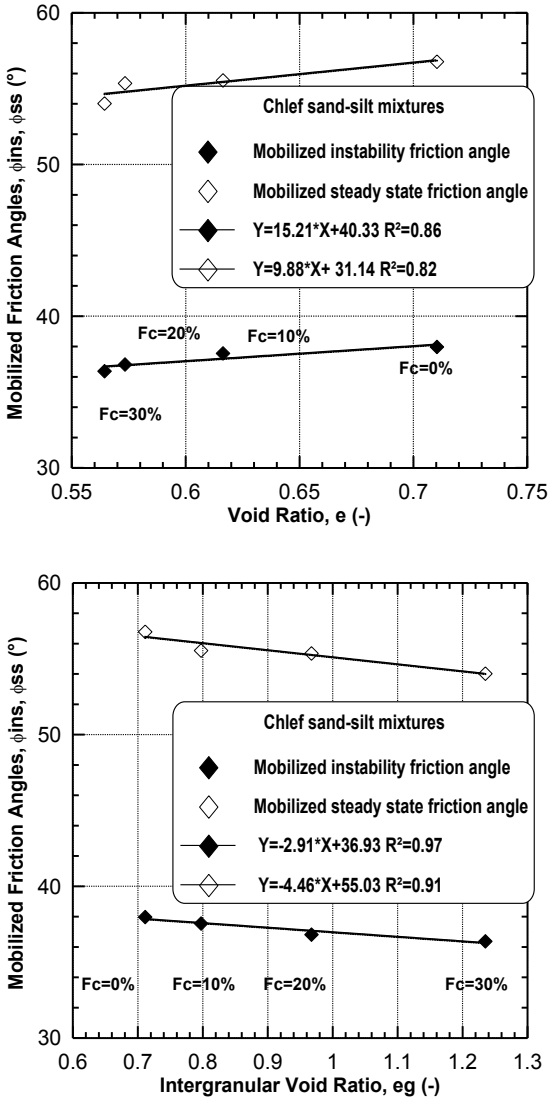

Figure 11. Mobilized friction angle versus void ratio and intergranular void ratio of sand-silt mixtures. (a) Void ratio, (b) Intergranular void ratio.

between the mobilized friction angles and consequently the liquefaction resistance and the intergranular void ratio rather than with the global void ratio for the Chlef sand-silt mixture samples reconstituted at an initial relative density (D_r=52%). This can be attributed to the higher global void ratio (lower fines content) exhibiting higher mobilized friction angles (Φ_{ins}, Φ_{ss}) compared to the higher intergranular void ratio (lower fines content) inducing lower mobilized friction angles (Φ_{ins}, Φ_{ss}).

7 EFFECT OF THE MOBILIZED FRICTION ANGLES ON THE MAXIMUM SHEAR STRENGTH

The influence of the mobilized friction angles at instability and steady state (Φ_{ins}, Φ_{ss}) on the maximum shear strength (q_{max}) of the Chlef sand-silt mixture samples reconstituted at an initial relative density (D_r=52%) are presented in this section. Data from the current study indicate that the mobilized instability friction angle and the mobilized steady-state friction angle decrease with a decrease of the maximum shear strength and increase of the fines content for both materials and a linear relationship is observed relating the maximum shear strength and the mobilized friction angles at the instability and steady states of the Chlef sand-silt mixtures. This behaviour is due to the silty grains acting as voids, leading to a decrease of the force between the inter-silty sand particles and consequently the decreasing of the maximum shear strength of the Chlef sand-silt mixtures. This is parallel to the findings of [11, 13 and 27]. The following expression is proposed to evaluate the relationship between the maximum shear strength (q_{max}), the mobilized instability friction angle, and the mobilized steady-state friction angle (Φ_{ins}, Φ_{ss}) of the tested materials, respectively:

$$\left(q_{max}\right) = a * \left(\Phi_{ins}, \Phi_{SS}\right) + c \qquad (3)$$

Table 5 shows the coefficients a, c and the corresponding coefficient of determination (R^2) for the materials under consideration:

Table 5. Coefficients a, c and R^2 for equation (3).

Chlef sand-silt mixtures	Confining pressure	a	c	R^2
Mobilized instability friction angle	100 kPa	208.42	-7540.59	0.97
	200 kPa	164.27	-5827	0.95
	300 kPa	200.99	-7113.31	0.93
Mobilized steady state friction angle	100 kPa	415.56	-25545.7	0.74
	200 kPa	100.38	-5280.88	0.88
	300 kPa	130.15	-6852.06	0.96

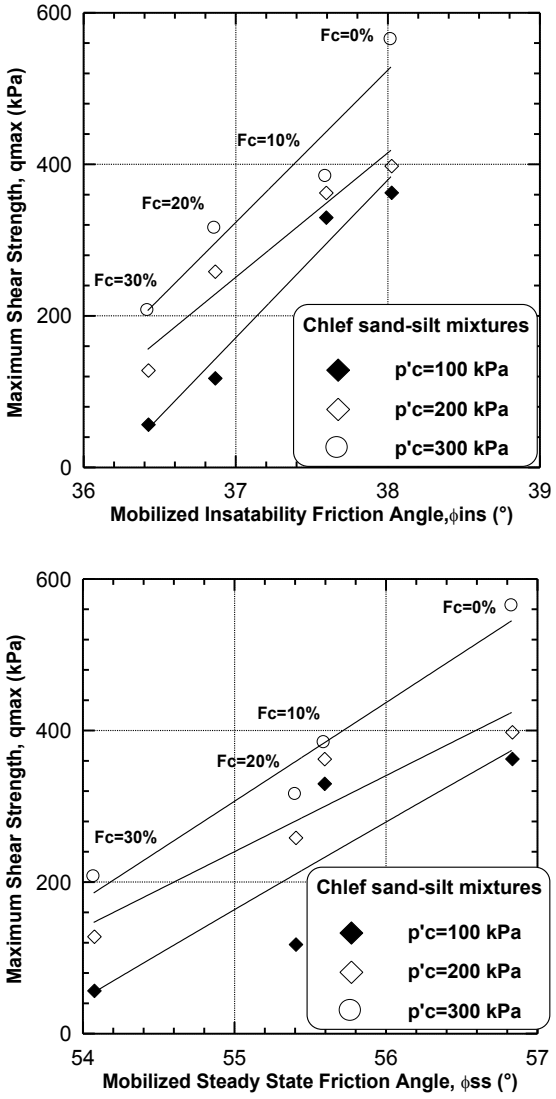

Figure 12. Maximum shear strength versus mobilized friction angles of the Chlef sand-silt mixtures. (a) Mobilized instability friction angle, (b) Mobilized steady-state friction angle.

8 EFFECT OF GRANULOMETRIC CHARACTERISTICS ON THE MOBILIZED FRICTION ANGLES

The effect of grain size (D_{30}, D_{60}), effective diameter (D_{10}) and mean grain size (D_{50}) on the mobilized instability friction angle and mobilized steady-state friction angle (Φ_{ins}, Φ_{ss}) of the Chlef sand-silt mixtures are presented in this section. It can be seen from Figure 13a, b that the mobilized friction angles at instability and steady state decrease with the decrease of the various grain size parameters and increase of the fines

content from F_c=0% to 30% according to a logarithmic relationship for the tested Chlef sand-silt mixture samples reconstituted at an initial relative density (D_r=52%). Moreover, it is clear that the different graded sand-silt mixtures with smaller grain sizes (D_{10}, D_{30}, D_{50} and D_{60}) exhibited the smaller mobilized instability friction angle and mobilized steady-state friction angle (Φ_{ins}, Φ_{ss}) inducing the greater liquefaction susceptibility of the Chlef sand-silt mixtures. Figure 13c presents the effect of the coefficient of uniformity (C_u) on the mobilized instability friction angle and the mobilized steady-state friction angle (Φ_{ins}, Φ_{ss}) of the Chlef sand-silt mixtures. It is clear from this plot that the mobilized instability friction angle and the mobilized steady-state friction angle decease in a logarithmic manner with the increase in the coefficient of uniformity for the range of fines content F_c=0% to F_c=30% of the Chlef sand-silt mixture samples reconstituted at an initial relative density (D_r=52%). This increase might result from the role of the low plastic silty fines (I_p=5%) in increasing the contractiveness of the Chlef sand-silt mixture samples for a given relative density leading to a decrease in the mobilized instability friction angle and the mobilized steady-state friction angle values and consequently to an increase of the excess pore-water pressure and a decrease of the undrained shear strength (liquefaction resistance).The following expression is suggested to evaluate the relationship between the mobilized instability friction angle, the mobilized steady-state friction angle (Φ_{ins}, Φ_{ss}), the grain size (D_{30}, D_{60}), the effective diameter (D_{10}) and the mean grain size (D_{50}) of the Chlef sand-silt mixtures, respectively:

$$\left(\Phi_{ins},\Phi_{SS}\right)=a*\log\left(D_{10},D_{30},D_{50}\ and\ D_{60}\right)+c \qquad (4)$$

Tables 6 show the coefficients a, c and the corresponding coefficient of determination (R^2) for the selected material under consideration:

Table 6. Coefficients a, c and R^2 for equation (4).

Chlef sand-silt mixtures	Grain size	a	c	R^2
Mobilized instability friction angle	D_{10}	0.49	38.74	0.99
	D_{30}	0.93	38.55	0.87
	D_{50}	4.66	40.33	0.98
	D_{60}	6.11	40.14	0.92
Mobilized steady state friction angle	D_{10}	0.74	57.76	0.91
	D_{30}	1.45	57.55	0.87
	D_{50}	7.14	60.29	0.93
	D_{60}	9.91	60.21	0.98

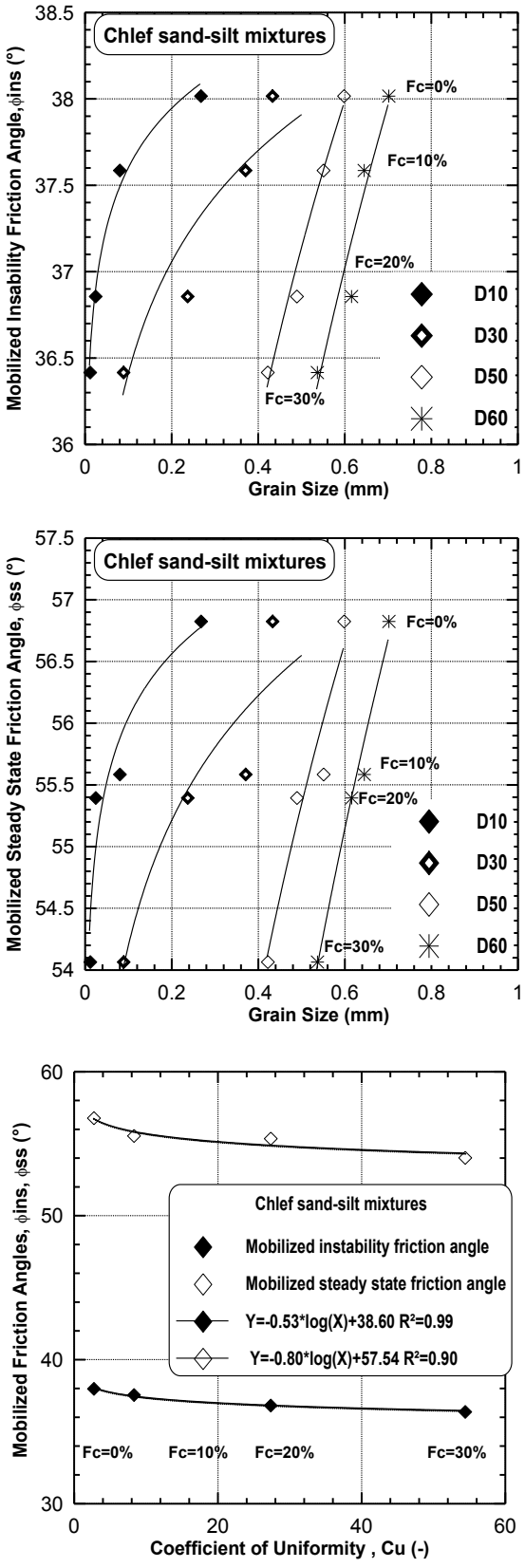

Figure 13. Mobilized friction angles versus grain size of the Chlef sand-silt mixtures. (a) Mobilized instability friction angle, (b) Mobilized steady-state friction angle, (c) Coefficient of uniformity.

9 EFFECT OF GRADING CHARACTERISTICS RATIOS ON THE MOBILIZED FRICTION ANGLES OF THE CHLEF SAND-SILT MIXTURES

The effects of the effective diameter ratio (D_{10R}=D_{10sand}/$D_{10mixture}$), the mean grain size ratio (D_{50R}=D_{50sand}/$D_{50mixture}$), and the coefficient of uniformity ratio (C_{UR}=C_{usand}/$C_{umixture}$) on the mobilized instability friction angle and the mobilized steady-state friction angle (Φ_{ins}, Φ_{ss}) of the Chlef sand-silt mixtures are presented in Figure 14. It is observed from Figure 14a and Figure 14b that the mobilized friction angles during instability and steady state correlate very well ($0.91 \leq R^2 \leq 0.99$) with the effective diameter ratio (D_{10R}=D_{10sand}/$D_{10mixture}$) and the mean grain size ratio (D_{50R}=D_{50sand}/$D_{50mixture}$) according to a logarithmic relationship for the Chlef sand-silt mixture samples reconstituted at the initial relative density under consideration (D_r=52%). The mobilized instability friction angle and the mobilized steady-state friction angle decrease with the increase of D_{10R}, D_{50R} and the fines content ranging from F_c=0% to 30% for the tested materials. Moreover, it is clear from Figures 14a,b for the different graded Chlef sand–silt mixtures that the higher effective diameter ratio (D_{10R}=D_{10sand}/$D_{10mixture}$) and mean grain size ratio (D_{50R}=D_{50sand}/$D_{50mixture}$), the smaller the mobilized friction and steady-state angles (Φ_{ins}, Φ_{ss}) the higher the liquefaction sensitivity of the Chlef sand-silt mixture samples. Figure 14c shows clearly that the mobilized instability friction angle and the mobilized steady-state friction angle (Φ_{ins}, Φ_{ss}) decrease logarithmically with the decrease of the coefficient of uniformity ratio (C_{UR}=C_{usand}/$C_{umixture}$) as the fines content increases from F_c=0% to 30%. The obtained data indicate that the lower the coefficient of uniformity ratio, the lower the mobilized friction angles at instability and in the steady state, the more the liquefaction susceptibility of the Chlef sand-silt mixture samples. The introduced grading characteristics ratios (D_{10R}, D_{50R}, and C_{UR}) appear as suitable parameters that could be used to characterize the Chlef sand-silt mixture liquefaction susceptibility for the fines content range and the initial relative density under consideration.

10 CONCLUSION

An experimental investigation was carried to study the effects of low plastic fines and gradation characteristics (D_{10}, D_{30}, D_{50}, D_{60} and C_u) and granulometric characteristics ratios (D_{10R}, D_{50R} and C_{UR}) on the mobilized friction angle during the instability and steady-state lines of Chlef sand-silt through a series of triaxial compres-

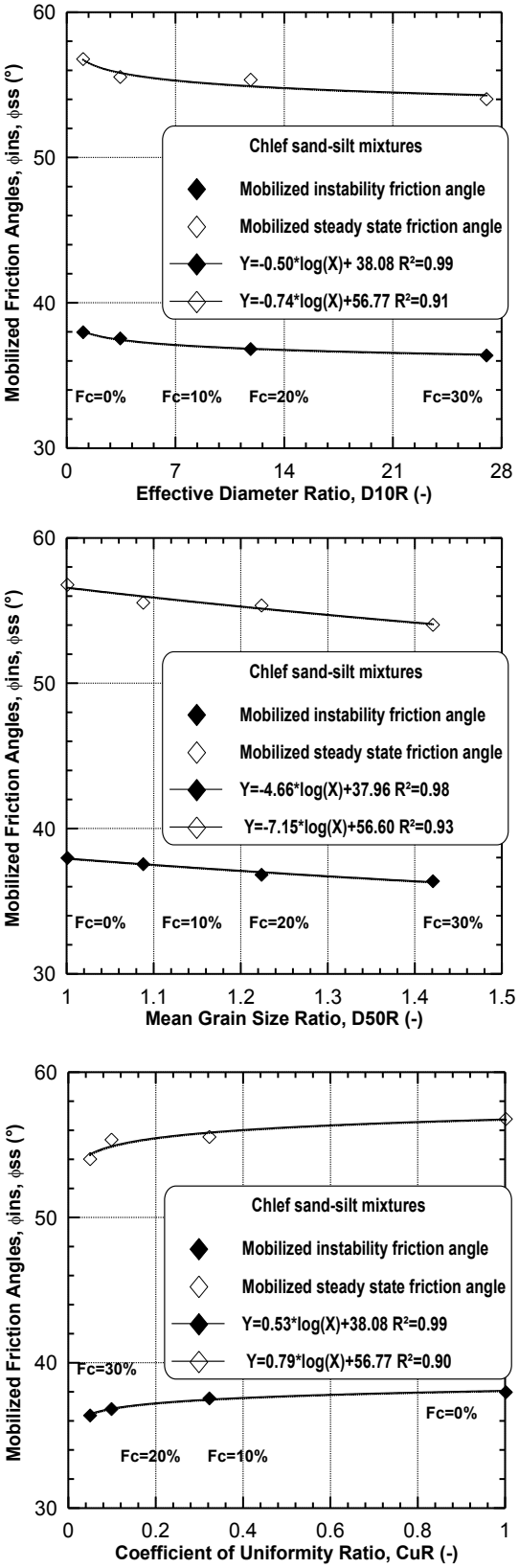

Figure 14. Mobilized friction angles versus grain size ratio of the Chlef sand-silt mixtures. (a) Effective diameter ratio, (b) Mean grain size ratio, (c) Coefficient of uniformity ratio.

sion tests that were carried out on reconstituted medium dense samples (D_r=52%) and subjected to three different confining pressures (P_c'=100 kPa, 200 kPa and 300 kPa). In light of the experimental evidence, the following conclusions can be summarized:

1. Undrained monotonic triaxial compression tests showed that the silty fines and consequently the generated grading characteristics of the sand-silt mixture samples control, in a significant manner, the instability and steady-state mobilized friction angle.

2. The test results indicate that the mobilized instability and steady-state friction angles decrease linearly with the decrease of the maximum shear strength of the Chlef sand-silt mixture. This decrease in the mobilized friction angle leads to an increase in the instability zone and consequently to a decrease in the undrained shear resistance of the used materials. Our results are in good agreement with the findings of [13, 27].

3. The mobilized instability and steady-state friction angles decrease with the increase of the silty fines content. However, they decrease with the decrease of the initial global void ratio and the increase of the intergranular void ratio for the tested materials.

4. The obtained data indicate that the mobilized instability friction angle and the mobilized steady-state friction angle can be correlated with the gradation characteristics such as D_{10}, D_{30}, D_{50}, D_{60} and C_u, D_{10R}, D_{50R}, and C_{UR} of the tested sand-silt mixture samples. In addition, the mobilized friction angles at instability and steady state decrease logarithmically and linearly with the decrease of the grain size (D_{10}, D_{30}, D_{50} and D_{60}), respectively. Moreover, the mobilized instability friction and the mobilized steady-state friction angle decrease in a logarithmic manner with the increase of the coefficient of uniformity for the Chlef sand-silt mixtures.

5. The mobilized friction angle at instability and the steady state, and the granulometric characteristics ratio [(D_{10R}=D_{10sand}/$D_{10mixture}$), (D_{50R}=D_{50sand}/$D_{50mixture}$) and (C_{UR}=C_{usand}/$C_{umixture}$)] display good logarithmic correlations. Indeed, the mobilized instability friction angle and the mobilized steady--state friction angle decrease with an increase of the effective diameter ratio and the mean grain size ratio (D_{10R} and D_{50R}). However, they decrease with the decrease of the coefficient of uniformity ratio (C_{UR}) for the range of tested fines contents.

REFERENCES

[1] ASTM D 4253-00. 2002. Standard test method for maximum index density and unit weight of soils using a vibratory table. Annual Book of ASTM Standards. American Society for Testing and Materials, West Conshohocken, 1–14.

[2] ASTM D 4254-00. 2002. Standard test method for minimum index density and unit weight of soils and calculation of relative density. Annual Book of ASTM Standards. American Society for Testing and Materials, West Conshohocken, 1–9.

[3] Baki, M.A.L., Rahman. M.M., Lo, S.R. 2014. Predicting onset of cyclic instability of loose sand with fines using instability curves. Soil Dynamics and Earthquake Engeering 61-62, 140-151. DOI. org/10.1016

[4] Bayat, M., Bayat, E. 2012. Effect of grading characteristics on the undrained shear strength of sand: review with new evidences. Arab journal of Geosciences 6, 11, 4409-4418. DOI 10.1007/s12517-012-0670-y

[5] Belkhatir, M., Arab, A., Della, N., Missoum, H., Schanz, T. 2010. Liquefaction resistance of Chlef river silty sand: effect of low plastic fines and other parameters. Acta Polytechnica Hungarica 7, 2, 119–137.

[6] Belkhatir, M., Arab, A., Missoum, H., Della, N., Schanz, T. 2011. Laboratory study on the liquefaction resistance of sand-siltmixtures: effect of grading characteristics. Granular Matter 13, 599–609. DOI:10.1007=S10035-011-0269-0

[7] Belkhatir, M., Arab, A., Della, N., Schanz, T. 2012. Experimental study of undrained shear strength of silty sand: effect of fines and gradation. Geotechnical and Geological Engineering 30, 5, 1103-1118. DOI 10.1007/s10706-012-9526-1

[8] Belkhatir, M., Schanz, T., Arab, A., Della, N., Kadri, A. 2014. Insight into the effects of gradation on the pore pressure generation of sand–silt mixtures. Geotechnical testing journal 37, 5, 922-931. DOI: 10.1520/GTJ20130051

[9] Benahmed, N., Canou, J., Dupla, J.C. 2004. Structure initiale et propriétés de liquéfaction statique d'un sable. Comptes Rendus Mécanique 332, 887-894. DOI:10.1016/S1631-0721(04)00185-8

[10] Castro, G. 1969. Liquefaction of Sands. Doctoral thesis, Harvard Soil Mechanics Serie n°81. Harvard Univerity Cambridge Massachussetts.

[11] Cherif Taiba, A., Mahmoudi, Y., Hazout, L., Belkhatir, M., Schanz, T. 2015 Experimental Investigation into the Effect of Granulometric Characteristics Ratio on Undrained Shear Strength of Sand-Silt Mixtures" 13th Arab Structural Engi-

neering conference, University of Blida 1, Algeria.
[12] Cherif Taiba, A., Belkhatir, M., Kadri, A., Mahmoudi, Y., Schanz, T. 2016. Insight into the effect of granulometric characteristics on the static liquefaction susceptibility of silty sand soils. Geotechnical and Geological Engineering journal 34, 1, 367–382. DOI 10.1007/s10706-015-9951-z
[13] Cherif Taiba, A., Mahmoudi, Y., Belkhatir, M., Kadri, A., Schanz, T. 2017a. Experimental Characterization of the Undrained Instability and Steady State of Silty Sand Soils under Monotonic Loading Conditions. International Journal of Geotechnical Engineering 12, 5, 513-529. DOI: 10.1080 /19386362.2017.1302643
[14] Cherif Taiba, A. 2017b. Laboratory Study on Susceptibility of Liquefaction of Silty Sand Soils: Effect of Size and Shape of Grain. PhD Thesis. University of Chlef, Algeria.
[15] Cherif Taiba, A., Mahmoudi, Y., Belkhatir, M., Schanz, T. 2018. Experimental Investigation into the Influence of Roundness and Sphericity on the Undrained Shear Response of Silty Sand Soils. Geotechnical Testing Journal 41, 3. DOI.10.1520/ GTJ20170118
[16] Della, A., Arab, M., Belkhatir, M. 2011. Effect of confining pressure and depositional method on the undrained shearing response of medium dense sand. Journal of Iberian Geology 37, 1, 37-44. DOI: 10.5209/rev_JIGE.2011.v37.n1.3
[17] Huang, Y.T., Huang, A.B., Kuo, Y.C., Tsai, M.D. 2004. A laboratory study on the undrained strength of a silty sand from Central Western Taiwan. Soil Dynamics and Earthquake Engineering 24, 733–743. DOI.org/10.1016/j.soildyn.2004.06.013
[18] Lade, P.V., Duncan, J.M. 1973. Cubical triaxial tests on cohesionless soil. Journal of Soil Mechanics and Foundation Division 99, 10, 793-812.
[19] Lade, P.V. 1992. Static instability and liquefaction of loose sandy slopes. Journal of Geotech Engineering 118, 1, 51–71. DOI.org/10.1061/ (ASCE)0733-9410
[20] Lade, P.V., Yamamuro, J.A. 1997. Effects of nonplastic fines on static liquefaction of sands. Canadian Geotechnocal Journal 34, 6, 918–928. DOI. org/10.1139/t97-052
[21] Liu, Y.J., Li, G., Zhen, Y.Y., Dano, C., Hicher, P.Y., Xiao, H.X., Wang, J.H. 2014. Influence of grading on the undrained behavior of granular materials. Symposium about :Recent Advances in the Mechanics of Granular and Porous Media at the European Solid Mechanics Conference in Graz, Austria.
[22] Mahmoudi, Y., Cherif Taiba, A., Hazout, L., Belkhatir, M., Schanz, T. 2015a. Laboratory Study on Shear Behavior of Overconsolidated Sand: Effect of the Initial Structure. 13th Arab. Structural. Engineering. Conference, Blida, Algeria.
[23] Mahmoudi, Y., Cherif Taiba, A., Belkhatir, M., Schanz, T. 2015b. Experimental investigation on shear strength of overconsolidated soils: Effect of fines content. 7th Symposium on construction in seismic zones, Chlef, Algeria.
[24] Mahmoudi, Y., Cherif Taiba, A., Belkhatir, M., Schanz, T. 2016a. Experimental Investigation on Undrained Shear Behavior of Overconsolidated Sand-Silt Mixtures: Effect of Sample Reconstitution. Geotechnical Testing Journal 39, 3, 515–523. DOI:10.1520/GTJ20140183. ISSN 0149-6115
[25] Mahmoudi, Y., Cherif Taiba, A., Belkhatir, M., Arab, A., Schanz, T. 2016b. Laboratory study on undrained shear behaviour of overconsolidated sand-silt mixtures: effect of the fines content and stress state. International Journal of Geotechnical Engineering 12, 2, 118-132. DOI: 10.1080/19386362.2016.1252140
[26] Mahmoudi, Y., Cherif Taiba, A., Hazout, L., Belkhatir, M., Schanz, T. 2017. Laboratory Research in to the Effects of depositional methods and initial confining Stress on Undrained Instability of sand-silt mixtures. International Symposium on Construction Management and Civil Engineering (ISCMCE-2017) Skikda-Algeria.
[27] Mehdi Abedi, Shahaboddin Yasrobi. 2010. Effects of plastic fines on the instability of sand. Soil Dynamics and Earthquake Engineering 30, 3, 61-67. DOI.org/10.1016
[28] Monkul, M.M., Yamamuro, J.A. 2011. Influence of silt size and content on liquefaction behavior of sands. Canadian Geotechnical Journal 48, 6, 931-942. DOI.org/10.1139/T11-001
[29] Monkul, M.M., Etminan, E., Senol, A. 2016. Infleunce of coefficient of uniformity and base sand gradation on static liquefaction of loose sand with silt. Soil Dynamics and Earthquake Engineering 89, 185-197. DOI.ORG/10.1016
[30] Norimasa Yoshimoto, Yang Wu, Masayuki Hyodo, Yukio Nakata 2016. Effect of relative density on the shear behaviour of granulated coal ash. Goemechanics and Engineering: an international journal 10, 2, 207-224. DOI: 10.12989/gae.2016.10.2.207
[31] Pitman, T.D., Robertson, P.K., Sego, D.C. 1994. Influence of fines on the collapse of loose sands. Canadian Geotechnical Journal 31, 5, 728–739. DOI.ORG/10.1139/T94-084
[32] Polito, C.P. 1999. The effects of non-plastic and plastic fines on the liquefaction of sandy soils. PhD Thesis, Virginia Polytechnic Institute and State University, Virginia, USA.

[33] Singh, S. 1994. Liquefaction characteristics of silts. Special Geotechnical Publication 44, ASCE.
[34] Sladen, J.A., D'Hollonder, R.D., Krahn, J., Mitchell, D.E. 1985. Back analysis of the Nerlek berm liquefaction slides. Canadian Geotechnical Journal 22, 579-588. DOI:10.1139/t85-076
[35] Troncoso, J.H., Verdugo, R. 1985. Silt content and dynamic behaviour of tailing sands. In: Proceedings of 12th International Conference on Soil Mechanics and Foundation Engineering, San Francisco, 1311–1314.
[36] Vaid, Y.P., Fisher, J.M., Kuerbis, R.H., Negussey, D. 1990. Particle Gradation and Liquefaction. Journal of Geotechnical Engineering. 116, 4, 698–703. DOI.org/10.1061/(ASCE)0733-9410
[37] Yamamuro, J.A., Covert, K.M. 2001. Monotonic and cyclic liquefaction of very loose sands with high silt content. Journal of Geotechnical and Geoenvironmental Enginering 127, 4, 314–24. DOI:10.1061/(ASCE)1090-0241
[38] Yamamuro, J.A., Wood, F.M., Lade, P.V. 2008. Effect of depositional method on the microstructure of silty sand. Canadian Geotechnical Journal 45, 11, 1538-1555. DOI:10.1139/T08-080
[39] Yang, S.L., Sandven, R., Grande, L. 2006. Instability of sand-silt mixtures. Soil Dynamics and Earthquake Engineering 26, 2-4, 183–190. DOI. ORG/10.1016
[40] Yilmaz,Y., Mollamahmutoglu, M., Ozaydin,V., Kayabali, K. 2008. Experimental investigation of effect of grading characterstics on the liquefaction resistance of various graded sands. Engneering Geology 100, 3-4, 91-100. J100 :91-100. DOI:10.1016.
[41] Yoshimine, M., Ishihara, K. 1998. Flow potential of sand during liquefaction. Soils and Foundations 38, 3, 189–198. DOI.org/10.3208/sandf.38.3_189

NAVODILA AVTORJEM

Vsebina članka

Članek naj bo napisan v naslednji obliki:

- Naslov, ki primerno opisuje vsebino članka in ne presega 80 znakov.
- Izvleček, ki naj bo skrajšana oblika članka in naj ne presega 250 besed. Izvleček mora vsebovati osnove, jedro in cilje raziskave, uporabljeno metodologijo dela, povzetek izidov in osnovne sklepe.
- Največ 6 ključnih besed, ki bi morale biti napisane takoj po izvlečku.
- Uvod, v katerem naj bo pregled novejšega stanja in zadostne informacije za razumevanje ter pregled izidov dela, predstavljenih v članku.
- Teorija.
- Eksperimentalni del, ki naj vsebuje podatke o postavitvi preiskusa in metode, uporabljene pri pridobitvi izidov.
- Izidi, ki naj bodo jasno prikazani, po potrebi v obliki slik in preglednic.
- Razprava, v kateri naj bodo prikazane povezave in posplošitve, uporabljene za pridobitev izidov. Prikazana naj bo tudi pomembnost izidov in primerjava s poprej objavljenimi deli.
- Sklepi, v katerih naj bo prikazan en ali več sklepov, ki izhajajo iz izidov in razprave.
- Vse navedbe v besedilu morajo biti na koncu zbrane v seznamu literature, in obratno.

Dodatne zahteve

- Vrstice morajo biti zaporedno oštevilčene.
- Predložen članek ne sme imeti več kot 18 strani (brez tabel, legend in literature); velikost črk 12, dvojni razmik med vrsticami. V članek je lahko vključenih največ 10 slik. Isti rezultati so lahko prikazani v tabelah ali na slikah, ne pa na oba načina.
- Potrebno je priložiti imena, naslove in elektronske naslove štirih potencialnih recenzentov članka. Urednik ima izključno pravico do odločitve, ali bo te predloge upošteval.

Enote in okrajšave

V besedilu, preglednicah in slikah uporabljajte le standardne označbe in okrajšave SI. Simbole fizikalnih veličin v besedilu pišite poševno (npr. *v*, *T* itn.). Simbole enot, ki so sestavljene iz črk, pa pokončno (npr. Pa, m itn.). Vse okrajšave naj bodo, ko se prvič pojavijo, izpisane v celoti.

Slike

Slike morajo biti zaporedno oštevilčene in označene, v besedilu in podnaslovu, kot sl. 1, sl. 2 itn. Posnete naj bodo v katerem koli od razširjenih formatov, npr. BMP, JPG, GIF. Za pripravo diagramov in risb priporočamo CDR format (CorelDraw), saj so slike v njem vektorske in jih lahko pri končni obdelavi preprosto povečujemo ali pomanjšujemo.

Pri označevanju osi v diagramih, kadar je le mogoče, uporabite označbe veličin (npr. *v*, *T* itn.). V diagramih z več krivuljami mora biti vsaka krivulja označena. Pomen oznake mora biti razložen v podnapisu slike.

Za vse slike po fotografskih posnetkih je treba priložiti izvirne fotografije ali kakovostno narejen posnetek.

Preglednice

Preglednice morajo biti zaporedno oštevilčene in označene, v besedilu in podnaslovu, kot preglednica 1, preglednica 2 itn. V preglednicah ne uporabljajte izpisanih imen veličin, ampak samo ustrezne simbole. K fizikalnim količinam, npr. *t* (pisano poševno), pripišite enote (pisano pokončno) v novo vrsto brez oklepajev. Vse opombe naj bodo označene z uporabo dvignjene številke[1].

Seznam literature

Navedba v besedilu

Vsaka navedba, na katero se sklicujete v besedilu, mora biti v seznamu literature (in obratno). Neobjavljeni rezultati in osebne komunikacije se ne priporočajo v seznamu literature, navedejo pa se lahko v besedilu, če je nujno potrebno.

Oblika navajanja literature

V besedilu: Navedite reference zaporedno po številkah v oglatih oklepajih v skladu z besedilom. Dejanski avtorji so lahko navedeni, vendar mora obvezno biti podana referenčna številka.

Primer: »..... kot je razvidno [1,2]. Brandl and Blovsky [4], sta pridobila drugačen rezultat…«

V seznamu: Literaturni viri so oštevilčeni po vrstnem redu, kakor se pojavijo v članku. Označimo jih s številkami v oglatih oklepajih.

Sklicevanje na objave v revijah:

[1] Jelušič, P., Žlender, B. 2013. Soil-nail wall stability analysis using ANFIS. Acta Geotechnica Slovenica 10(1), 61-73.

Sklicevanje na knjigo:
[2] Šuklje, L. 1969. Rheological aspects of soil mechanics. Wiley-Interscience, London
Sklicevanje na poglavje v monografiji:
[3] Mitchel, J.K. 1992. Characteristics and mechanisms of clay creep and creep rupture, in N. Guven, R.M. Pollastro (eds.), Clay-Water Interface and Its Rheological Implications, CMS Workshop Lectures, Vol. 4, The clay minerals Society, USA, pp. 212-244..
Sklicevanje na objave v zbornikih konferenc:
[4] Brandl, H., Blovsky, S. 2005. Slope stabilization with socket walls using the observational method. Proc. Int. conf. on Soil Mechanics and Geotechnical Engineering, Bratislava, pp. 2485-2488.
Sklicevanje na spletne objave:
[5] Kot najmanj, je potrebno podati celoten URL. Če so poznani drugi podatki (DOI, imena avtorjev, datumi, sklicevanje na izvorno literaturo), se naj prav tako dodajo.

Podatki o avtorjih

Članku priložite tudi podatke o avtorjih: imena, nazive, popolne poštne naslove, številke telefona in faksa, naslove elektronske pošte. Navedite kontaktno osebo.

Sprejem člankov in avtorske pravlce

Uredništvo si pridržuje pravico do odločanja o sprejemu članka za objavo, strokovno oceno mednarodnih recenzentov in morebitnem predlogu za krajšanje ali izpopolnitev ter terminološke in jezikovne korekture. Z objavo preidejo avtorske pravice na revijo ACTA GEOTECHNICA SLOVENICA. Pri morebitnih kasnejših objavah mora biti AGS navedena kot vir.

Vsa nadaljnja pojasnila daje:

Uredništvo
ACTA GEOTECHNICA SLOVENICA
Univerza v Mariboru,
Fakulteta za gradbeništvo, prometno inženirstvo in arhitekturo
Smetanova ulica 17, 2000 Maribor, Slovenija
E-pošta: ags@um.si

INSTRUCTIONS FOR AUTHORS

Format of the paper

The paper should have the following structure:

- A Title, which adequately describes the content of the paper and should not exceed 80 characters;
- An Abstract, which should be viewed as a mini version of the paper and should not exceed 250 words. The Abstract should state the principal objectives and the scope of the investigation and the methodology employed; it should also summarise the results and state the principal conclusions;
- Immediately after the abstract, provide a maximum of 6 keywords;
- An Introduction, which should provide a review of recent literature and sufficient background information to allow the results of the paper to be understood and evaluated;
- A Theoretical section;
- An Experimental section, which should provide details of the experimental set-up and the methods used to obtain the results;
- A Results section, which should clearly and concisely present the data, using figures and tables where appropriate;
- A Discussion section, which should describe the relationships shown and the generalisations made possible by the results and discuss the significance of the results, making comparisons with previously published work;
- Conclusions, which should present one or more conclusions that have been drawn from the results and subsequent discussion;
- A list of References, which comprises all the references cited in the text, and vice versa.

Additional Requirements for Manuscripts

- Use double line-spacing.
- Insert continuous line numbering.
- The submitted text of Research Papers should cover no more than 18 pages (without Tables, Legends, and References, style: font size 12, double line spacing). The number of illustrations should not exceed 10. Results may be shown in tables or figures, but not in both of them.
- Please submit, with the manuscript, the names, addresses and e-mail addresses of four potential referees. Note that the editor retains the sole right to decide whether or not the suggested reviewers are used.

Units and abbreviations

Only standard SI symbols and abbreviations should be used in the text, tables and figures. Symbols for physical quantities in the text should be written in Italics (e.g. *v*, *T*, etc.). Symbols for units that consist of letters should

be in plain text (e.g. Pa, m, etc.).
All abbreviations should be spelt out in full on first appearance.

Figures

Figures must be cited in consecutive numerical order in the text and referred to in both the text and the caption as Fig. 1, Fig. 2, etc. Figures may be saved in any common format, e.g. BMP, JPG, GIF. However, the use of CDR format (CorelDraw) is recommended for graphs and line drawings, since vector images can be easily reduced or enlarged during final processing of the paper.

When labelling axes, physical quantities (e.g. *v*, *T*, etc.) should be used whenever possible. Multi-curve graphs should have individual curves marked with a symbol; the meaning of the symbol should be explained in the figure caption. Good quality black-and-white photographs or scanned images should be supplied for the illustrations.

Tables

Tables must be cited in consecutive numerical order in the text and referred to in both the text and the caption as Table 1, Table 2, etc. The use of names for quantities in tables should be avoided if possible: corresponding symbols are preferred. In addition to the physical quantity, e.g. *t* (in Italics), units (normal text), should be added on a new line without brackets.
Any footnotes should be indicated by the use of the superscript[1].

LIST OF references

Citation in text

Please ensure that every reference cited in the text is also present in the reference list (and vice versa). Any references cited in the abstract must be given in full. Unpublished results and personal communications are not recommended in the reference list, but may be mentioned in the text, if necessary.

Reference style

Text: Indicate references by number(s) in square brackets consecutively in line with the text. The actual authors can be referred to, but the reference number(s) must always be given:

Example: "... as demonstrated [1,2]. Brandl and Blovsky [4] obtained a different result ..."

List: Number the references (numbers in square brackets) in the list in the order in which they appear in the text.

Reference to a journal publication:
[1] Jelušič, P., Žlender, B. 2013. Soil-nail wall stability analysis using ANFIS. Acta Geotechnica Slovenica 10(1), 61-73.

Reference to a book:
[2] Šuklje, L. 1969. Rheological aspects of soil mechanics. Wiley-Interscience, London

Reference to a chapter in an edited book:
[3] Mitchel, J.K. 1992. Characteristics and mechanisms of clay creep and creep rupture, in N. Guven, R.M. Pollastro (eds.), Clay-Water Interface and Its Rheological Implications, CMS Workshop Lectures, Vol. 4, The clay minerals Society, USA, pp. 212-244.

Conference proceedings:
[4] Brandl, H., Blovsky, S. 2005. Slope stabilization with socket walls using the observational method. Proc. Int. conf. on Soil Mechanics and Geotechnical Engineering, Bratislava, pp. 2485-2488.

Web references:
[5] As a minimum, the full URL should be given and the date when the reference was last accessed. Any further information, if known (DOI, author names, dates, reference to a source publication, etc.), should also be given.

Author information

The following information about the authors should be enclosed with the paper: names, complete postal addresses, telephone and fax numbers and E-mail addresses. Indicate the name of the corresponding author.

Acceptance of papers and copyright

The Editorial Committee of the Slovenian Geotechnical Review reserves the right to decide whether a paper is acceptable for publication, to obtain peer reviews for the submitted papers, and if necessary, to require changes in the content, length or language.
On publication, copyright for the paper shall pass to the ACTA GEOTECHNICA SLOVENICA. The AGS must be stated as a source in all later publication.

For further information contact:

Editorial Board
ACTA GEOTECHNICA SLOVENICA
University of Maribor,
Faculty of Civil Engineering, Transportation Engineering and Architecture
Smetanova ulica 17, 2000 Maribor, Slovenia
E-mail: ags@um.si

NAMEN REVIJE

Namen revije ACTA GEOTECHNICA SLOVENICA je objavljanje kakovostnih teoretičnih člankov z novih pomembnih področij geomehanike in geotehnike, ki bodo dolgoročno vplivali na temeljne in praktične vidike teh področij.

ACTA GEOTECHNICA SLOVENICA objavlja članke s področij: mehanika zemljin in kamnin, inženirska geologija, okoljska geotehnika, geosintetika, geotehnične konstrukcije, numerične in analitične metode, računalniško modeliranje, optimizacija geotehničnih konstrukcij, terenske in laboratorijske preiskave.

Revija redno izhaja dvakrat letno.

AIMS AND SCOPE

ACTA GEOTECHNICA SLOVENICA aims to play an important role in publishing high-quality, theoretical papers from important and emerging areas that will have a lasting impact on fundamental and practical aspects of geomechanics and geotechnical engineering.

ACTA GEOTECHNICA SLOVENICA publishes papers from the following areas: soil and rock mechanics, engineering geology, environmental geotechnics, geosynthetic, geotechnical structures, numerical and analytical methods, computer modelling, optimization of geotechnical structures, field and laboratory testing.

The journal is published twice a year.

AVTORSKE PRAVICE

Ko uredništvo prejme članek v objavo, prosi avtorja(je), da prenese(jo) avtorske pravice za članek na izdajatelja, da bi zagotovili kar se da obsežno razširjanje informacij. Naša revija in posamezni prispevki so zaščiteni z avtorskimi pravicami izdajatelja in zanje veljajo naslednji pogoji:

Fotokopiranje

V skladu z našimi zakoni o zaščiti avtorskih pravic je dovoljeno narediti eno kopijo posameznega članka za osebno uporabo. Za naslednje fotokopije, vključno z večkratnim fotokopiranjem, sistematičnim fotokopiranjem, kopiranjem za reklamne ali predstavitvene namene, nadaljnjo prodajo in vsemi oblikami nedobičkonosne uporabe je treba pridobiti dovoljenje izdajatelja in plačati določen znesek.

Naročniki revije smejo kopirati kazalo z vsebino revije ali pripraviti seznam člankov z izvlečki za rabo v svojih ustanovah.

Elektronsko shranjevanje

Za elektronsko shranjevanje vsakršnega gradiva iz revije, vključno z vsemi članki ali deli članka, je potrebno dovoljenje izdajatelja.

COPYRIGHT

Upon acceptance of an article by the Editorial Board, the author(s) will be asked to transfer copyright for the article to the publisher. This transfer will ensure the widest possible dissemination of information. This review and the individual contributions contained in it are protected by publisher's copyright, and the following terms and conditions apply to their use:

Photocopying

Single photocopies of single articles may be made for personal use, as allowed by national copyright laws. Permission of the publisher and payment of a fee are required for all other photocopying, including multiple or systematic copying, copying for advertising or promotional purposes, resale, and all forms of document delivery.

Subscribers may reproduce tables of contents or prepare lists of papers, including abstracts for internal circulation, within their institutions.

Electronic Storage

Permission of the publisher is required to store electronically any material contained in this review, including any paper or part of the paper.

ODGOVORNOST

Revija ne prevzame nobene odgovornosti za poškodbe in/ali škodo na osebah in na lastnini na podlagi odgovornosti za izdelke, zaradi malomarnosti ali drugače, ali zaradi uporabe kakršnekoli metode, izdelka, navodil ali zamisli, ki so opisani v njej.

RESPONSIBILITY

No responsibility is assumed by the publisher for any injury and/or damage to persons or property as a matter of product liability, negligence or otherwise, or from any use or operation of any methods, products, instructions or ideas contained in the material herein.

9 771854 017001

University of Maribor
Faculty of Civil Engineering, Transportation Engineering and Architecture
www.fgpa.um.si

SLOVENSKO GEOTEHNIŠKO DRUŠTVO
SLOVENIAN GEOTECHNICAL SOCIETY
www.sloged.si

University of Ljubljana
Faculty of Civil and Geodetic Engineering
Faculty of Natural Sciences and Engineering
www.fgg.uni-lj.si
www.ntf.uni-lj.si

SLOVENSKO DRUŠTVO ZA PODZEMNE GRADNJE
SLOVENIAN SOCIETY FOR UNDERGROUND STRUCTURES
www.ita-slovenia.si